2015-01-28

# Teleoperation of MRI-Compatible Robots with Hybrid Actuation and Haptic Feedback

Weijian Shang
*Worcester Polytechnic Institute*

# Teleoperation of MRI-Compatible Robots with Hybrid Actuation and Haptic Feedback

by

Weijian Shang

A Dissertation

Submitted to the Faculty of the

WORCESTER POLYTECHNIC INSTITUTE

in partial fulfillment of the requirements for the

Degree of Doctor of Philosophy

in

Mechanical Engineering

by

_____

December, 2014

Approved:

_____

Prof. Gregory S. Fischer, Advisor

_____

Prof. John M. Sullivan Jr., Committee Member

_____

Prof. Cagdas D. Onal, Committee Member

_____

Prof. Iulian I. Iordachita, Committee Member
(Johns Hopkins University)

_____

Prof. Raghvendra V. Cowlagi, Graduate Committee Representative

# Abstract

Image guided surgery (IGS), which has been developing fast recently, benefits significantly from the superior accuracy of robots and magnetic resonance imaging (MRI) which is a great soft tissue imaging modality. Teleoperation is especially desired in the MRI because of the highly constrained space inside the closed-bore MRI and the lack of haptic feedback with the fully autonomous robotic systems. It also very well maintains the human in the loop that significantly enhances safety.

This dissertation describes the development of teleoperation approaches and implementation on an example system for MRI with details of different key components. The dissertation firstly describes the general teleoperation architecture with modular software and hardware components. The MRI-compatible robot controller, driving technology as well as the robot navigation and control software are introduced.

As a crucial step to determine the robot location inside the MRI, two methods of registration and tracking are discussed. The first method utilizes the existing Z shaped fiducial frame design but with a newly developed multi-image registration method which has higher accuracy with a smaller fiducial frame. The second method

is a new fiducial design with a cylindrical shaped frame which is especially suitable for registration and tracking for needles. Alongside, a single-image based algorithm is developed to not only reach higher accuracy but also run faster. In addition, performance enhanced fiducial frame is also studied by integrating self-resonant coils.

A surgical master-slave teleoperation system for the application of percutaneous interventional procedures under continuous MRI guidance is presented. The slave robot is a piezoelectric-actuated needle insertion robot with fiber optic force sensor integrated. The master robot is a pneumatic-driven haptic device which not only controls the position of the slave robot, but also renders the force associated with needle placement interventions to the surgeon. Both of master and slave robots mechanical design, kinematics, force sensing and feedback technologies are discussed. Force and position tracking results of the master-slave robot are demonstrated to validate the tracking performance of the integrated system. MRI compatibility is evaluated extensively. Teleoperated needle steering is also demonstrated under live MR imaging.

A control system of a clinical grade MRI-compatible parallel 4-DOF surgical manipulator for minimally invasive in-bore prostate percutaneous interventions through the patient's perineum is discussed in the end. The proposed manipulator takes advantage of four sliders actuated by piezoelectric motors and incremental rotary encoders, which are compatible with the MRI environment. Two generations of optical limit switches are designed to provide better safety features for real clinical use.

The performance of both generations of the limit switch is tested. MRI guided accuracy and MRI-compatibility of whole robotic system is also evaluated. Two clinical prostate biopsy cases have been conducted with this assistive robot.

# Acknowledgements

I am honored to have the chance to thank all of those who helped me to make this dissertation possible.

I would like to first express my greatest gratitude to my advisor, Prof. Gregory Fischer for his thoughtful guidance and generous support through the years. As a researcher, you are so talented, dedicated to the cutting-edge technologies which benefit the health of human life. As a teacher, you tirelessly guide me with your broad knowledge towards my career goals and give me generous support and great advices on my decisions.

I would like to thank Prof. Iulian Iordachita for the guidance during our collaboration, especially during my visit at JHU. I am grateful to having the chance to work with you.

I would also like to thank Prof. John Sullivan, Prof. Cagdas Onal and Prof. Raghvendra Cowlagi for being my committee members and giving me valuable advices to make my dissertation stronger.

I am so lucky to have my labmates whom I spent every day with like a family.

Thank you to Michael Delph, Chris Nycz, Zhixian Zhang, Adnan Munawar, Hanlin Hong, Miaobo Li, Xiaoan Yan, Yuanfang Gui, Satyanarayana Janga, Dr. Guangda Lu and especially Gang Li, Niravkumar Patel, Dr. Hao Su, Dr. Gregory Cole, Kevin Harrington, Alexandra Camilo, Yunzhao Ma, Wenzhi Ji, Yi Wang and Tim Van Kawijk who directly worked with me in the same projects.

I would like to thank all of the collaborators. They are Prof. Clare Tempany, Prof. Nobuhiko Hata, Prof. Junichi Tokuda, Dr. Kemal Tuncali from Brigham and Women's Hospital, Harvard Medical School; Dr. Sohrab Eslami, Dr. Kiyoung Kim from Johns Hopkins University and many others. I would also like to thank my colleagues for providing me their generous help on my research. They are Prof. Cosme Furlong, Dr. Ivo T. Dobrev, Prof. Reinhold Ludwig, Prof. Gene Bogdanov, Peter Hefti from WPI; Dr. Shaokuan Zheng from UMass Medical School and Prof. Russell Taylor, Nathan Bongjoon Cho from JHU.

And of course I want to thank WPI mechanical and robotics engineering staff members: Barbara Edilberti, Barbara Furhman, Statia Canning, Randy Robinson, Pam St. Louis, and Tracey Coetzee.

Also, I want to thank my friends who make my life colorful. They are Ruixiang Du, Xianchao Long, Qian He, Jia Wang, Mi Tian, Dr. Jun Yang, Dr. Yue Wang, Zhijia Jin, Lei Zhang, Dr. Hao Yu, Yang Ge, Mianzhi Wang, Xiaoran Chen, Weiyuan Tie, Yi Ding, Ming Luo, Yao Wang, Haocheng Li, Haoran Wang, Yijun Dong, Xin Su, Kehui Chen, Weina Lu, Wenchang Xiao, Yacan Gao, Ruikun Luo, Dr. Jienan Ding,

Haogang Cai, Wen Guo, Dr. Tianquan Jin, Xingchi He, Changyu He, Dr. Yiqing Lu, Yunfeng Gao, Li Xu, Yafang Chen, Bowei Tang, and so many others.

I would like to thank Congressionally Directed Medical Research Programs and National Institute of Health for the funding support.

Finally, I want to express my love to my parents Pingping Wang and Jinqi Shang for supporting me studying in US and the understanding of me not being able to visit them often. I also want to thank Xiaofeng Shang, Bernard Katz, Amanda Rui Jin and Willow Liu Yang, who are my family members here in US for their help through all these years.

Special thank to my girlfriend Shuaimin Liu. Thanks for bringing me joy and happiness everyday. I love you.

In the end, I am grateful to all of the help and support I got to make this dissertation possible.

# Dedication

This dissertation is dedicated to my parents Pingping Wang and Jinqi Shang.

# Contents

# List of Tables

# List of Figures

# Acronyms

**ABS** Acrylonitrile Butadiene Styrene

**AMP** Linear Amplifier

**ASTM** American Society for Testing and Materials

**BRW** Brown-Roberts-Wells

**BWH** Brigham and Women's Hospital

**CAD** Computer-aided Design

**CPI** Counts Per Inch

**CPR** Counts Per Revolution

**CHIC** Cylindrical Helix Imaging Coordinate

**CT** Computed Tomography

**CZ** Central Zone

**DAC** Digital-to-Analog Converter

**DICOM** Digital Imaging and Communications in Medicine

**DOF** Degree of Freedom

**EPI** Echo Planar Imaging

**ERF** Electro-Rheological Fluids

**FBG** Fiber Bragg Grating

**FDA** Food and Drug Administration

**FEA** Finite Element Analysis

**FLASH** Fast Low-Angle Shot

**fMRI** functional Magnetic Resonance Imaging

**FOV** Field of View

**FPGA** Field Programmable Gate Array

**FPI** Fabry-Perot Interferometer

**GUI** Graphical User Interface

**IGT** Image-Guided Therapy

**IRB** Institutional Review Board

**LPR** Light Puncture Robot

**LPS** Left Posterior Superior

**LVDS** Low-Voltage Differential Signaling

**MRI** Magnetic Resonance Imaging

**NEMA** National Electronic Manufacturers Association

**NIH** National Institutes of Health

**OLS** Ordinary Least Square

**OTS** Optical Tracking System

**PCA** Principal Component Analysis

**PCa** Prostate cancer

**PZ** Peripheral Zone

**RAS** Right Anterior Superior

**RF** Radio Frequency

**RFA** Radio Frequency Ablation

**RMS** Root Mean Square

**SMA** Shape Memory Alloy

**SNR** Signal-to-Noise Ratio

**TRUS** Transrectal Ultrasound

**TZ** Transition Zone

**US** Ultrasound

**VHDCI** Very-High-Density Cable Interconnect

**XML** Extensible Markup Language

# Chapter 1

# Introduction

## 1.1 Background and Motivation

Image-guided therapy (IGT), through the use of medical imaging to plan, perform, and evaluate surgical procedures and therapeutic interventions, brings surgeries much more precision and less invasiveness. Its first concept was proposed more than a century ago in 1908 [1], but it started to flourish in the early 90 s with the establishment for the Image-Guided Therapy program at Brigham and Women's Hospital (BWH) [2]. As one of the most commonly used modalities of image-guided therapy, Magnetic Resonance Imaging (MRI) has been evolving since its debut in 80 s, from the clam shell type, cylinder, double donuts to closed bore type, from less than 1 Tesla to 21.1 Tesla [3]. The stronger magnetic field brings the higher signal-to-noise ratio (SNR) thus improves spatial and temporal resolution. It surpasses other imaging

modalities with better soft tissue imaging ability while having volumetric, real-time multi-parametric imaging and maintaining no ionizing radiation at all. Taking advantage of aforementioned features, interventional MRI is becoming a great alternative to conventional Computed Tomography (CT) and ultrasound (US)-guided interventions.

It seems natural that MRI guided robotic interventions are the next leap in the medical field since it combines the superior imaging ability of MRI with the great precision of robots, but challenges are still here that prevent it from being commonly used such as electromagnetic compatibility and highly constrained close-bore area. Also, there are still trade-offs between imaging resolution and speed. High image quality requires longer imaging time to acquire and faster imaging speed could only get images with lower resolution.

### 1.1.1 Advantages of MRI for Diagnosis and Therapy

MRI is a medical imaging technique used in radiology to investigate the anatomy and physiology of the body. It is widely used for medical diagnosis, and is a great way of performing needle based interventions because of the following advantages. Firstly, it takes images without the use of ionizing radiation like CT, enabling the potential of long-time continuous imaging without harming the patient. Secondly, in addition to the three standard planes (Sagittal, Coronal or Transverse), MR images

could be easily acquired in arbitrary planes in single scan without moving the patient. Thirdly, soft tissue body parts are especially favorable for MRI with superior contrast which makes the tumor identification in soft tissue easier. Functional MRI (fMRI) also allows the visualization of certain brain activities.

On the other side, there are certain disadvantages too. MRI scanners are more expensive than CT and patients with metal implants or some foreign bodies are not safe with MRI.

### 1.1.2 Background on MRI-Compatible Interventional Systems

As mentioned before, MRI is an ideal guidance modality since it provides high quality, volumetric, multi-parametric, real-time imaging. It also offers excellent soft tissue contrast without ionizing radiation. Thus it has a unique potential for monitoring therapies [4]. Using robotic systems inside MRI is a perfect match of the high resolution visual capability of MRI and high accuracy manipulation capability of robotic surgical systems.

Although deploying robotic devices in the MRI environment attracts more attention and the benefit from it is being realized by the research community and medical professionals, the compatibility to the highly restricted environment is still one of the biggest challenges.

The American Society for Testing and Materials (ASTM) made a detailed classification [5] for the MRI-compatibility of devices as shown in Table 1.1 on page 5. Qualitatively, it is described as:

MRI-Safe: An item that poses no known hazards resulting from exposure to any MRI environment. MRI-safe items are composed of materials that are electrically nonconductive, nonmetallic, and nonmagnetic.

MRI-Conditional: An item with demonstrated safety in the MRI environment within defined conditions. At a minimum, address the conditions of the static magnetic field, the switched gradient magnetic field and the radiofrequency fields. Additional conditions, including specific configurations of the item, may be required.

MRI-Unsafe: An item which poses unacceptable risks to the patient, medical staff or other persons within the MRI environment.

It is clear that any devices with electricity are excluded from MRI-safe option since electric current generates magnetic field, and it usually requires conductive wires for those devices to operate. Obviously, the traditional electromagnetic motors are definitely MRI-unsafe, but pneumatic actuators could be fully MRI-safe if no conductive and metallic material is used. Hydraulic actuation could also be MRI-safe, but it could potentially have other problems such as leakage. Piezoelectric actuators, which may not contain any metal parts as they are entirely made of ceramic materials, could only qualify for MRI-conditional since it uses electrical signals to actuate.

From the material prospective, needless to emphasize that any ferromagnetic ma-

Table 1.1: ASTM MRI-compatibility definition

| | |
|---|---|
| MRI-Safe   | An item that poses no known hazards resulting from exposure to any MR environment. MRI-safe items are composed of materials that are electrically nonconductive, nonmetallic, and nonmagnetic. |
| MRI-Conditional   | An item with demonstrated safety in the MR environment within defined conditions. At a minimum, address the conditions of the static magnetic field, the switched gradient magnetic field and the radiofrequency fields. Additional conditions, including specific configurations of the item, may be required. |
| MRI-Unsafe   | An item which poses unacceptable risks to the patient, medical staff or other persons within the MR environment. |

terial such as steel is prohibited in the MRI room close to or in the MRI bore. Copper, titanium and nitinol are not MRI-safe but have been found to be nonmagnetic thus can be MRI-conditional, but conductive materials are not necessarily safe with configurations like resonant lengths or loops. Plastic, rubber and ceramic are the ideal materials that are MRI-safe.

In our case, piezoelectric motors are used and some non-ferromagnetic materials like copper and aluminum are used to ensure some essential functions and strength at the places such as rails and set screws. And the needle is typically made of titanium or nitinol. So it is at most MRI-conditional.

There is another MRI-compatibility definition that separates the MRI room into

different parts with different impacts to the environment, procedure and patient: GE defines MRI room with four zones to discuss MRI-compatibility [6]. It is shown in Table 1.2 on page 6.

Table 1.2: GE definition of MRI-compatibility based on zones

| | |
|---|---|
| Zone 1 | If it may remain in the imaging volume and in contact with the patient throughout the procedure and MRI scanning |
| Zone 2 | If it may remain in the imaging volume and in contact with the patient throughout the procedure and scanning but is not located in the image's region of interest |
| Zone 3 | If it will typically be used within the imaging volume, but will be removed during scanning or when not in use |
| Zone 4 | If it is suitable for use in the magnet room during the procedure when kept more than one meter from the iso-center or beyond the 200 Gauss (20 m Tesla) line |

Recent years have witnessed the blossom of MRI-guided robotic systems for varies applications. The first manipulator for needle insertion for MRI-guided neurosurgery was developed by Masamune et al. [7].

From actuation perspective of view, MRI-guided surgical robots could be clustered

into these four categories: 1. pneumatic-driven, 2. hydraulic-driven, 3. piezoelectric-driven and 4. other driving methods. For any of those categories, MRI-compatibility is always the highest priority. A thorough comparison test of SNR of pneumatic, nanomotion, Shinsei motors under 1.5T and 3T MRI with custom made controller [8] either inside the room or outside the room [9] was done by Fischer et al. The result shows that when controller is outside the room, SNR of pneumatic motors has almost no drop, but nanomotion and shinsei motor has 20% and 80% SNR drop respectively. When the controller is inside the room, SNR of pneumatic motors still has almost no drop, but nanomotion and shinsei motor has 10% and 90% SNR drop respectively.

Pneumatic actuation is inherently MRI-safe if the right materials are used and valves placed in the right locations. Thus has the best SNR result reported so far. Chen et al. introduced a 10-mm diameter MRI-conditional stepper motor [10] with an impressive SNR drop of only 2.49%. Recently, Stoianovici et al. also discussed a MRI-safe pneumatic-driven robot for endorectal prostate biopsy [11]. Although pneumatic actuation may have great MRI-compatibility, it is actually hard to control due to its dynamic properties. Both Yang and Wang proposed several complex sliding mode control schemes for position control of pneumatic actuator [12], [13]. But still either the accuracy is not ideal [11], or the response time is long [14]. Although with high accuracy, hydraulic actuation is not widely used because of the safety concerns like being nonbackdrivable, leakage and high pressure. Piezoelectric actuation is gaining more attention recently due to its great dynamic properties such as fast response and

high positioning accuracy. But Koseki et al. reported 93% SNR loss in 0.3T open MRI [15] and 44% SNR loss reported by Song [16]. So that enormous amount of effort has been put on improving its MRI-compatibility [17].

To further avoid ergonomic issues associated with performing needle insertion inside the scanner bore, teleoperation system is getting more attraction by allowing surgeon control the master device outside of the bore with slave following the motion of master to insert the needle. One approach is to place the master outside of the MRI room, but inside the console room by using existing [18] or custom master device [19]. In this case, the master is not necessarily required to be MRI-compatible that makes it a wider choice of existing devices or materials. Master robot being placed in different room with patient makes surgeon inconvenient to reach the patient if needed. Letting the surgeon operates the master beside the bore in the MRI room allows direct observation and easy access to the patient. But the master device needs to be fully MRI-compatible to work inside the MRI room. Different approaches have been done with the design of MRI-compatible master device [20], [21], [22]. Moreover, enabling force sensing and haptic feedback inside the MRI room is more challenging. Fiber optic force sensors [23], [24], [25], [26] have been widely considered as the good solution for that while load cell is also a feasible solution. A thorough review could be found later in Section 1.4: Literature Review.

### 1.1.3 Diagnosis and Therapy of Prostate Cancer

#### 1.1.3.1 Anatomy of the Prostate

The prostate of a healthy human is said to be slightly larger than a walnut. It secretes most of the fluid in semen that goes to urethra which runs through prostate from bladder to the penis. The prostate is surrounded by the bladder, the penis and the rectum and can be felt during a rectal exam. Thus it is easy to reach the prostate by needle from rectum, perineum or gluteus.

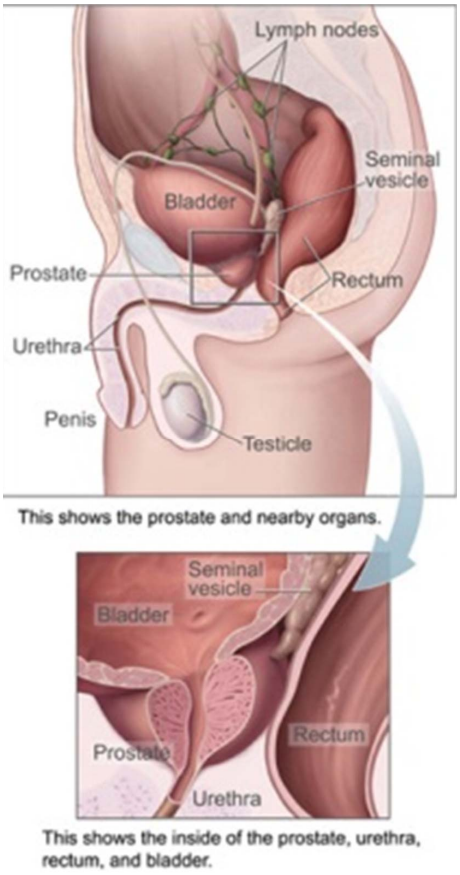


Figure 1.1: Prostate anatomy © [27].

The prostate itself could be divided by four distinct zones [28] which are peripheral zone (PZ), central zone (CZ), transition zone(TZ) and anterior fibro-muscular zone (or stroma).

#### 1.1.3.2 Traditional Prostate Interventions

Prostate cancer (PCa) is the most common cancer in men in the United States, accounting for about 29,480 deaths annually [29]. Transrectal Ultrasound (TRUS) guided biopsy is the current standard diagnostic procedure for prostate cancer with the real-time imaging ability at low cost [30]. In most biopsy procedures 8-12 biopsy samples are taken at different suspicious areas. However, it suffers from a poor cancer detection rate of 29-44.4% which has been reported in several studies [31], [32]. Some areas such as the anterior prostate and apex are out of reach and always under-sampled or never sampled. The exact location of cancer cannot be determined when a diagnosis of PCa is made. Thus unnecessary treatment might be performed. Those clinically insignificant cancer area may never cause harm or PCa related death if left undetected and untreated.

An alternative method to TRUS guided procedure is transperineal template guided prostate biopsy. A grid placed on the perineum is with 5mm $\times$ 5mm guiding holes (Fig. 1.2). Via these holes, biopsy could be taken from all zones throughout the prostate. More advantages are found for this procedure comparing to the TRUS guided biopsy. Firstly, despite of pubic bone, all zones of prostate could be reached,

anterior and apical areas of the prostate are more easily sampled. Secondly, 5mm incremental biopsy locations make the detection rates of cancer significantly higher than TRUS biopsy. Thirdly, transperineal route makes the rate of sepsis lower since the biopsies are note taken through rectum and it can be applied to patients who cannot undergo TRUS-guided biopsy due to previous colectomy [33].

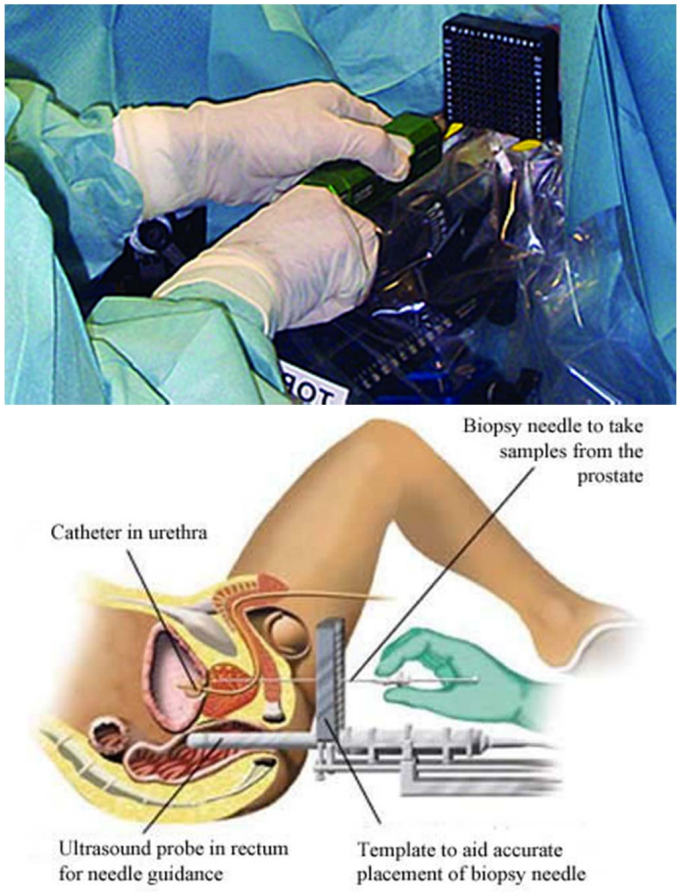


Figure 1.2: Transrectal Ultrasound guided biopsy ©www.nuadamedical.co.uk

By making the template MRI-compatible, the template guided prostate biopsy could be taken inside the MRI with live imaging and without moving the patient in and out during the procedure. But, still surgeon needs to mentally register the

MRI images and hence several insertions are needed to get to the desired location. Multiple times of imaging is usually performed during one insertion to ensure the correct depth is reached.

In terms of prostate cancer treatments, therapeutic methods include radical prostatectomy, external beam radiation combined with hormonal therapy, radioactive seed implantation (brachytherapy), or active surveillance. Brachytherapy and ablative therapy are often used with the guidance of transrectal ultrasound to eradiate or ablate cancer tumors.

As one of the therapeutic methods, brachytherapy is the delivery of seeds containing radioactive material either temporarily or permanently to a diseased site by insertion. Pre-operative imaging is usually required for the surgical planning. Mostly guided by US, the contemporary brachytherapy has been performed successfully transrectally. But sometimes the placement of the radioactive sources is not ideal [34]. It is also performed with CT or fluoroscopy guidance which is not ideal because it exposes patient and surgeon to ionizing radiation [35]. Either of the US, CT or fluoroscopy method suffers from poor image quality of soft tissue or the needle [36].

### 1.1.4 Motivation of Robot-Assisted Intraoperative MRI Intervention

The robot-assisted intraoperative MRI intervention could reduce procedure time by letting the interventions happen inside the scanner bore without moving the patient out. It increases the intervention accuracy by using the robotic device with high precision closed-loop position control. Mental registration and tracking of the surgical device are not necessary since the sensors and fiducials on robotic device enable the automatic registration and tracking. Taking advantage of teleoperation system, ergonomic problem is avoided while the surgeon doesnt lose the control of the surgical device. Finally, working with robot together, intraoperative imaging could improve the diagnosis and therapy outcomes.

## 1.2 MRI-compatible Actuation Techniques

MRI provides superior soft-tissue contrast compared to other imaging modalities. However, due to its high magnetic field, it severely restricts the instruments allowable in the scanner. Needless to emphasize that any ferromagnetic material is prohibited in the MRI room close to or in MRI bore. Most of the motors used on robots fall into this category. Only a few types of them made of material without any metal or with non-ferromagnetic material could be MRI-compatible.

Some actuation paradigms that may be compatible with MRI environments in-

clude pneumatic actuation [11], hydraulic actuation [19] and ultrasonic piezoelectric actuation [16], [17] to nonconventional actuation including electrostrictive polymer [37], electro-rheological fluids (ERF) [38], Shape Memory Alloy [39] and MRI-driven actuation [40].

Pneumatic actuation is the most prevalent technology by far for its great MRI compatibility. The pneumatic actuator itself is usually totally made of non-magnetic material that it is intrinsically MRI-compatible. Fischer et al. reported that this kind of actuator has almost no SNR drop in either 1.5T or 3T MRI scanner [9]. Stoianovici et al. also showed that their pneumatically actuated robot has the SNR change of 0.1% due to the robot and of 0.71% due to its motion [11]. Although pneumatic actuation technology has great MRI-compatibility results, acquiring high precision position control is still below expectations. Because of the dynamic characterization, the control scheme is always complex. Wang et al. proposed three different sliding mode control schemes for pneumatic cylinder driven by two piezoelectric valves [13]. The long pneumatic transmission makes it even harder, and Yang et al. also demonstrated three SMC methods to perform position control with 10 m transmission line [12].

Hydraulic actuation is not as popular as pneumatic and piezoelectric actuations in MRI-compatible applications mostly because of the safety concerns. Comparing medical air supplies, saline, oil or other agents for hydraulic actuation must be biocompatible and must be kept with no leakage. It requires a closed system and thus either permanently connected or have to purge lines. On the other hand, hydraulic

actuation is nonbackdrivable, robust, with high accuracy and could supply much more power output than pneumatic and piezoelectric actuations. The working pressure of oil is 15-25 bar which is much higher than 6 bar in normal pneumatic systems [41]. Another hydrodynamic-driven robot designed by Gassert et al. in [19] has a transmission up to 10m and a maximum pressure of 100 bar.

Piezoelectric actuation gains traction recently for its good dynamic properties, easiness of control and compact shape. In the meantime, its MRI-compatibility is doubtful because of the required high frequency driving signal. For example, Shinsei USR60 motor(Shinsei Corp., Tokyo, Japan) requires a drive frequency of 40kHz with 130Vrms. Piezo LEGS®Linear 6N (PiezoMotor Uppsala, Sweden) requires a driving signal of 750 to 3kHz with Vpp = 48V. Fischer et al. reported that nanomotion and Shinsei motor has 20% and 80% SNR drop respectively when the controller is outside the room. SNR of nanomotion and shinsei motor has 10% and 90% SNR drop respectively when the controller is inside the room [9]. A needle manipulator for radiofrequency ablation(RFA) is designed by Sato et al. [42]. The 2-DOF robot is driven by ultrasonic motors. Tracking is done by POLARIS optical tracking system and tracking markers placed on the robot. There is 1.2% SNR decrease in 0.2T open MRI system with accuracy of 0.8 mm$\pm$0.29 mm while the requirement is said to be 5 mm.

Koseki et al. proposed a piezoelectric-driven endoscope manipulator for transnasal neurosurgery with Shinsei motors in open MRI [15]. It has a great position

accuracy of 0.03 mm but the SNR loss is 93% in 0.3T open MRI. Another Shinsei untrasonic motors driven needle guide template is evaluated in [16], by Song et al. It is said to be with a SNR drop of 44% which is better than the previous one but is still relatively significant.

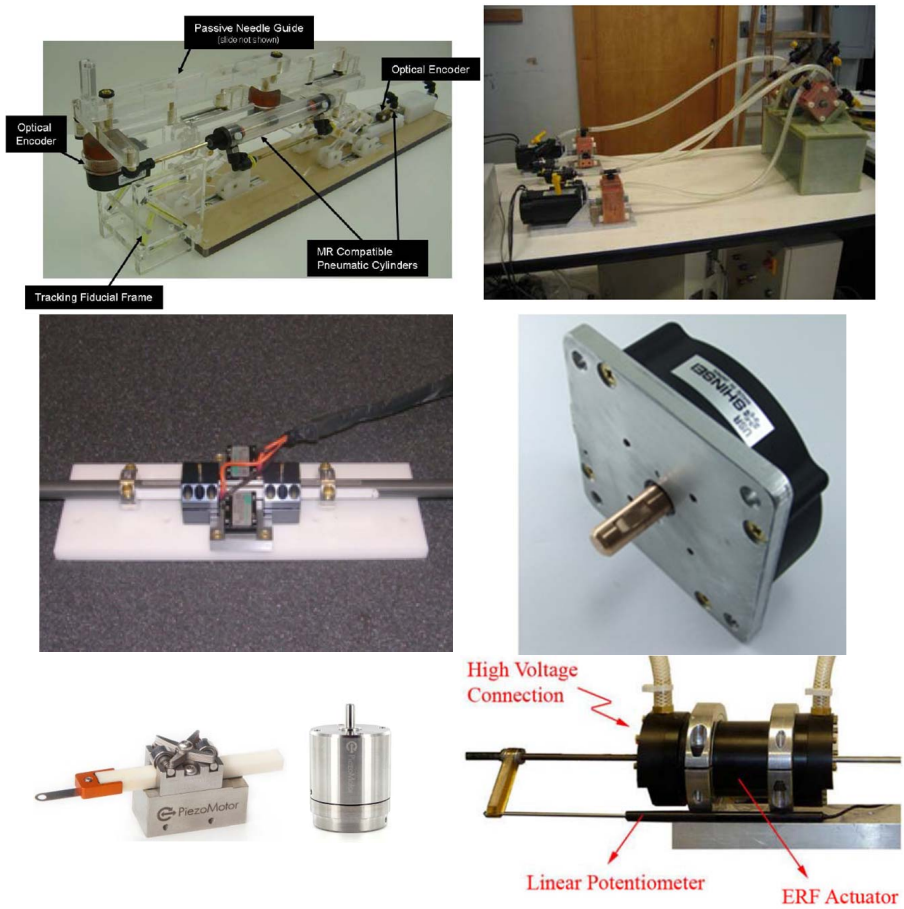


Figure 1.3: Examples of MRI-compatible actuators: a) Pneumatic actuator © [43], b) Hydraulic actuator © [44], c) Nanomotion motors © [9], d) Shinsei USR60 motor(©http://www.shinsei-motor.com/), e) PiezoMotor PiezoLEGS(TM) (©http://www.piezomotor.com/), f) electro-rheological fluids (ERF) © [44]

To take advantage of the high positioning accuracy of piezoelectric motors while still maintaining the good MRI-compatibility, Cole et al. developed a customized

piezoelectric motor driver which could be placed inside the MRI room [45]. Piezo LEGS motors are tested with the MRI and the result shows that it has less than 5% SNR loss in 3T MRI [17] [46]. More thorough review could be found in Section 1.4.1.

## 1.3 MRI-Compatible Teleoperation and Haptics

Although MRI has already demonstrated superior soft tissue contrast and shown a great ability of working together with robots to provide better clinical outcomes, the limited MRI bore space restricts the physician from performing needle insertion such as prostate biopsy while patient is being scanned inside the bore. The robotic systems could be classified in three categories on the basis of how the surgeon interacts with them: supervisory, telesurgical, and shared systems [47]. The teleoperated system is particularly favorable for MRI-guided intervention because it not only allows the surgeon to directly control the procedure, but also avoids ergonomic issues associated with performing it inside the scanner bore. Fig. 1.4 shows a robot assisted prostate biopsy inside a 3T MRI bore at BWH. As we could see that even it has already been assisted by robot, the highly constrained area inside the MRI bore is still a major issue for reaching the working space.

MRI-guided needle insertion procedure could be easily controlled without ergonomic issues with the implementation of teleoperation system but the haptic feed-

Figure 1.4: A surgeon is performing robot assisted prostate biopsy inside the highly tight MRI bore at BWH.

back experienced by the surgeon which provides useful information is also removed. Thus adding haptic feedback to the MRI-compatible master-slave teleoperation system is the solution to those issues and could still keep the desired safety with surgeries. Firstly, an MRI-compatible needle placement robot (slave) should be designed with high positioning accuracy for the motion of needle. Secondly, a series of sensors, such as position encoders and optical trackers should be integrated and fused to register as well as display the surgical tool information with the pre-operative or intra-operative MRI images. Multi-platform registration like ultrasound-MRI or CT-MRI registration is also possible to be integrated for improving the surgical outcome. Thirdly, the design should be compact that is capable of circumventing the limited space. Most importantly, the described teleoperation system allows surgeon to perform the operation from beside the patient in the scanner room, but outside the constrained scanner

bore, where the surgeon could control the master robot to teleoperate the slave robot with simultaneous manipulation and visualization. Force feedback is also crucial to teleoperation system which sacrifices it to achieve the aforementioned benefits.

Recently, several MRI-compatible robotic systems have been reported. Some of the manipulators have been developed and could be able to serve as the slave robot from a teleoperation perspective. Stoianovic et al. developed an MRI-safe robot for endorectal prostate biopsy [11]. Li et al. presented an MRI-guided robot for aortic replacement [48]. Krieger et al. designed a piezoelectric-actuated needle guide [49]. Fischer et al. also demonstrated a pneumatic-driven robot for transperineal prostate needle placement [50]. And both [51, 52] have more detailed review. For the MRI-compatible force sensing and haptic devices, all of [53], [54], [41] and [19] utilized fiber optic force sensors but their haptic devices were with different technologies such as electrostatic, hydrodynamic or pneumatic actuation. For the MRI-compatible master-slave system, Seifabadi et al. [20, 55] did the accuracy evaluation of a 1-DOF teleoperation system and also proposed a teleoperated needle steering system but neither has force feedback. Tse et al. [56] developed a master-slave device with admittance force feedback with neural network speed model. More thorough review could be found in the review section of 1.4.3 and 1.4.4.

## 1.4 Literature Review

### 1.4.1 MRI-Guided Surgical Robots

As mentioned before, MRI is an ideal guidance modality since it provides high quality, volumetric, multi-parametric, real-time imaging. It also offers excellent soft tissue contrast without ionizing radiation. Thus it has a unique potential for monitoring therapy [4]. Using robotic systems inside MRI is a perfect match of the high resolution visual capability of MRI and high accuracy manipulation capability of robotic surgical systems.

With the invention of MRI, recent years have witnessed the blossom of MRI-guided robotic systems for varies of applications. The first manipulator for needle insertion for MRI-guided neurosurgery was developed by Masamune et al. [7].

From actuation perspective of view, MRI-guided surgical robots could be mainly categorized in four types: pneumatic-driven, hydraulic-driven, piezoelectric-driven and other driving methods.

Fischer et al. did a thorough comparison test of SNR of pneumatic, nanomotion, Shinsei motors under 1.5T and 3T MRI with custom made controller [8] either inside the room or outside the room [9]. The result shows that when controller is outside the room, SNR of pneumatic motors has almost no drop, but nanomotion and shinsei motor has 20% and 80% SNR drop respectively. When the controller is inside the room, SNR of pneumatic motors still has almost no drop, but nanomotion and shinsei

motor has 10% and 90% SNR drop respectively.

#### 1.4.1.1 Pneumatic-Driven Robots

Most recently, Stoianovici et al. discussed a MRI-safe endorectal prostate biopsy robot [11] which was built of nonmagnetic and electrically nonconductive materials. The robot utilizes PneuStep motor  a type of pneumatic stepper motor to archive the positioning accuracy of 2.58 mm. MRI-compatibility factors such as deterioration and SNR change are also discussed in the paper. A comprehensive set of preclinical tests for MRI-compatibility was proposed in [6]. Chen et al. introduced a 10-mm diameter MRI-conditional stepper motor [10], which rotates in angular steps of 60° with a maximum torque of 2.4 mNm. It is said to be the smallest MRI-conditional pneumatic stepper motor. Compared to existing pneumatic motors, this motor is smaller in size and could be controlled easily with nonpressure dependent output which is only related to the spring stiffness and the dimensional parameters. The motor design can be altered for a larger output torque by just increasing the spring stiffness without changing its size. But the mechanical structure is actually more complex than the traditional pneumatic cylinders. An impressive SNR drop of 2.49% was recorded. Zuo et al. demonstrated another snake-like robot for single port access surgery inside MRI [57]. Its outer sheath could be either rigid or flexible controlled by a pneumatic shapelocking mechanism and the double curvature structure allows it to curve in four directions. Yang et al. presented a control of an MRI-compatible 1-DOF needle-driver

robot with pneumatic actuation with long transmission lines [12]. Wang et al. also proposed three different sliding mode control schemes for pneumatic cylinder driven by two piezoelectric valves [13]. To perform breat biopsy under continuous MRI, a pneumatically actuated robot was designed and implemented by Yang et al. [14]. The cantilever-like robot, which has complex kinematics, is not stable and could introduce error easily. Nine-meter pneumatic transmission lines require complex control method and the position accuracy is not guaranteed. It is shown in the paper that a 75 mm step response time is 20 s which is much slower than piezoelectric motors. Another pneumatic actuated robot was designed by Li et al. [48] for aortic valve replacement. It consists of a 5-DOF positioning module and a 3-DOF valve delivery module. The position error is said to be 1.14 mm$\pm$0.33 mm.

Being as the first commercial MRI-compatible robotic system, INNOMOTION is a pneumatic robot for accurate needle positioning [58]. The 6-DOF robot arm is attached to a 260° arch mounted to the patient table. Tests were done in both 1T and 1.5T scanners and the max error in three directions is reported to be less than 1 mm. But the problem with this system arises when used in closed bore MRI. It is difficult to advance the needle manually without moving the patient table out of the bore to perform the needle insertion. A light puncture robot (LPR) was designed by Zemiti, Bricault et al. [59] [60] for the similar application of abdominal and thoracic punctures. It has a compact body-supported architecture which is designed to follow the respiratory movements of patients body. The 5-DOF LPR robot consists of two

parts: a 3-DOF needle-holder and a 2-DOF support frame. A unique pneumatic actuation mechanism was developed based on clock-making principles. 7 m long tubes are used to connect the robot controller and air compressor to the pneumatic actuators which have 3 Hz bandwidth and 9 cm/s insertion speed. The system is said to have 1 mm accuracy, 0.5 mm repeatability, and about 10% SNR drop in 1.5 T MRI.

#### 1.4.1.2 Hydraulic-Driven Robots

Yu compared hydrodynamic and pneumatic actuation in [41]. The oil of Orcon Hyd 32 is used in hydrodynamic actuation. Being accepted as a lubricant with incidental food contact, it is said to be appropriate for biomedical applications. The working pressure of oil is 15-25 bar which is much higher than 6 bar in normal pneumatic systems. Although no leakage was reported in the paper, this could still be a potential safety issue. While the pneumatic actuation is backdrivable, sensitive/soft and with medium accuracy, the hydrodynamic actuation is nonbackdrivable, robust, with high accuracy. Another hydrodynamic-driven robot was designed by Gassert et al. in [19]. The hydraulic system has a transmission up to 10m and a maximum pressure of 100bar.

#### 1.4.1.3 Piezoelectric-Driven Robots

A motorized needle guide template is evaluated in [16], by Song et al. This motorized template has two DOFs- horizontal and vertical translations, both driven by Shinsei untrasonic motors. It is said to be with an accuracy of 0.94mm with a standard deviation of 0.34 mm, while with a SNR drop of 44% which is relatively significant. Cole and Wang et al. developed a piezoelectric actuated robotic system for neural interventional procedures such as the treatment of Parkinsons syndrome known as deep brain stimulation [17] [46]. Piezo LEGS motors are used to actuate the 2-DOF neuro robot with RCM feature. The MRI result shows that it has less than 5% SNR loss in 3 T MRI. Larson et al. designed a 5-DOF robotic stereotactic device for breast biopsy and therapeutic interventions inside the MRI [61]. To keep the ultrasonic motors as far away from the scanner as possible, telescoping shafts are used to transmit the motion from motors to device. The robot is reported to have $\pm$ 1 mm accuracy with 0.64 mm repeatability. MRI-compatibility wise, the paper claims that the robot is totally invisible in the MR images, but lacks of SNR and distortion reports. Koseki et al. proposed an endoscope manipulator for trans-nasal neurosurgery with piezoelectric actuation in open MRI [15]. Four out of five DOFs of the robot were installed and all of which were designed to be driven by Shinsei motors. It has a great position accuracy of 0.03 mm but the SNR loss is 93% in 0.3 T open MRI.

#### 1.4.1.4 Robots with Other Driving Technologies

A general-purpose MRI-compatible manipulation system is presented in [62]. The main robotic arm is supported on an arc-shaped structure and the end effector is for needle insertion. There are totally five DOFs, all of which are manually actuated. Phantom needle insertion is presented in the paper but no accuracy reported. One major problem with pneumatic driving technique is archiving the accurate position control. A lot of efforts have been put on modeling the new control methods. Comparing to the traditional MRI-compatible driving technologies such as piezoelectric, pneumatic and hydraulic, MRI-powered robot is a new research direction of MRI-compatible robotics. The actuator discussed in [40] is comparable to an electric motor. The stator is comprised of the MRI scanner. The rotor, rotating portion of the actuator contains ferromagnetic material. Even though, it is claimed in the paper that the ferromagnetic part is small in volume and can be located outside the imaging region of interest so that there is no effect to SNR at imaging region. It is demonstrated in a 1.5 T scanner, but more analytical results are needed to evaluate the MRI-compatibility. Similar to [57], Ho proposed a meso-scale shape memory alloy (SMA) actuated neurosurgical robot [39]. The snake-like robot could navigate in a confined anatomical environment, and is driven by changing temperature up to $60°C$.

More detailed reviews could be found in papers from Gassert [63], [64], Jolesz [4], and Chinzei [65].

### 1.4.2 Registration and Tracking for MRI-Guided Robots

Robot-assisted surgical interventions have been developed rapidly in the last decade, especially for cancer treatment [66]. Although the robot itself has a high targeting accuracy, the position and orientation of the surgical tool with respect to the patient anatomy in the intraoperative images are always crucial [67]. This brings up the desire of high accurate robot registration and tracking [68].

#### 1.4.2.1 Active Tracking Coils

High tracking accuracy and speed could be acquired by using active tracking coil which is one of the major ways for doing robot registration and tracking under MRI environment [69]. Krieger showed a prostate intervention robotic system with a single-loop endorectal imaging coil integrated [49]; Derbyshire introduced a MRI scan plane tracking system by using several locater coils which could be connected to body coil [70]; Hillenbrand designed a more complex opposed-solenoid phased array catheter coil for intravascular MRI tracking [71] [72]. Although it is fast and accurate, drawbacks like the requirement of special scanner programming, limitations of scanner channel and special design of electronic hardware are potential problems for this kind of method [73].

#### 1.4.2.2 Self-resonant Imaging Coils

Self-resonant imaging coil does not require special programming for MRI scanner and the design is simple [74] [75]. But fabrication problem arises as it requires a fixed resonant frequency which relies on the accurate value of inductance and capacitance. It also brings the problem when changing from one MRI scanner to another [76].

#### 1.4.2.3 Passive Fiducial Frames

Both single- and multi-image registration and tracking methods have been shown in prior works. Both DiMaio and Susil discussed passive single-image registration and tracking approach in MRI and CT environment [77] [78]; Lee proposed several numerical algorithms to make the single image, 6-DOF registration more accurate [79]. Comparing to single-image method, with a specially designed fiducial frame, we have also developed a multi-image registration approach which gives more reliability by using one more DOF information between different slices when dealing with relatively poor image quality [80].

Compared to the use of either active or passive coils, passive fiducials have a better adaptability and do not have requirements of special programming nor protocol limitations. Z-frame [78] as an example, is made of seven fiducial tubes that configure a set of Z shapes in three orthogonal planes. Because of its square shape and relatively large size, it is inconvenient to be placed at needle tip. By eliminating the error from robot kinematics and manufacturing, better robot accuracy could be acquired by

placing the fiducial frame as close to the end effector as possible, such as [81], even if the registration accuracy is similar. Because, errors from kinematics and control could be avoided as much as possible and calibration error is also minimized for localization comparing to those passive fiducial designs which are bulky in size and could only be placed on robot base.

### 1.4.3 Teleoperation and Haptics Technologies

The teleoperated system not only allows the surgeon to directly control the procedure, but also avoids ergonomic issues associated with performing it inside the scanner bore. It is gaining popularity recently.

Gassert et al. demonstrated a hydrostatic teleoperation system [19]. A conventional actuator is placed outside the scanner room with a bydrostatic connection to a MRI-compatible slave placed inside the MRI scanner. The force and motion is transmitted with a preload of 15 bar. Interaction force with human is measured with a ligh intensity based force sensor and the human force control bandwidth is around 20Hz. The functional MRI-compatibility is also demonstrated. Another hydraulic teleoperation system is proposed by Kokes et al. for the application of radiofrequency ablation(RFA) of breast tumors inside MRI [18]. Instead of building their own master robot, PHANToM haptic device(SensAble Technologies, Version 1.5A) is used. A force/torque sensor(JR3 Model No. 20E12A-I25) is integrated in the slave robot with the resolution of 0.0002N and 0.00025Nm. The feasibility and accuracy of

hydraulic actuation with long transmission lines is demonstrated as well as its MRI-compatibility and the ability of tumor detection via haptic feedback. Pneumatic and piezoelectric-driven technology is also widely used in teleoperation systems. Seifabadi et al. demonstrated a pneumatic-driven slave robot with a piezoelectric-driven master robot [20]. The master device uses a pair of HR4 Nanomotion motors to apply 28N force together. The position tracking accuracy is below 0.1 mm in all three experimental trails while the acceptable error is said to be 3mm. Then, the master device got updated in [55] with rotary PiezoLEG motor but the Peaucellier-Lipkin mechanism is not perfect linear motion. By using the robot in [14] as slave robot, Yang et al. designed a master with similar kinematics of parallel mechanism and pneumatic actuators [21]. The parallel mechanism is with unilateral control while the needle driver is with bilateral control. It has similar force profile recorded with whats shown in Chaper 4. Within our group, Su et al. showed the first concept of our teleoperation system with Novint Falcon (Novint Technologies, Inc., Albuquerque, NM) as the master and light intensity based force sensor integrated in slave robot [82]. Later a fully redesigned teleoperation system is described in [22]. An updated piezoelectric slave robot with new Fabry-Perot Interferometer (FPI) based force sensor [26] is controlled by a pneumatic-driven master robot.

Other than aforementioned teleoperation systems, MRI-compatible haptic device has also been paid a lot of attention too. Riener et al. designed a 1-DOF haptic device with two coils that produce a Lorentz force induced by the static magnetic

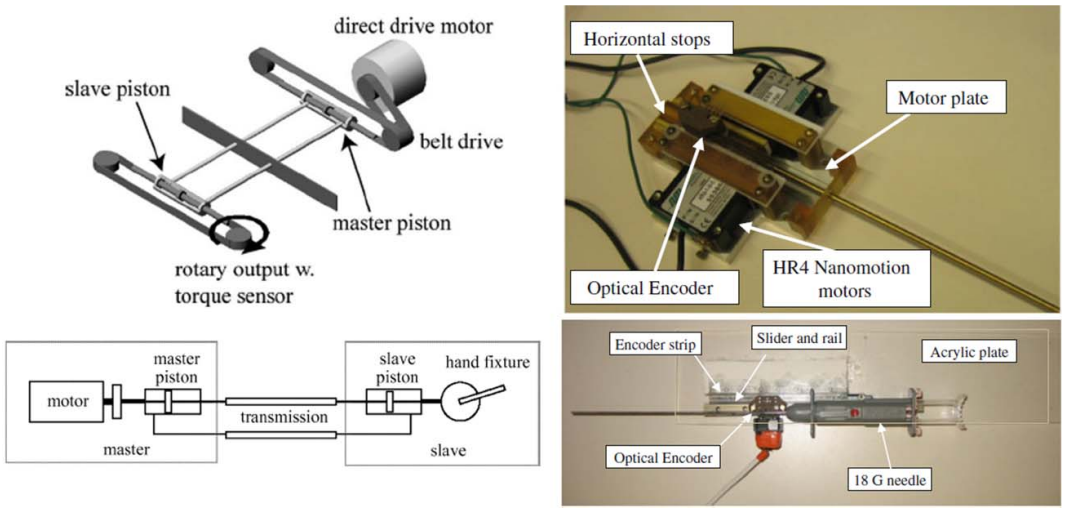


Figure 1.5: Examples of MRI-compatible teleoperation systems 1: left: hydrostatic teleoperation system developed by Gassert et al.© [19], right: teleoperation system with pneumatic-driven slave robot with a piezoelectric-driven master built by Seifabadi et al.© [20]

field of the MRI scanner [83]. Different control architectures for haptic interactions are enabled by MRI-compatible optical angular encoder and force sensor. The haptic device was tested in a 3 T MRI with a distance of 1m to the iso-center of the scanner. With the current up to 1 A, the generated torque of this haptic device is up to 4 Nm. A 2-DOF electrostatic haptic joystick designed for neuroscience studies in an MRI/fMRI is shown in [54]. To achieve MRI-compatibility, optical displacement sensor FUE200C1004 with mirror and electrostatic motors were utilized. With a maximum force output of 18 N, the device is highly backdrivable. It is said to have better performance in comparison to the commercial ultrasonic motors. A fiber optic force sensor was also fabricated with approximately 100 Hz bandwidth. Admittance control is used to perform haptic rendering. Chapuis et al. designed an ultrasonic motor driven haptic device with and differential/brake system and admittance control

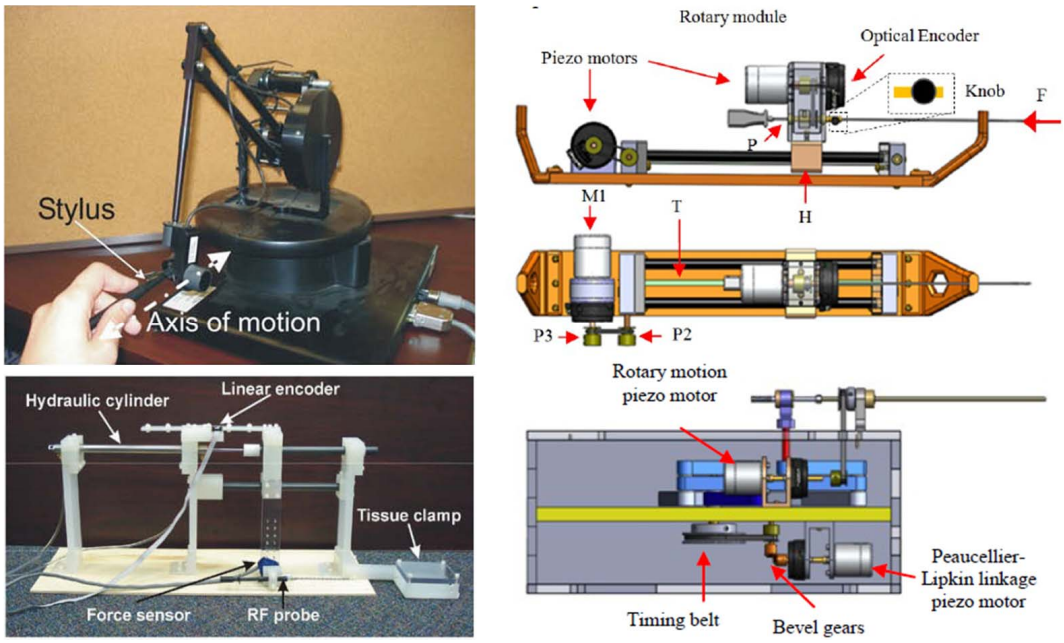


Figure 1.6: Examples of MRI-compatible teleoperation systems 2: left: hydraulic teleoperation system for RFA of breast tumors designed by Kokes et al.© [18], right: another teleoperation system developed by Seifabadi et al.© [55]

[84]. By taking advantage of the ultrasonic motor, it has a high bandwidth over 1k Hz. Another admittance controlled haptic device is proposed by Tse et al. [56]. Driven by PiezoLEG motor, it has a maximum force output of 15N. Although high force output and high bandwidth could be reached by using ultrasonic motors, but the drawback is that it is nonbackdrivable and thus suffers from quickly wearing out and failure in a short operation duration. To overcome this issue, Turkseven designed a pneumatic-actuated 1-DOF haptic master device [53]. Shang et al. also designed a pneumatic-driven 2-DOF master robot [22] which is much user friendly than piezoelectric-driven devices.

Stability and transparency are always the fundamental requirements for the con-

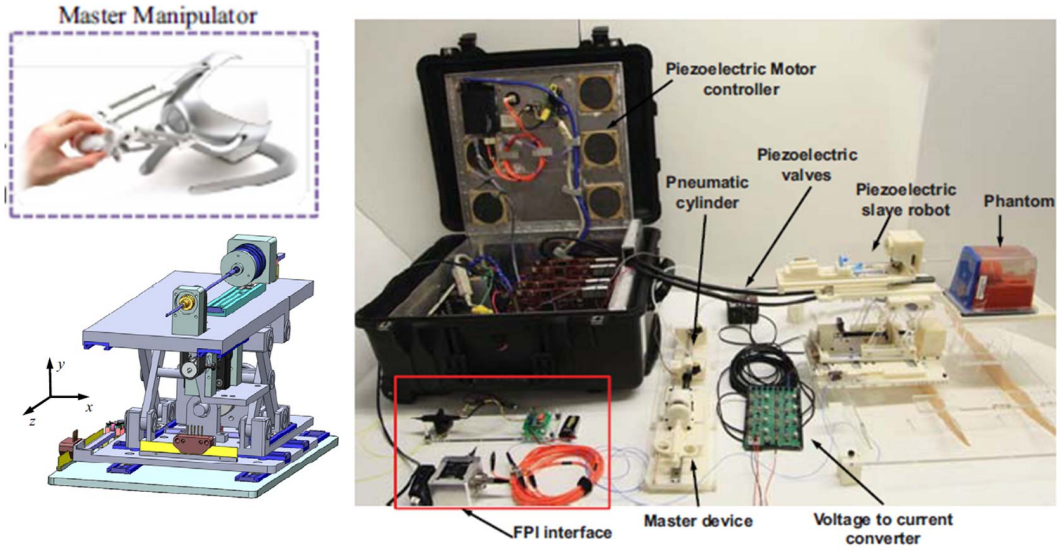


Figure 1.7: Examples of MRI-compatible teleoperation systems 3: left: teleoperation concept design by Su et al.© [82], right: teleoperation system with piezoelectric-driven slave robot with a pneumatic-driven master developed by Shang et al.

trol of teleoperation system. In general, the most common method for bilateral control is impedance control, where the virtual force is used to connect master and slave robots to track each other. In another word, the force applied back is not the real force at the slave side, instead, it is a virtual force. Force sensor is not required in this method because the force applied to the master robot is controlled by the position interaction with the environment. In this case, some interaction between the slave robot and the environment and the mechanical impedance of the slave robot will be presented as force feedback which is not always what we want. Admittance control, however, is where the force difference is used to control the position. It is good for slow and accurate movement control. But, four-channel control architectures have the best transparency. As an example, position forward/force feedback system could be four-channel system if it incorporate both master and slave position and force

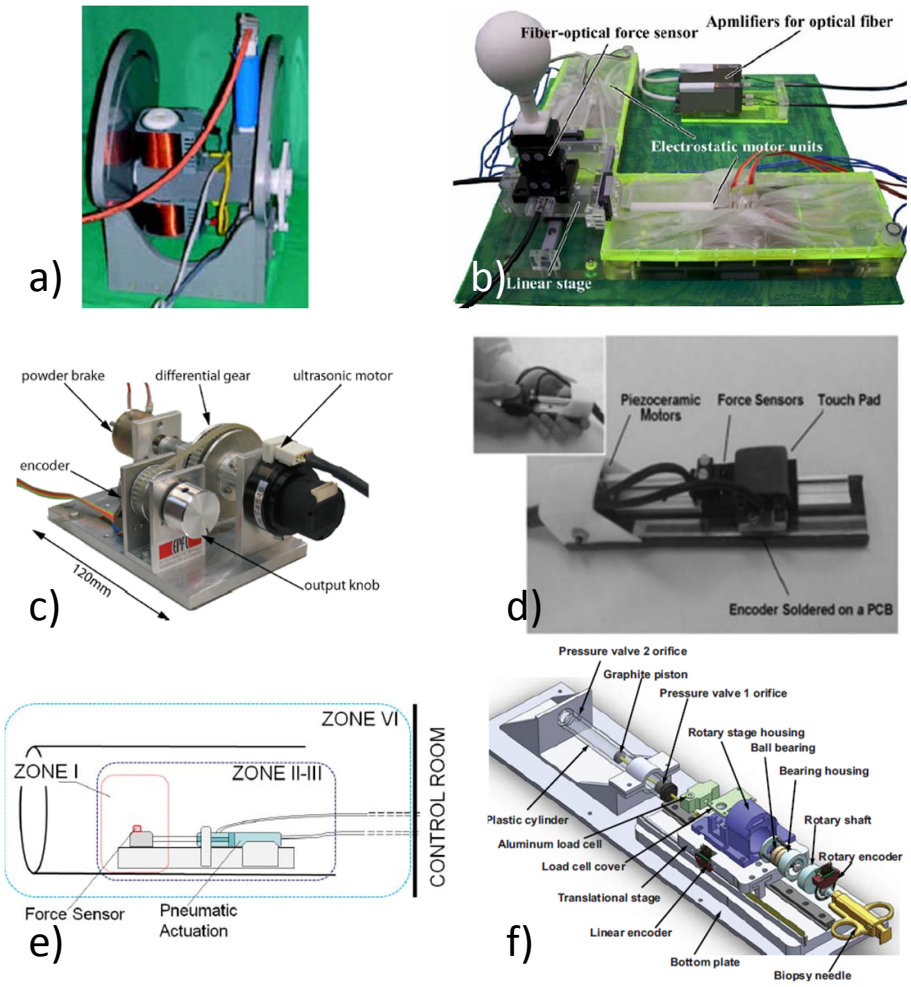


Figure 1.8: Examples of MRI-compatible haptic devices: a) 1-DOF haptic device with two coils that produce a Lorentz force induced by the static magnetic field of the MRI scanner designed by Riener et al.© [83], b) A 2-DOF electrostatic haptic joystick developed by Hara et al. for neuroscience studies in an MRI/fMRI © [54], c) Chapuis et al. designed an ultrasonic motor driven haptic device with and differential/brake system and admittance control© [84], d) An admittance controlled haptic device proposed by Tse et al.© [56], e) A pneumatic-actuated 1-DOF haptic master device developed by Turkseven et al.© [53], f) A pneumatic-driven 2-DOF master robot designed by Shang.

information. A review of teleoperation control architectures could be found in [85] and [86].

### 1.4.4 MRI-Compatible Force Sensing Technologies

#### 1.4.4.1 Intensity Modulated Fiber Optic Force Sensor

Intensity modulated sensor is most popular among three types of fiber optic force sensors due to its several undeniable advantages: simple principle, simple design, low cost and easy signal processing. There are basically two types of intensity modulated sensors: transmissive and reflective. Transmissive type relies on a pair of emissive fiber and receiver element which could be photodetector or single, dual or quad fibers [23]. Reflective type is able to minimize the number of fiber used but requires a mirror reflection [87].

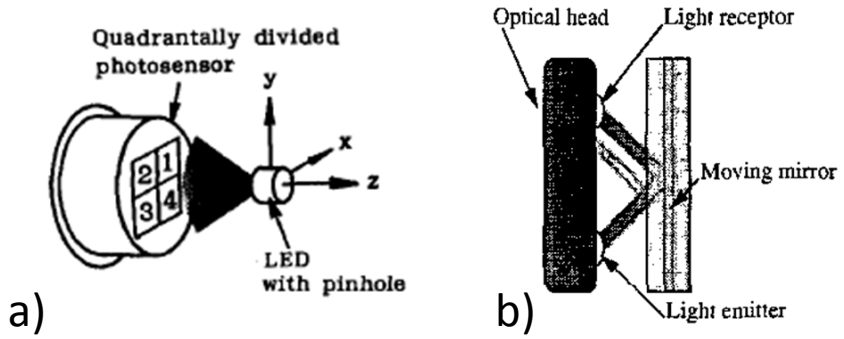


Figure 1.9: Two types of intensity modulated fiber optic force sensor: a) Transmissive © [23], b) Reflective © [88]

Back in 1990, Hirose et al. developed an optical 6-DOF force/torque sensor based on transmissive light intensity principle [23] (Fig. 1.10). The flexure is robust and with high stiffness that sensor could stand against noise without special processing. Three 2-DOF sensor units are arranged with 120° between each other to make it totally 6-DOF. Calibration shows no hysteresis that it doesnt require complex signal

processing system. The accuracy is reported to be ±1.5%, ±0.44 N, ±0.03 Nm, ±3%. Based on the same principle, Takahashi later improved the sensor design and had it tested inside a 1.5T MRI [89]. One emitting fiber is attached to the moving part, and four fibers are used as four-quadrant receptor. A high luminance LED was adopted to address the issue of instability caused by light source since the ratio of the amount of change of emitted light quantity is only with little portion of the total intensity. Tada did further research on this kind of sensor [90] and got the improved accuracy of 1.0% of full scale of 0-6 N. The MRI test was also reported first time with 1.03-3.11% SNR loss in 2T MRI that it is below the max acceptable SNR loss of 10% [91]. With two 2-dof sensor, 3-dof force sensing is achieved by using two micrometers aligned in orthogonal directions [92]. 3% of full scale resolution was found with the rang of 0-15 N in vertical, -8-8N in horizontal directions. It was tested in a 4.7 T experimental MRI with 10% SNR loss. Another 2-DOF force sensor was discussed in [93]. It utilizes transmissive parallel plate structure and measure the change of the focal point. 1.6% of full scale resolution was found on 0-3 N full scale. A reflective sensor was designed by Turkseven et al. [53]. By using a specially designed mechanism, the deformation is amplified and the amplification ratio could be adjusted by changing geometric parameters without compromising the compactness of the structure.

As mentioned before, light intensity modulated fiber optic sensors suffer from the instability caused by fiber bending, fiber length change and light source instability. To overcome these problems, some works have been done such as [94] [95] (Fig.

1.11). Polygerinos et al. designed a light intensity modulated sensor for cardiac catheterization [96], only ranging from 0-0.5 N with the resolution 0.005-0.01 N. The sensing range was later increased to 00.85 N in an updated version [95], with relatively small hysteresis, nonlinear calibration was also performed. Riener [83] and Yu [41] proposed differential force sensor with similar design with one emitting and two receiving fibers (Fig. 1.10). A small dislocation caused by force applied to the sensor changes the amount of light received by the two opposing fibers. To make the system less sensitive to unstable, diffused or absorbed light in the fibers, the force is determined by the relative rather than absolute intensity changes.

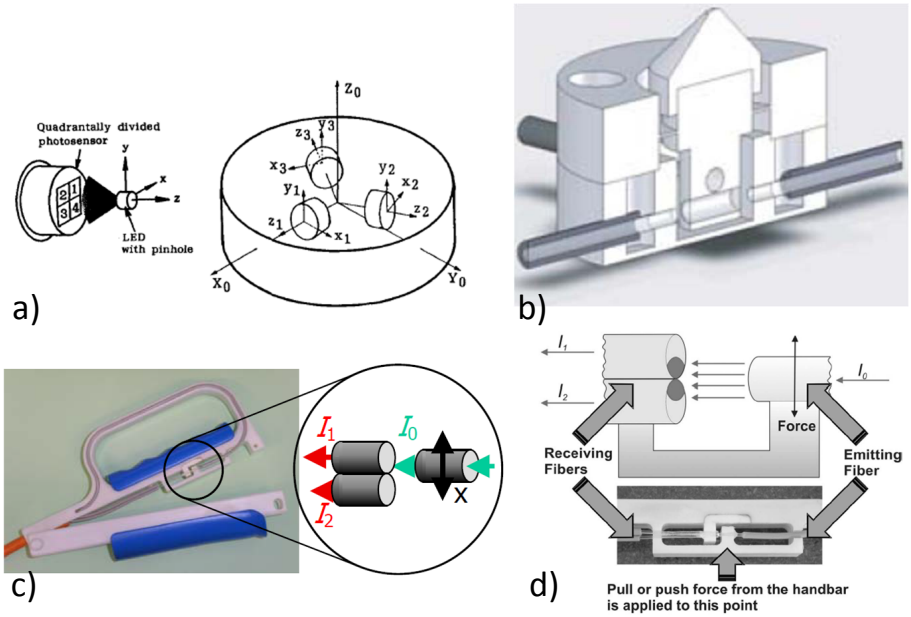


Figure 1.10: Transmissive intensity modulated fiber optic force sensor: a) An optical 6-DOF force/torque sensor based on transmissive light intensity principle designed by Hirose et al.© [23], b) with two 2-dof sensor, 3-dof force sensing is achieved by Tada et al. by using two micrometers aligned in orthogonal directions© [92], c) Riener et al. proposed differential force sensor with one emitting and two receiving fibers© [83], d) Yu et al. designed a differential force sensor similar to Riener's© [41]

Recently, with the rapid prototyping technology becoming more and more popular, Kesner et al. [97] designed a force sensor flexure fabricated with 3-D printer (Fig. 1.11). The accuracy is 0.2N within the range of 0-10N. Another reflective based force sensor is proposed by Tan [98]. Although the elastic frame structure is designed by using a topology optimization algorithm, the 3-DOF force sensor has significant hysteresis. Its forcing range is 0-6N with 25Hz bandwidth.

A triaxial catheter-tip force sensor for MRI-guided cardiac procedures was designed by Polygerinos et al. [99]. Similar design has also been done by Peirs et al. [100]. A bent-tip based fiber optic sensor was discussed by Puangmali et al. in [101]. It is developed for laparoscopic palpation that can be used to localize tissue lesions or nodules under an organs surface. Su et el. developed a low cost intensity modulated force sensor with a spherical convex mirror to focus light and decrease light loss [24].

#### 1.4.4.2 Wavelength Modulated Fiber Optic Force Sensor

Spectrum or the phase of the light is also used as other ways of measuring force. One example of wavelength modulated fiber optic force sensing technic is FBG. The emitted broadband light changes its spectrum as it travels between different media. The wavelength of both reflected and transmitted light shifts when the property of media of different refractive indices changes. Even micro bending of the optic fiber could affect the wavelength of the light. Thus the applied force could be known [96].

Since the first in-fiber Bragg grating was demonstrated by Hill et al. in 1978, many

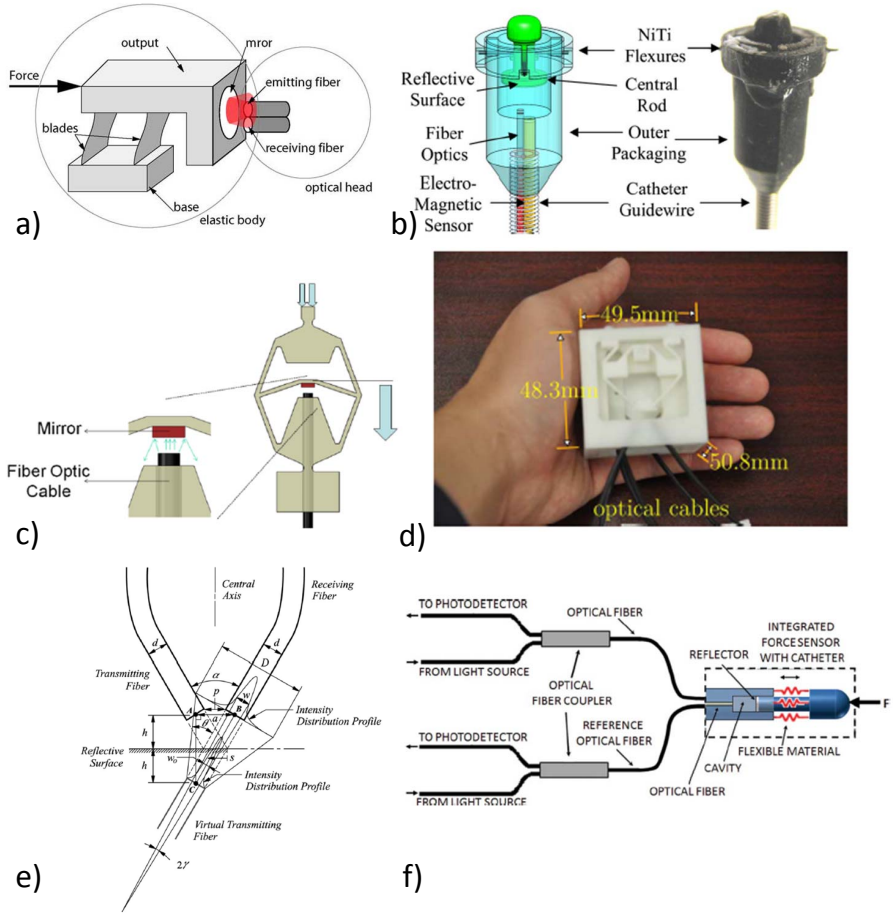


Figure 1.11: Reflective intensity modulated fiber optic force sensor: a) A reflective force sensor developed by Gassert et al.© [87], b) a reflective force sensor designed by Kesner et al. with flexure fabricated with 3-D printer© [97], c) reflective force sensor developed by Turkseven et al. with specially designed mechanism allows the amplification adjusted by changing its geometric parameters© [53], d) the elastic frame structure of the force sensor developed by Tan et al. is designed by using topology optimization but still with significant hysteresis© [98], e) a bent-tip based reflective force sensor discussed by Puangmali et al.© [94], f) reflective force sensor for cardiac catheterization © [95]

groups have been utilizing this technology in medical applications. Yokoyama et al. incorporated the FBG sensor into the distal part of an ablation catheter for lesion size prediction [102]. The force sensor(Touch+, Endosense) consists of three optical fibers with diameter of 0.125 mm each and a deformable body (elastic polymer) to

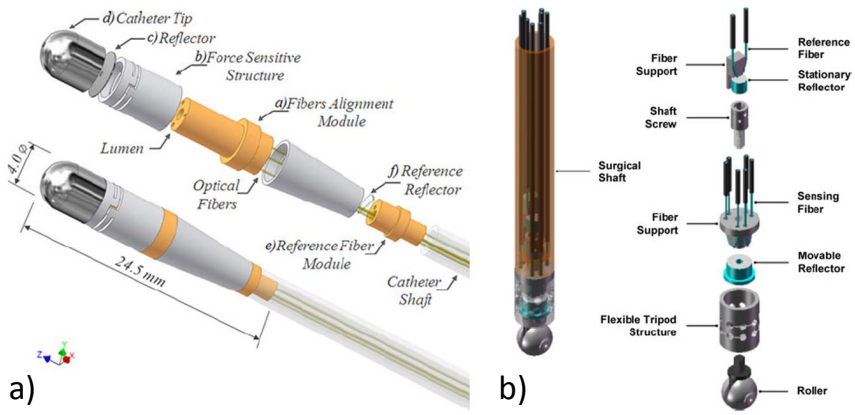


Figure 1.12: Catheter-like intensity modulated fiber optic force sensor: a) A triaxial catheter-tip force sensor for MRI-guided cardiac procedures designed by Polygerinos et al.© [99], b) a bent-tip based fiber optic sensor was discussed by Puangmali et al.© [101]

measure micro deformations that correlate with force applied to the catheter tip (Fig. 1.13). Light wavelengths between 1520 and 1570 nm is used and reflected by FBG on the deformable body at the distal end of the optical fibers, near the tip of the catheter.

Another interesting implementation of FBG sensors is an exoskeletal end-effector design by Park et al. [103]. The sensitivity of the FBG sensor used here is about $1.2pm/\mu\epsilon$ at center wavelength of 1550nm. As small as $0.1\mu\epsilon$ strain could be detected. It is shown that the strain response of FBGs is linear with no indication of hysteresis at temperatures up to $370°C$. Four FBG strain sensors are embedded in the shell with 90-degree rotational symmetry. One more sensor is placed at the center of the finger for temperature compensation. A group from Johns Hopkins University also utilized FBG sensors in eye surgery tool [25] [104]. Three FBG sensors are used to achieve

a 2-DOF force sensing micro-forceps design (Fig. 1.13). Recently, a MRI-compatible soft tissue indentor is designed with FBG sensors by Moerman et al. [105].

FBG not only could be used as a force sensor but also a shape sensor. By putting several FBG sensors in serial in the needle, Park et al. demonstrated an estimation method for needle shape and deflection [106].

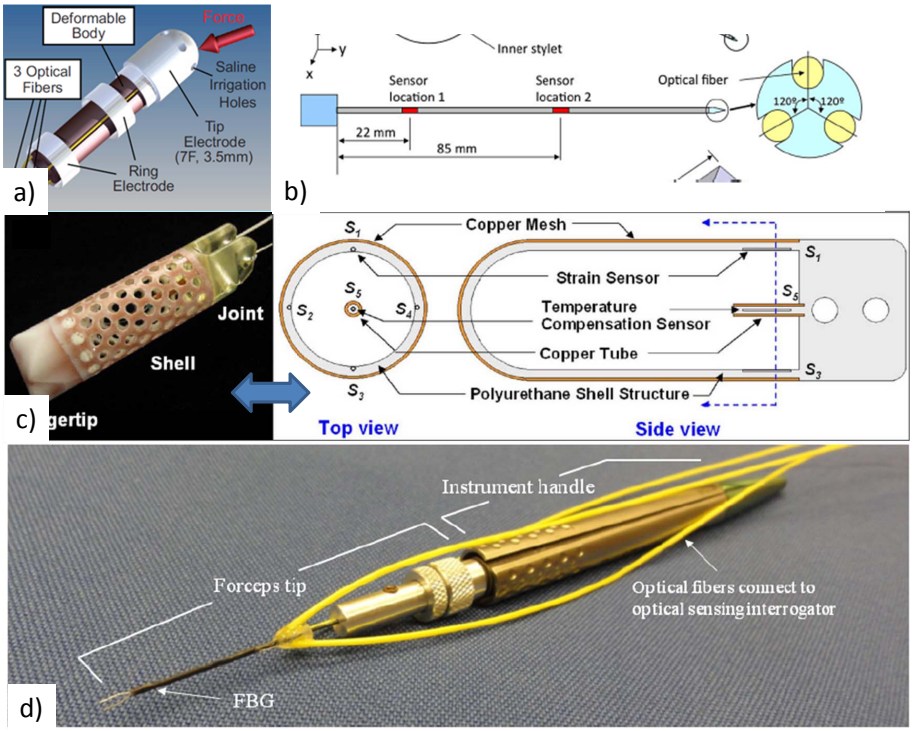


Figure 1.13: Wavelength modulated fiber optic sensor: a) an ablation catheter with the FBG sensor incorporated into the distal part by Yokoyama et al. for lesion size predicting© [102], b) FBG sensor used for needle shape estimation© [106], c) an exoskeletal end-effector design with five strain sensors© [103], d) an eye surgery tool with FBG sensor integrated© [104]

#### 1.4.4.3 Phase Modulated Fiber Optic Force Sensor

The fiber optic sensor could also be built based on the phase variations of a light field. It is more sensitive than the intensity based sensors because a small change in the optical path can result in a large fluctuation in the phase. Examples of phase modulated fiber optic sensors include the Mach-Zehnder interferometer, the Michelson interferometer and the Fabry-Perot interferometer [107].

FPI is a multiple-beam interferometer. As a result, the output intensity of FPI is very sensitive to the change of phase delay. However, FPI also suffers from some limitations, like sensitivity to the source coherence length and frequency jitter and having a complex shape of the transduction function [107].

Within our group, Su et al. evaluated a FPI sensor with bench top setup [108], and then proposed an implementation method to MRI-guided needle placement robot [109]. Shang et al. designed the optical transmission and signal processing system [26] and evaluated it with the haptic teleoperation system inside the MRI [22].

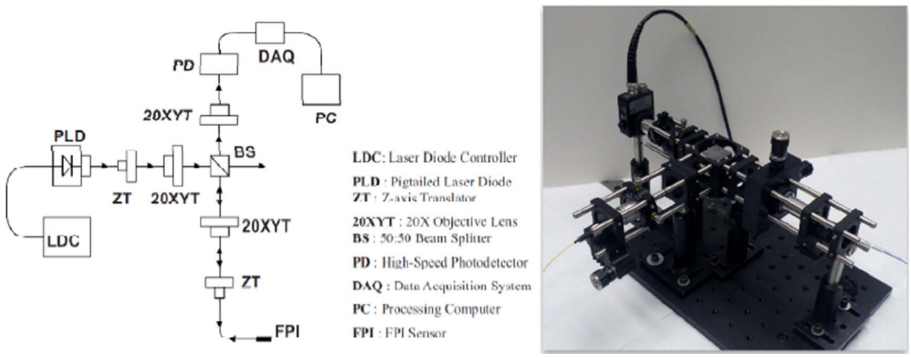


Figure 1.14: Phase modulated fiber optic force sensor: Within our group, Su et al. evaluated a FPI sensor with bench top setup© [108]

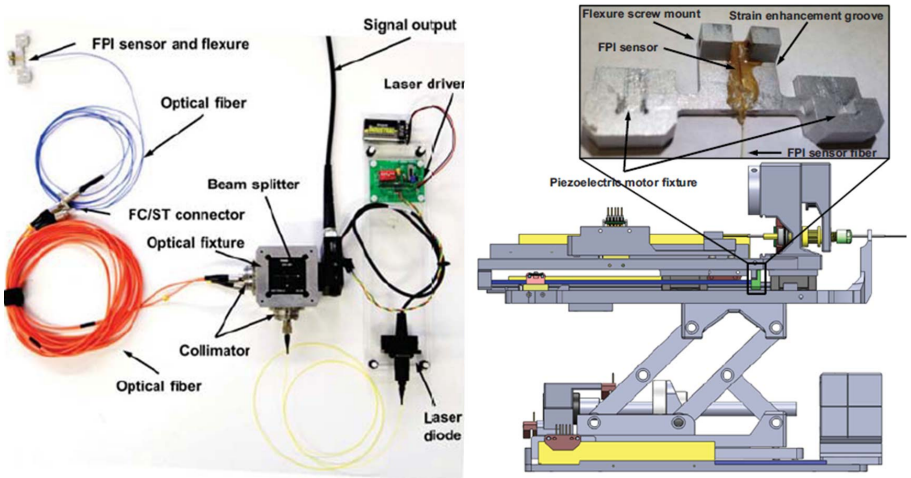


Figure 1.15: Phase modulated fiber optic force sensor: Shang et al. designed the optical transmission and signal processing system and evaluated it with the haptic teleoperation system inside the MRI

## 1.5 Dissertation Contributions

As mentioned in previous sections, the development of MRI-guided teleoperation system is still work in progress. Different driving and sensing technologies have been discussed separately as individuals but without a ultimate solution presented. Further, the evaluation of the system especially for the definition and evaluation metrics of MRI-compatibility are still not clear.

This dissertation focuses on systematic development of a complete MRI-compatible teleoperation system, proposes a clear system architecture as well as feasible clinical workflow. Different robot registration methods, force sensing and feedback technologies as well as the thorough performance evaluation has been discussed. MRI-compatibility definition and evaluation metrics are also summarized which could be used as future guidelines for developing such similar MRI-compatible systems. The

major contributions of this dissertation are as follows:

1) System architecture for general MRI-compatible teleoperated robotic system with real-time MRI-guidance is designed by using modular functional software and hardware parts. A feasible workflow of clinical procedure for performing teleoperated prostate biopsy is proposed with minimal modification from current clinical procedure.

2) Two different robot registration and tracking technologies are developed with fiducial based method. A multi-image registration method with a smaller Z shaped fiducial frame is proposed with sub-pixel accuracy. It is proven to be more accurate than other single-image registration methods.

3) A new reconfigurable cylindrical helix imaging coordinate (CHIC) fiducial frame is designed. Its registration algorithm is also developed. In addition, a performance enhanced CHIC fiducial frame with integrated passive self-resonance coils is also studied. Its great potential of improving the performance of current tracking method is shown by the feasibility study.

4) An approach of master-slave teleoperation system is developed with hybird piezoelectric and pneumatic actuation technologies. A piezoelectric-actuated slave robot is designed with 3-DOF stage for aligning the robot to hold another 3-DOF needle driver for needle steering. A 2-DOF pneumatic-driven master device with load cell force sensor is designed to interact with human user with haptic feedback.

5) A novel FPI fiber optic force sensor is designed and integrated into the slave

robot for needle insertion force sensing. And a compact opto-mechanical system is developed.

6) A bilateral control scheme and an impedance control scheme are designed. The performance of the teleoperation system is evaluated analytically. The position and force tracking accuracy and bandwidth are examined.

7) The performance of the teleoperation system inside MRI is evaluated, which includes thorough analysis of the MRI-compatibility; teleoperated needle steering inside MRI with teleoperated insertion and autonomous steering; 2-DOF teleoperated needle steering inside MRI and force feedback.

8) A system control architecture of a clinical grade 4-DOF surgical manipulator is developed. Two generations of limit switch are designed and evaluated. The extensive per-clinical evaluation of the system is performed with MRI accuracy assessment and MRI-compatibility test.

9) Conducted two clinical prostate biopsy trials with the clinical grade 4-DOF surgical robotic system.

## 1.6 Dissertation Overview

This dissertation is composed of four main chapters, chapter 2 to 5.

In chapter 2, the architecture of the teleoperated robotic system is developed with the modular hardware and software system so that the MRI-compatible teleopera-

tion with real-time MRI-guidance is achieved. To get a better understanding of the whole system, different modules of the architecture will be introduced including MRI-compatible robot controller, registration, control software and communication. The detailed design for the application of prostate intervention will be dig into more in the following chapters. Finally a workflow for clinical procedure for the application of performing teleoperated prostate biopsy is proposed.

In chapter 3, we focus on the development of fiducial type registration and tracking methods. One of the methods utilizes the existing Z shaped fiducial frame design but we propose a multi-image registration method which has higher accuracy with a smaller fiducial frame. The second method is a new design with a cylindrical shaped fiducial frame which is especially suitable for registration and tracking for needles. Alongside, a single-image based algorithm is developed to not only reach higher accuracy but also run faster. In addition, a feasibility study done here shows that with self-resonance coils attached, the CHIC fiducial frame gives even better imaging result that could significantly increase the fiducial imaging speed to have better real-time tracking performance.

In chapter 4, a surgical master-slave teleoperation system for the application of percutaneous interventional procedures under continuous MRI-guidance is presented. This system consists of a piezoelectrically actuated slave robot for needle placement with integrated fiber optic force sensor utilizing FPI sensing principle. The sensor flexure is optimized by FEA and embedded to the slave robot for measuring needle

insertion force. A novel, compact opto-mechanical FPI sensor interface is also integrated into the MRI robot control system. A pneumatical-actuated haptic master robot is developed to render the force associated with needle placement interventions to the surgeon. An aluminum load cell is implemented and calibrated to close the impedance control loop of the master robot. A force-position control algorithm is developed to control the hybrid actuated system. Teleoperated needle insertion is demonstrated under live MR imaging, where the slave robot resides in the scanner bore and the user manipulates the master beside the patient outside the bore. Force and position tracking results of the master-slave robot are demonstrated to validate the tracking performance of the integrated system.

Chapter 5 introduces the control of robotic system for clinical transperineal prostate interventions under live MRI guidance. The proposed modular system communicates between each module and with MRI system using OpenIGTLInk over Ethernet. A 4-DOF robot with parallel mechanism is designed for needle placement with ultrasonic motors and is precisely controlled by a custom MRI-compatible robot controller discussed in chapter 2. Two generations of limit switches are design for the important safety and accuracy considerations. To be fully ready for clinical use, comprehensive pre-clinical evaluations of the system are performed. MRI-compatibility of the system is evaluated in a 3 Tesla MRI scanner, showing the SNR loss of less than 18%. The accuracy of this robotic system is tested to be with an in plane translational RMS error of 1.402 mm at the needles tip. The first two clinical trials of the robot

performing prostate biopsy have been conducted at Brigham and Women's Hospital (BWH) in Boston in May, 2014.

Finally, the conclusion and the future work is discussed in chapter 6.

# Chapter 2

# System Architecture and Workflow for MRI-Guided Teleoperation System

Part of this chapter has been published as

H. Su, **W. Shang**, G. A. Cole, G. Li, K. Harrington, A. Camilo, J. Tokuda, C. M. Tempany, N. Hata, and G. S. Fischer, "Piezoelectrically actuated robotic system for MRI-guided prostate percutaneous therapy," Mechatronics, IEEE/ASME Transactions on, vol. 1, no. 1, pp. 1-12, 2014.(In press) [110]

G. Li, H. Su, G. A. Cole, **W. Shang**, K. Harrington, A. Camilo, J. G. Pilitsis, and G. S. Fischer, "Robotic system for MRI-guided stereotactic neurosurgery," Biomedical Engineering, IEEE Transactions on, vol. 1, no. 1, pp. 1-11, 2014.(In press) [111]

**W. Shang**, H. Su, G. Li, and G. S. Fischer, "Teleoperation system with hybrid pneumatic-piezoelectric actuation for MRI-guided needle insertion with haptic feedback," in Intelligent Robots and Systems (IROS), 2013 IEEE/RSJ International Conference on. IEEE, Conference Proceedings, pp. 4092-4098. [22]

Li G, Su H, **W. Shang**, Tokuda J, Hata N, Tempany CM, Fischer GS, "A Fully Actuated Robotic Assistant for MRI-Guided Prostate Biopsy and Brachytherapy," SPIE Medical Imaging (Image-Guided Procedures, Robotic Interventions, and Modeling Conference), Orlando, USA, Feb. 2013. SPIE [112]

Su H, Cardona D, **W. Shang**, Cole GA, Rucker C, Webster III R, Fischer GS, "A MRI-Guided Concentric Tube Continuum Robot with Piezoelectric Actuation: A Feasibility Study," IEEE ICRA 2012 International Conference on Robotics and Automation, Saint Paul, Minnesota, USA, May 2012 (Best medical robotics paper finalist). [113]

and

Su H, **W. Shang**, Harrington K, Camilo A, Cole GA, Tokuda J, Hata N, Tempany CM, Fischer GS, "A Networked Modular Hardware and Software System for MRI-guided Robotic Prostate Interventions," SPIE Medical Imaging, San Diego, USA, Feb. 2012. [114]

## 2.1 Overview

The robot-assisted intraoperative MRI intervention could reduce procedure time by letting the interventions happen inside the scanner bore without moving the patient out. By using the robotic device with high precision closed-loop position control, it increases the intervention accuracy. Mentally registering and tracking the surgical device are not necessary any more since the sensors and fiducials on robotic device enable the automatic registration and tracking.

An increasing number of MRI-guided robot assisted procedures have been performed recently. Such as the robot assisted transperineal prostate biopsy at BWH [16], transrectal prostate biopsy at Radboud University Nijmegen Medical Centre [115], and breast biopsy also from Radboud University Nijmegen Medical Centre [116]. But for all of these three approaches, the final biopsies are still performed manually which have significant ergonomic problem. The limited MRI bore space restricts the physician from performing needle insertion such as prostate biopsy while patient is being scanned inside the bore. Performing biopsy in a tightly constraint area in an awkward position could have potentially problem to patient and cause fatigue to physician. Fig. 2.1(left) shows the MRI-guided prostate biopsy using a motorized needle guide template [117]. Fig. 2.1 (right) shows another approach of MRI-guided prostate biopsy using a needle guide robot [118]. Both of the two robotic-assisted prostate biopsies were at BWH. As it is shown in the figure, surgeon is unable to monitor the navigation software or real-time images when performing needle insertion inside the bore.

Figure 2.1: (Left): The MRI-guided prostate biopsy using a motorized needle guide template [117]©2012 IOP Publishing. (Right): Another approach of MRI-guided prostate biopsy using a needle guide robot.

To overcome these problem, the robotic devices are made towards either fully automated or teleoperated directions. Comparing the fully automated approach, teleoperation system avoids the ergonomic problem while still keeps the surgeon in the control loop. Not letting the surgeon lose the control of the surgical device makes it a better approach that could be accepted for clinical use.

In this chapter, the teleoperated robotic system is focused. The architecture of the system is developed with the modular hardware and software system [22] that the MRI-compatible teleoperation with real-time MRI-guidance is reached. To get a better understanding of the whole system, different modules of the architecture will be introduced including MRI-compatible robot controller, registration, control software and communication. The detailed design for the application of prostate intervention will be dig into more in the following chapters. Finally a workflow for clinical procedure for the application of performing teleoperated prostate biopsy is proposed.

The contributions of this chapter are: 1) designed system architecture for general MRI-compatible teleoperated robotic system with real-time MRI-guidance by using modular functional parts; and 2) proposed a feasible workflow of clinical procedure for performing teleoperated prostate biopsy with minimal modification from current clinical procedure.

## 2.2 System Architecture

As shown in Fig. 2.2, the way that this teleoperation system works is to have the surgeon to operate haptic master device inside the MRI room and beside the bed while have the interventional slave robot close to the iso-center and follow the motion of the operator. The FPI fiber optic force sensor measures needle insertion force and reflects back to the surgeon by the pneumatic haptic device. The force controller regulates surgeon's force sensation by closing an impedance control force feedback loop with a master side strain gauge force sensor. This integration of the physician with the system would facilitate better access to the patient in emergency and psychologically more acceptable to the patients. Also, the whole procedure can be monitored from the MRI console outside of the MRI room as redundant safety mechanism.

The whole system consists of seven modules:

1) MRI scanner and the scanner console;

2) Surgical planning and navigation software;

3) Robot control software;

4) Fiber optic communication interface;

5) MRI-compatible robot controller;

6) Master robot;

and

7) Slave robot.

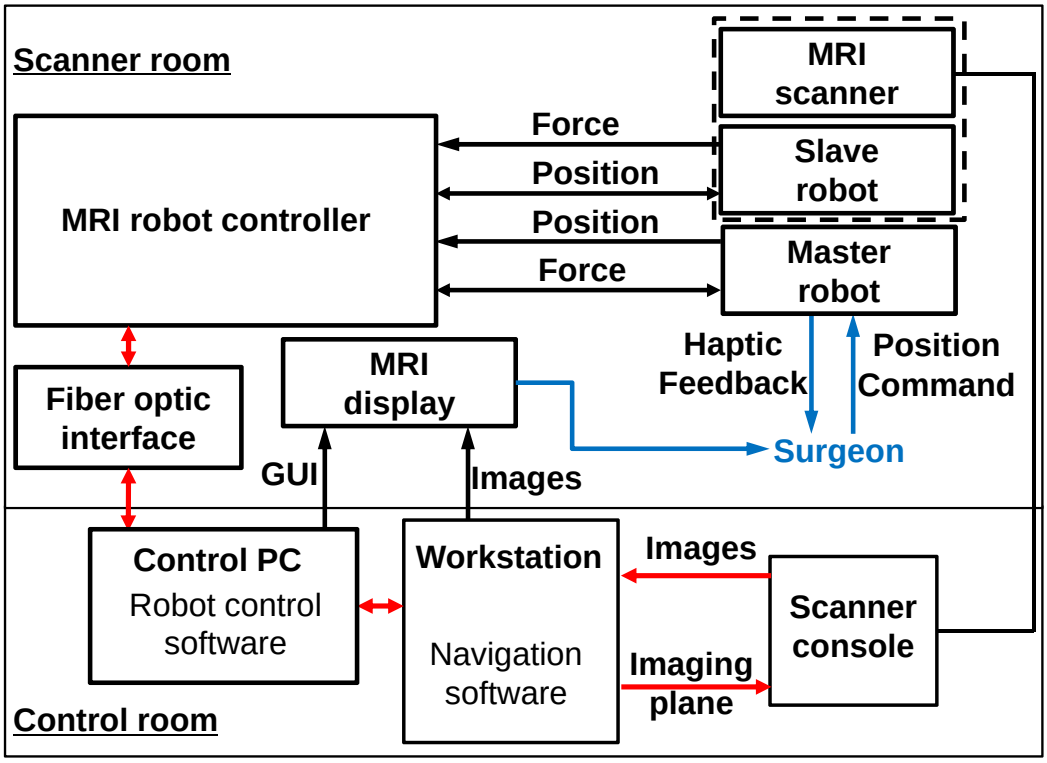


Figure 2.2: System architecture for MRI-guided teleoperated robotic system.

The system is designed to be modular, reconfigurable and scanner-independent. No specific or customized patch panel is required in any type of MRI scanner room except a waveguide tube to pass out a fiber optic cable for communication between

the robot controller inside the MRI room and the computers outside the room.

The red lines in Fig. 2.2 indicate the communication through network which makes the whole system modular. The parts on each side of every red line could be replaced for different applications as long as they follow the same communication protocol. The only non-network connection between two modules is the one between controller and robot. Well shielded Very-high-density cable interconnect (VHDCI) cable is used to ensure the proper transfer of motor and encoder signal while still with no interference to MRI. OpenIGTLink [119] is used as the communication protol to exchange control, position, and image data. Any surgical software that runs with OpenIGTLink is compatible with this system. Finally, the blue lines in Fig. 2.2 indicate the interaction between the surgeon and the system, specifically with the master robot and the display. Surgeon will be able to control the robot by giving the position command to the master device while having force feedback from this haptic device and also the visual feedback from the screen that displays the real-time MR images.

Fig. 2.3 and 2.4 on page 55 illustrate the actual system setup with all seven modules in MRI scanner room and console room. Detailed workflow will be discussed in Chapter 2.5.

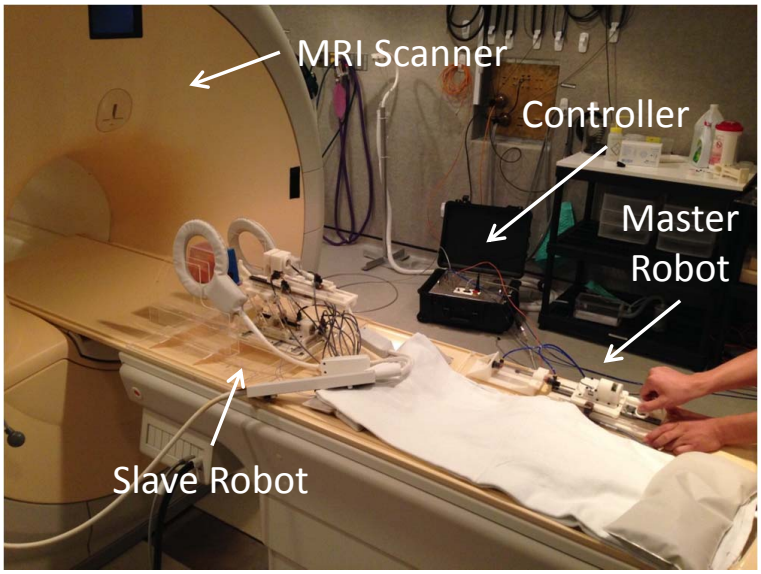


Figure 2.3: Actual system setup for MRI-guided teleoperated robotic system: Master-slave robots and robot controller inside the MRI room.

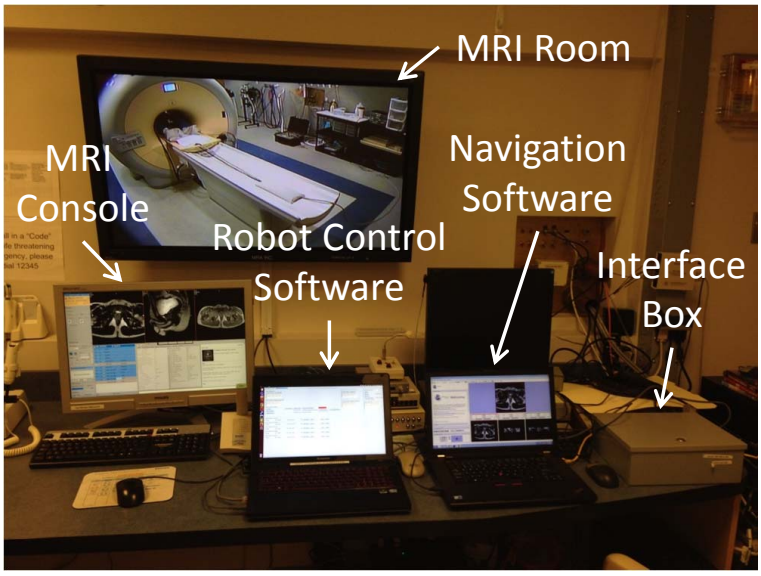


Figure 2.4: Actual system setup for MRI-guided teleoperated robotic system: Robot control software running in the console room.

## 2.3 MRI-Compatible Robot Controller

### 2.3.1 Piezoelectric Motors

As introduced before, piezoelectric actuation draws more and more attention because of its precision of positioning accuracy. Based on the driving signal, the piezoelectric motors could be categorized in two types: harmonic and non-harmonic. Harmonic motors, such as Nanomotion and Shinsei motors, utilize a sinusoidal signal with fixed/harmonic frequency at 38k-50k Hz. Velocity control of Nanomotion motors is usually done with the change of signal amplitude at 80-300 VRMS while for Shinsei motors, it is done through frequency control with the maximum speed occurs at the harmonic frequency. In the other hand, a much lower driving frequency is used for non-harmonic motors which are chosen to be in our applications, specifically PiezoLegs motors.

As shown in Fig. 2.5 [120], the PiezoLegs piezoelectric motor is a quasi-static leg actuator with four piezoelectric elements. The driving frequency for PiezoLegs motors ranges from 750 Hz to 3k Hz and its signal is not standard sinusoidal but an arbitrary waveform. The speed of the PiezoLegs motor is controlled by frequency. Each of four legs is an electrical bimorph stack. Four legs form in two pairs which are driven by 4-phase analog signal and two of them move together with the motion of their tip follows the specific driving waveform applied.

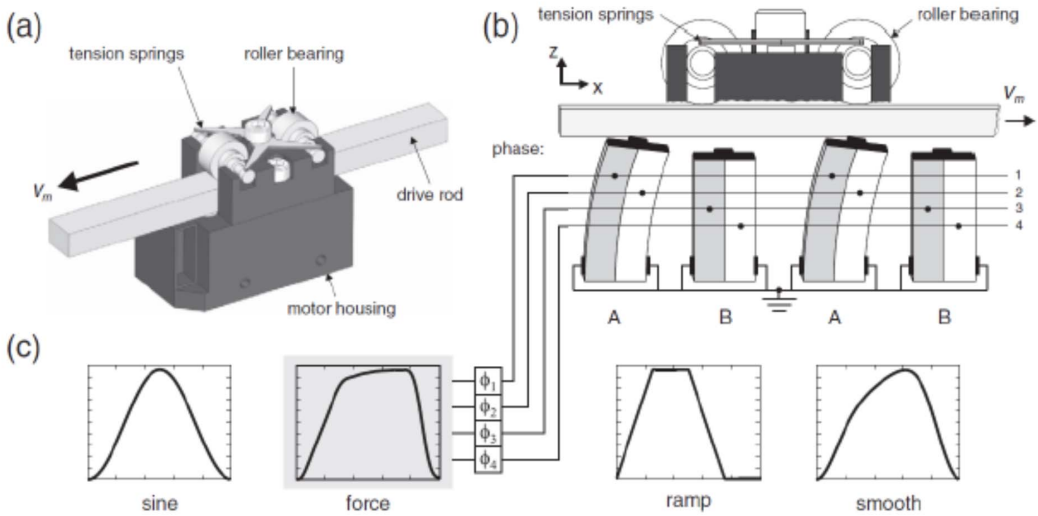


Figure 2.5: (a):Main components of PiezoLegs actuator, (b): Mechanical interaction between bimorph stacks and drive rod as well as the preload structures, and electrical driving signal and its relationship with bimorph stacks, (c): Examples of driving signals. Figure from [120]

### 2.3.2 Control Electronics

Previous research effort have shown that the SNR lose is up to 90% although the motor got well shielded and grounded and the major source of noise is from the driving signal [9]. By using commercially available drivers for piezoelectric motors, significant SNR lose and RF interference are observed since the signal is generated by low-pass filter from high frequency square wave.

In order to make clean driving signal, a custom driver for piezoelectric motors was developed in our lab collaboratively [45]. The driving waveform is stored in a SD card, and loaded to the internal RAM of field-programmable gate array (FPGA, Cyclone EP2C8Q208C8, Altera Corporation) by microcontroller (PIC32MX460F512L, Microchip Technology Inc) which read the desired position set point through Eth-

ernet. As the Piezoboard diagram shown in Fig. 2.6, the Low-Voltage Differential Signaling (LVDS) receiver on the control board connects to two quadrature encoders, one of which could be for slave joint and the other for corresponding master joint. Then the position and velocity servo control loop is performed to control the output sample rate of the FPGAs waveform synthesizer. The waveform signal goes through high power linear amplifiers and filter to output. The FPGA is also in charge of dealing with several analog I/Os, stall detection and overheat protection.

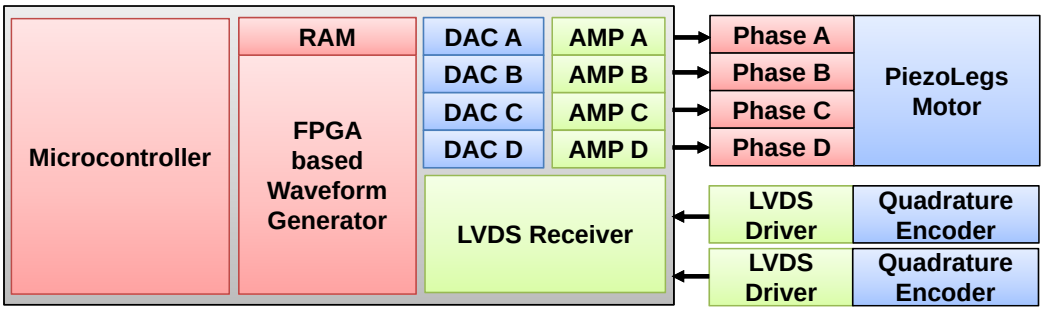


Figure 2.6: Block diagram of one piezoboard.

To eliminate the noise introduced from communication, a fiber optic Ethernet cable is used for communication between the robot controller inside the MRI room and the control PC outside the MRI room. On each side of fiber optic cable, media converter (MCM110SC2, Startech Corporation) is used to convert the signal between Ethernet and fiber optic signals.

Fig. 2.7 shows the closed and open controller box. The aluminum controller enclosure is put inside a plastic, wheeled travel case within the size limit of carry-on luggage to allow it to travel easily to different locations. The controller box could

hold up to eight Piezoelectric boards which could drive eight joints. The configuration shown in Fig. 2.7 is with five boards and one of which is for controlling the pneumatic actuator on master haptic device which will be introduced in Chapter 4. Electromagnetic interference is blocked as much as possible by using the aluminum case which is grounded as a Faraday cage.

VHDCI cables are used through serpentine wave guides on one side of the controller box to transport the control signal to Piezoelectric motors with grounded shielding all the way to the motor cases. The cables are kept straight to avoid the potential noise introduced by Lenz's law.

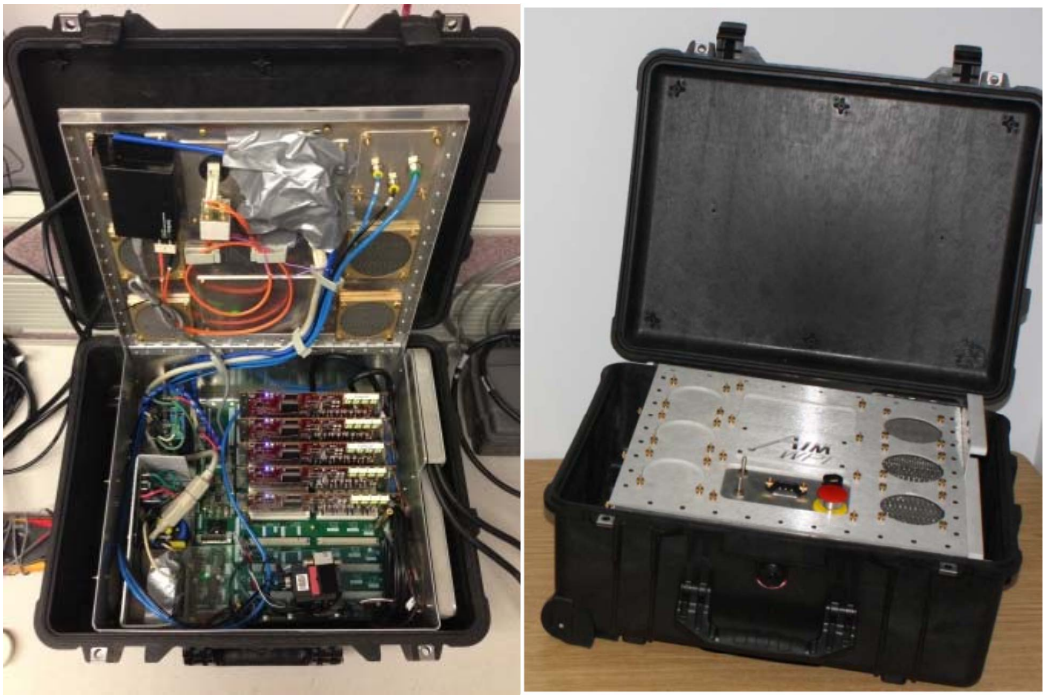

Figure 2.7: (Left): MRI-compatible robot controller with lid closed, (Right): inside view of the controller.

## 2.4 Control Software

The clinical workflow as well as the enhanced robot control is all managed by the robot control software which is developed collaboratively in our lab. The JAVA based software uses graphical user interface (GUI) to interact with surgeon and it consists of two major tabs. One is the main tab which includes robot registration, task and joint space robot control and position display. The other tab is dedicated for teleoperation and haptic feedback display.

As shown in Fig. 2.8, the main tab consists of four modules:

1) The upper left column is for robot registration and calibration. The registration matrix $T_Z^{RAS}$ could be acquired by either manually typing or receiving through OpenIGTLink communication. $T_{Robot}^{Z}$ is gotten from robot calibration.

2) The upper middle column is for displaying the target and current actual transformation matrices with 6-DOF position and orientation information.

3) The upper right column is designed for automatic motions including auto aligning the base, inserting the needle, performing biopsy and brachytherapy (dropping the seeds) and retracting the needle. The task space target transformation matrix could be manually entered in this column.

4) The lower part is the joint space control panel where the joint level target could be set individually by user directly or by filling the task space target pose on the upper right corner and calculated automatically by inverse kinematics. The current position for each joint is also shown respectively. This part is populated by Extensible Markup

Language (XML) file for each specific robot.

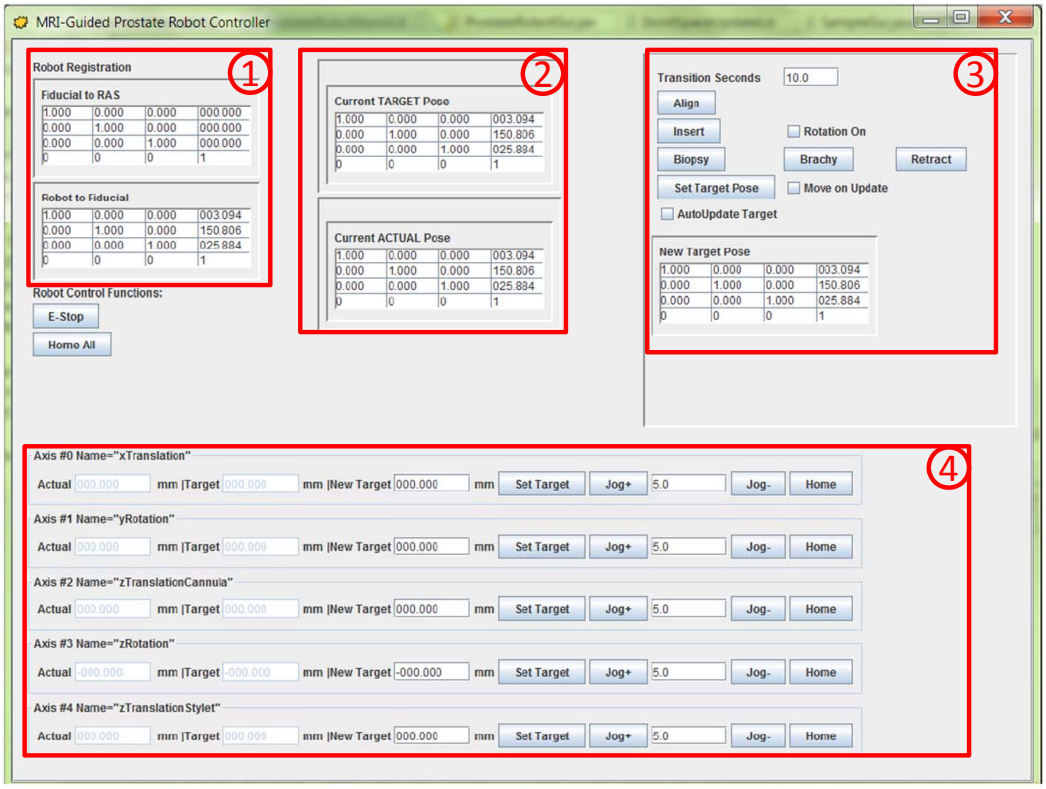


Figure 2.8: Main GUI of robot control software [110]. 1: robot registration and calibration; 2: target and current actual transformation matrices displaying; 3: robot motions with task space target transformation matrix; 4: joint space control panel.

XML is used to define the character of each joint for a specific robot. The name, scale factor from raw encoder reading to engineering units, the joint position limits, latch distance which is for homing, and control parameters such as PID values and frequency range are all set for each joint in XML file.

Teleoperation panel 2.9 also consists of four modules:

1) The upper left part is the master and slave joints selection. User could enable or disable and match specific joints on master and slave.

2) The middle part is for control parameters setup. Offset and scaling factor could be set separately for insertion and rotation joints. The maximum insertion depth could also be set to prevent the needle from overshooting which could potentially injure the patient.

3) The upper right column is designed for data visualization. The position and force information for each joint chosen is shown in this column.

4) The lower part is the direct pressure control for pneumatic actuator. This function is not required for normal teleoperation because the force applied by the pneumatic actuator is set by the feedback control algorithm but it is potentially useful for other applications.

Since registration process is not integrated in the control software, it is done by manual typing or with other programs such as the Matlab code made by Shang [80] or some navigation software, for example 3D Slicer and RadVision™, and the registration result is transferred to the robot control software through OpenIGTLink.

Navigation software is often used for surgery planning as well as monitoring. It is usually loaded with the pre-operative MR images and the potential target could be selected by Surgeon. During the procedure, the target is sent down to the robot control software through OpenIGTLink and the needle tip position could be sent up to the navigation software from robot control software also through OpenIGTLink. Fig. 2.10 shows 3D Slicer with the selected targets (yellow) and needle (blue). Fig. 2.11 shows another navigation software RadVision with selected targets.

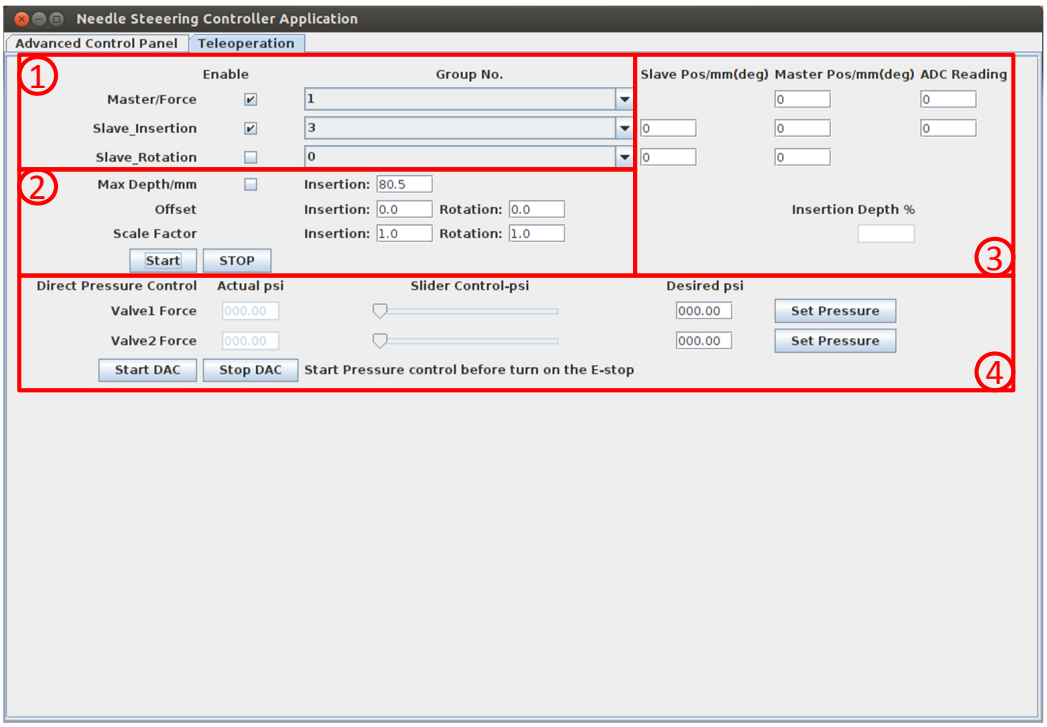


Figure 2.9: Teleoperation control tab of robot control software. 1: master and slave DOF selection; 2: control parameters setup; 3: master and slave information displaying; 4: direct pressure control of the pneumatic actuator.

## 2.5 Clinical Workflow

A number of robotic surgical systems fail to be used clinically because the workflow is different from the traditional procedure and brings too much learning and uncertainty to the robotic procedure. By learning the lessons from them, instead of fully automated, this system is teleoperated which keeps the surgeon in the loop and still have control of the needle insertion step. The workflow of the teleoperated system also mimics the traditional TRUS-guided prostate needle insertions. The whole workflow is mainly managed by the robot control software. Four major steps of operation form the workflow which is shown in Fig. 2.12.

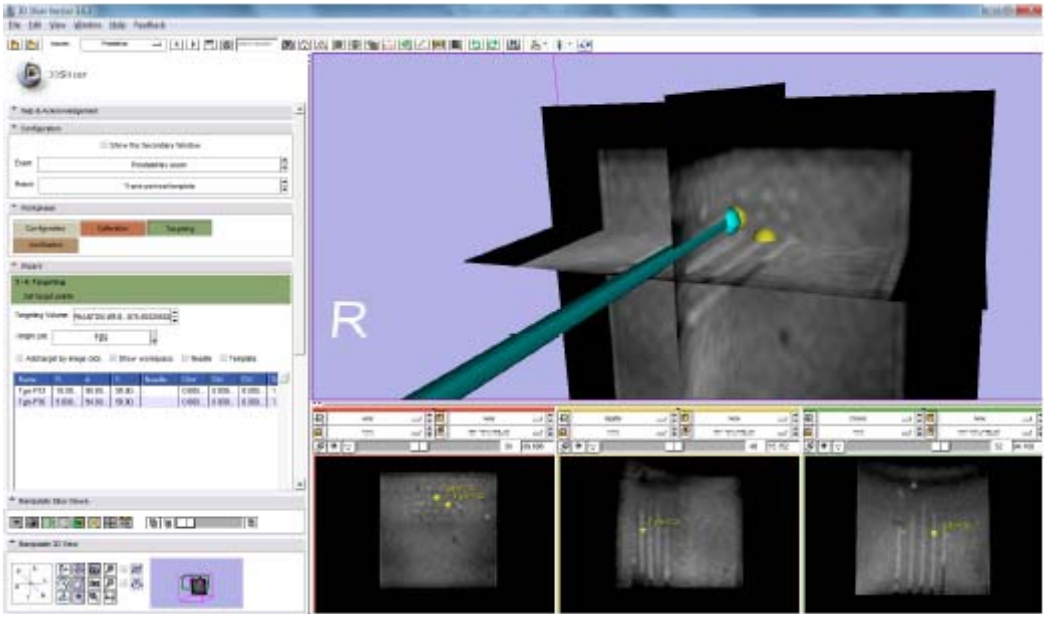


Figure 2.10: 3D Slicer with a virtual needle shown.

1) Preparation

When the patient arrives at the surgical scene, surgeon and nurses usually take quite a while to put the patient in bed with the right position still maintain patient comfort. In the meantime, the engineering team could set up the robot, start the robot controller, check the communication and initiate the robot to the home position. After all of those steps are done, both the master and slave robots will be draped. When the patient is properly positioned in bed, the slave robot will be put between patients legs and locked in position, and master robot will be placed outside of the scanner bore at the place where surgeon feels comfortable with.

2) Registration and Planning

A series of transverse MR images of the fiducial frame are acquired. Multi-slices registration is done by Matlab registration program. The registration result is trans-

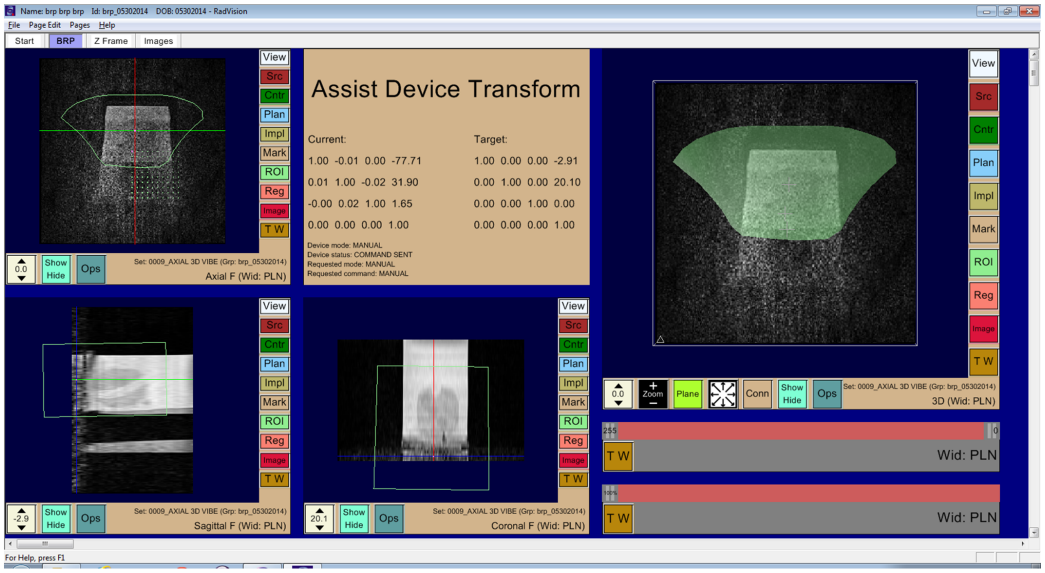


Figure 2.11: RadVision$^{TM}$user interface with selected targets in a prostate phantom.

ferred to robot control software through OpenIGTLink. The registration method will be discussed more in Chapter 3. A series of MR images of target area are taken again and those per-operative images are loaded to the navigation software such as 3D Slicer or RadVision through Ethernet. Targets are selected from the software.

3) Targeting and Verification

One of the selected targets is sent to the robot control software through OpenIGTLink. Once the robot control software receives it and the inverse kinematics will be done to calculate the joint positions.

Robot is firstly aligned to the target with the correct entry point, then teleoperation is started and surgeon could manipulate the master device to teleoperate the slave robot to perform the needle insertion and steering. The desired insertion depth could be set as the stop point to prevent the surgeon from inserting the needle

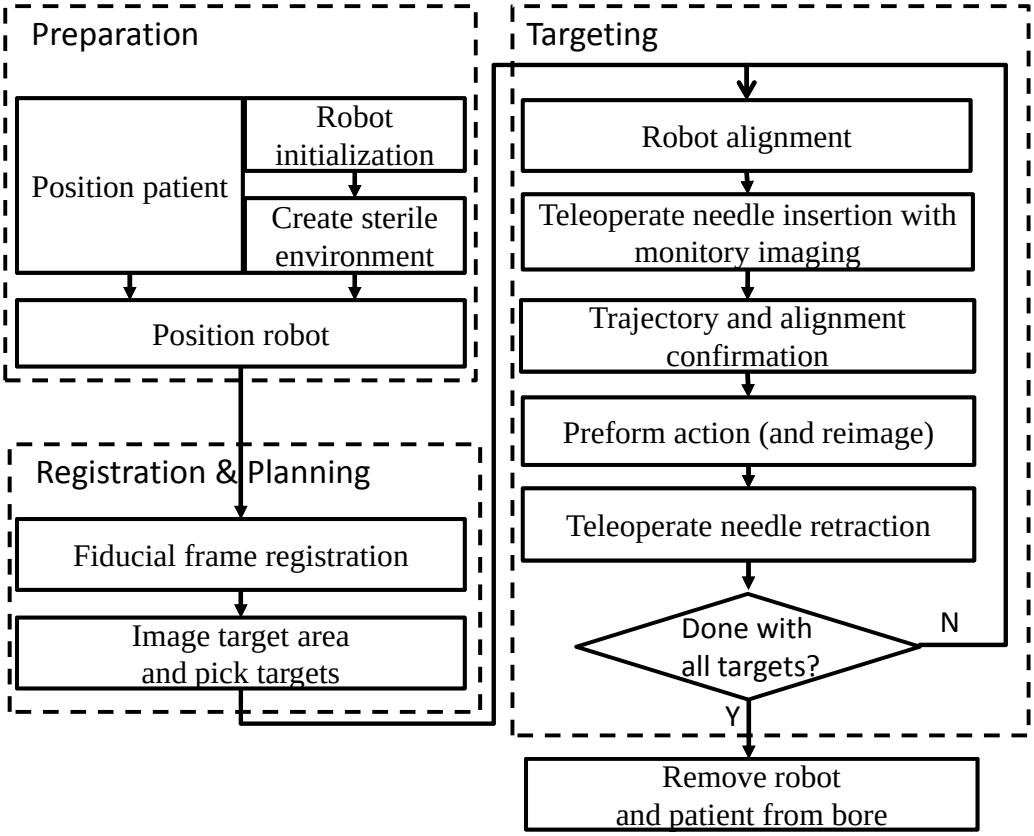


Figure 2.12: Clinical workflow of teleoperated needle insertion: 1: preparation; 2: registration and planning; 3: targeting; 4: finishing.

too deep. Real-time MR imaging will be performed while needle is being inserted. Surgeon could have both visual and haptic feedback.

The confirmation images are taken when the needle reaches the desired location. If the location is satisfactory to surgeon, the action will be performed such as biopsy or brachytherapy and it followed by another confirmation imaging.

Finally the needle is retracted by teleoperation and next targeting will be performed.

4) Finishing

If all the targets are reached and confirmed, the robot is removed from surgical scene before the patient.

## 2.6 Discussion and Conclusions

In this chapter, a system architecture for teleoperated robotic system is developed with the modular hardware and software that the MRI-compatible teleoperation with real-time MRI-guidance is reached. Different modules of the architecture are introduced, including MRI-compatible robot controller and the driving technology, registration, control software and communication. Finally a workflow of clinical procedure for the application of performing teleoperated prostate biopsy is proposed. The detailed design for the application of prostate intervention will be discussed with more details in the following chapters. Chapter 3 covers two different registration and tracking methods that make the step 2 of the workflow possible and two enabling robotic approaches for step 3 of the workflow will also be discussed in Chapter 4 and 5.

# Chapter 3

# Registration and Tracking Methods for MRI-Guided Interventions

Part of this chapter has been published as

**W. Shang**, Y. Ma, I. Dobrev, H. Su and G. S. Fischer, "Cylindrical helix imaging coordinate(CHIC) fiducial registration and tracking for image guided interventions," Biomedical Engineering, IEEE Transactions on. (In review) [121]

**W. Shang** and G. S. Fischer, "A high accuracy multi-image registration method for tracking MRI-guided robots," Proc. of SPIE Vol, vol. 8316, Conference Proceedings, pp. 83 161V-1. [80]

Y. Ma, I. Dobrev, **W. Shang**, H. Su, S. R. Janga, and G. S. Fischer, "CHIC: Cylindrical helix imaging coordinate registration fiducial for MRI-guided interventions," in Engineering in Medicine and Biology Society (EMBC), 2012 Annual Inter-

national Conference of the IEEE, Conference Proceedings, pp. 2808-2812. [122].

and

W. Ji, J. D. Matte, G. Li, Y. Ma, H. Su, **W. Shang**, and G. S. Fischer, "Reconfigurable fiducial-integrated modular needle driver for MRI-guided percutaneous interventions," Journal of Medical Devices, vol. 7, no. 3, pp. 030915, 2013, 10.1115/1.4024486. [123]

## 3.1 Overview

Robot-assisted surgical interventions have been developed rapidly in the last decade, especially for cancer treatment [66]. Although the robot itself has a high targeting accuracy, the position and orientation of the surgical tool with respect to the patient anatomy in the intraoperative images are always crucial [67]. This brings up the desire of high accurate robot registration and tracking [68].

In this chapter, we focus on the developing of two fiducial type registration and tracking methods. The first one utilizes the existing z shaped fiducial frame design but we propose a multi-image registration method which has higher accuracy with a smaller fiducial frame. The second method is a new design with a cylindrical shaped fiducial frame which is especially suitable for registration and tracking for needles. Alongside, a single-image based algorithm is developed to not only reach higher accuracy but also run faster. In addition, a feasibility study done here shows

that with self-resonance coils attached, the CHIC fiducial frame gives even better imaging result that could significantly increase the fiducial imaging speed to have better real-time tracking performance.

The contributions of this chapter are: 1) designed a multi-image registration method for the Z shaped fiducial frame with improved accuracy; 2) designed a new reconfigurable cylindrical helix imaging coordinate (CHIC) fiducial frame and registration algorithm with accuracy analysis; and 3) studied feasibility of a performance enhanced CHIC fiducial frame with integrated passive self-resonance coils.

## 3.2 Surgical Navigation Coordinates

Anatomical coordinate system is most importantly used in medical imaging. More intuitively, it is called patient coordinate system since all the names for its directions are with respect to patient position and orientation. Hence its three coordinate axes use the anatomical axes which are: anterior-posterior (A-P), inferior-superior (I-S) and left-right (L-R).

Correspondingly, three anatomical planes are formed based on the six directions. Transverse plane is perpendicular to S-I direction separates the head and feet. Coronal plane is perpendicular to A-P direction, separates the front from back. Sagittal plane is perpendicular to L-R direction separates left and right. Figure 3.1 shows three anatomical planes as well as six directions.

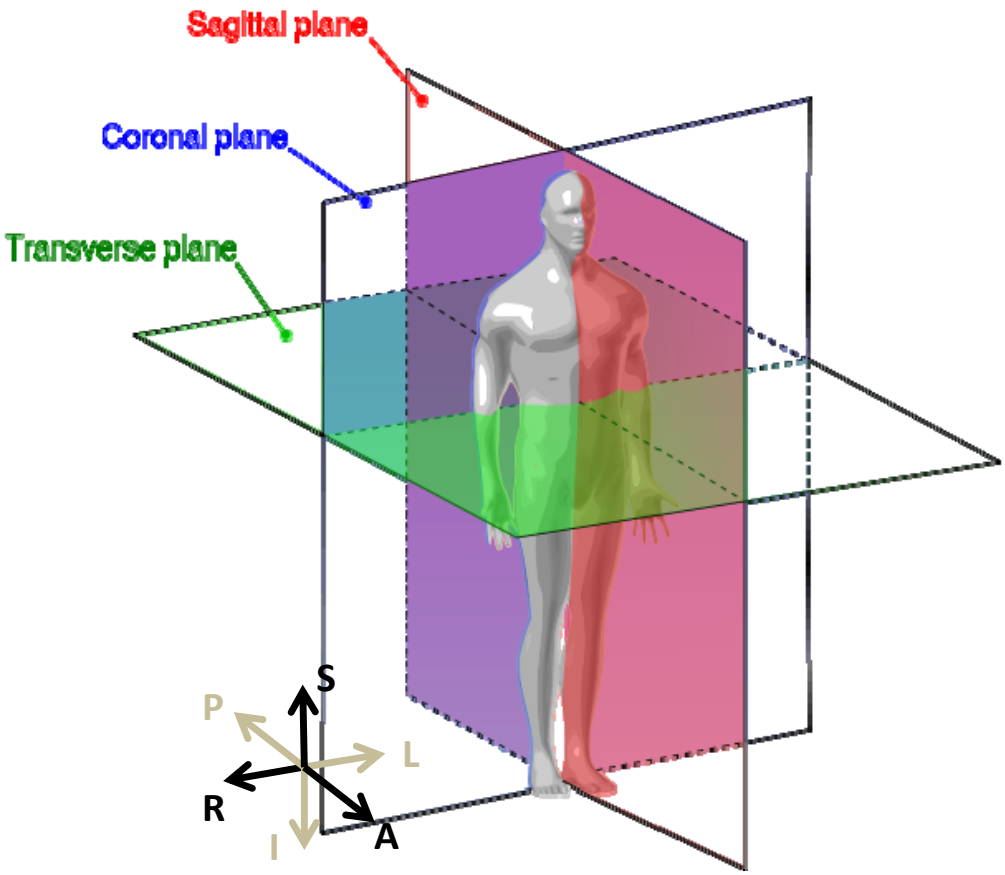


Figure 3.1: Three anatomical planes: transverse, coronal and sagittal plane. Six axes directions: anterior-posterior (A-P), inferior-superior (I-S) and left-right (L-R). Figure is adapted from `http://en.wikipedia.org/wiki/Anatomical_plane`. This file is licensed under the Creative Commons Attribution 3.0 Unported license.

More specifically, two coordinate systems are most commonly used in medical imaging. LPS (Left-Posterior-Superior) system and RAS (Right-Anterior-Superior) system, both are right-hand-system. LPS is used in Digital Imaging and Communications in Medicine (DICOM) images and RAS is used in 3D Slicer and the communication between surgeons and engineers.

## 3.3 Robot Registration

The purpose of robot registration is to find the location of the robot with respect to the patient in order to insert the needle to the correct position in patient, $T_{Tip}^{RAS}$. When the robot is registered based on imaging a fiducial frame attached to the robot, the target for robot could be given by using RAS coordinates. A series of homogeneous transformations is used to transfer the needle tip position from robot coordinate system to RAS coordinate system. The robot registration procedure could be demonstrated in Figure 3.2.

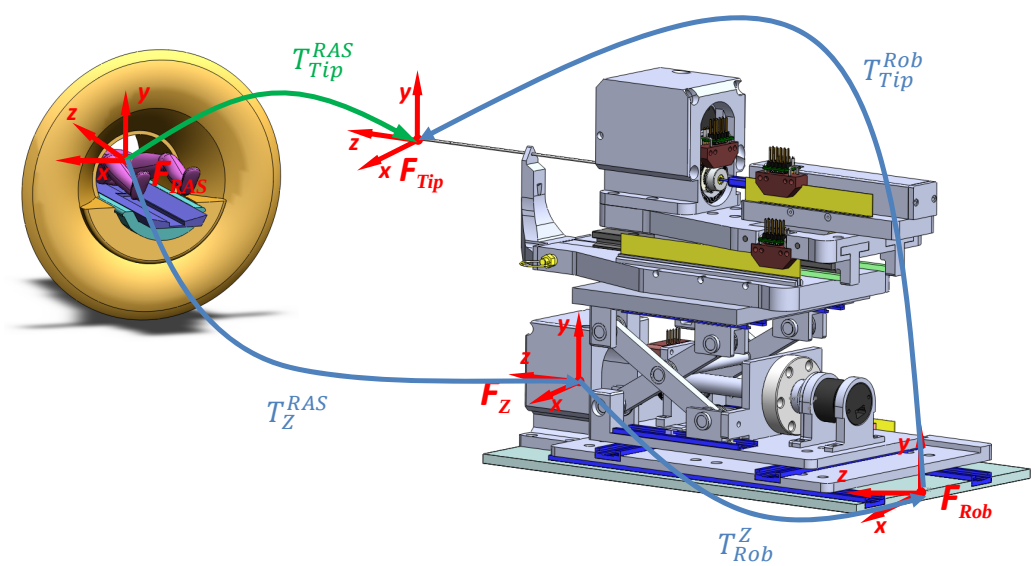


Figure 3.2: Robot registration transformation

$$T_{Tip}^{RAS} = T_{Z}^{RAS} \cdot T_{Rob}^{Z} \cdot T_{Tip}^{Rob} \tag{3.1}$$

where $T_{Tip}^{RAS}$ is the needle tip in RAS coordinate system, $T_{Z}^{RAS}$ is the fiducial's transformation matrix obtaining its 6-DOF position and orientation information. What shown here is the Z-frame fiducial based registration. $T_{Rob}^{Z}$ is the transformation between robot base and z-frame. Finally $T_{Tip}^{Rob}$ is the needle tip position with respect to the robot base. It is determined by robot forward kinematics.

## 3.4 Multi-image Z-frame Registration Method

In this section, a spatial localizing approach by using passive fiducial markers in MRI environment is introduced in order to get position and orientation of the MRI-guided robot. In prior work, 6-DOF registration has been performed by using a single image slice which provides convenience and speed at the expense of accuracy [115]. Here, a new approach [80] that multiple slices of the fiducal are used with principal component analysis (PCA) to determine the 6-DOF position and orientation of the frame on the robot with respect to the scanner. Also, to get higher accurate registration result, a new algorithm is used to calculate the centroids of fiducial points.

### 3.4.1 Z-Frame

The Z-frame fiducial and its single-image registration method was introduced by Susil et al. [78] in 1999. It adapted the original design of Brown-Roberts-Wells (BRW) frame from [124] [125]. As shown in Fig. 3.3(a), it is made of seven fiducial tubes that configure in three sets of Z shape in three orthogonal planes. The configuration of each plane is shown in Fig. 3.3(b) [78]. This Z-frame with BRW frame design is versatile that the position and orientation is fully encoded within each single image slice. Although Z-frame is firstly introduced for CT, by using MRI high contract agent, it is also proven to be a great registration and tracking method for MRI. In our design, each of the fiducial tube is filled with MRI high contrast gadolinium fluid (MRSpots, Beekley Corp., Bristol, CT) and placed in the 3D printed frame shown in Fig. 3.3(c). Fig. 3.3(d) illustrates one T2-weighted fast spin echo cross-section image of tracking fiducial frame.

Some examples of MRI-compatible robot with Z-frame integrated could be seen in Fig. The Z-frame is mounted in front of the robot on the base for both of the pneumatic-driven prostate biopsy robot designed by Fischer et al. [43] Fig. 3.4(left) and the piezoelectric needle insertion robot developed by Su and Shang Fig. 3.4(right).

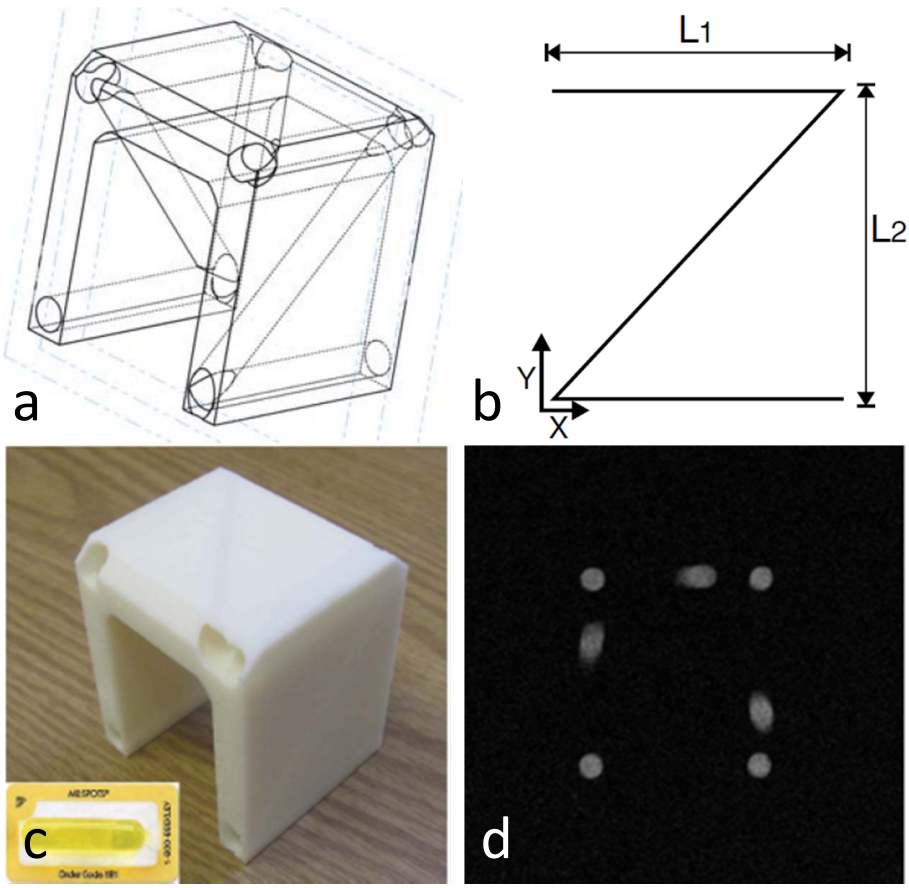


Figure 3.3: Z-frame: CAD model with cross-section planes(a);The configuration of each plane(b) [78]; 3D printed fiducial frame with a MRSpots(Beekley Corp., Bristol, CT) fiducial tube(c); one cross-section MR image of the Z-frame(d).

### 3.4.2 Registration Method

The flow chart of the detection and localization algorithm is shown in Fig. 3.5. The whole process could be separated into two major steps: Single image processing and inter-image processing. In the step of single image processing, after being read in, every interested z-frame MR image in the set gets reconstructed, then the centers of seven fiducial points are calculated. Finally they are numbered and matched to the fiducial pattern. After all of the images are processed by this procedure, the

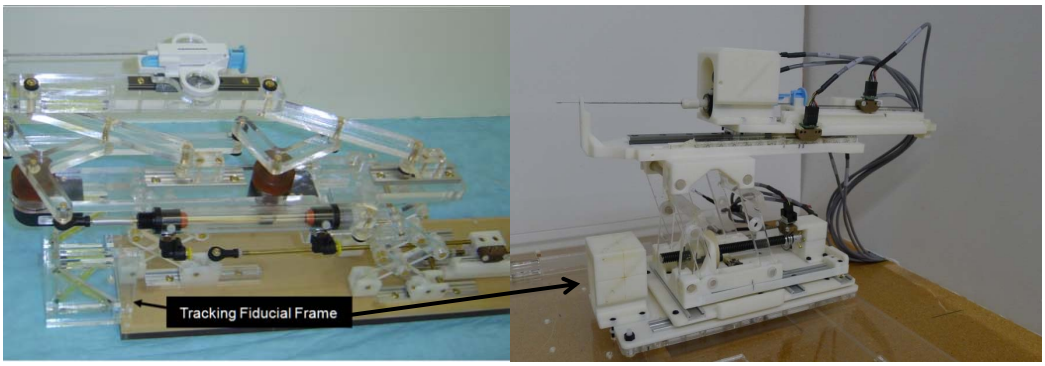


Figure 3.4: Z-frame fiducial modules mounted on the robots: A pneumatic robot developed by Fischer et al.(left) [43]; Needle insertion robot developed by Su and Shang(right).

inter-image processing takes place to fit the spatial lines of the seven fiducial tubes and finally calculates the Z-frame's position and orientation as a four by four transformation matrix $T_Z^{RAS}$.

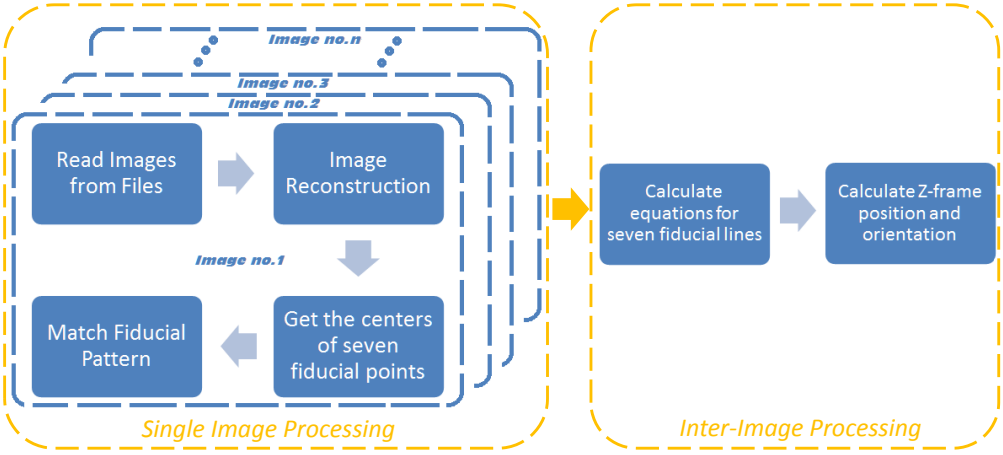


Figure 3.5: Fiducial detection and localization flow chart

Image reconstruction is done right after the images are read in. To avoid the irrelevant objects as much as possible, user is firstly asked to choose the region of interest (Fig. 3.6(left)). The selected region of image is then filtered with threshold, con-

verted to binary image and denoised. The threshold is automatically calculated from the selected region of interest. These steps give us a clearer image (Fig. 3.6(right)). Object size check is performed to make sure the anything left on the image are the actual seven fiducial points. Until this point, the first part of morphological method is done.

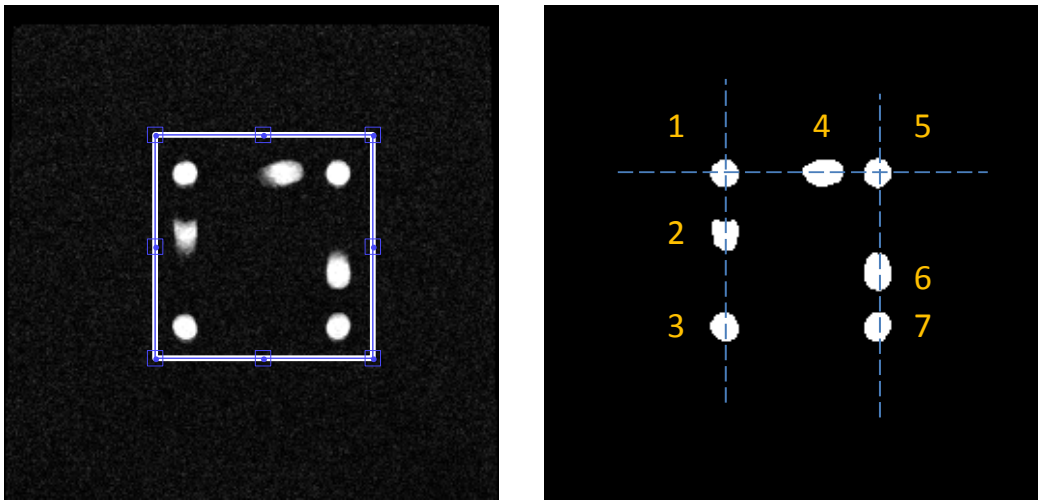


Figure 3.6: Original Z-frame MR image with the crop box shown (left); Binary image with fiducial point order number (right).

The second part of morphological method is getting the centers of seven fiducial points. There are several challenges when dealing with fiducial MR images. The images are not always as sharp as what is shown in Fig. 3.6. Irregular shape could happen when the off-the-shelf product (MRSpots, Beekley Corp., Bristol, CT) is used because there is an air bubble inside the fiducial tube. Fig. 3.7(upper left) shows a Beekley fiducial spot with air bubble in the upper left corner (red circle). Besides irregular shape, sometimes one of the fiducial points may look much dimmer than others, like Fig. 3.7(lower left). In this case, the image reconstruction may not be

able to get its complete shape, like Fig. 3.7(lower right). In some of prior works, the center of each fiducial point was found directly by finding its centroid [79]. This may be effective on high quality images with no bubbles or other artifacts, but is not robust. Therefore, in our work, unlike simply getting the centroid, we use a flipping method with ellipse model to reconstruct every fiducial point on the image, then the centers of reconstructed points were calculated to be used in localization later.

The flipping method could be described as following steps: 1. Get the binary image of a single fiducial point out; 2. Find the weighted centroid $(x_{c_0}, y_{c_0})$; 3. Use the current centroid as the origin to draw x and y axis in parallel to original image x and y axis; 3. Flip the fiducial image with respect to the new x and y axis. Take logical 'OR' operation between a pair of symmetrical pixels in both x and y directions. In result of this process, part of the absence caused by air bubble and some black pixels in the middle will be filled with the other half of the image which has the good shape. 4. Calculate the new centroid, if the difference between the old and new centroid is larger than a threshold, repeat step 3. If it does not change larger than the threshold, it means the irregular shape is compensated with good image and this last centroid is the final center point we want. The actual flipping calculation could be expressed as following equations:

$$x : \begin{cases} B(x_{c_0} - i, y_j) = B(x_{c_0} - i, y_j) || B(x_{c_0} + i, y_j) \\ \\ B(x_{c_0} + i, y_j) = B(x_{c_0} - i, y_j) || B(x_{c_0} + i, y_j) \end{cases} \quad i = 1, 2, 3..., j = 1, 2, 3... \quad (3.2)$$

$$y : \begin{cases} B(x_j, y_{c_0} - i) = B(x_j, y_{c_0} - i) || B(x_j, y_{c_0} + i) \\ \\ B(x_j, y_{c_0} + i) = B(x_j, y_{c_0} - i) || B(x_j, y_{c_0} + i) \end{cases} \quad i = 1, 2, 3..., j = 1, 2, 3... \quad (3.3)$$

where $B(x, y)$ denotes the binary value at the coordinate location of $(x, y)$. It is either 0 or 1 since this is a binary image. The $(x_{c_0}, y_{c_0})$ is the current weighted centroid coordinates. $i$ is the distance of the pixel currently being operated to the flipping axis. It starts from the closest pixel whose $i = 1$. $||$ denotes the logical $OR$ operator. After the current flipping is done to all the pixels for both x and y directions, the new centroid is calculated again as $(x_{c_1}, y_{c_1})$ to replace the $(x_{c_0}, y_{c_0})$ in these equations.

As a result, in Fig. 3.7, the red stars represent the boundaries of the fiducial point after the flipping method. Blue and red circle represent the center of original image and the image after the flipping method. From the upper right figure in Fig. we can see that the updated boundaries successfully cover the air bubble. If we manually fit an ellipse to the image, it is obvious that the updated center (red circle) is closer to

the ideal center than the original center (blue).

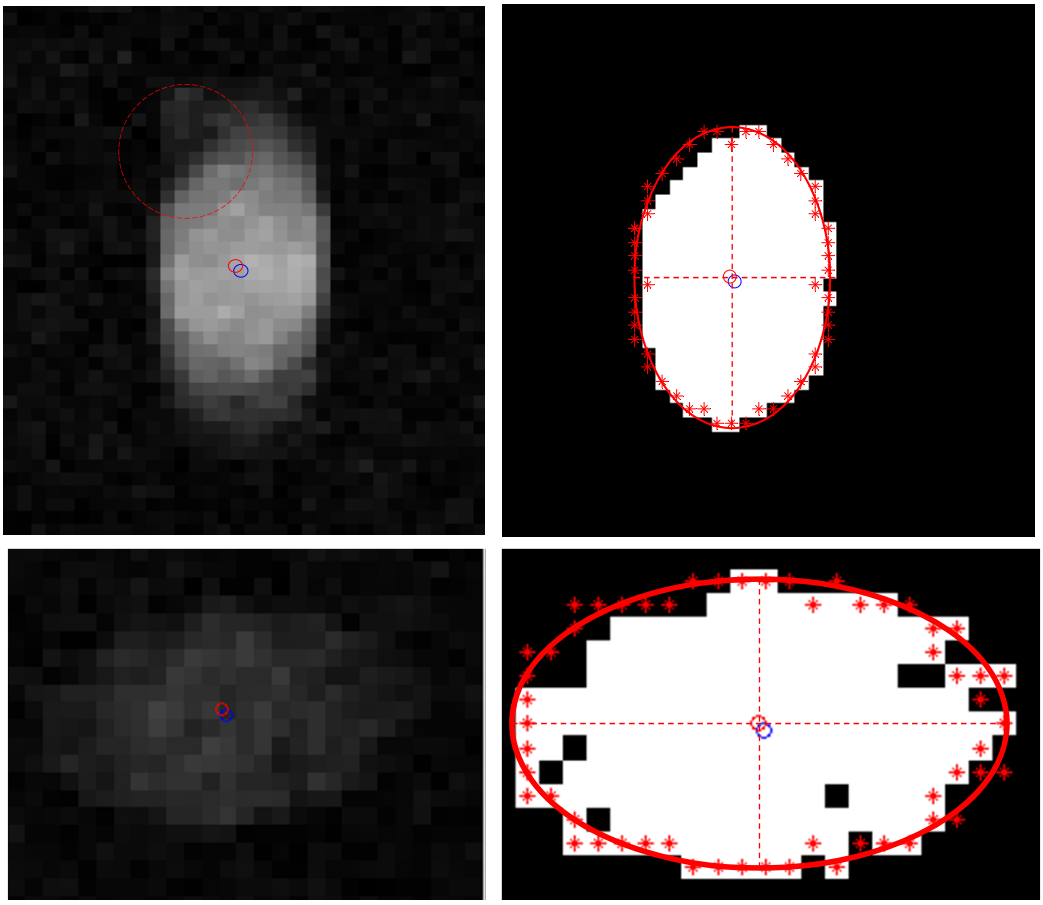

Figure 3.7: In all figures, red circles denote the center gotten from flipping method, and the blue circles denote the center gotten from traditional weighted centroid method. A fiducial point with an air bubble on its upper left corner(red dashed circle)(upper left), the same fiducial point with boundaries got from the flipping method, manually fitted ellipse and the center of ellipse(upper right). Another fiducial point with low contrast to the background(lower left) and the boundaries got from flipping method and manully fitted ellipse with center(lower right). From both upper right and lower right figure, it is obvious that the center got after flipping method(red circle) is closer to the ideal center than the center got from traditional weighted centroid method(blue circle).

After all seven fiducial points are done with the flipping method, by using the geometric character of Z-frame, they are assigned with number(Fig. 3.6(right)) and

put in the correct order for the spatial fitting later. This step is not as trivial as it looks like. There are several steps to number all the points in the correct order.

Before starting to talk about the procedures, it should be noticed that principal component analysis (PCA) is used instead of the ordinary least square (OLS) fitting. As shown in Fig. 3.8, the OLS minimizes the error between the dependent ($y$) and the model. PCA minimizes the error orthogonal (perpendicular) to the model line. In most of the cases, the dependent y is a function of x so it is natural to just consider the error between y and the model. But in our case, the y is not dependent to x. They should be equally treated and the error should be both considered. Thus, theoretically, it makes PCA a better approach than OLS.

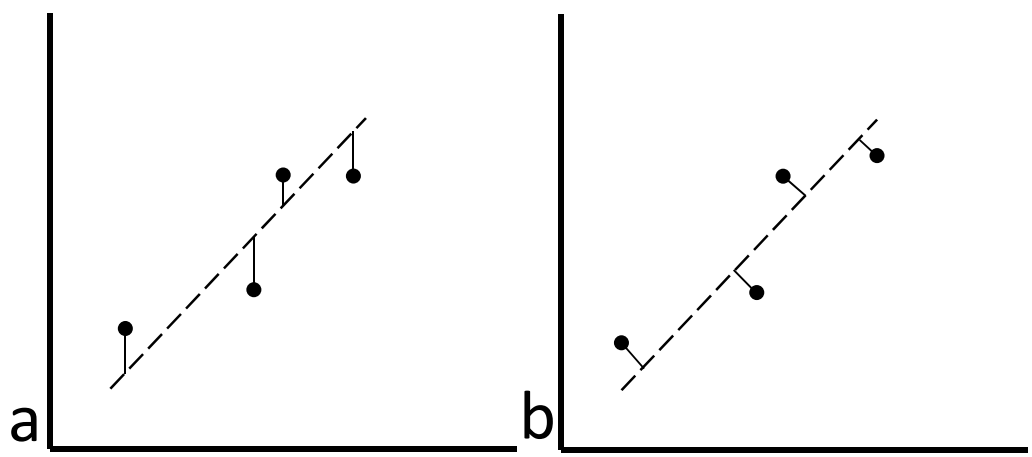


Figure 3.8: Ordinary least square (OLS) fitting method (a); principal component analysis (PCA) fitting method (b).

The actual steps for numbering all the points in the correct order are as follows:

1) Get the distances between every two arbitrary points by the following equation:

$$D(i,j) = \sqrt{(x_i - x_j)^2 + (y_i - y_j)^2}, i = 1, 2...7, j = 1, 2...7 \tag{3.4}$$

This is saved for later use.

2) Fit any three arbitrary points to a straight line with the normalized vector of 3.5 by PCA method. Getting the coefficients and scores (residual errors) for each fitted line.

$$v = [v_x, v_y] \tag{3.5}$$

As shown in Fig.3.6(right), there are only three perfectly fitted lines with residual error small enough. Following show the three vectors for one example image:

$$\begin{cases} v_1 = [-0.0035, 1] \\ v_2 = [1, -0.0046] \\ v_3 = [0.0037, 1] \end{cases} \tag{3.6}$$

3) Next is to distinguish which line is which. This is done by comparing the perpendicularity between each two of the three lines by the following equation:

$$v_i \cdot v_j = v_{ix} v_{jx} + v_{iy} v_{jy}, (i \neq j) \tag{3.7}$$

Ideally, $v_i \cdot v_j = 0$, but practically, since they are fitted vectors, they are not per-

fectly perpendicular to each other. An estimated small threshold is used to determine the perpendicularity. After this step, we could find out the line which is perpendicular to both of two other lines. Combining the position of the other two lines in x direction, all three lines could be distinguished.

4) Finally, by using the geometric properties of the fiducial points forming each line, all the points could be numbered as shown in 3.6(right). The distances in 3.4 are also used for numbering and double check of the result in order to make the whole method more rigid.

After getting the coordinate information for the points on every image we need, PCA fitting methods were used to fit the seven fiducial lines of the Z-frame in 3D space. Finally, the 6-DOF position and orientation information of the fiducial frame is acquired from these seven fitted lines as a four by four transformation matrix $T_Z^{RAS}$.

The algorithm was implemented in Matlab. Fig. 3.9 shows a Matlab 3D plot of centers of fiducial points on each image and seven fitted fiducial lines in RAS patient coordinate.

### 3.4.3 Accuracy Analysis

In order to determine the registration accuracy, we designed a testing platform which was manufactured by laser-cutter with pre-determined positions and orientations (Fig. 3.10). As the ground truth, relative positions and orientations were tested in the experiment. Several groups of images were taken at each position and orienta-

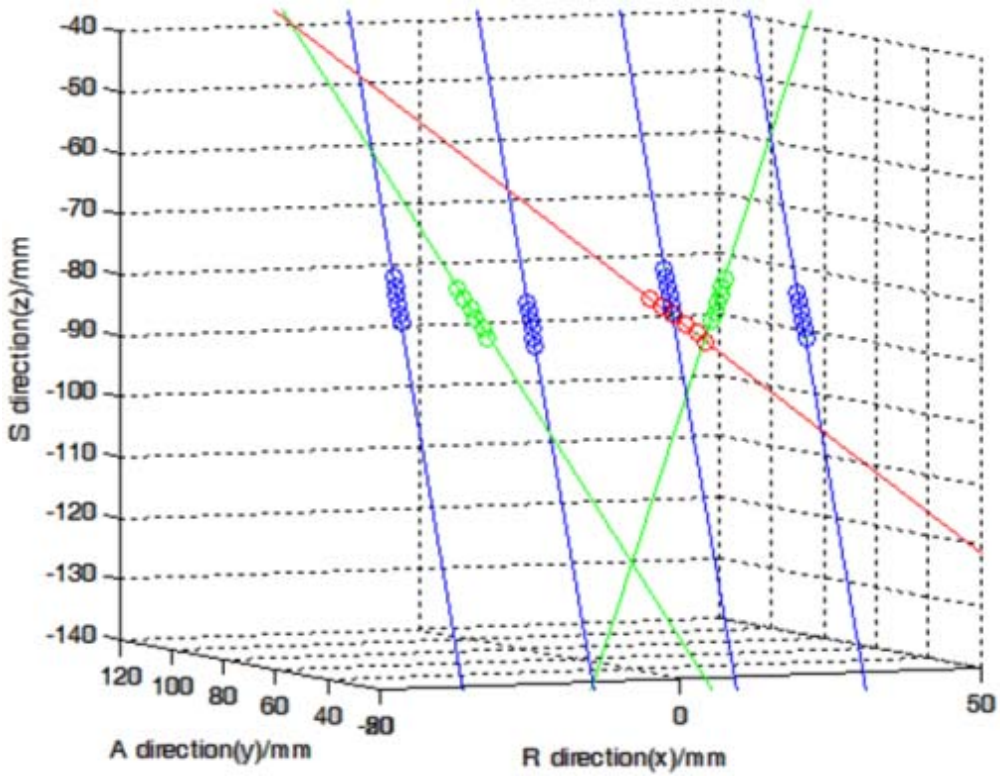


Figure 3.9: Matlab plot of the spatial pose of the Z-frame by using 5 images. The circles represent the located fiducial centroids in each image, the blue lines represent the 4 horizontal fiducial tubes, the green lines represent the angles tubes on the sides, and the red line represents the angled tube on the top surface.

tion. The relative changes were calculated after to test the registration accuracy.

Relative displacement of 85 mm and rotation angles of $5°, 10°, 15°$ were tested during the experiment. The errors which include the displacement error and angular error are defined as the difference between the manufacturing parameters and the registration results. At each position and orientation, several groups of images were taken. Within each groups, different number of images were used to do a one-time-registration. Three, four, five, six and seven images were used separately. The average displacement error of all registrations by using different number of images was 0.27

Figure 3.10: Z-frame accuracy test platform placed on patient bed inside MRI. The fiducial frame could be placed on the platform with a relative displacement of 85mm and rotation angles of $5°, 10°, 15°$.

mm, the average angular error was 0.16°. Since the pixel size was 0.5 mm × 0.5 mm, this method was proven to have sub-pixel accuracy which is ideal for the registration and tracking of MRI-guided robots. By saying sub-pixel accuracy, it means that images containing well defined points processed by algorithm to reliably measure their position with the accuracy exceeding the nominal pixel resolution of that image. The probability distribution of the displacement error is shown in Fig. 3.11. All of the displacement errors were below 0.8 mm among 120 samples, 94.2% percent of the errors were below 0.6mm and the maximum error was 0.75mm. Both displacement and angular errors of the multi-image registration method are summarized in Table 3.1 on page 86.

To prove the advantage of high accuracy of multi-image registration, a comparison

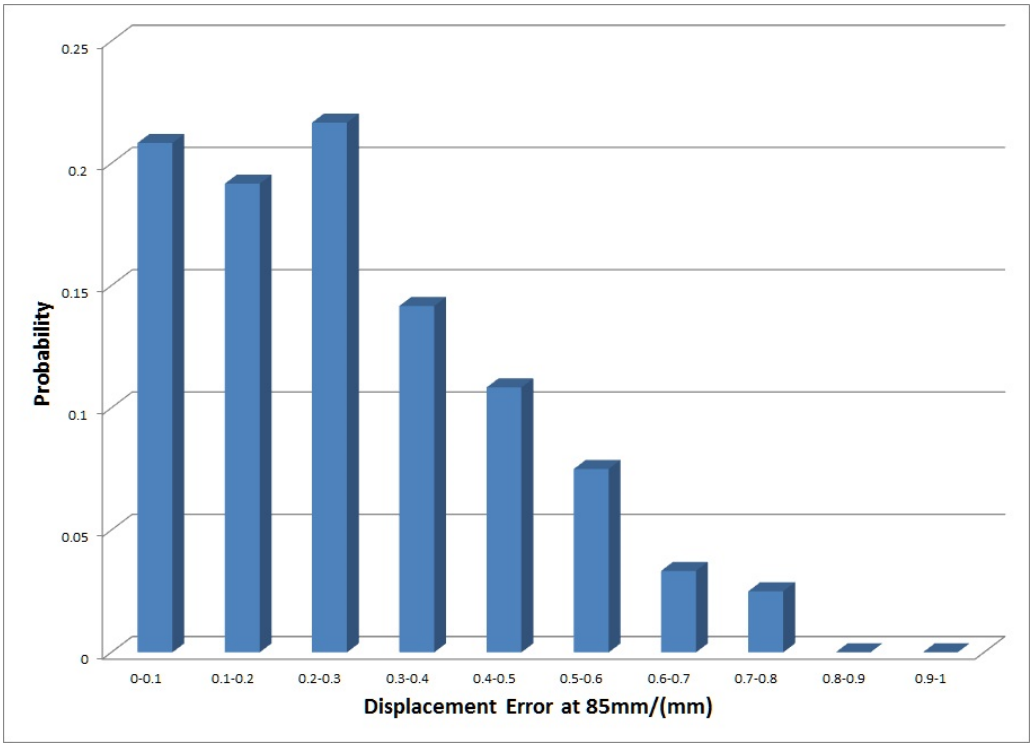


Figure 3.11: Probability distribution of displacement error. All of the errors are found below 0.8mm.

was done between multi- and single-image registration methods. Table 3.2 on page 87 shows the results of both multi- and single-image registration. Susil's test 1 was the offset error of holder pose [78]. Susil's test 2 was the offset error of the needle tip [78]. Lee's test was the average displacement error of four algorithms [79]. DiMaio's displacement error was the average out-of-plane(z) error [77]. Compared to the prior

Table 3.1: Multi-image localization accuracy

| | Average Error | Standard Deviation | RMS Error | Data Points |
|---|---|---|---|---|
| Displacement | 0.27mm | 0.18mm | 0.33mm | 120 |
| Rotation | 0.16° | 0.46° | 0.46° | 248 |

Susil's work [78] and DiMaio's work [77], the angular error when using the multi-image method decreased by 0.19° and 0.15° and the displacement error decreased by 0.11 mm, 0.35 mm and 0.08 mm which shows a significant accuracy increase from single-to multi-image method. One exception we could see from the Table 3.2 on page 87 is that the displacement error in DiMaio's work was 0.089 mm which was smaller than any of other works including our multi-image method. That is because the displacement tested in our work was 85mm which was much longer than the displacement tested by DiMaio [77], only from 0 to 18 mm.

Table 3.2: Accuracy comparison between multi-and single-image methods

| | | Displacement error | Rotation error |
|---|---|---|---|
| Multi-image Method | Our work | 0.27mm | 0.13° |
| Single-image Method | Susil's test 1 | 0.38mm | 0.32° |
| | Susil's test 2 | 0.63mm | N/A |
| | Lee's test | 0.35mm | N/A |
| | DiMaio's test | 0.089mm | 0.28° |

Accuracy comparison between multi-and single-image methods. Susil's test 1 was the offset error of holder pose [78]. Susil's test 2 was the offset error of the needle tip [78]. Lee's test was the average displacement error of four algorithms [79]. DiMaio's displacement error was the average out-of-plane(z) error [77].

To find how the number of images used affects the registration accuracy, we compared the accuracy results from four groups, which are using three, four, five and seven images to approach one-time-registration. The comparison is shown in Fig. 3.12. We could see from the figure that the angular error has a relative significant drop of 0.03° at the change of using of three to four images, and the displacement

error has a relative significant drop of 0.1mm at the change of using of five to six images.

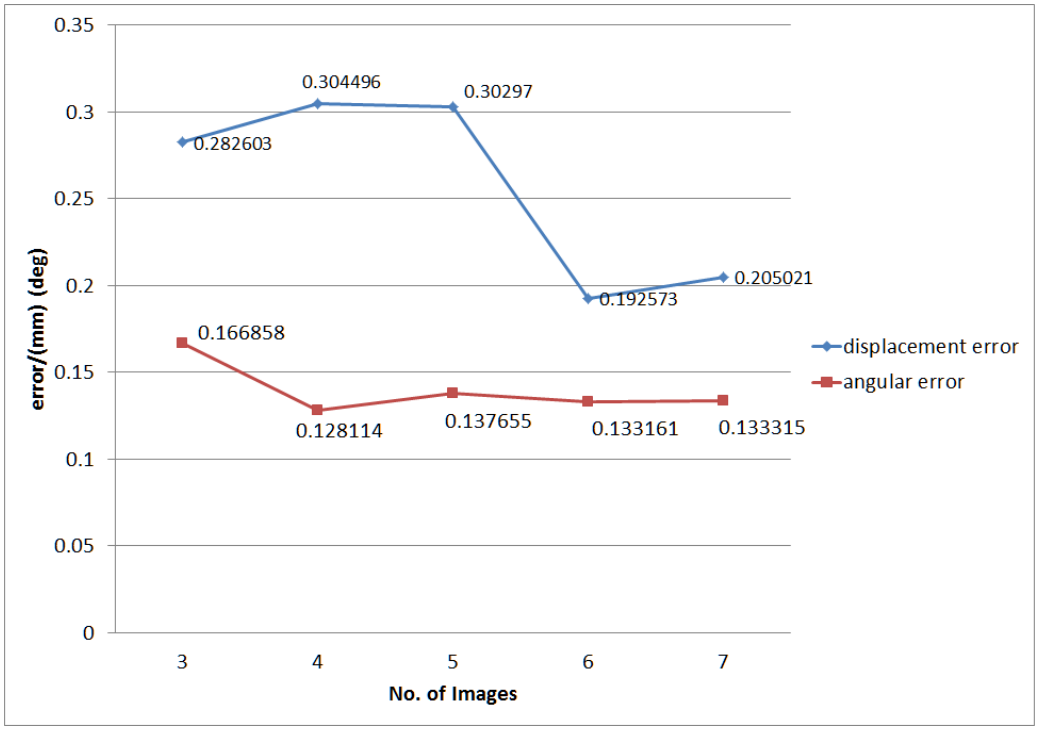


Figure 3.12: Accuracy comparison between different number of images evenly distributed in the acquisition volume.

### 3.4.4 Conclusion and discussion

In this work, we achieved multi-image registration with sub-pixel accuracy. The errors of both displacement and angle were well below 1mm and 1°. The average displacement error is 0.27 mm, maximum is 0.69 mm. The average angular error is 0.16°, maximum is 0.49°. The average error is sub-pixel level.

The comparisons have proven that the advantage of high accuracy of multi-image

registration method is significant. Although we got a good performance of this method, there are several improvements we could apply in the future. In this study, we are using multiple images to approach a one-time-registration after initial setup of the robot. The technique may be utilized for interactive tracking as well, with the trade-off being number of images acquired & acquisition speed vs. registration accuracy. It is possible that some of the images only contain part of fiducial information. For example, only six fiducial points were shown in one image. It is better in the future to make the fiducial pattern fitting function more robust to recognize partial fiducial information. Sometimes, even if the partial fiducial could be recognized, the flipping method could potentially introduce more error if its shape is off too much. And quantitatively, how much fiducial shape difference could be overcome by the flipping method is still left to be studied. Although having high accuracy, this method requires the acquisition of several images which take more time than single-image registration method. A compromise should be made between the sufficient accuracy and registration speed.

In the future, a new fiducial frame will be designed to make it more compact with the robotic system. New fiducial tubes with thinner cross sections will be used to make the whole size smaller. Also, smaller cross section would decrease the error produced during finding of centroids of the fiducial points.

Finally, the performance of real-time registration, navigation and tracking will be tested in the near future by implementing this work into a MRI-guided surgical robot.

## 3.5 Cylindrical Helix Imaging Coordinate (CHIC) Fiducial Frame Registration and Tracking Method

This section presents a single-slice based stereotactic registration and tracking technique along with the design of a compact and novel fiducial frame for assisting robotic devices or interventional instruments to perform needle intervention under different imaging modalities. Designed with a unique geometrical fiducial pattern, a novel passive Cylindrical Helix Imaging Coordinate (CHIC) fiducial frame is utilized to determine its all six degree-of-freedom by using only a single cross-section image. It can be attached near the distal end of the robot for the purpose of getting target tissue image and surgical tool position synchronously. Combining the Gaussian image recognition and least-square fitting methods, the robustness and accuracy of this registration and tracking fiducial remain high while the overall physical size is minimized. The MRI-compatible design allows it to be conveniently used under a variety of imaging systems such as CT, ultrasound and MRI. The 3D printed fiducial frame, which has a modular and reconfigurable design, is easily to change the size and other parameters based on the requirements. 25 experimental groups with different poses are successively scanned along specific sequence in MRI experiment to evaluate the accuracy and robustness of the tracking algorithm. The overall translational

RMS error is 0.208mm with standard deviation of 0.241mm for totally 300 samples. The overall angular RMS error is 0.425° with standard deviation of 0.524° for totally 150 samples. The accuracy of registration and tracking technique achieves sub-pixel accuracy which is ideal for clinical use.

### 3.5.1 Fiducial Design

#### 3.5.1.1 Structural model

The design of the CHIC registration frame [122] utilizes the similar technique as Brown-Roberts-Wells (Z-frame) did [77], [78] to detect transverse depth information by a higher density of tubular fiducial shifting along central axis regularly, see Fig. 3.13(a). It consists of four fixed cruciate markers (red), three axial position markers (blue) and two axial twist markers (green). All of the nine fiducial tubes have the same diameter of $d$, and on a circle that with the radius of $r$.

Fig. 3.13(b) shows only three blue helix tubes change their position when transverse shifts along the central axis. So the blue spots are used for getting transverse depth information and called axial position markers, see Fig. 3.13(c). While there are four red straight tubes which always keep a cruciate position with each other. These fixed cruciate markers are mainly used for reconstructing ellipse in ellipse plane and used as reference points for calculating blue tubes' rotation angle. For a representative fiducial configuration, each blue axial position marker keeps a 20° included angle

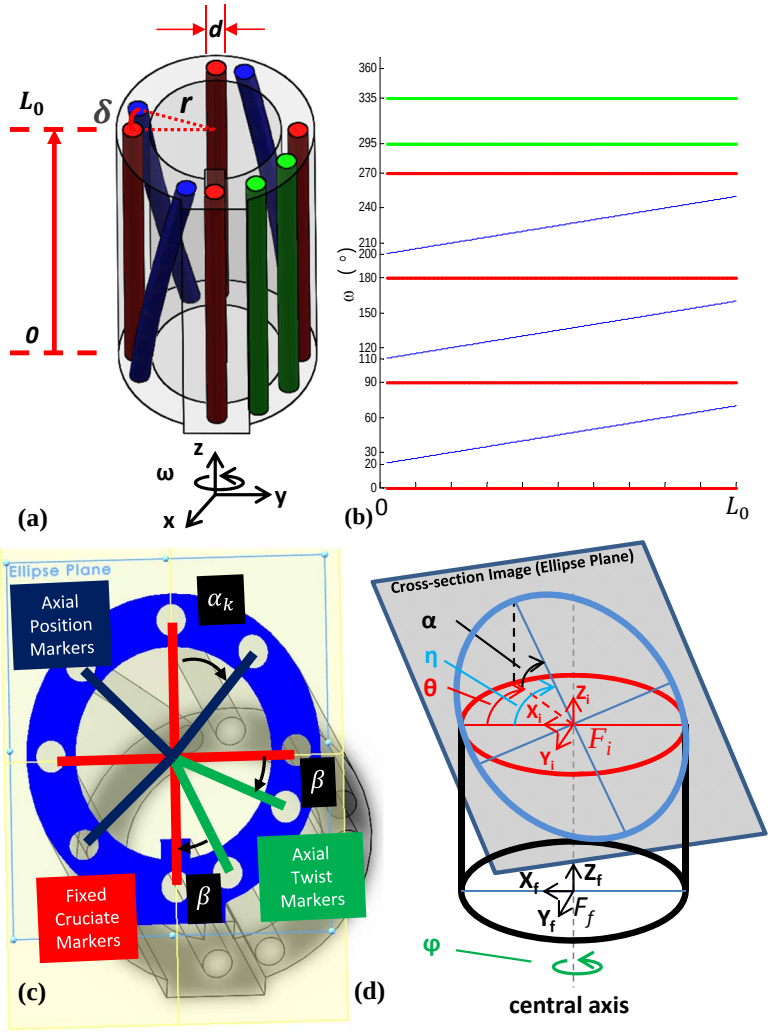


Figure 3.13: a) A representative configuration of the tubular fiducial marker position. $\omega$, shifts along central axis, z. The CAD drawing of CHIC fiducial frame includes different type of tubes with different colors: four fixed cruciate markers (red), three axial position markers (blue) and two axial twist markers (green). All of the nine fiducial tubes have the same diameter of $d$, and on a circle that with the radius of $r$. b) The corresponding plot of each tube. c) Every arbitrary cross-section has a unique registration pattern of tubular fiducial markers: Fixed cruciate markers (red) and axial position markers (blue) to determine the depth along central axis, axial twist markers (green) to determine the twist angle and all centroid of tubes were fitted into elliptical curve to determine the pose of ellipse plane. d) Reference frame for CHIC fiducial frame. $F_f$ is adhered to central point of transverse image and it is the primary fixed frame being adhered to robot.

offset $\delta$ (as shown in Fig. 3.13(a)) with close red fixed cruciate marker respectively at both cylindrical ends in order to always keep identifiable distance for image recognition, even at the extreme pose of the scanning plane. The last two green straight tubes are called axial twist markers which do not equally divide the quadrant where they belong to, but form a 25° included angle $\beta$ (as shown in Fig. 3.13(c)) with close red fixed cruciate marker at central point respectively in order to avoid confusing with blue axial position marker at certain transverse position. The projected spot pattern of all makers on four quadrant of ellipse plane form an asymmetric distribution, no matter how blue tubes shift. So that we can get the rotation of CHIC fiducial frame itself along central axis. And, they also improve the accuracy of ellipse fitting.

It should be emphasized again that the overall design of the fiducial is modular and scalable for different applications. As shown in Fig. 3.14, $L_0$ is the total length of the fiducial frame, $D$ is the diameter of the circle that all the centers of fiducial tubes are on, $D = 2r$ where $r$ is shown in Fig. 3.13(a). All of these parameters as well as $d$ and $\delta$ are adjustable based on different needs and requirements. As a result, the maximum detectable tilt angle $\gamma$ (Fig. 3.14) could be decided.

#### 3.5.1.2 Mathematical model

The registration algorithm of this fiducial frame utilizes a single-slice based fiducial registration method which skillfully extracts 6-DOF information from only one arbitrary transverse image as shown in Fig. 3.13(c). The function of different mark-

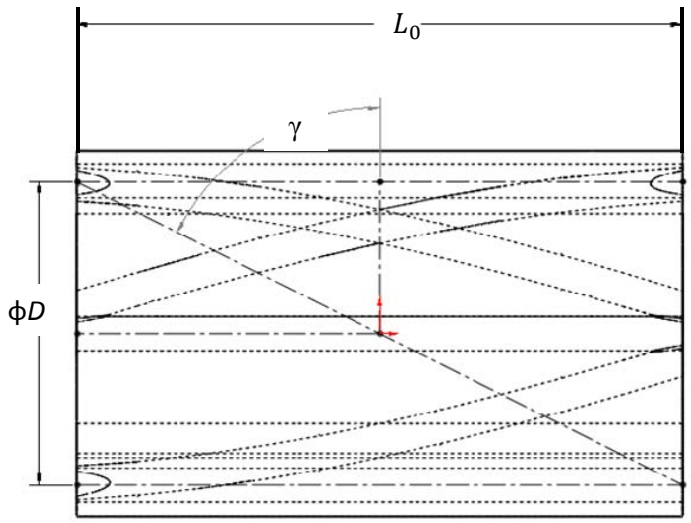


Figure 3.14: Lateral perspective view of the CHIC fiducial frame. $L_0$ is the total length of the fiducial frame, $D = 2r$ where $r$ is shown in Fig. 3.13(a), $\gamma$ is the maximum detectable tilt angle. Modified from [122]

ers will be explained in detailed through this part, including sections of reference frame for rotation and extraction of 6-DOF information. A general parametric form of ellipse equation was used for fitting:

$$\begin{cases} X(t) = X_c + a\cos t\cos\eta - b\sin t\sin\eta \\ Y(t) = Y_c + a\cos t\sin\eta + b\sin t\cos\eta \end{cases} \tag{3.8}$$

where parameter $t$ varies from 0 to $2\pi$. $(X_c, Y_c)$ is the center of the ellipse, and $\eta$ is the angle between the X-axis and the major axis of the ellipse.

a) Reference frame definitions

The Reference frame for single-slice based registration is illustrated in Fig. 3.13(d). The gray plane is transverse image including a central point $P_0(x_0, y_0, z_0)$ which con-

tains all three DOF information about translation. The black coordinate frame $F_f$ on the bottom is set as primary fixed frame, and all steps of sub-rotation is done with respect to it. $F_i$ (red) is related to the primary frame $F_f$ with the same $x$ and $y$ directions but with a displacement along central z axis which is the distance between the origin of $F_f$ and the origin of $F_i$ ($P_0$). Other three DOF about rotation will be achieved by three sub-rotation steps noted as R1: Twist ($\varphi$), R2: Elevation ($\alpha$) and R3: Direction ($\eta$). Azimuth angle ($\theta$) is a forward correction which can not be measured directly from transverse image and it will be further introduced later.

b) Calculation of 3-DOF information about rotation

The three rotational DOF can be decided completely by three angles: twist angle ($\varphi$), elevation angle ($\alpha$) and direction angle ($\eta$). The Twist angle can be directly measured by the mean rotary angle of four red fixed cruciate markers diverging from each original 0°, 90°, 180° and 270° position referenced by two green axial twist markers. Here the pairwise symmetry of these four fixed cruciate markers will counteract the distortion of included angle between each other which is caused by transverse tilt during averaging process. The Elevation angle shown in Fig. 3.13(c), just as its name suggesting, is the projective angle between the major and minor axis of the ellipse equation at central point $P_0$ after ellipse plane reconstruction:

$$Elevation(\alpha) = \cos^{-1}\left(\frac{r_{minor}}{r_{major}}\right) \tag{3.9}$$

where $r_{minor}$ and $r_{major}$ are minor and major axis of ellipse equation respectively.

The direction angle which is equals to $\eta$ in ellipse equation can be immediately measured after ellipse plane reconstruction.

After the obtaining of three angles about rotation, we can posture the robot to arbitrary spatial angle by just following a specific three steps of sub-rotation with respect to the fixed frame $F_f$ in sequence of z, y and z again as Fig. 3.15 shows. Consider the last sub-rotation step R3 will have after effect on twist angle that generates an additional rotation along twist called azimuth angle ($\theta$). It can be deduced by rotation rule: orbital movement will bring same spin effect on rigid body. The conversion equation can be finally simplified as $\theta = \eta$, therefore the last rotation with respect to z axis is $\varphi - \theta = \varphi - \eta$. These three rotations are shown as:

$$R_{z,(\varphi-\eta)} = \begin{pmatrix} \cos(\varphi-\eta) & -\sin(\varphi-\eta) & 0 \\ \sin(\varphi-\eta) & \cos(\varphi-\eta) & 0 \\ 0 & 0 & 1 \end{pmatrix} \tag{3.10}$$

$$R_{y,\alpha} = \begin{pmatrix} 1 & 0 & 0 \\ 0 & \cos\alpha & -\sin\alpha \\ 0 & \sin\alpha & \cos\alpha \end{pmatrix} \tag{3.11}$$

$$R_{z,\eta} = \begin{pmatrix} \cos\eta & -\sin\eta & 0 \\ \sin\eta & \cos\eta & 0 \\ 0 & 0 & 1 \end{pmatrix} \tag{3.12}$$

Finally, because all sub-rotation are respect to the fixed frame, they are multiplied together in the reverse order to obtain total rotation matrix as following:

$$R = R_{z,\eta} \cdot R_{y,\alpha} \cdot R_{z,(\varphi-\eta)} \tag{3.13}$$

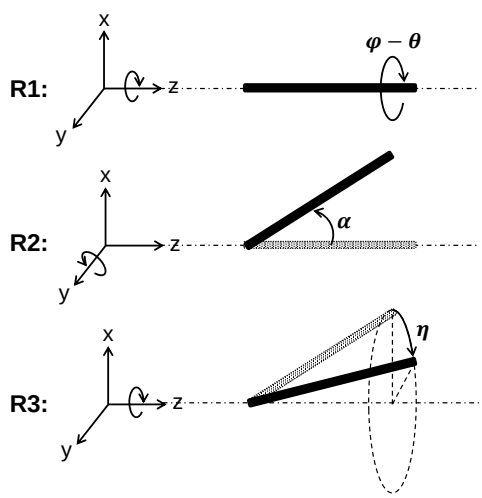


Figure 3.15: Illustration of three sub-rotation steps rotating with respect to the fixed frame $F_f$ to locate robot at arbitrary poses. [121]

c) Calculation of 3-DOF information about translation

As mentioned before, the central point $P_0$ includes all three DOF information about translation in its spatial coordinate $x_0$, $y_0$ and $z_0$. The $x_0$ and $y_0$ can be straightforwardly obtained from $X_c$ and $Y_c$ in the ellipse equation after ellipse plane reconstruction while how to exactly estimate $z_0$ is a geometric conundrum. Previous Fig. 3.13(b) shows the blue axial position markers shift their included angle with corresponding red fixed cruciate markers linearly along central axis. This can be formulized as:

$$z_k = \frac{\alpha_k - 2\delta}{\omega}(k = 1, 2, 3) \tag{3.14}$$

where $\alpha_k$, see Fig. 3.13(c), is the included angle between one pair of blue and red spots, $z_k$ is the space distance along central z axis in Fig. 3.13(c) corresponding with $\alpha_k$, $\delta$ is the initial angular offset which is equal in the both ends of the cylinder and $\omega$ is the pitch of the helix tube that defines this tubular fiducials in dimensions of angle/distance (degree/mm). For instance, the length of one testing CHIC frame is $50cm$ and the offset in each side is $20°$ which means the maximum shifting range of each blue axial position markers is $50°$, the $\omega$ will be $1°/cm$ for every blue helix tube. It should be noticed that this is defined on normal section along central axis of CHIC frame yet real transverse usually stay in arbitrary pose which does not overlap with any normal section along central axis. Fig. 3.16(a) illustrates this difference: the gray plane with central point $O$ is transverse plane which contains a blue spot $B$ cutting from one of axial position marker and a red spot $R$ cutting from corresponding fixed cruciate marker of $B$. The red circle plane with central point $O'$ is the normal section passes through $B$. We could only recognize dashed line angle $\angle BOR$ directly from transverse image, however, the conversion relation between space and rotation according to aforementioned definition force us to calculate solid line angle $\angle BO'R'$ where $R'$ is projection of $R$ on red normal section. Then we still have to calculate $OO'$ to transfer $z_{o'}$ to $z_o$ . The conversion from $\angle BOR$ to $\angle BO'R'$ as well as acquiring correction distance $OO'$ will be illustrated by two steps, as shown in Fig. 3.16(b) and

Fig. 3.16(c).

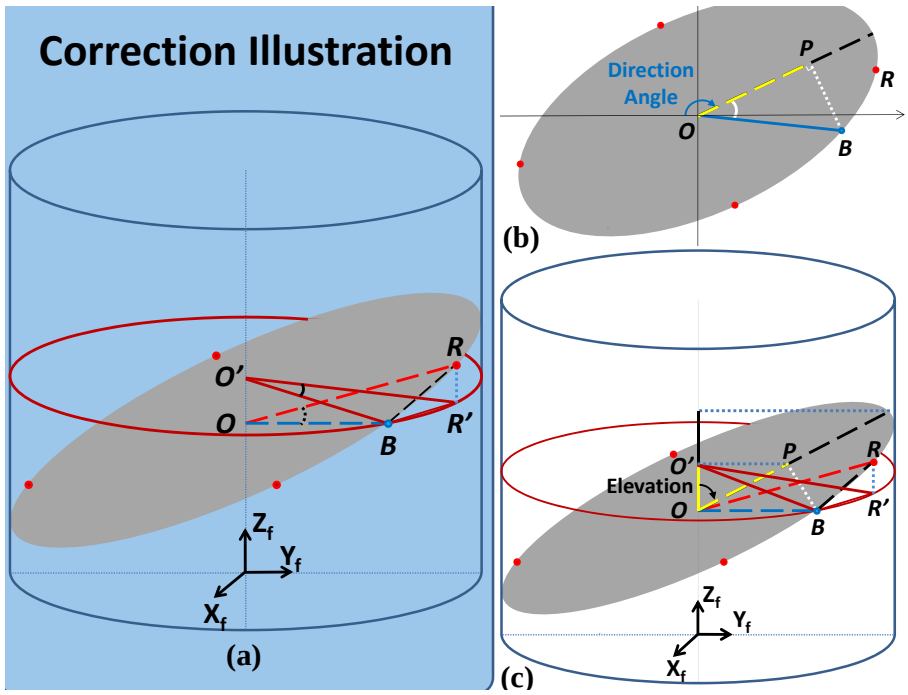


Figure 3.16: (a) The illustration of correction from arbitrary transverse to normal section. The gray plane with central pont $O$ is transverse plane where contains a blue spot $B$ cutting from one of axial position marker and a red spot $R$ cutting from corresponding fixed cruciate marker of $B$. The red circle plane with central point $O'$ is the normal section passes through $B$. $R'$ is projection of $R$ on red normal section. (b) and (c) are two steps to illustrate of conversion from $\angle BOR$ to $\angle BO'R'$. [121]

The first step will begin with the 2D transverse image, as shown in Fig. 3.16(b). $OP$ can be calculated by:

$$OP = OB \cdot \sin \angle BOP \tag{3.15}$$

where $P$ is the projection of $B$ on major axis of ellipse plane. Then we obtain $OO'$ in the step (c):

$$OO' = OP \cdot \sin(Elevation) = OP \cdot \sin\alpha \tag{3.16}$$

where $O'$ is the projection of $P$ on central axis of CHIC fiducial frame. And we can do similar work to gain $RR'$ which is projected pedal of $OR$ on red normal section. Next, we first get $BR'$ by the Pythagorean Theorem:

$$BR'^2 = BR^2 - RR'^2 \tag{3.17}$$

Because there is $O'B = O'R = r_{minor}$ inside the red normal section, so we can reason out $\angle BO'R'$ by law of cosines:

$$\angle BO'R' = \cos^{-1}\left(\frac{O'B^2 + O'R'^2 - BR'^2}{2 \cdot O'B \cdot O'R'}\right) \tag{3.18}$$

$$= \cos^{-1}\left(\frac{2r_{minor}^2 - BR'^2}{2r_{minor}^2}\right) \tag{3.19}$$

Now plug $\angle BO'R'$ into Equation 3.14 to estimate the depth of $O'$ and then eliminate correction distance $OO'$ to obtain depth of $O$:

$$z_k = z_{O'} - OO' = \frac{\angle BO'R' - 2\delta}{\omega}(k = 1, 2, 3) \tag{3.20}$$

In order to minimize error, repeat the same step in Equation 3.20 to estimate other two blue spots. Finally, the depth information $z_0$ of central point $P_0$ will be the

average of three depth of O getting from three blue spots:

$$z_0 = \frac{\Sigma z_k}{3}(k = 1, 2, 3) \tag{3.21}$$

Finally, we have got all three components of the central point $P_0$:

$$P_0 = \begin{pmatrix} x_0 \\ y_0 \\ z_0 \end{pmatrix} = \begin{pmatrix} X_c \\ Y_c \\ z_0 \end{pmatrix} \tag{3.22}$$

d) Calculation of transformation matrix

Most of the robot controls are depended on transformation matrix, so the last is to piece together a tracking transformation matrix $T_{Track}$ from rotation matrix R in Equation 3.13 and central point $P_0$ in Equation 3.22:

$$T_{Track} = \begin{bmatrix} R & P_0 \\ \mathbf{0} & 1 \end{bmatrix} \tag{3.23}$$

where R is rotation matrix, $P_0$ is 3 x 1 column vector of central point and $\mathbf{0}$ is 1 x 3 zero row vector.

### 3.5.2 Image Recognition

Although the mathematical model is precisely developed, image recognition still plays an important role in acquiring a good accuracy. Centroid localization and ellipse fitting are the two steps of image recognition that will be discussed below:

#### 3.5.2.1 Centroid localization

The primary step of image recognition is centroid localization, which crucially decides the accuracy of algorithm. Therefore, it is also the major focus of most of the image preprocessing techniques. A traditional way to localize the central point of each tracking spot is utilizing weighted geometric mean of valid pixel set in threshold-filtered image which is processed by using Otsu's method as filter [126]. Since there are certain unexpected small bubbles existing in tracking gelatin or gadolinium fluid sometimes, which could bring dark shadow in certain tracking spots during imaging to introduce calculation error, a better method is used to increase the robustness of centroid measurement during raw image analysis. The intensity of each tracking spot is assumed to follow 2D Gaussian distribution [48], [76] in Equation 3.24.

$$f(x,y) = \frac{1}{2\pi\sigma_x\sigma_y\sqrt{1-r'^2}} \cdot exp[\frac{1}{1-r'^2}(-\frac{(x-x_0)^2}{2\sigma_x^2} + \frac{r(x-x_0)(y-y_0)}{\sigma_x\sigma_y} - \frac{(y-y_0)^2}{2\sigma_y^2})] \tag{3.24}$$

where $r'$ is correlation between $x$ and $y$ directions, $\sigma_x$ and $\sigma_y$ are standard deviation

in $x$ and $y$ directions. $x_0$ and $y_0$ are the coordinates of tracking spot we expect to estimate from the registration.

Then each single tracking spot in the MR images was fitted to this Gaussian intensity distribution model, see Fig. 3.17. A comparison of centroid calculation by Gaussian model and traditional weighted centroid calculation for the same bubble affected tracking spot are shown in Fig. 3.18(b). So the Gaussian model performs better especially in the situation when bubble or noise happens in the fiducial tracking spots.

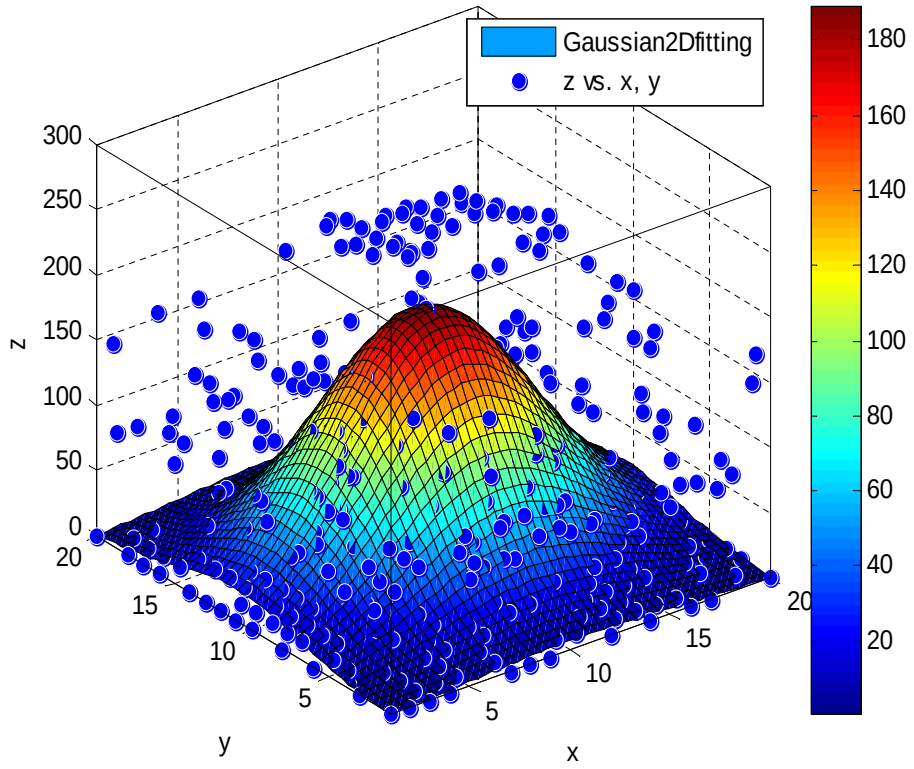


Figure 3.17: Using Gaussian distribution model to refit pixels' intensity for one bubble affected tracking spot.

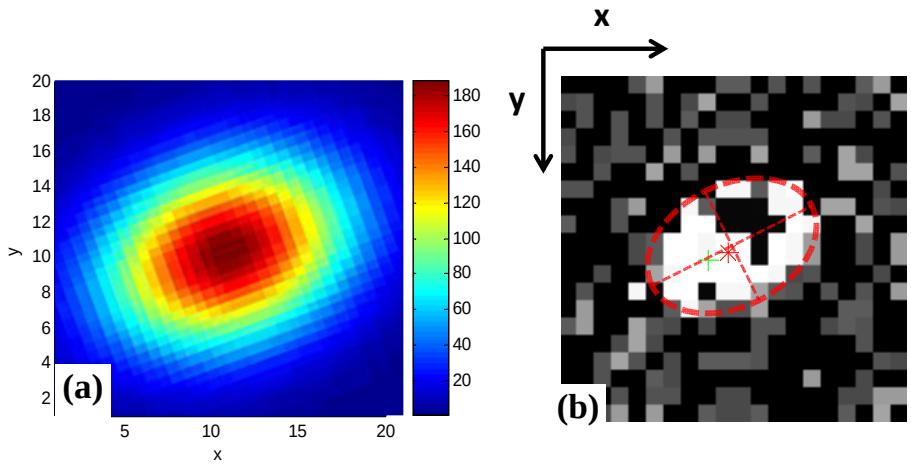


Figure 3.18: (a) the aerial view of Gaussian distribution fitting results for one tracking spot. (b) green "+" is the centroid gets from traditional weighted centroid calculation while red "∗" is the centroid gets from Gaussian intensity distribution model.

#### 3.5.2.2 Ellipse fitting in the image plane

The result of ellipse plane reconstruction also decides the accuracy of transverse pose detection which in turn is dependent on the distribution of tracking spots generated by tubular fiducial pattern around the circumference of cylindrical fiducial frame. The high contrast nine fiducial tubes inside CHIC fiducial frame provide adequate tracking spots in the transverse image to guarantee very high robustness for ellipse plane reconstruction using least-square approach.

To classify tracking spots in the transverse image into different types of markers, the first step is to counterclockwisely arrange all tracking spots along ellipse by the coordinates of their centroids before exactly matching them into each type of markers. Then the four red fixed cruciate markers can be recognized by searching four successive odd or even tracking spots in the ellipse that the sum of their included angle at central

point is 360° (within a reasonable tolerance of $\sigma = 0.5°$). Finally, the two green axial twist markers which make an asymmetric distribution within four cruciate quadrants will be found by checking the number of tracking spots in each cruciate quadrant. However, a double-check will be done here to make sure we make right recognition at first step before marking the rest of spots as blue axial position markers. Because the blue spots may shift into certain conditions where they can form the same crossed diagonal line at central point together with one of green spots just totally same as four red fixed cruciate markers do. So whether the two included angles between each green axial twist marker and close red fixed cruciate marker at central point are both around 25° (within the same tolerance $\sigma = 0.5°$) need to be checked, and the program need to find next four crossed spots in loop if they are not. Once marking all types of markers, least-square method is adopted to fit their centroids into an elliptical curve which is shown in Fig. 3.19 by using the model as shown in Equation 3.8.

After getting the ellipse equation from these two steps of image recognition, the mathematical model discussed in Section 3.5.1.2 is applied to get the final transformation matrix. The whole process is realized with Matlab.

### 3.5.3 Input and Output Interface

Besides assisting robot to adjust its movement during interventional operation, registration and tracking assistant system also provides a visual feedback about real pose of the robot part. To achieve these goals, the system implements a Digital Imag-

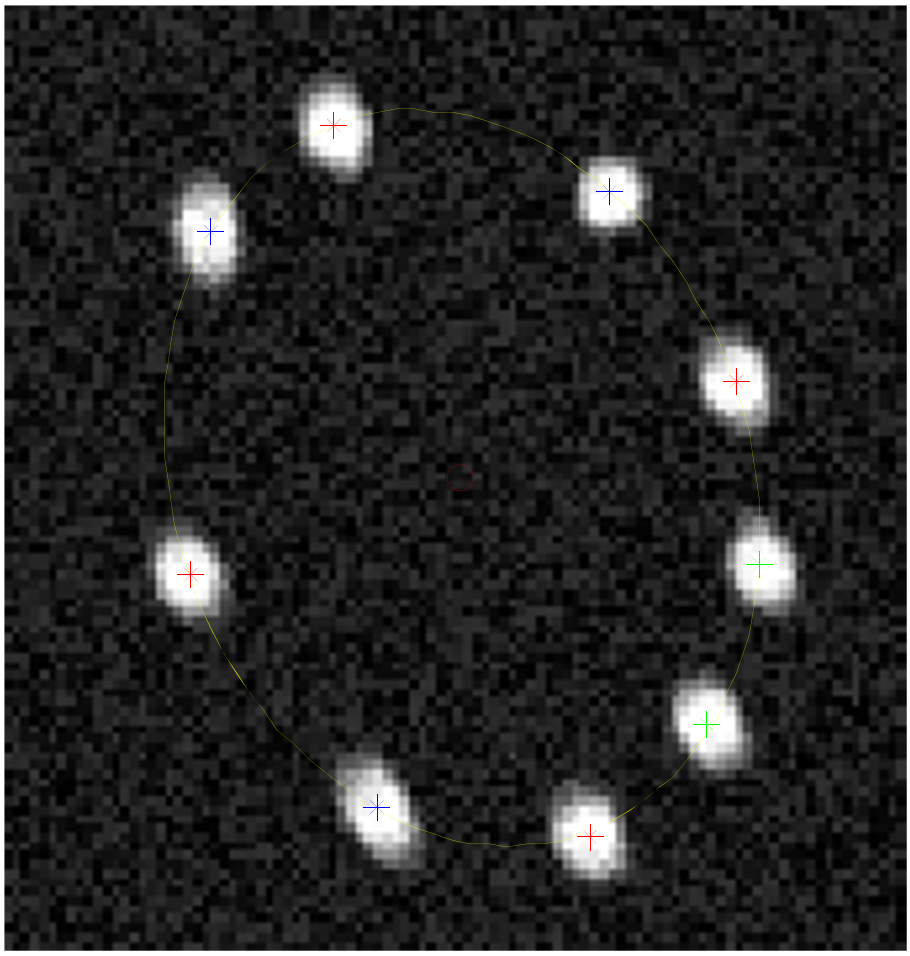

Figure 3.19: Ellipse plane reconstruction after measurement and classification of the centroids.

ing and Communications in Medicine (DICOM) server as input interface and data base that undertakes bidirectional communication with internal module. This module buffers raw MRI scanning images in real time and extracts small valid tracking area from large raw image data to track module processing then receives corresponding transformation matrix for storage all via network connection. The standardized communications protocol named OpenIGTLink makes it possible to supervise and manipulate robot remotely by running this module in the operating rooms far from

MRI scanner [119] [127]. On the other hand, two outputs are set up for movement correction and visual feedback. The user interface module running on Matlab platform provides a direct way to track surgical procedure in real time while correction feedback module will send the correction of transformation matrix to robot controller for shrinking deviation. A user interface of visual feedback is shown in Fig. 3.20.

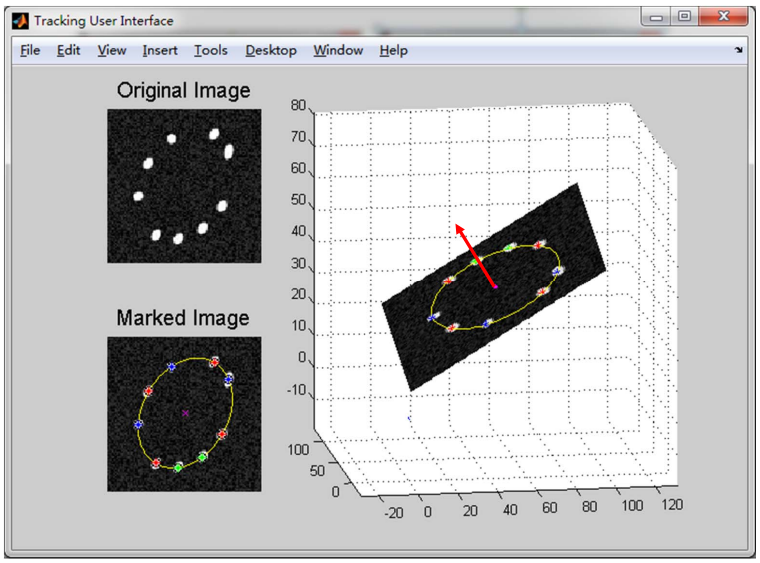


Figure 3.20: CHIC fiducial Matlab user interface.

## 3.5.4 Experiments and Results

### 3.5.4.1 Experiments

To evaluate the performance of this fiducial system, we fabricated a representative example embodiment of it. The main body of this example fiducial frame made by 3D printing was a tubular cylinder with height of $L_0$=50 mm, outer diameter of 30 mm,

inner diameter of 20 mm and fiducial tube diameter of d=3 mm. Interior tubular fiducials were filled with high MRI contrast gelatin or gadolinium fluid (MR-Spots, Beekley Crop., Bristol, CT) and provided ample tracking spots in the transverse image to guarantee detection accuracy and stability of image analysis algorithm.

To evaluate its accuracy with real MR images, several groups of images were taken with different orientations. A Philips 3T MRI scanner was used and all images were acquired with following scanning parameter: TR = 3000 ms; TE = 90 ms; flip angle = 90°; slice thickness = 2 mm; pixel spacing = 0.5 mm × 0.5 mm; FOV = 80 mm × 80 mm; and pixel size = 160 × 160. The experimental groups were successively scanned along depth axis $z_f$ with fixed step length but in variables on both vertical axis $x_f$ and horizontal axis $y_f$. We also successively set scanning planes relative to CHIC fiducial frame at various tilt angles and twist angles to obtain a series of transverse images to evaluate the accuracy of omnidirectional rotation, see fig. 3.21(a). The alteration of tilt angle after twist will lead to both elevation angle and direction angle change: elevation and direction angle are equal to tilt angle at the same time. There were 5 groups for tilt angle and twist angle respectively (tilt angle at 0°, 10°, 20°, 30°, 40° and twist angle at 0°, 5°, 10°, 15°, 20°) forming 25 groups of different combination of tilt angle and twist angle in total. Furthermore, two identical CHIC fiducial frames were connected in series by a 50 mm long concentric connector to make an internal contrast within a group and also test expandability for long discrete measurement application along depth. The stepping rotation of both twist angles and tilt angles

were achieved by MRI scanner itself which was much precisely than moving fiducial frames manually. Fig. 3.21(b) is the photo of the real setup of the experiment. This experiment was also using a MRI head coil to enhance imaging definition while the central axis of two concentric fiducial frames was placed along the central axis of head coil. And the phantom container was the place where we put aqueous contrast medium for MRI scanner getting a proper imaging window of contrast ratio which was close to human tissue. By using image data provided by 25 groups, registration and tracking performance was evaluated by two aspects after: translation and rotation.

#### 3.5.4.2 Accuracy Assessment

1. Evaluation of translation

Ten groups that include five groups of different twist angles and other five groups of different tilt angles were selected. Ten sequential slices were picked from each group to evaluate the accuracy of translation tracking. The relative positions and angles were known precisely from the MR image acquisition parameters, and that this information was used as a ground truth to assess accuracy buy not utilized by the tracking algorithm. The 2D central point of each transverse image should be unchangeable after registration and only transverse depth varies. The ground truth of this accuracy analysis is the location of the MRI scan-plane which is pre-defined and with fixed increments between images. As shown in Fig. 3.22, the RMS error of $x_0$ , $y_0$ and $z_0$ is 0.074 mm, 0.227 mm and 0.270 mm respectively. Specifically, the

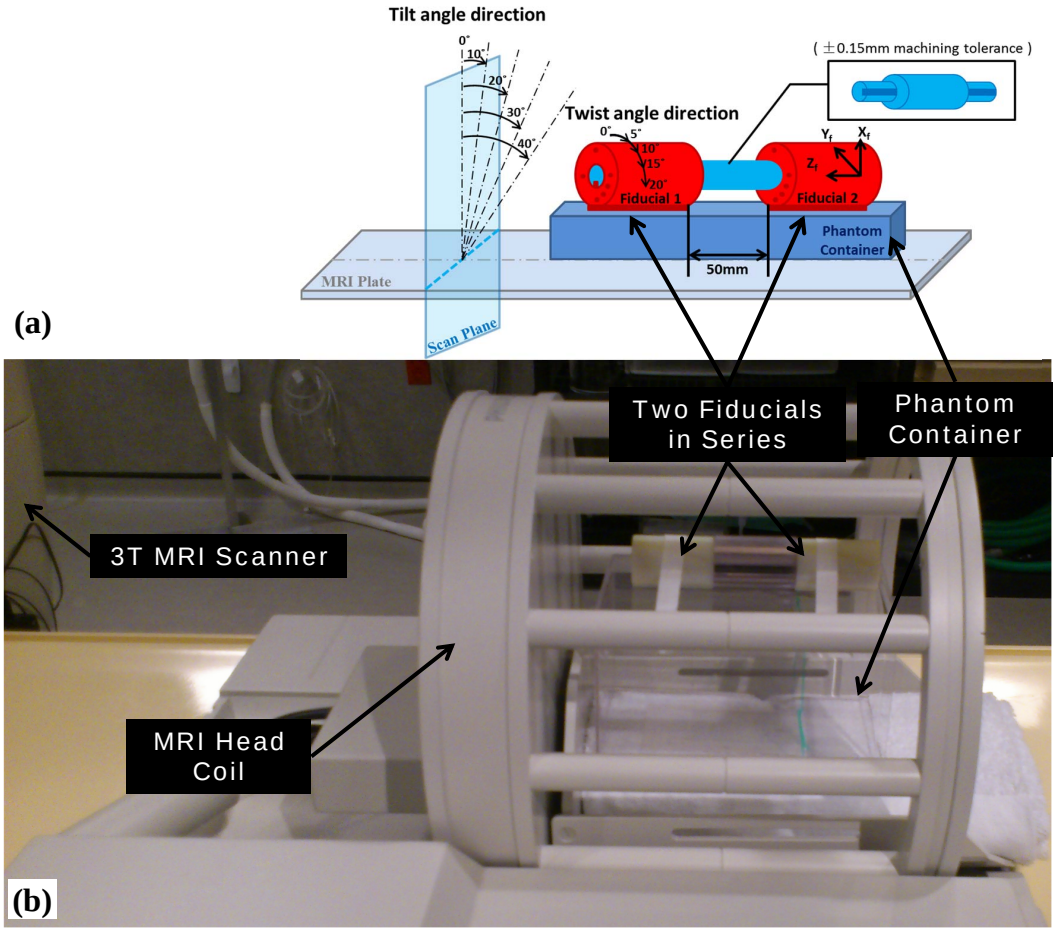


Figure 3.21: (a) Experiment schematic. Two fiducials being connected in series by a 50 mm long concentric connector were placed on a phantom container. (b) The photo of the real installment of the whole experiment setting. This experiment used the MRI head coil inside 3T main coil to enhance imaging definition.

detection of $z_0$ changing along central axis were presented in Fig. 3.23 separately. It has a RMS error of 0.270 mm and standard deviation of 0.275 mm. The overall translational RMS error is 0.208 mm and standard deviation is 0.241 mm for totally 300 samples. Since the pixel size is 0.5 mm $\times$ 0.5 mm, our results here achieved sub-pixel accuracy which is ideal.

2. Evaluation of rotation

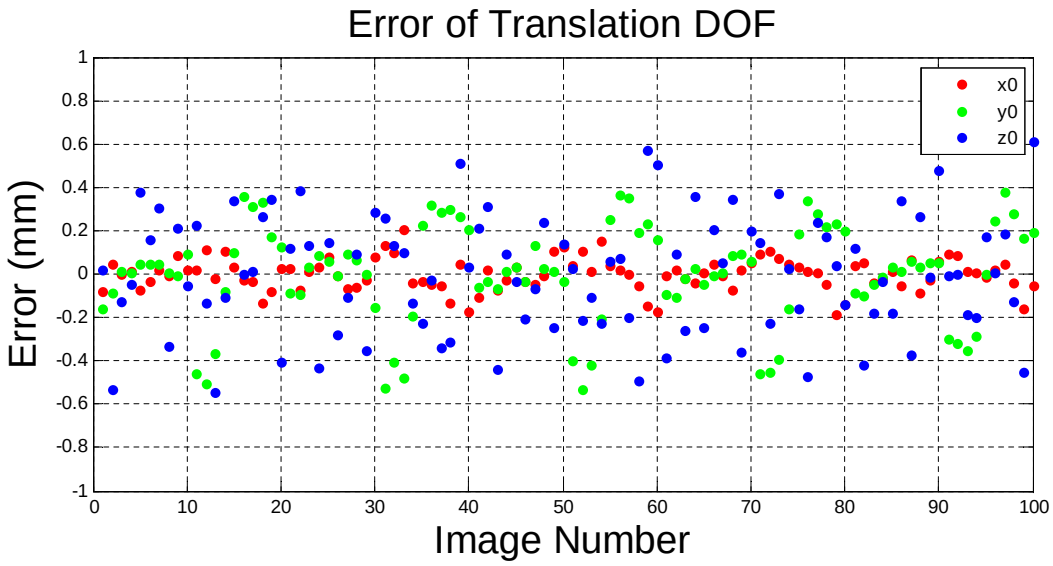


Figure 3.22: RMS error measurement results of translation DOF from 100 slices under different twist and tilt angles. The RMS error of $x_0$ , $y_0$ and $z_0$ is 0.074 mm, 0.227 mm and 0.270 mm respectively.

Results of the rotation accuracy study are shown in Fig. 3.24. The detection of successive twist angles ($\varphi$), elevation angles ($\alpha$) and direction angles ($\eta$) are listed in plot (a), (b) and (c). In each case, 50 slices were selected from five control groups of tilt or twist and the true value of corresponding step length was also superimposed into the same plot. Similar to the previous evaluation of position, the ground truth of this rotation accuracy analysis is the pre-defined orientation of the MRI scan-plane. The RMS error of twist, elevation and direction angle is 0.426°, 0.379° and 0.465° respectively. The overall angular RMS error is 0.425° and standard deviation is 0.524° for totally 150 samples.

Statistical analysis of tracking errors are summarized in Table 3.3 on page 114.

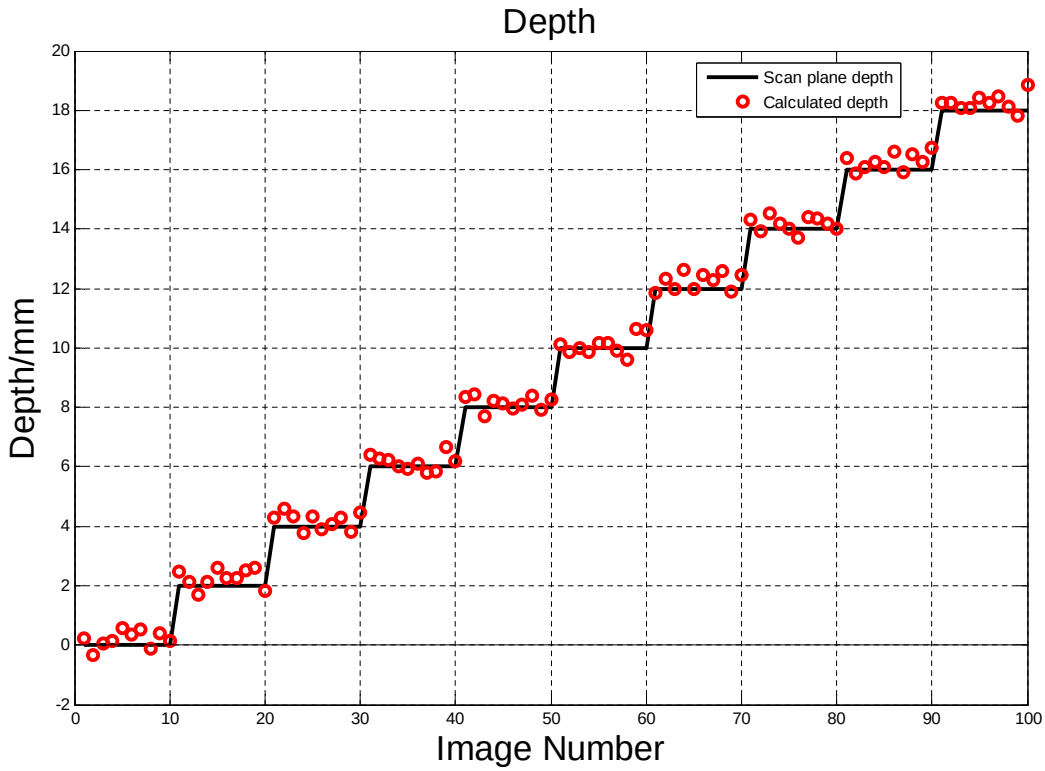


Figure 3.23: Detection of motion in depth with 2 mm regular step distance along z axis with RMS error of 0.270 mm and standard deviation of 0.275 mm.

### 3.5.5 Discussions

A fiducial design as well as a corresponding registration and tracking system were developed for close-loop control of robot in intervention under different imaging modalities. This system integrates a DICOM server, a portable registration and tracking algorithm modular with the OpenIGTLink network communication, as well as the user interface for the physician to coordinate the procedure and control the robot. Moreover, not only for CT and ultrasound, the size of this system was compact enough for using inside the constrained MRI bore and compatible completely under MRI environment without any artifact or disturbance appearing in the image.

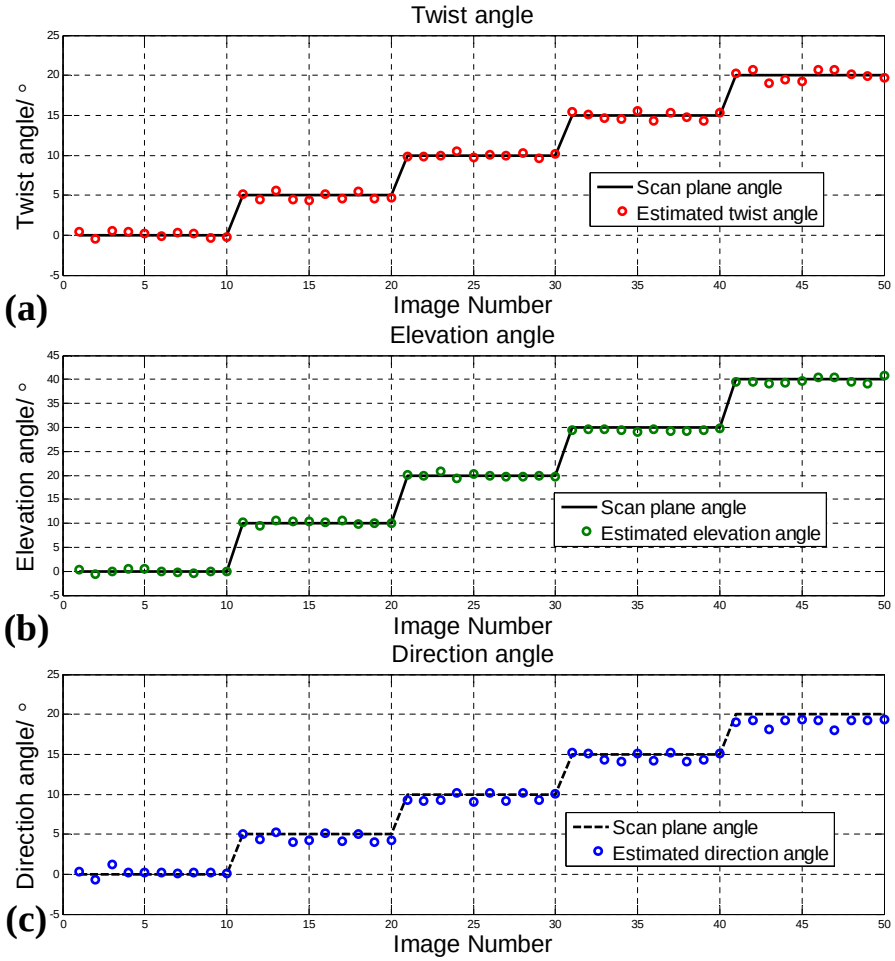


Figure 3.24: Detection of motion in each rotation DOF: (a) Twist angle with RMS error of 0.426° and standard deviation of 0.432°, (b) Elevation angle with RMS error of 0.379° and standard deviation of 0.453° and (c) Direction angle with RMS error of 0.465° and standard deviation of 0.603°.

It is a standalone system that achieves registration and tracking without any additional instruments or supports just like the MRI experiment showed before. The error shown in Table 3.3 on page 114 demonstrates outstanding tracking accuracy when detecting pose of scanning plane just by a single 2D transverse image. For this demonstrated fiducial configuration, all tracking errors are within 0.5° except

Table 3.3: Statistical analysis of 6-DOF tracking errors.

| | | RMS Error | Standard Deviation | Samples |
|---|---|---|---|---|
| Translation | $X_0$ | 0.074mm | 0.110mm | 100 |
| | $Y_0$ | 0.227mm | 0.247mm | 100 |
| | $z_0$ (Depth ) | 0.270mm | 0.275mm | 100 |
| | Overall | 0.208mm | 0.241mm | 300 |
| Rotation | Twist | 0.426° | 0.432° | 50 |
| | Elevation | 0.379° | 0.453° | 50 |
| | Azimuth | 0.465° | 0.603° | 50 |
| | Overall | 0.425° | 0.524° | 150 |

standard deviation of direction angle is 0.609° due to direction angle is sensitive with any delicate error at completely vertical condition. But considering the dimension of fiducial frame's caliber of 250 mm, this defect cannot belittle virtues. Meanwhile, these results also attest that it is doable to utilize single-slice based fiducial detection methods to assist robot or instrument motion in order to synchronize with registration and tracking. However, we have to notice that this accuracy depends upon the pixel size which in our experiment is $\frac{\text{field of view}}{\text{image dimension}} = 0.5mm$. And this assistant system is primarily suitable for tracking motion with relative slow pace as is a common setting among most of clinical robot in consideration of safety. We have to admit that this assistant system is not feasible for tracking fast motion such as free-hand operation due to long imaging time of MRI contrast medium for getting high definition, however, people most care about precision rather that speed of robot assisted surgeries.

On the other hand, various dimensions of CHIC fiducial frame will be adopted in

other surgeries like shown in Fig. 3.25. Not only MRI applications, but also CT or ultrasound procedures, all have different image protocols. so that it is required to do further work to evaluate its ways of modification and accuracy under different imaging conditions before launching it into other applications. Generally, as it is shown in the design, making the fiducial frame larger in overall diameter and longer in length will both improve its accuracy, but at the same time, it is still the more compact the better. We are still working on testing different fiducial frames with different sizes to quantify the effects of each parameter to the accuracy. After all, the fiducial frames will be made into a set of typical size and labeled corresponding errors so that by just installing a ready-made and calibrated fiducial frame into robot or instrument, it is ready for a new type of surgery.

As a supreme imaging modality for soft tissue, MRI becomes much more commonly used recently. For using under MRI, we are also trying to wrap the fiducial frame with passive tracking coil to reduce imaging time by resonating with MRI main coil so that it can track rapid movement and be extended to free hand surgery. Although bringing non-ferromagnetic tracking coil in system may lead to image distortion, tracking algorithm can be amended to eliminate these disturbance with valid tracking area [128]. In this work, no ferromagnetic metals have been used in order to get full MRI-compatibility to guarantee imaging quality at the cost of imaging time but evidently, an elaborate non-ferromagnetic tracking coil will dramatically shrink imaging time with minimum image distortion [129].

Finally, a better user interface and feedback control output will be developed for this assistant system to deal with complex conditions. It will allow physician to manipulate robot or instrument along pre-marked path synchronized with real time tracking.

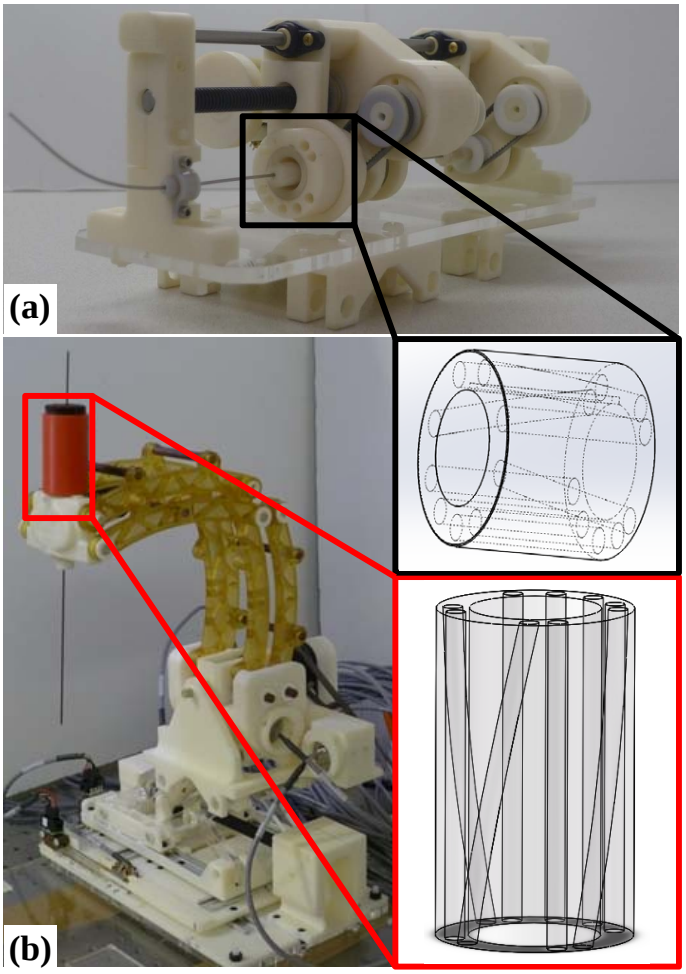


Figure 3.25: (a) Modular needle driver with CHIC fiducial integrated [123], (b) CHIC frame fiducial frame demonstrated on our stereotactic neurosugery robot [122].

## 3.6 Performance Enhanced CHIC with Passive Resonant Coils

It is always required for robotic assisted surgeries to have a good visual tracking system such as endoscopy to monitor and give surgeon real-time visual feedback of current position of the surgical tool as well as the target tissue. But for the needle inserted into the tissue, optical visual feedback is not possible since the tissue is not always transparent. Shown as an artifact, the needle is visible in MR image which has good soft tissue contrast and real-time imaging ability, but several drawbacks prevent it from being the most ideal tracking method. Firstly, there is a compromise between short imaging time and the image quality that the needle, fiducial tubes as well as the tissue is not shown very good in the real-time images. Secondly, acquiring high resolution images is not impossible but getting that usually requires several seconds per single image due to the MR imaging principle. Thirdly, even in the high resolution image, the artifact for an 18G needle (0.05 in or 1.27 mm in diameter) is about 5 mm large which is not ideal for a precise needle tracking.

One way to solve the problem is using resonant coil around the fiducial to increase the local magnetic field by introducing instant resonant magnetic field so that the contrast medium in the fiducial could be more bright than usual. Higher definition of the fiducial tube could be gotten still with fast MR imaging protocol with small flip angle.

### 3.6.1 Proof of Concept

A resonant circuit which is a second order LC circuit as shown in Fig. 3.26(a), could store energy and oscillate at resonant frequency. For being used in MRI, the resonant frequency of the LC circuit should be the same as the imaging frequency of the MRI system. The Phillips Achieva 3 T MRI scanner we deal with works at 128 MHz under normal operating conditions.

The equation for resonance effect of a LC circuit is

$$f_0 = \frac{1}{2\pi\sqrt{LC}} \tag{3.25}$$

and the approximate inductance formula is

$$L = \frac{D^2 \times 4T^2}{18d + 40l} \tag{3.26}$$

where $f_0$ is the resonance frequency, $L$ is inductance, $C$ is capacitance, $d$ is the diameter of the coil, $l$ is the total length of the coil, $T$ is the total turns of the coil, as shown in Fig. 3.26(b).

Base on the principle, two testing prototype were made 3.26(c), with commercially available 6 mm diameter Beekley fiducial tube and 3 mm diameter straw filled with gelatin as contrast agent. A MRI-compatible variable capacitor with the range of 1 6pF is used for both prototype. Both of them were well-tuned with 128MHz resonant frequency.

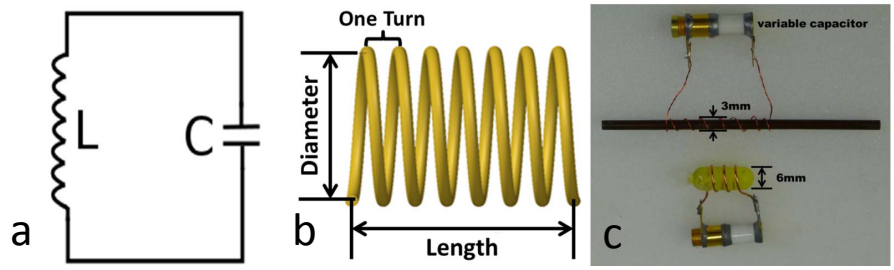


Figure 3.26: (a) Second order LC resonant circuit, (b) Parameters for a coil, (c) Two prototypes of coil testing structure.

A preliminary test was done with these two prototypes and a original Beekley fiducial tube as control as shown in Fig. 3.27.

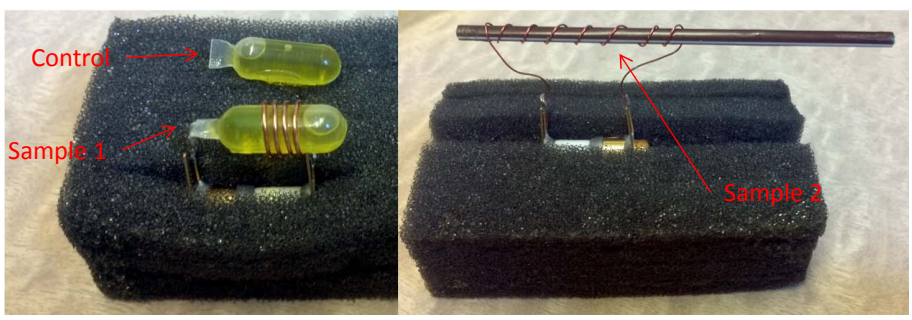


Figure 3.27: Resonant coil preliminary test setup: Sample 1 is the Beekley fiducial tube with coil. Sample 2 is the straw filled with gelatin with coil. Control is an original Beekley fiducial tube.

A real-time fast low-angle shot (FLASH) pulse sequence was used with the Imaging frequency = 128 MHz, FOV=250 mm x 250 mm, TE=4.53 ms, TR= 9.37 ms, FA=2°, BW=217 Hz, Slice thickness=2 mm, Space between slices=3 mm, pixel size = 560 × 560, Pixel spacing = 0.446 mm × 0.446 mm.

Fig. 3.28 shows the MR images of two samples with the control fiducial. Both of sample 1 and 2 are much brighter than the control group which is the original Beekley fiducial tube without coil.

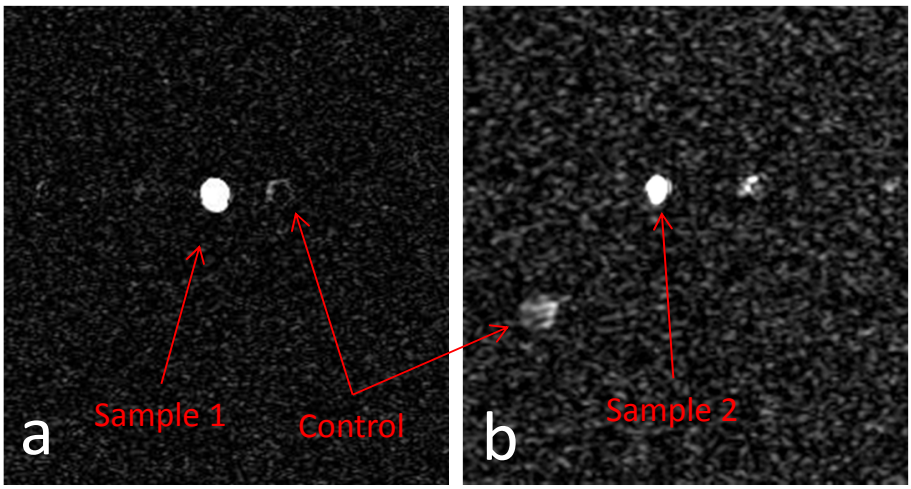


Figure 3.28: Resonant coil preliminary test MR images: Both of sample 1 and 2 are much brighter than the control group which is the original Beekley fiducial tube without coil.

### 3.6.2 Coil Design

With the successful preliminary passive coil test with a single fiducial tube, it was adapted to CHIC fiducial tube. Two approaches have been tested as shown in Fig. 3.29. By placing the coil inside the fiducial tube with contact to the imaging agent, the original CHIC fiducial design stays the same. In the other hand, wrapping the coil outside of the fiducial tube could avoid contacting with the contrast agent but the whole fiducial frame was redesigned as shown in Fig. 3.29(c) and (d). Both of them were tuned and tested inside the MRI scanner with the same imaging protocol described above.

The result shown in Fig. 3.30 indicate that both prototypes with coils outside and inside have much brighter signal than the control group. The prototype with coils outside is even brighter than the one with coils inside the fiducial tubes.

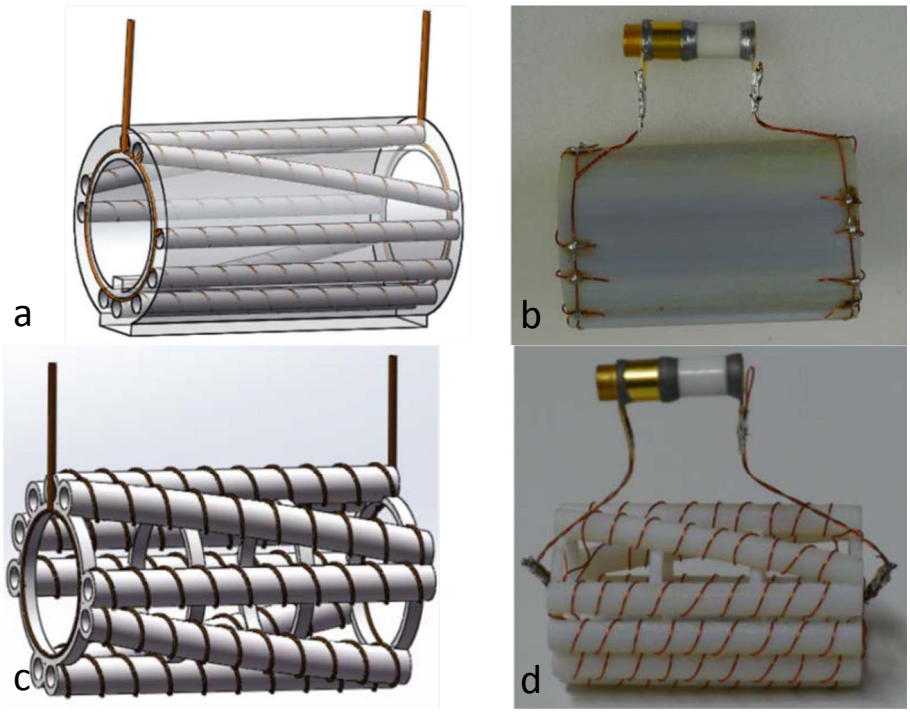


Figure 3.29: Inside coil design(a) with CHIC fiducial tube and its prototype(b); outside coil design(c) with modified CHIC fiducial tube and its prototype(d).

What was unexpected was that from the lateral view (Fig. 3.31) that it was too sparse for the coils to form a homogeneous brightness through the length of the fiducial tube. This also explains why each fiducial point shown in 3.30(b) or (c) are not with the same brightness.

To address this issue, 1/8 inch wide flat wires were used to replace the round wires as shown in Fig. 3.32. MR images showed the improved result as seen in Fig. 3.33.

### 3.6.3 Discussions

One observation needs to be brought to discussion is that during single coil experiment, several phantoms of the fiducial tube were shown around it as shown in Fig. 3.34. The initial guess was that the perfect match between the resonant frequency of the coil and MR imaging frequency generated the strongest signal but phantoms as well. When the frequency was not a perfect match, the phantoms disappeared. The reseaon could be the phase-wrapping or the ringing effect and the proper solution was still left to be found.

## 3.7 Discussion and Conclusions

In this chapter, two types of passive fiducial based registration methods and one performance enhanced fiducial with self-resonance coils have been introduced.

In the first work, multi-image registration with sub-pixel accuracy is achieved. The errors of both displacement and angle are well below 1 mm and 1°. The average displacement error is 0.27 mm, maximum is 0.69 mm. The average angular error is 0.16°, maximum is 0.49°. The average error is sub-pixel level.

In the second work, a cylindrical fiducial design, as well as a corresponding registration and tracking system were developed for close-loop control of robot in intervention under different imaging modalities. Not only for CT and ultrasound, the size of this system was compact enough for using inside the constrained MRI bore and

compatible completely under MRI environment without any artifact or disturbance appearing in the image. The overall translational RMS error is 0.208 mm and standard deviation is 0.241 mm for totally 300 samples. Since the pixel size is 0.5 mm $\times$ 0.5 mm, our results here also achieved sub-pixel accuracy which is ideal. The overall angular RMS error is 0.425° and standard deviation is 0.524° for totally 150 samples.

Although this two methods reach similar accuracy result, the CHIC fiducial is definitely smaller in size which gives more flexibility in real implementations. By placing the fiducial close to the end effector, the robot accuracy could be potentially improved since part of the robot calibration and kinematic error could be eliminated in the robot kinematic chain. Comparing to the flipping method, which is based on binary images, the Gaussian fitting method is even more robust because it directly applied to the gray image which has intermediate values between 0 and 1 of binary images. The use of Gaussian distribution is an assumption made based on the size of the fiducial used and previous literatures. It works well in CHIC fuducial but might not be the best choice of model when the fiducial tubes have larger diameter which could make the center area a flat top that doesn't fit to the Gaussian distribution. In the future, the more accurate mathematical model still needs to be discovered and the relationship between the model and the size of the fiducial tube is another open research topic.

In the third work, self-resonance coils have been implemented into the current CHIC fiducial frame and the preliminary result shows that both prototypes with coils

outside and inside have much brighter signal than the control group. The prototype with coils outside is even brighter than the one with coils inside the fiducial tubes. It has the potential to reduce the imaging time significantly and increase the tracking speed.

For both of the fiducial based designs, it is interesting to find out the relationship between the fiducial size, image used for one-time registration and the accuracy. Initial thought is that smaller cross section would decrease the error produced during the finding of centroids of the fiducial points but it also increases the difficulty of distinguishing and locating the fiducial center.

Finally, the performance of real-time registration, navigation and tracking of the CHIC fiducial frame will be tested in the near future by actually implementing this work into a MRI-guided surgical robot.

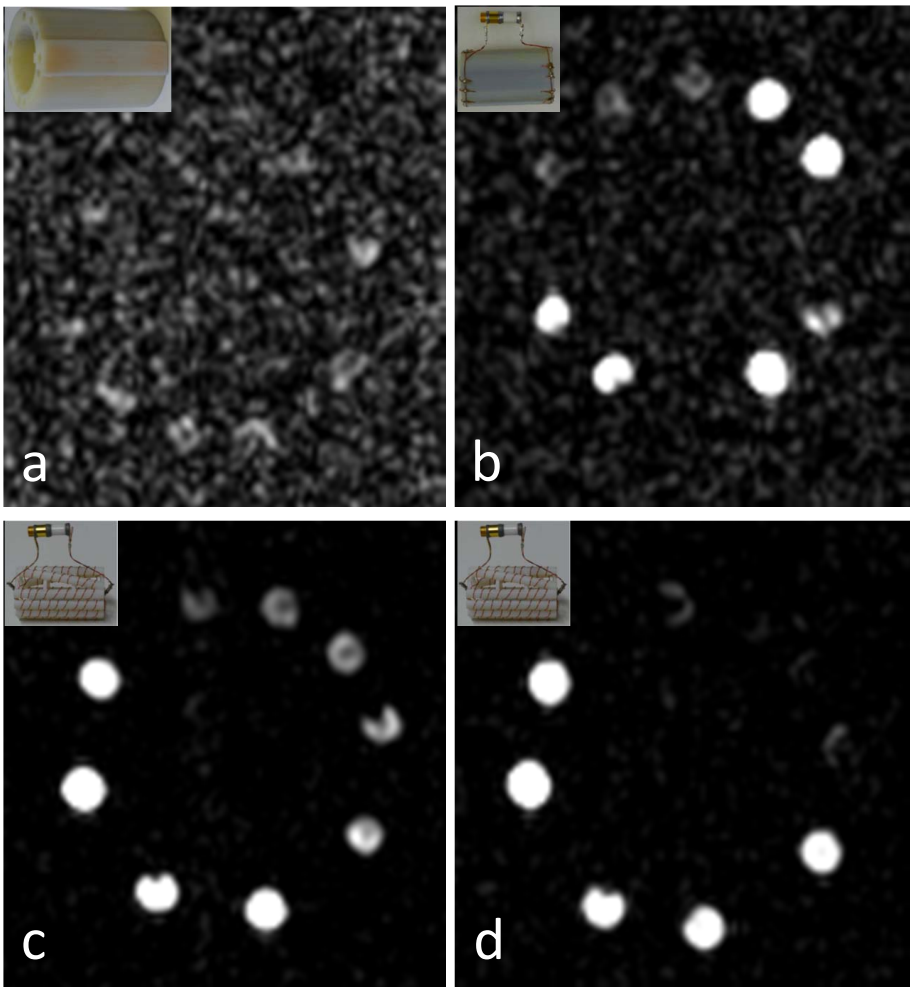


Figure 3.30: MR images of CHIC fiducial tube with resonant coils: (a) control group which is the CHIC fiducial frame without coils, (b) MR image of CHIC fiducial frame with coils inside each tube, (c) MR image of CHIC fiducial frame with coils outside each tube, (d) MR image of CHIC fiducial frame with coils outside each tube, but the contrast agent in upper right four tubes were removed.

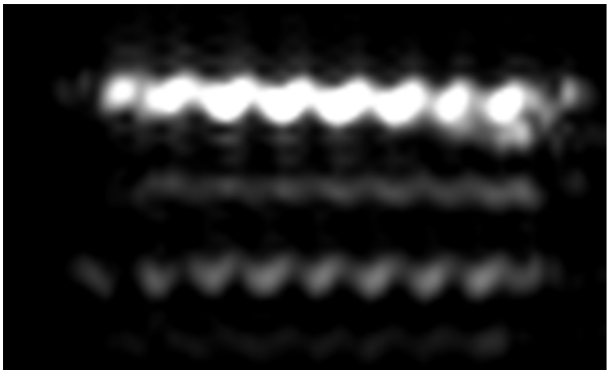

Figure 3.31: Lateral MR images of resonant coil with CHIC fiducial tube shows the inhomogeneity along the length of the fiducial because of the thin wire.

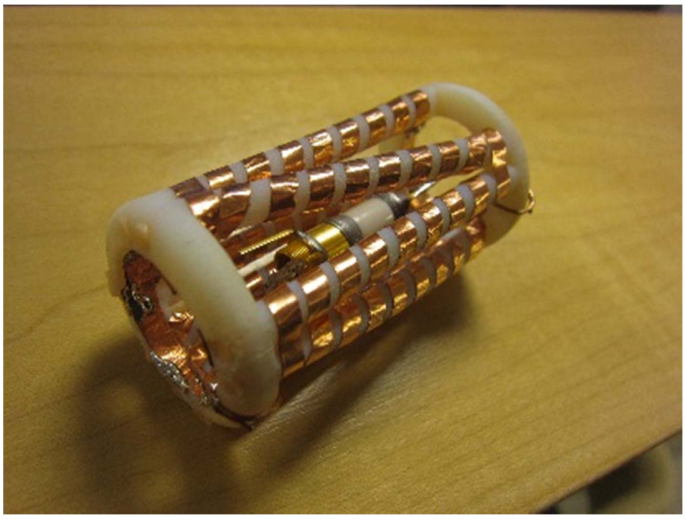

Figure 3.32: 1/8 inch wide flat wires were used to replace the round wire for CHIC fiducial.

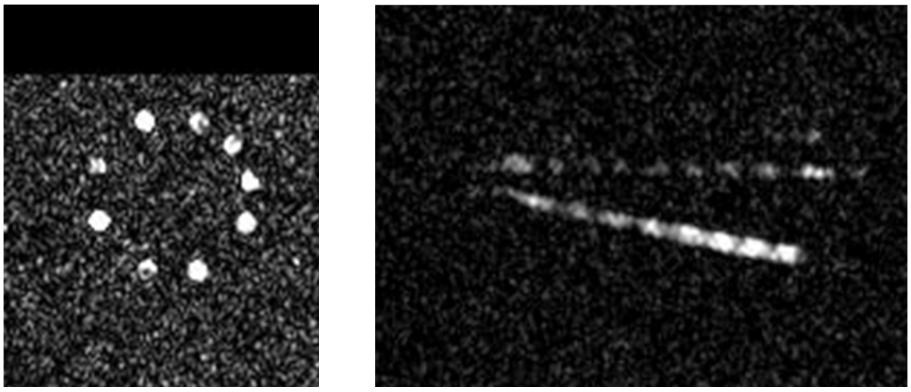

Figure 3.33: MR images of CHIC fiducial tube with 1/8 inch wide flat wires. (a)Transverse view shows all fiducial points with similar brightness, (b)lateral view shows improved homogeneity.

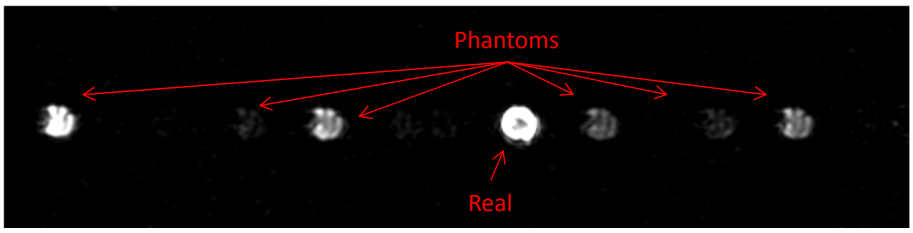


Figure 3.34: Fiducial point with its phantoms.

# Chapter 4

# MRI-Guided Teleoperation for Prostate Needle Interventions

Part of this chapter has been published as

H. Su, **W. Shang**, G. Cole, G. Li, K. Harrington, A. Camilo, J. Tokuda, C. M. Tempany, N. Hata, and G. S. Fischer, "Piezoelectrically actuated robotic system for MRI-guided prostate percutaneous therapy," Mechatronics, IEEE/ASME Transactions on, vol. 1, no. 1, pp. 1-12, 2014.(In press) [110]

**W. Shang**, H. Su, G. Li, and G. S. Fischer, "Teleoperation system with hybrid pneumatic-piezoelectric actuation for MRI-guided needle insertion with haptic feedback," in Intelligent Robots and Systems (IROS), 2013 IEEE/RSJ International Conference on. IEEE, Conference Proceedings, pp. 4092-4098. [22]

**W. Shang**, H. Su, G. Li, C. Furlong, and G. S. Fischer, "A fabry-perot interfer-

ometry based MRI-compatible miniature uniaxial force sensor for percutaneous needle placement," in SENSORS, 2013 IEEE. IEEE, Conference Proceedings, pp. 1-4. [26]

N. A. Patel, T. v. Katwijk, G. Li, P. Moreira, **W. Shang**, S. Misra, and G. S. Fischer, "Closed-loop flexible needle steering with real-time mri guidance," IEEE ICRA 2015 International Conference on Robotics and Automation. (In review) [130]

and

G. Li, N. A. Patel, **W. Shang** and G. S. Fischer, "Modeling of continuous uncoupled rotation velocity-independent (curv) asymmetric tip needle steering," IEEE ICRA 2015 International Conference on Robotics and Automation. (In review) [131]

## 4.1 Overview

Teleoperation is desired for prostate needle interventions inside MRI that it could release the surgeon from highly constrained workspace. But by using traditional teleoperation master device, the haptic feedback experienced by hand is removed since there is no force feedback. Bringing haptic feedback to the teleoperation master-salve system has several requirements and challenges need to be addressed. Firstly, the needle placement (slave) robot should be MRI-compatible because it is close to the iso-center of the scanner and it is kept beside the patient in the scanner room during real-time imaging. The design should also be compact to be placed in the limited working area. Secondly, high systematic positioning accuracy should be maintained

by the using of series of sensing methods such as optical trackers and encoders for registering the robot as well as doing closed-loop control. Thirdly, force needs to be acquired from both master and slave devices by using sensors which are MRI-compatible. Finally, the master haptic device should be intuitive that it should make no confusion to users. Force needs to be applied to surgeon by the haptic device through the best choice of motor which should be easy to control, backdrivable, and MRI-compatible.

Several MRI-compatible robots have been reported, some of which could serve as the slave robot. Examples are like [11], [48], [49], [50], [51], [52]. Haptic master devices could be found in [53], [54], [41] and [19]. As whole MRI-compatible master-slave systems, Seifabadi et al. [20, 55] and Tse et al. [56] are some of the examples. More extensive review could be found in section 1.4.

The contributions of this chapter are: 1) designed a piezoelectric-actuated slave robot with 3-DOF stage for aligning the robot to hold another 3-DOF needle driver for needle steering; 2) designed a FPI force sensor and compact opto-mechanical system for needle insertion force sensing; 3) designed a 2-DOF pneumatic-driven master device with load cell force sensor to interact with human user with haptic feedback; 4) conducted MRI-compatibility evaluation of the teleoperation robotic systems; 5) evaluated MRI-guided teleoperated needle steering; and 6) evaluated position and force tracking accuracy and dynamic performance of the teleoperation system.

## 4.2 Design Requirements

### 4.2.1 Degree of freedom and workspace of the robot

Letting the robot insert the needle through perineal wall, patient need to lie inside the MRI bore in the semi-lithotomy position. Basically, the robot motion could be separated into two steps: target alignment and needle insertion. Two modules are designed to totally decouple this two steps that make the procedure with max safety. A 3-DOF Cartesian stage is dedicated for alignment which is done in Cartesian space. Another 3-DOF needle driver has two coaxial insertion motions which enable the coordinated motion for biopsy and brachytherapy. One more DOF for rotation allows the needle steering.

On the master robot side, since the goal of the master robot is for controlling the needle placement, it has two DOFs. One is for general needle insertion, the other is for rotation.

The typical human prostate is about 50 mm in the lateral direction (L-R), 35 mm in the anterior-posterior direction (A-P) and 40 mm in depth (S-I). Also based on prostate's relative position to the skin in the body, the workspace of the robot could be defined as: 50mm in vertical (100 - 150 mm above the patient bed), 25 mm in lateral from the center of the workspace, and 150 mm in needle insertion depth to reach the back of the prostate from the surface at the perineum.

### 4.2.2 MRI-compatibility

The compatibility to the highly restricted MRI environment is one of the biggest challenges for designing robotic system working inside the MRI. By combing the two ways of MRI-compatibility definition mentioned in section 1.1.2, the requirement for both slave and master robot could be set. For the slave robot, it remains in the imaging volume since real-time imaging is done when the needle is being inserted. And it definitely has contact with the patient throughout the procedure and MRI scanning. So the requirement for the slave robot should be zone 1 MRI-conditional. For the master robot, it is kept out of the imaging volume all the time but still within the 200 Gauss line that this area is between the definition of zone 3 and zone 4. To be safe, the requirement for the master robot should be zone 3 MRI-conditional.

Besides qualitative definitions, quantitative merits are also used to evaluate the MRI compatibility of the device. The effects of device to the MR image quality is evaluated by signal-to-niose ratio (SNR) and the geometric distortion based on the NEMA standard (MS2-2008) [132]. The detailed experiment and analysis will be discussed in section 4.8.

### 4.2.3 Sterilization

The majority part of the slave robot is designed to be draped during clinical use and is not required to be sterilized. Only the parts which have contact with needle

or patient are required to be sterilized such as the needle guide, collet, collet nut and collet screw shaft.

All of the parts except the handle of the master robot could be covered with the drape and are not touched by surgeon directly. The handle that is touched by surgeon during the surgery could be detached from the shaft and sterilized individually.

## 4.3 Slave Robot

For the application of the prostate intervention, the whole mechanical motion could be separated into three tasks: entry point alignment, needle insertion and action performing such as performing biopsy or dropping radioactive seeds. Collaboratively designed in our lab, the slave robot has six degrees of freedom and consists of two modules: Cartesian stage module and needle driver module, each of which has three degrees of freedom. So functionally, the Cartesian stage is responsible for the entry point alignment and the needle driver is in charge of needle insertion and action performing.

To fulfill the MRI-compatibility requirement for materials, the majority part of the robot structure is made of plastic by rapid prototyping machines (Dimension 1200es, Stratasys, Inc., USA and Objet Connex260, Stratasys, Inc., USA). Plastic bearings (Igus Inc., USA) are also widely used at the rotational joints. To maintain the strength while minimize the friction and MRI interference; aluminum rails with

plastic carriages (both from Igus Inc., USA) are used for prismatic joints. On the choice of actuators and sensors, as it is mentioned in Section 2.3, PiezoLegs motors are chosen because of its fast response time and high position accuracy. Optical encoders (U.S. Digital, USA) are used for both linear and rotary position tracking. The linear encoder (EM1-0-500-I) has the resolution of 500 counts per inch (CPI). Combining with the PC5 differential driver makes it $500 \times 4 = 2000$ cpi which is 0.0127mm/count. The rotary encoder (EM1-1-1250-I) has the resolution of 1250 counts per revolution (CPR). Similarly, combining with the PC5 differential driver makes it $1250 \times 4 = 5000$ CPR which is $0.072°/count$. The MRI-compatibility of the encoder has been tested both previously [50] and in this work which is shown in Section 4.8.

This modular design decouples the basic alignment job from more application specific job which could be for prostate interventions as shown in this work or neuro interventions such as deep brain stimulation or ablation.

### 4.3.1 Cartesian Motion Module

Several iterations have been designed for the Cartesian motion module. The first version is shown in Fig. 4.1 with the SolidWorks model on the left and the actual prototype on the right. The scale problem caused by linear motor for the vertical motion is successfully avoided by the use of scott-russel scissor mechanism. Combing with lead screw, the rotary motion is transferred to linear vertical motion.

Although this design fulfilled all the requirements very well, it suffers from insta-

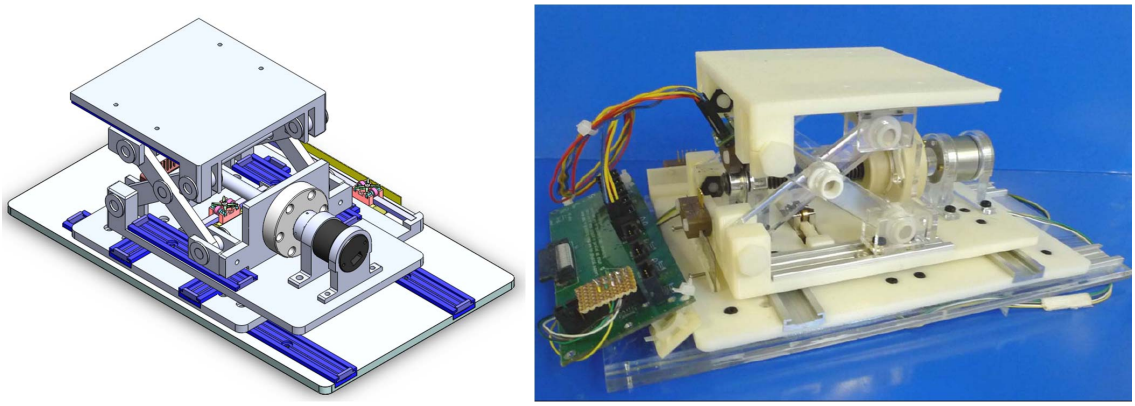

Figure 4.1: First version of the Cartesian stage design: SolidWorks model(left), prototype (right).

bility problem. When the stage is around its highest position, the upper joints are too close to each other and close to the front of the stage. It leaves the upper module's center of gravity out of support which results in the tilting of the top stage. Thus the second iteration was designed to address this problem.

Fig. 4.2 shows the exploded view as well as the prototype of the revised design. The original single scott-russel scissor mechanism is replaced with a double scott-russel scissor mechanism (no. 15) which gives the upper joints fixed distance that could very well support the upper module with its center of gravity always within the supports of four joints.

With stage 1 fixed to the ground, stage 2 and 3 move horizontally driven by two of the same linear motors (PiezoLegs LL1011C, PiezoMotor AB, Sweden). The same as the first iteration, vertical motion is provided by a rotary motor (PiezoLegs, LR80, PiezoMotor AB, Sweden) with an aluminum anodized lead screw with 2 mm pitch.

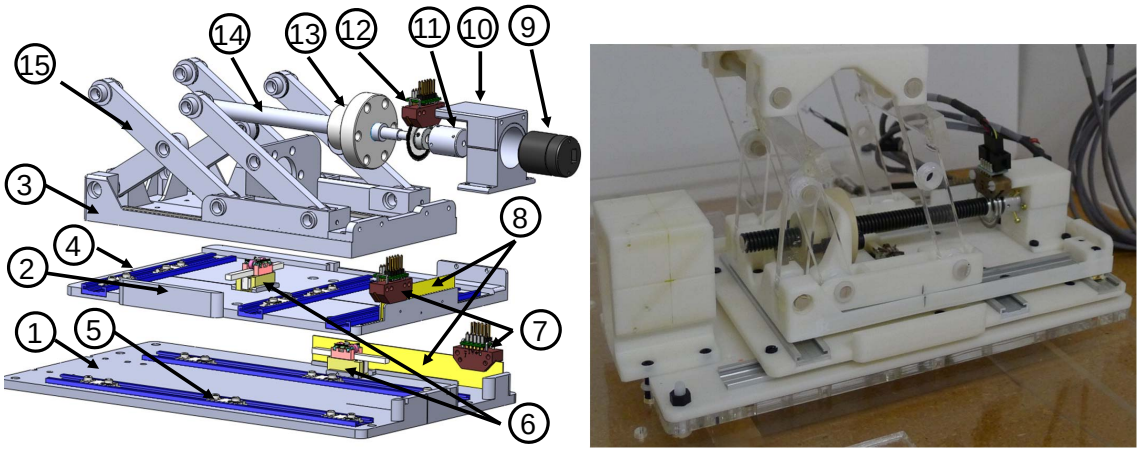


Figure 4.2: Left: Exploded view of the new Cartesian stage design: 1.base stage, 2.linear stage, 3.lateral stage, 4.aluminum rails, 5.plastic carriages, 6.linear piezo motors, 7.linear encoders, 8.linear encoder straps, 9.rotary piezo motor, 10.rotary motor housing, 11.motor coupler, 12.rotary encoder with disk, 13.screw nut, 14.lead screw, 15.scott-russel scissor mechanism; Right: prototype of the new Cartesian stage.

### 4.3.2 Needle Driver Module

On top of the Cartesian stage is the 3-DOF needle driver. As shown in Fig. 4.3, 1-DOF outer tube insertion is provided by a pair of piezoelectric motors since the trasperineal prostate needle placement normally requires 18 N force but one piezoelectric motor could only provide 10 N force. A collinear insertion DOF - inner stylet insertion is driven by another linear piezoelectric motor. The outer tube could also rotate with the actuation from a rotary motor with the speed of 1.5 cm/s. The needle driver is designed to be able to perform biopsy or brachytherapy by the cannula-stylet coordinated motion of two linear DOFs. By using the collet design, it fits a wide variety of needle ranging from 25 gauge (0.51 mm) to 16 gauge (1.65 mm). The plastic needle guide with a press-fit quick release mechanism, collet nut, and guide

sleeve that have direct contact with the needle are therefore readily detachable and sterilizable. [110]

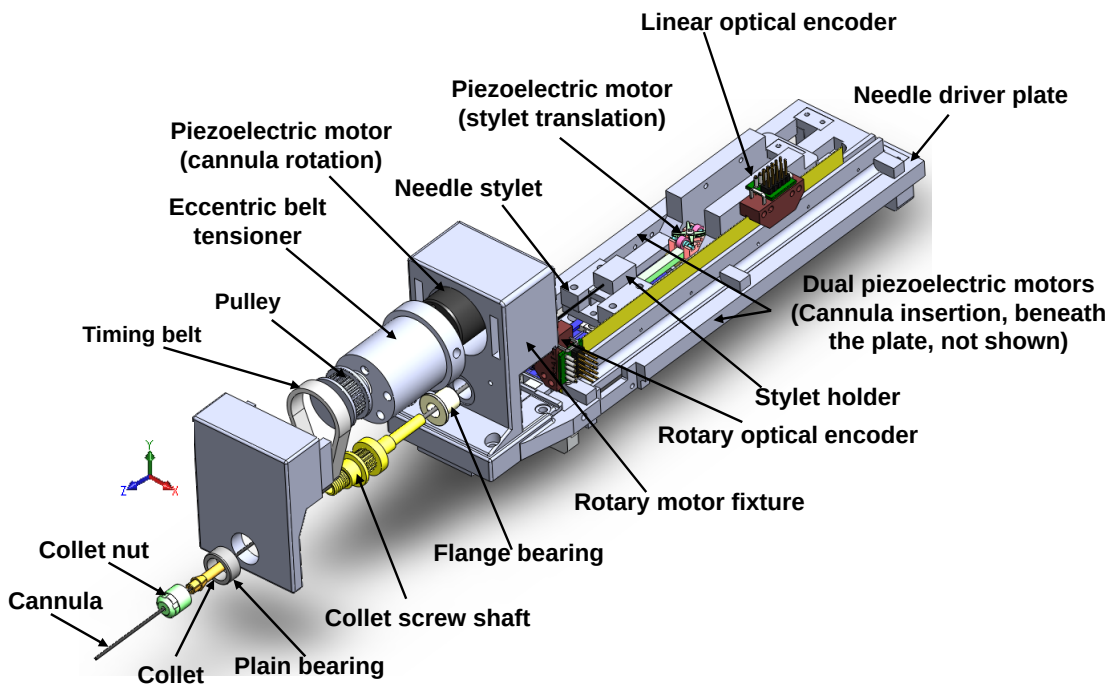


Figure 4.3: Exploded view of the needle driver module. [110]

This needle driver serves as the actual slave robot which could be controlled by the master discussed in Section 4.5.

### 4.3.3 Robot Kinematics

With the navigation coordinate relation, we can substitute the kinematics into the kinematic chain to calculate the needle tip position and orientation. The vertical motion of the robot is provided by actuation of the scissor mechanism. A linear motion in the Superior-Inferior (SI) direction produces a motion in the Anterior-

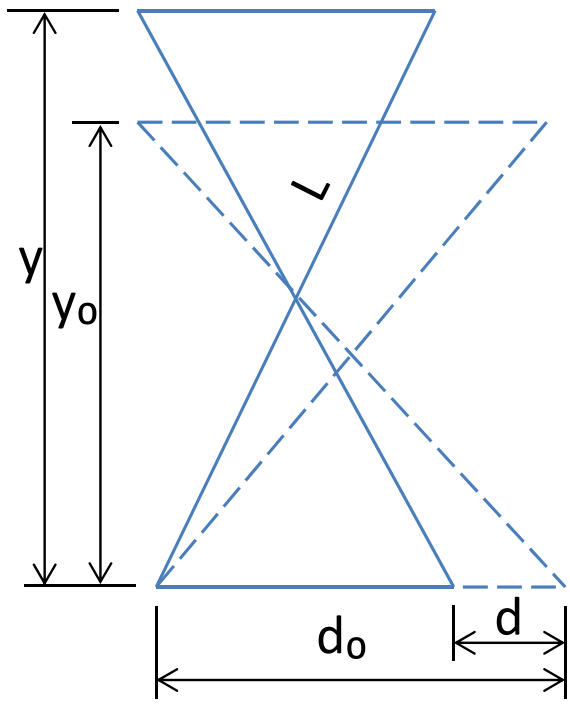


Figure 4.4: kinematics of scissors mechanism: Dashed lines indicate the original position, solid lines indicate the changed location.

Posterior (AP) direction. The forward kinematics of the robot with respect to the fiducial frame is defined as:

$$
\begin{aligned}
x(R) &= q_1 + x_{offset} \\
y(A) &= \sqrt{L^2 - (d_0 - d)^2} + y_0 + y_{offset} \\
z(S) &= q_3 + q_4 + z_{offset}
\end{aligned}
\tag{4.1}
$$

where $L$ is the length of the scissor bar, $d_0$ is the initial horizontal position, $d = \frac{q_2}{360} \cdot p$ is the horizontal linear motion of the lead screw due to the rotary motor motion and $p$ is the lead screw pitch. $y_0 = \sqrt{L^2 - d_0^2}$ is the initial vertical position of the stage related to $d_0$. An illustration of kinematics of the scissors mechanism is shown in Fig.

4.4. $q_1$,$q_2$,$q_3$,$q_4$ are joint space motion of the x-axis motor translation (unit: mm), y-axis rotary motor ration (unit: degree), z-axis motor translation (unit: mm) and needle driver insertion translation (unit: mm).

The three offset terms in Equation 4.1 are corresponding to the homogeneous transformation matrix $T^{Z}_{Rob}$ in Equation 3.1. $q_4$ is corresponding to the transformation $T^{Rob}_{Tip}$ and the remainder of Equation 4.1 is corresponding to the transformation $T^{Z}_{Rob}$.

## 4.4 Flexure Design and Opto-mechanical Design for Slave Robot with FPI Force Sensing

To achieve force sensing within the required range for needle placement, a flexure mechanism design is presented here. The early study [108] shows that the original opto-mechanical design is bulky and difficult to be integrated inside MRI scanner room with the piezoelectric motion control system. The developed more compact and portable opto-mechanical laser driver and interrogator is imperative for MRI applications.

### 4.4.1 Principle of Fabry-Perot Interferometer

The main part of a Fabry-Perot strain sensor is a cavity which contains semi-reflective mirrors. Light is partially transmitted and partially reflected. The sensing gauge length is the distance between fused weldings and generally form the nanometer level distance between the two fiber tips. As shown in Fig.4.5, $L_{cavity}$ is the original cavity length when there is no force. $2\delta$ is the change of the cavity length when a force is applied. Two red light paths shown in Fig.4.5 interfere with each other creating black and white fringes which are different from the ones created by two black light paths. The detection of different fringe intensities will be resulted from the change of optical path length when cavity length is changed by the applied force.

The whole sensing method can be quantified through the summation of two waves [134]. At a given power for planar wave fronts, the reflected intensity equation could be written as below by multiplying the complex conjugate and applying Euler's identity.

$$I = A_1^2 + A_2^2 + 2A_1^2A_2^2cos(\phi_1 - \phi_2) \tag{4.2}$$

where $A_1$ and $A_2$ are the amplitude coefficients of the reflected light. The equation 4.2 can be modified to represent only intensities by substituting $A_i^2 = I_i(i = 1, 2)$ and $\phi_1 - \phi_2 = \Delta\phi$ as

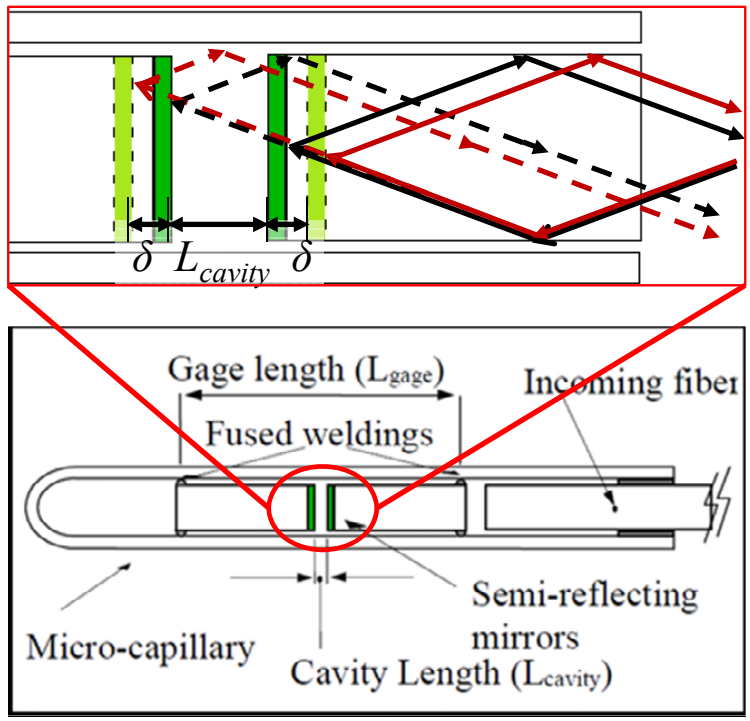


Figure 4.5: FPI sensor element diagram(lower) and its sensing principle with light paths(upper). Figure modified from [133]

$$I = I_1 + I_2 + 2I_1I_2cos(\Delta\phi) \tag{4.3}$$

### 4.4.2 Flexure Design for Integration with Slave Robot

As mentioned previously, Fabry-Perot interference fiber optic sensor offers several advantages over other optical sensing methods. Firstly, in contrast to purely intensity modulated techniques, FPI, a combined intensity and phase modulated interferometry, provides absolute force measurement. It is independent of light source power variations – a common problem that occurs due to flexing of fiber optic cables. Sec-

ondly, taking advantage of multi-mode fiber, adverse effect of thermal and chemical changes could be minimized. Thirdly, the ability to be miniaturized in scale allows it to be integrated to surgical tools like catheters or needles. In addition to biocompatibility, it is sterilization tolerant with ethylene oxide and autoclave. Most importantly, because it relies on simple interference pattern based voltage measurement, signal conditioning is simple in comparison with FBG sensors. The FPI fiber sensor (FOS-N-BA-C1-F1-M2-R1-ST, FISO Technologies, Inc., Canada) is relatively inexpensive (about $250) and can be designed to be disposable. Its operating temperature is $-40°$ to $250°$. The sensing strain ranges from $\pm 1000\mu\epsilon$ to $\pm 5000\mu\epsilon$ with resolution 0.01% of full scale.

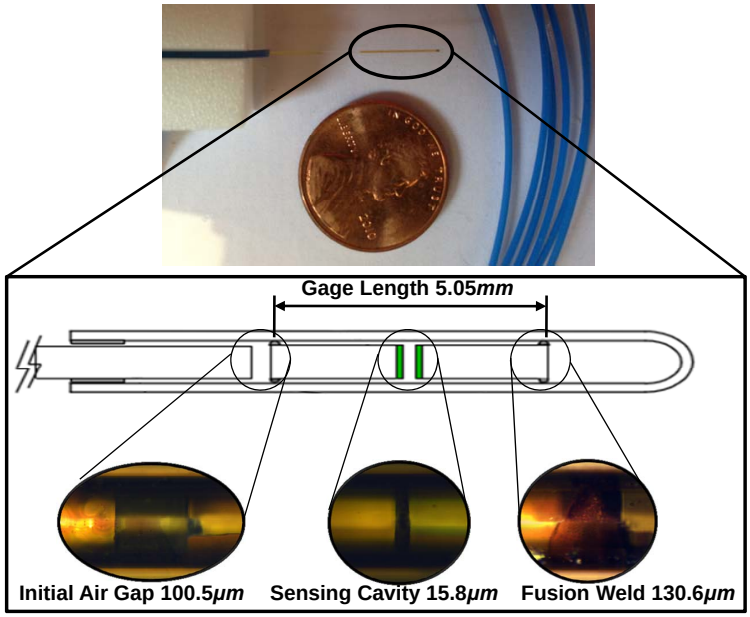


Figure 4.6: Actual FPI sensor element(upper) and a detailed view shown in inset(lower). [26]

The strain is calculated in the following formula:

$$\varepsilon = \frac{\Delta L}{L_{gage}} = \frac{L_{cavity} - L_o}{L_{gage}} \tag{4.4}$$

as shown in Fig. 4.6, $L_{cavity}$ is the length of the Fabry-Perot sensing cavity, in nanometers (varies between $8,000$ and $23,000$nm), $L_{gage}$ is the gage length (space between the fused weldings), in millimeters. $L_o$ is the initial length of the Fabry-Perot cavity, in nanometers $\varepsilon$ is the total strain measurement, in $\mu$ strain.

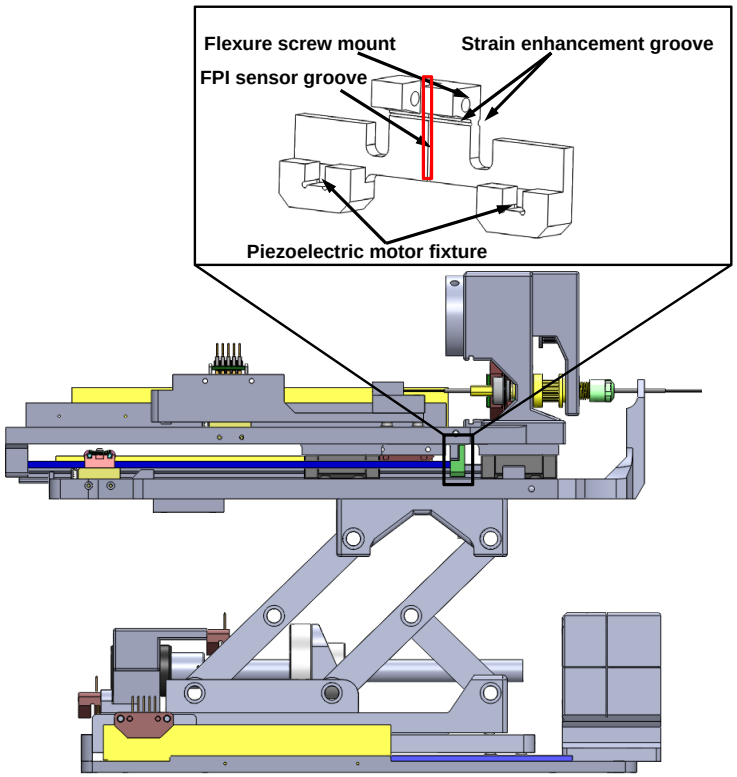


Figure 4.7: FPI flexure integrated in the MRI-compatible needle placement robot.

A flexure is designed to hold the FPI sensor and to be integrated with the prostate needle driver as shown in Fig. 4.7. The FPI fiber sensor is embedded inside the sensor groove vertically in Fig.4.8. Two flexure screw mounts are used to couple with

the robot mechanism. The length of sensing region is 10mm, and the center of active sensing region is 5mm away from the distal end of the fiber. Thus horizontal strain enhancement groove is located 5.75mm from the top of the flexure and 9.75mm from the bottom to allocate the full length of the fiber. The intersection of FPI sensor groove and strain enhancement groove is the center of active sensing region to maximize the sensing capability. The sensor installation involves a two-step procedure: After metal surface is well prepared by surface abrasion and neutralizer application, fiber cable is bonded by applying a very small drop (less than 1mm) of 5-minutes epoxy about $3mm$ away from the micro capillary and laying on adhesive slowly with a linear motion parallel to the gage orientation.

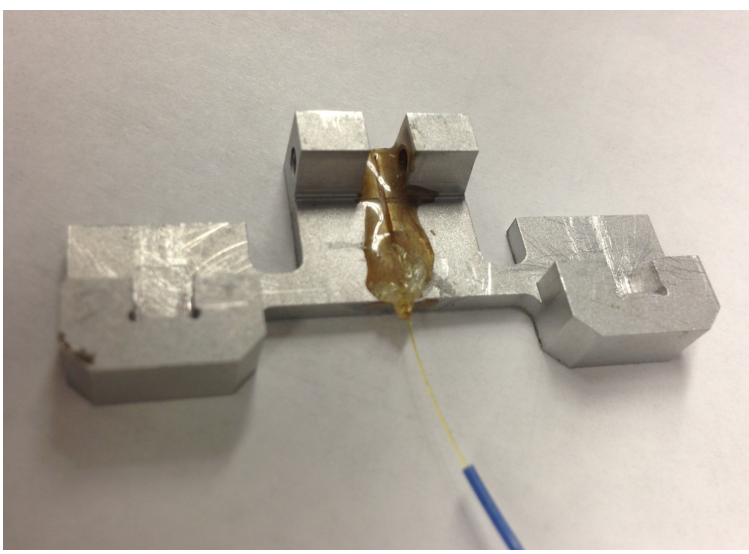

Figure 4.8: Actual flexure with FPI sensor attached.

Two piezoelectric motor fixture slots are used to constrain the piezoelectric motor drive rods, in combination with a quick disconnect fixture block. Aluminum alloy

6061 with Young's Modulus of 69GPa is used as the material of the flexure. Certain plastic materials could also be used to replace the aluminum alloy if they have similar properties. As shown in Fig.4.9, finite element analysis (FEA) confirms that the design is capable of measuring 20 Newton needle insertion force. A strain enhancement groove, also developed through FEA, optimizes the flexure design, enhances the dynamic range and ensures that the strain is within the sensing range of FPI.

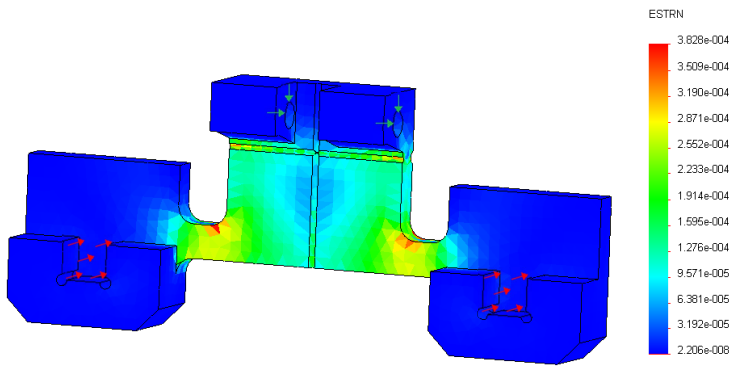


Figure 4.9: Finite element analysis result. Red arrows indicate the applied force, which is 10 Newton for each area, totally 20 Newton axial force. Green arrows indicate the fixed surface.

### 4.4.3 Compact and Portable Opto-mechanical Design

The preliminary benchtop opto-mechanical FPI interface system has been introduced in [108]. The dimension of the system is about $80cm \times 80cm$ which is unacceptable for putting into our MRI-compatible robot controller box. To address this issue, we have designed a whole new system based on the same principle. The major

innovation is the miniature optical fixture shown in Fig. 4.10. It consists of two collimators that connect laser source and FPI sensor with a photo detector on the third face and a beam splitter at center. This small fixture got the size of system shrunk from about $80cm \times 80cm$ to about $10cm \times 10cm$ thus it could be easily put into the controller box.

The final design is shown in Fig.4.11. A laser driver (LD1100, Thorlabs, Inc., USA) provides constant power with continuous laser output adjustment. The light comes out of pigtailed laser diode (LPS-635-FC ,Thorlabs, Inc., USA) and passes through the cube-mounted pellicle beam splitter (CM1-BP1, Thorlabs, Inc., USA). Two collimator (FiberPort PAF-X-2-532, Thorlabs, Inc., USA) are placed in orthogonal orientation inside an aluminum optical fixture. A 10 meter long optical fiber is connected to the FPI fiber cable through a FC/ST connector. The reflected light signal is detected by the photo detector and the voltage signal is sent to the control board. All of the optical system is enclosed inside the piezoelectric motor controller box with only one fiber coming out.

### 4.4.4 FPI Sensor Calibration

The calibration was conducted by adding standard weights on the FPI sensor flexure. The weights were put on a stage which has the same contact direction, positions and area as the real motor driving rods contact with the flexure, so that the measured force was in the same direction as the real needle force direction. The calibrated system can

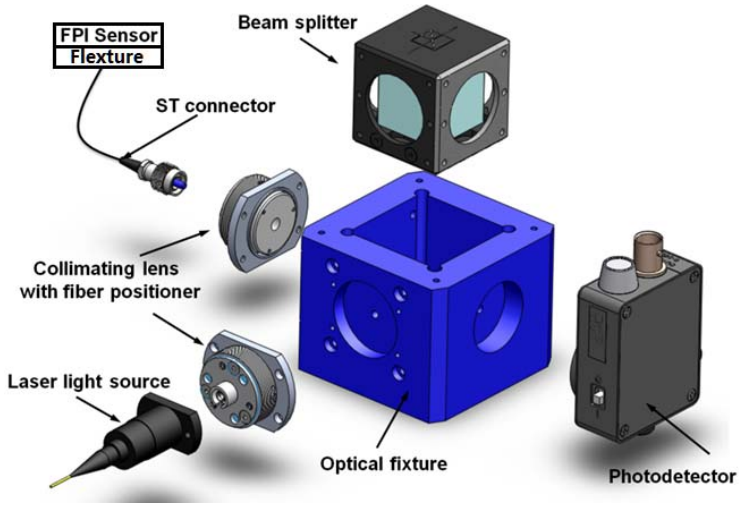


Figure 4.10: The optical fixture with two collimators, a photo detector and a beam splitter all together.

be seen in the voltage-force graph shown in Fig. 4.12. The dots shown in the figure represent the actual measurements. The calibrated curve was fitted to a sinusoidal function which is the theoretical relationship between the force and voltage. The output voltage follows this sinusoidal pattern that repeats over an increasing applied force. The relationship between force and final output voltage signal is

$$u = 0.944\cos(0.668f - 0.025) + 4.989 \tag{4.5}$$

where $f$ is the force in Newtons and $u$ is the voltage in volts. The root mean square (RMS) error of the calibration is 0.318 N. As a sinusoidal function, the mapping between the voltage and force is not 1:1 in the whole range. So that only the first half is used for measurement here. In the future, a stronger material will be used to make sure the whole desired force range drops in the 1:1 mapping part. Also, a pair

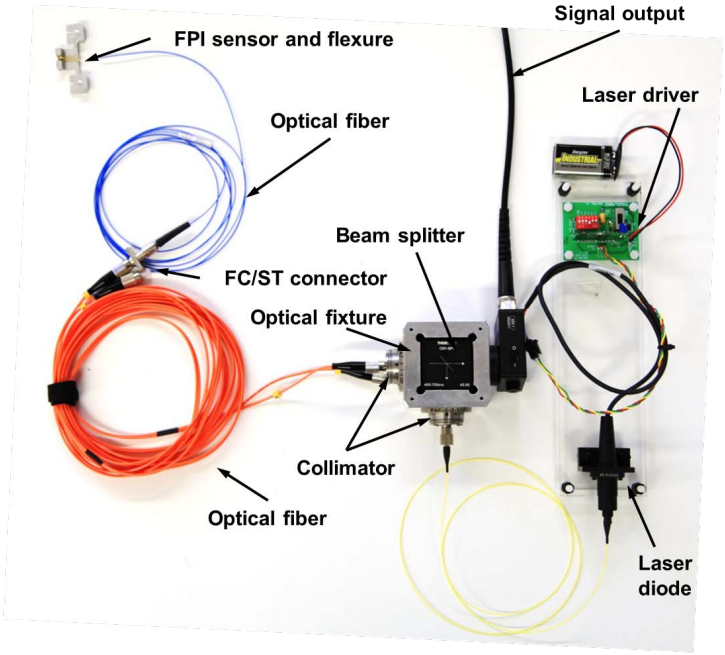


Figure 4.11: The compact opto-mechanical design of FPI interfaces that are capable of residing inside MRI-compatible robot controller box.

of the FPI elements with 90° out of phase forming a quadrature force sensor could also solve the mapping problem.

## 4.5 Master Robot with Strain Gauge Force Sensing

The search for actuation approaches for haptic device with force feedback has been arduous since it requires to be MRI-compatible, reliable, and robust. Piezoelectric motors have been evaluated in our research group, as well as in [56] [84] with admittance control to regulate force outputs or novel mechanism design [135] as haptic

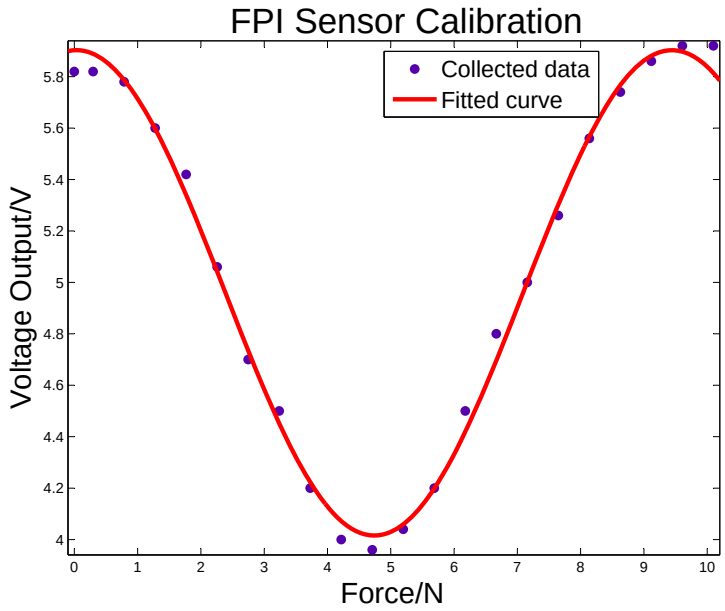


Figure 4.12: FPI sensor calibration result.

actuators. However, our experience shows that this kind of motor is inherently non-backdrivable and relies on friction interaction between piezoelectric elements and the motor drive rod or ring, and therefore suffers from quickly wearing out and failure in a short operation duration [13]. Pneumatic actuation has been used for MRI-compatible master robots, since it can be designed without ferrous components or electrical signals and more importantly, the pressure output has a direct relationship with control signal which makes the force control much easier than piezoelectric motors. Thus pressure regulated pneumatics becomes a natural choice as an actuator for a haptic master device. To our knowledge, this is the first development for MRI-guided surgical applications by utilizing hybrid pneumatic-piezoelectric actuation for master-slave control, respectively.

As shown in Fig. 4.13, the haptic master device includes a rotation encoded module to sense the rotation motion of the virtual needle's handle for steering, and also a translational module that provides pneumatically actuated haptic force feedback. A key feature of this design is that it decouples the rotation and translation motion. The bearing housing follows the rotation of the shaft actuated by user manual rotation of the biopsy needle. Then the outer ring of the ball bearings is rotated correspondingly. The inner ring of the ball bearing maintains not rotated, but transmits the insertion force exerted by the translation module. The two angular contact ball bearings (Igus, Inc., East Providence, RI, USA) are placed against each other to provide better support to axial direction force.

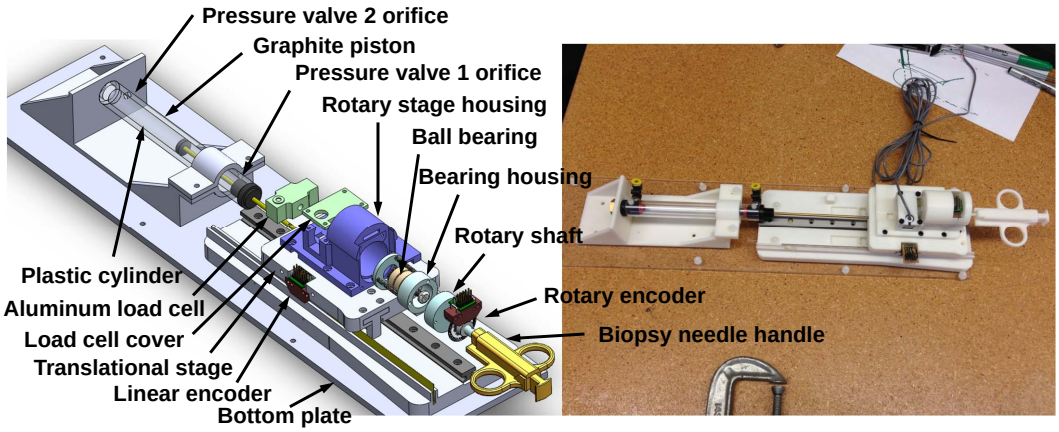


Figure 4.13: CAD model and prototype of the pneumatic haptic master device with decoupled rotation and translation mechanisms. An aluminum load cell is calibrated to measure interaction force between the user and the biopsy needle. A custom MRI-compatible pneumatic cylinder is used to render force. The mechanism includes a rotation, translation, and the haptic module that provides pneumatically actuated haptic force feedback.

## 4.6 Teleoperation Control System

Fig. 4.14 illustrates the control system schematic. In the middle of the figure, piezoelectric controller which contains several piezoelectric driver boards is in charge of the core control of the robot. The controller takes the position and force information of both master and slave robots, perform the closed-loop PID control, and send out the signal to the piezo motors on slave robot and piezoelectric valves for driving the pneumatic motor on master robot.

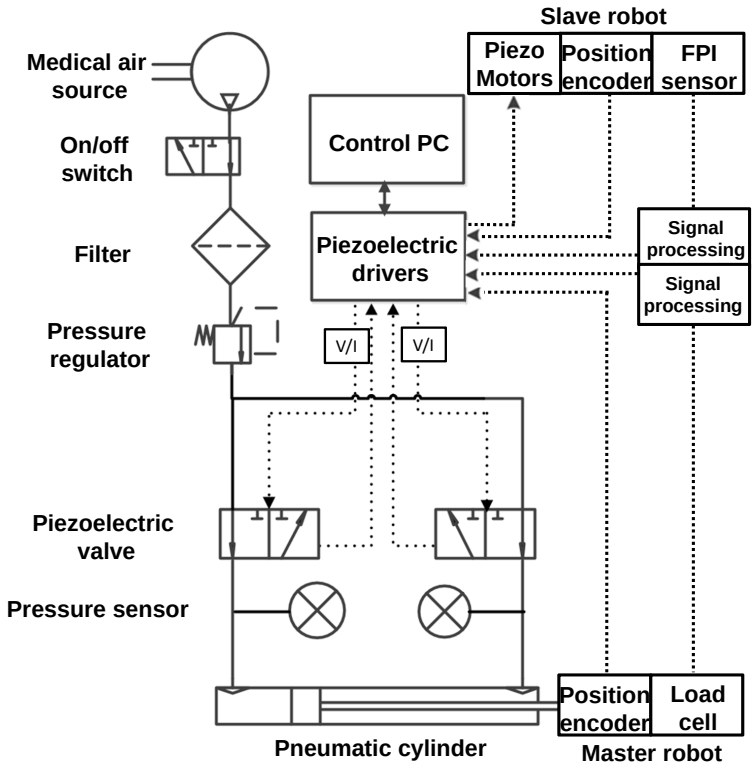


Figure 4.14: Mechanical and electrical connection of the master-slave system, where solid line shows the mechanical connection, dotted line shows the electrical connection and signal flow. The MRI-compatible robot controller supports analog input/output for force sensing and piezoelectric valve control in addition to piezoelectric motor actuation.

A custom MRI-compatible pneumatic cylinder [50], which is regulated by an opposing pair of high speed piezoelectric pressure regulator valves (PRE-I, Hoerbiger, Germany), is used to render force. With a fast response time of 10ms and a relationship between pressure and control current by 2 mA/bar (1 bar is $100,000$ Pa), this MRI-compatible piezoelectric valve can regulate pressure up to 689 kPa with control input ranging from 0 to 20 mA. A linear voltage to current (V/I) conversion circuit board is designed to transmit the $0-48$ V analog output from the piezoelectric motor controller [113] to the desired current. Two pressure sensors (PX309-100G5V, Omega, USA) are used to measure the pressure output of the valves. All of the valves, circuit board and pressure sensors are enclosed inside the controller box located in the scanner room to eliminate the distance between the valves and pneumatic cylinders as much as possible in order to reduce the cylinder response time. An aluminum load cell (MLP-10, Transducer Techniques, USA) with 44.45 Newton sensing range is also used on master robot to measure interaction force applied to the biopsy needle handle by the user.

The actual force generated by the opposing pair of piezoelectric valves is

$$F_a = P_1 A_1 - P_2 A_2 \tag{4.6}$$

where $P_1$ and $P_2$ are pressure of the two chambers, $A_1$ and $A_2$ are the piston areas.

Two control schemes could be used to get the desired control force $F_a$: bi-lateral control or impedance control which will be introduced separately.

### 4.6.1 Bi-Lateral Control

As it is shown in Fig. 4.15, bi-lateral force-position control could be running for the teleoperation system. It consists of two parallel control loop: position control loop and force control loop. On the slave side, the position control loop is formed by using the position encoder feedback from both master and slave robots and PID control method is used to drive the piezoelectric motors on slave robot. In the meantime, the other part of the bi-lateral control - force control is done on the master piezoboard. The force from FPI sensor on the slave robot and the force measured from the load cell on the master robot are sent to the master piezoboard to control the differential pneumatic valves on the master robot to apply the force feedback.

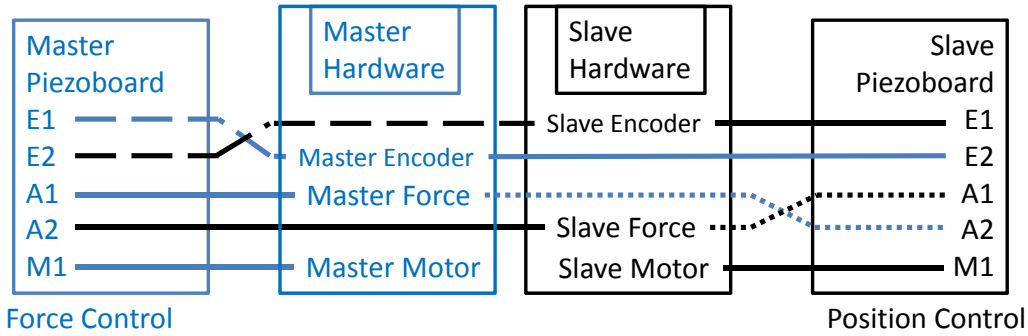


Figure 4.15: Signal diagram of the master-slave system, where solid lines show the information which is transfered and used in bi-lateral control, the dashed lines show the additional information used for impedance control, the dotted lines show the information could be potentially useful in the future for admittance control. For each piezoboard, E1 and E2 denote the encoder input channels, A1 and A2 denote the analog input channels and M1 is the motor channel.

In this case, the desired force $F_{LC}^{d}$ measured by the load cell is equal to the force measured from the FPI sensor on the slave robot which is $F_{LC}^{d} = F_{FPI}$. The actual

force $F_a$ applied in equation 4.6 is calculated by the difference from the current load cell force sensor on master and the FPI force sensor on slave.

$$\begin{cases} x_{slave} = x_{master} \\ F_a = k_B \cdot (F_{LC} - F_{LC}^d) = k_B \cdot (F_{LC} - F_{FPI}) \end{cases} \tag{4.7}$$

where $k_B$ is the scaling factor, $F_{FPI}$ is the force measured from the FPI sensor on the slave robot and $F_{LC}$ is the force measured from the load cell on the master robot. So the actual output pressure of each valve is calculated as follows:

$IfF_{FPI} \geq 0:$

$$IfF_a \geq 0, \begin{cases} P_1^d = \frac{1}{A_1}(F_{FPI} + F_a + P_{20}A_2) \\ P_2^d = P_{20} \end{cases} \tag{4.8}$$

$$IfF_a < 0, \begin{cases} P_1^d = \frac{1}{A_1}F_{FPI} + P_{10} \\ P_2^d = -\frac{1}{A_2}(F_a - P_{10}A_1) \end{cases} \tag{4.9}$$

$IfF_{FPI} < 0:$

$$IfF_a \geq 0, \begin{cases} P_1^d = \frac{1}{A_1}(F_{FPI} + F_a + P_{20}A_2) \\ P_2^d = -\frac{1}{A_2}F_{FPI} + P_{20} \end{cases} \tag{4.10}$$

$$IfF_a < 0, \begin{cases} P_1^d = P_{10} \\ P_2^d = -\frac{1}{A_2}(F_{FPI} + F_a - P_{10}A_1) \end{cases} \tag{4.11}$$

where $P_{10}$ and $P_{20}$ are initially set pressure of the two chambers.

### 4.6.2 Impedance Control

Similar to the bi-lateral control, the position of the slave robot is controlled by using the position encoder feedback from both master and slave robots and PID control method is used to drive the piezoelectric motors on slave robot. But differently, the force on the master side is controlled by the difference of the the assumed and the actual slave insertion position, as shown in equation 4.12.

$$F = k \cdot \Delta x \tag{4.12}$$

The actual impedance control for our robot is shown in equation 4.13:

$$\begin{cases} x_{slave} = x_{master} \\ F_a = F_{LC}^d = k_I \cdot (x_e - x_{slave}) \end{cases} \tag{4.13}$$

where $K_I$ is the scaling factor or the stiffness, $x_e$ is the assumed insertion position of the slave robot and $x_{slave}$ is the actual slave robot position. $x_e$ could be either from the pre-defined trajectory model or simply the current master position.

Similar to equation 4.8 - 4.11, the actual output pressure of each valve is calculated as follows:

$$IfF_a \geq 0, \begin{cases} P_1^d = \frac{1}{A_1}(F_a + P_{20}A_2) \\ P_2^d = P_{20} \end{cases} \tag{4.14}$$

$$IfF_a < 0, \begin{cases} P_1^d = P_{10} \\ P_2^d = -\frac{1}{A_2}(F_a - P_{10}A_1) \end{cases} \tag{4.15}$$

where $P_{10}$ and $P_{20}$ are initially set pressure of the two chambers.

## 4.7 Evaluation and Experimentation of The Master-Slave Teleoperation System

In order to test and evaluate the whole master-slave teleoperation system, four sets of experiments were performed on position tracking accuracy, position tracking bandwidth, force tracking bandwidth as well as position-force tracking evaluation on needle insertion with phantom. The experimental setup is shown in Fig. 4.16. From left to right in the figure are robot controller, pneumatic driving system and optic force sensing system, master robot and slave robot.

### 4.7.1 Master-Slave Position Tracking Accuracy Evaluation

The position tracking accuracy is the most critical specification of the system. As shown in Fig. 4.17, the base of the master robot was fixed on the table. The insertion axis was moved by a slider-crank mechanism which was built from acrylic by laser

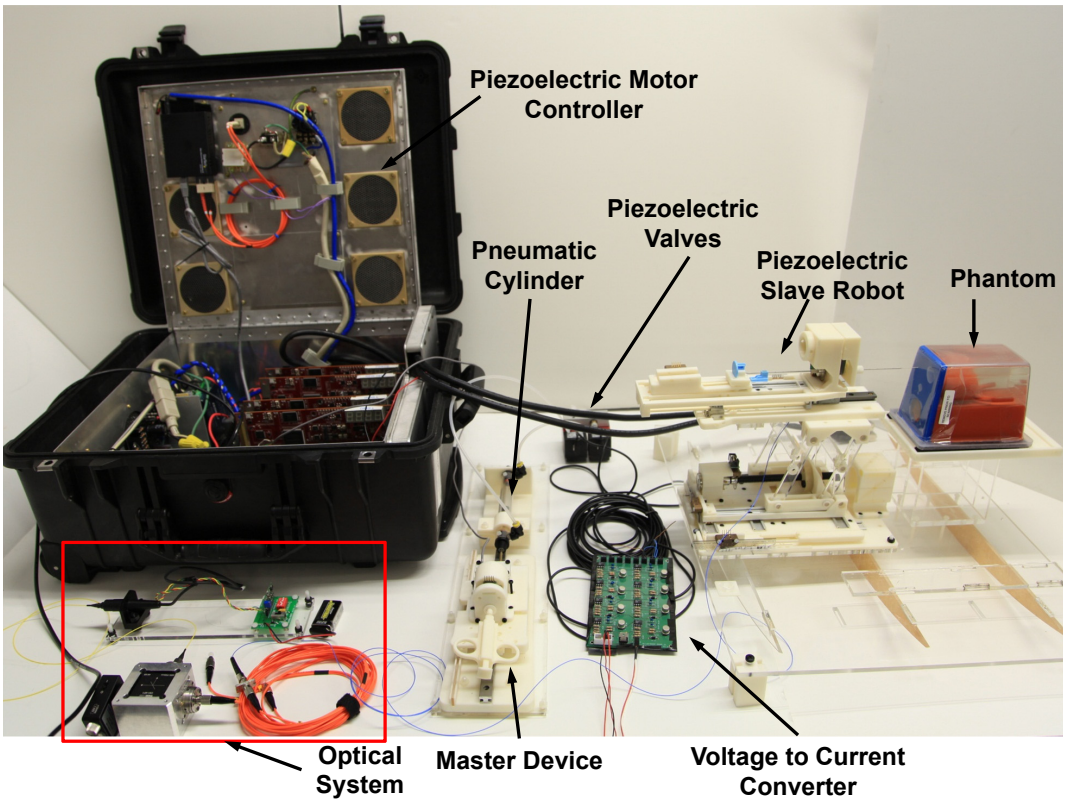


Figure 4.16: Master-slave bench-top experimental setup.

cutter. A DC motor (GM9434D812, Pittman, PA) moving at a constant rotary speed drove the master robot. The position tracking between master and slave was running at the speed of 1k Hz which is an important factor for the system's stability and transparency. As shown in Fig. 4.18, the slave robot's insertion axis tracked the master robot motion in a range of about 77.444 mm. Both of positions of the master and slave were recorded and the data sampling rate was 200 Hz, which means within 85 s of the experiment, 17,000 groups of data were collected. The overall position RMS error between the master and slave positions was 0.107 mm. The maximum error observed was 0.660 mm. The fastest tracking speed during the test was 7.618

mm/s, which was sufficient for manual needle insertion procedures.

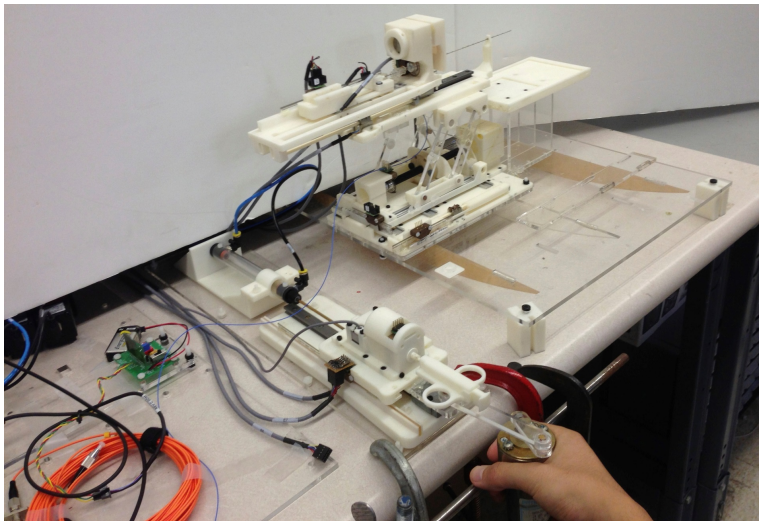

Figure 4.17: Master-slave position tracking accuracy and bandwidth experimental setup. The master robot was controlled by a DC motor with slider-crank mechanism and the slave robot follows the motion of the master robot.

### 4.7.2 Master-Slave Position Tracking Bandwidth Evaluation

As one of the dynamic properties, position tracking bandwidth is also important to our mechatronic system. A bandwidth experiment was performed with the same setup shown in Fig. 4.17. By increasing the speed of the DC motor, the speed of the master device also increased so that the position tracking performance was able to be recorded with different tracking speed. As shown in Fig. 4.19, the slave robot's insertion axis tracked the motion of the master robot in a range about 80.086 mm. During the 170 s experiment, the master's speed was increased from 2.4 mm/s to

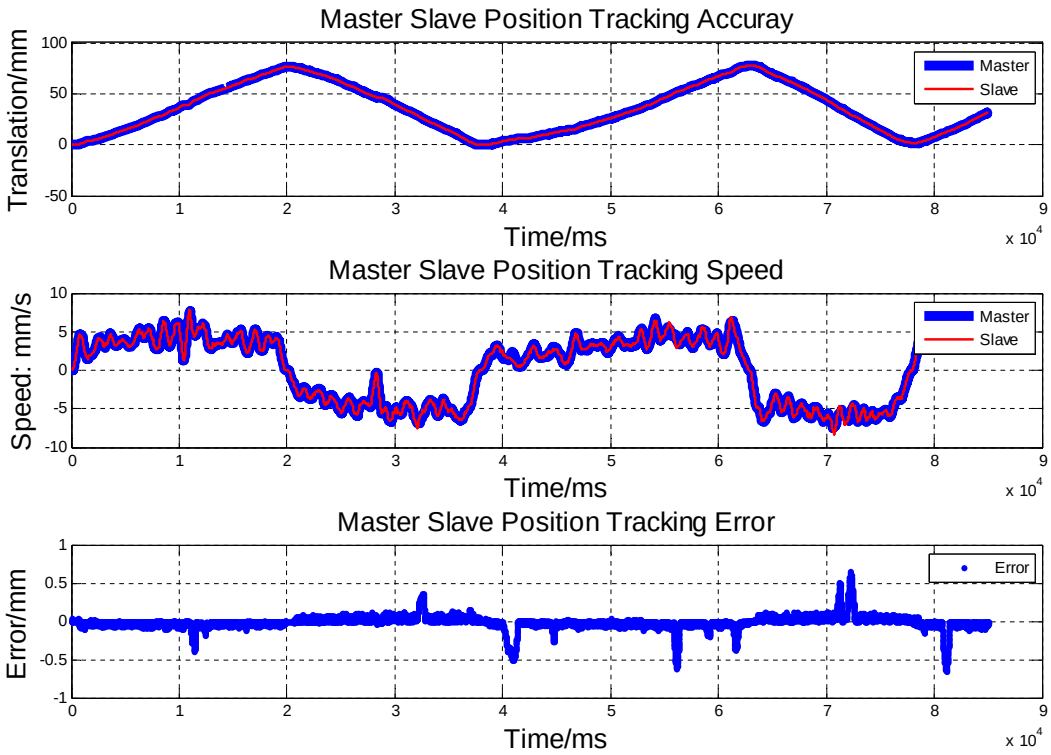


Figure 4.18: Master-slave position tracking accuracy results and its error. 17,000 groups of data were collected in 85 seconds of experiment, with an overall position tracking RMS error of 0.107 mm.

132.7 mm/s, and 34,000 groups of data were collected. The maximum points on error plot were connected for getting a better understanding of the change of error over time. The -3 dB point, which is treated as the bandwidth point, was calculated and found on the curve by linear interpolation. The tracking bandwidth was found to be 0.03 Hz with the total travel of 160.172 mm. Its corresponding speed was 4.805 mm/s.

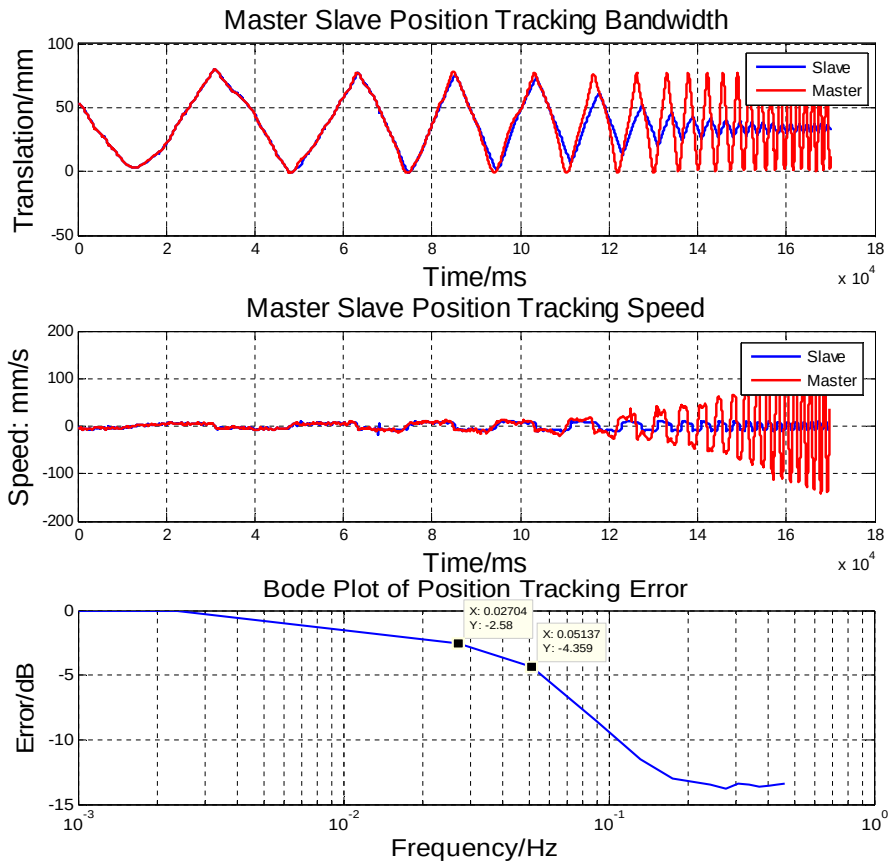


Figure 4.19: Master-slave position tracking bandwidth test results. The tracking bandwidth was found to be 0.03 Hz with the total travel of 160.172 mm. It is equivalent to 4.805 mm/s.

### 4.7.3 Master Robot Force Tracking Bandwidth Evaluation

Beside the position tracking evaluations, the force tracking was further evaluated in a benchtop setting. A force bandwidth experiment was conducted by controlling the master robot with a pre-defined force signal. The master robot was pushed against a rigid fixture to maintain solid stabilization of the biopsy needle interface. It was

commanded to track the force from a simulated FPI sensing of slave robot. As it is mentioned before, two piezoelectric valves provide pressure pushing against to each other in order to create differential force output. For the purpose of evaluation, a chirp (time varying frequency) voltage signals are used as simulated FPI reference forces. The reference chirp force signal is defined as $F^d = a\sin(2\pi ft) + b$, where $a = 7, b = 9, f = 0.01t$. Fig. 4.20 demonstrates that the tracking capability of the chirp signal as its frequency increased. The same analysis was done with force as what was done with position. From the -3 dB point on max error curve, the bandwidth frequency was found to be 5.508 Hz. We have also shown the preliminary force tracking of 1 Hz sinusoidal force signal in [22], whereas the one from [41] is much slower at 0.1 Hz with a similar tracking performance.

### 4.7.4 Master-Slave Position-Force Tracking Evaluation on Needle Insertion with Phantom

Following the individual position and force evaluations, was the phantom experiment with both position and force evaluation. As shown in Fig. 4.21, the master robot was controlled by hand, teleoperating the slave robot to insert the needle into phantom. The position and force of both master and slave were recorded to evaluate the performance of the system.

The recorded data successfully shows the whole insertion process which could be

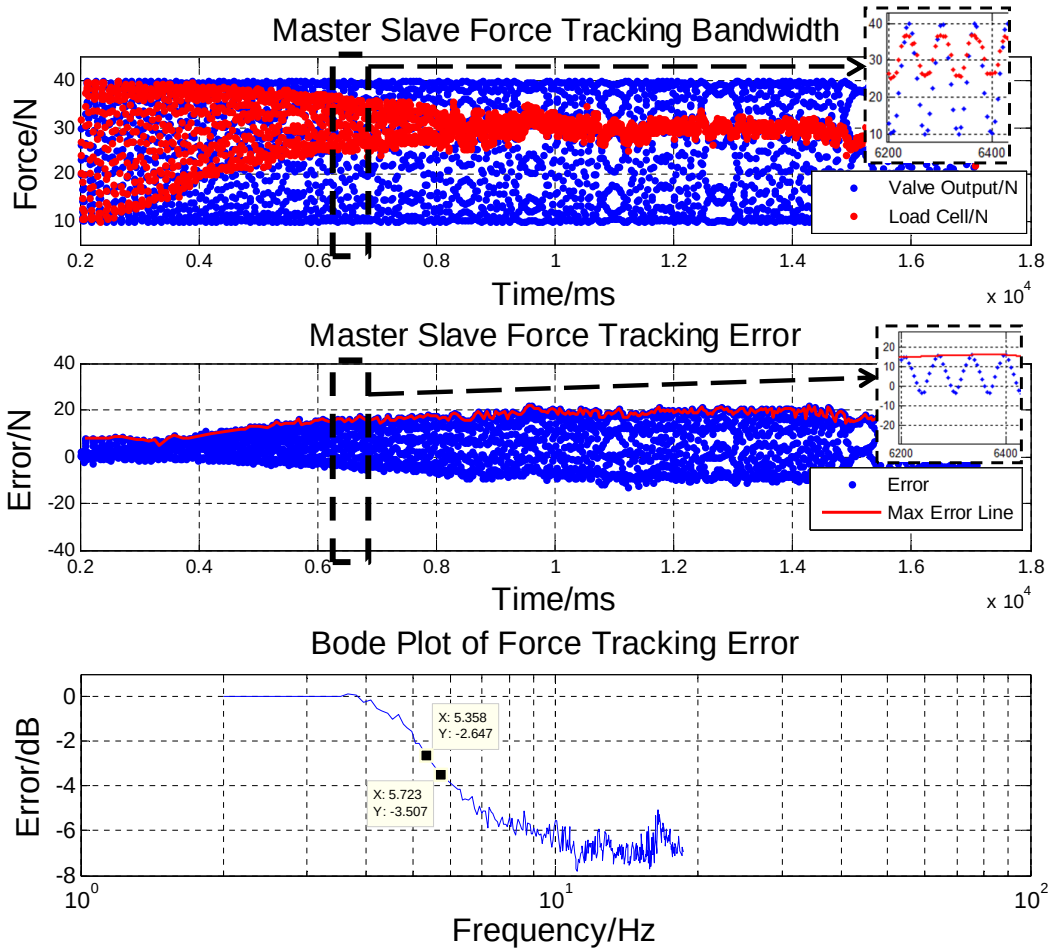


Figure 4.20: Master-slave force tracking bandwidth test results. The master robot was regulated to track a chirp signal from 1.5Hz to 18.6Hz to evaluate the bandwidth the force control system. The tracking bandwidth was found to be 5.508Hz.

demonstrated in three phases: Phase 1: Free space/pre puncture, Phase 2: Contact/deformation and Phase 3: Post puncture. In Fig. 4.22, photo a) is a shot of phase 1 in which the needle was still in free space and didn't contact with the phantom. Photo b) is a shot of phase 2 that pushed by the needle, the phantom deformed. Photo c) is a shot of phase 3 that the needle punctured into the phantom.

From the Matlab plots in Fig. 4.22 we can tell that in phase 1, the slave robot

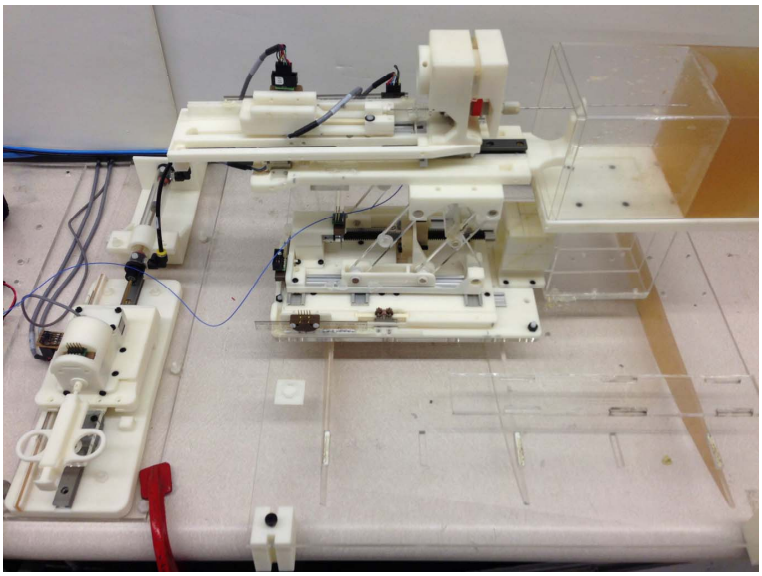

Figure 4.21: Master-slave position-force tracking phantom experiment setup. The master robot was controlled by hand, teleoperating the slave robot to insert the needle into phantom. The position and force of both master and slave were recorded to evaluate the performance of the system.

followed the master robot very well as the position RMS error was 0.0146mm, and the maximum position error was 0.0635mm. The force measured from slave robot was 0N. As it went to the phase 2, which means the needle on slave robot had contact with the phantom and started to push the surface of the phantom but not punctured through, the force measured from slave robot started to increase so that the force applied to master robot increased too. The speed of both master and slave robots was slower than phase 1, and position error between slave and master robot increased. The position RMS error in phase 2 was 0.2554mm and the maximum position error was 0.6731mm. In the last phase, the needle punctured through the surface of the phantom. The force went down, which led to a jump of position of master robot and caused a suddenly big position error of 1.0414mm. But the slave robot quickly

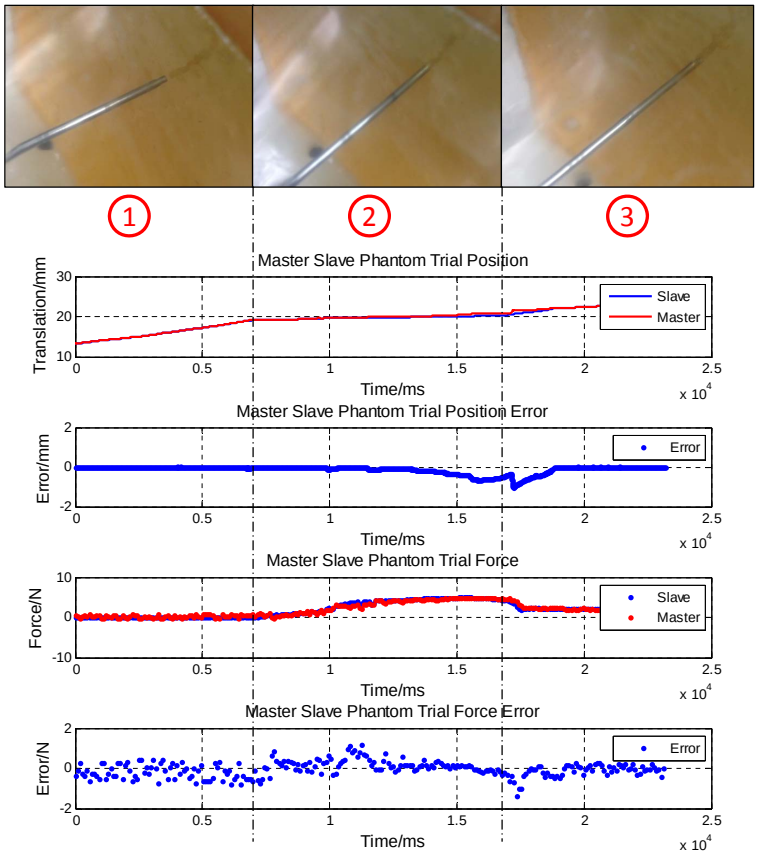


Figure 4.22: Master-slave phantom insertion results. The master robot is manually moved and the insertion axis of slave robot tracks this motion in 27.6 seconds with 0.318 mm RMS error.

followed up with master robot and lowered the RMS error to 0.0143mm.

## 4.8 MRI-Compatibility Evaluation

The effects of device to the MR image quality is evaluated in the following two ways:

1) Signal-to-noise ratio (SNR) based on the National Electrical Manufacturers Association (NEMA) standard MS1-2008 [136].

There are several setup requirements need to meet: The specification volume (or

imaging volume) must be at least $20cm \times 20cm$ with RF body coil. At least a 10 centimeter diameter circle should be signal-producing volume of the phantom. $T1 < 1200ms$, $T2 > 50ms$ for the imaging protocols. An example image is shown in Fig.4.23. The red square indicates the sample region for signal and the blue square indicates the sample region for noise.

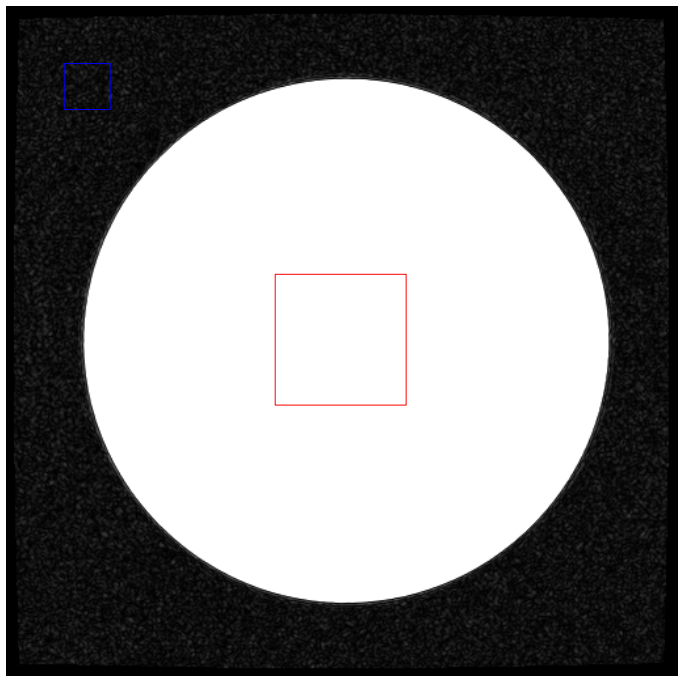

Figure 4.23: SNR calculation method: The comparison of the red square which indicates the sample region for signal and the blue square which indicates the sample region for noise.

And the actual calculation is based on the following equations:

$$Mean(Noise) = \frac{Mean(R_{background})}{1.25} \tag{4.16}$$

$$SNR = \frac{Mean(Signal)}{Mean(Noise)} \tag{4.17}$$

Where $Mean(Noise)$ is the average intensity of the noise, $Mean(R_{background})$ is the average intensity of the region within the blue square on the background. The denominator of 1.25 is from equation 8 in [136]. Mean(Signal) is the average intensity of the signal which is inside the red square. SNR is the calculated signal to noise ratio.

2) Geometric Distortion based on the NEMA standard (MS2-2008) [132].

In addition to the image signal intensity analysis, distortion analysis is also needed for evaluating the geometric effects. As shown in Fig. 4.24, the small circles mark the position of pins in the phantom. Each red line connects a pair of pins for measuring. There are totally eight pairs of pins used.

The actual calculation is based on the comparison of the measured distance on image and the actual phantom distance between a pair of the pins.

$$D = Max\{100 \times \frac{|L_m - L_a|}{L_a}\} \tag{4.18}$$

Where $L_m$ is the distance measured on image, $L_a$ is the actual phantom distance, $D$ is the geometric distortion. In the real case, no matter how many images are taken for each sequence, the geometric distortion $D$ is the maximum percentage difference among all those images.

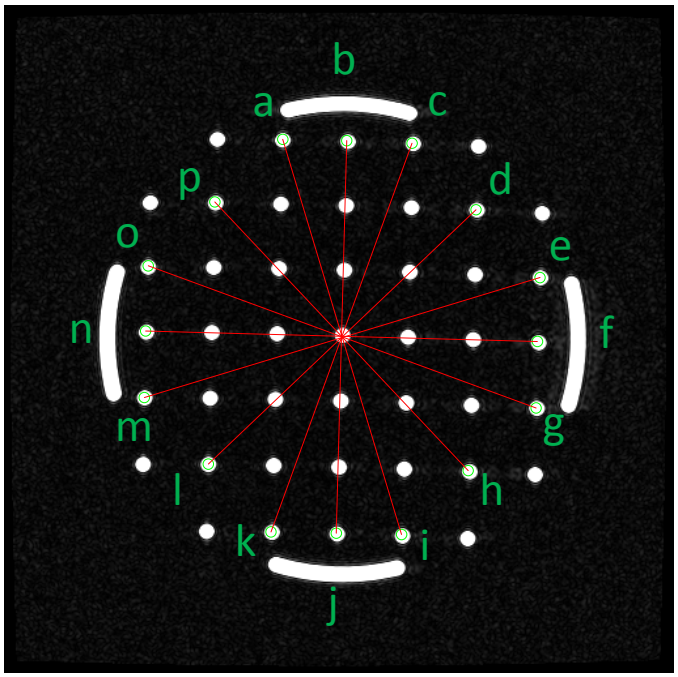


Figure 4.24: Distortion calculation method: The small circles mark the position of pins in the phantom. Each red line connects a pair of pins for measuring. There are totally eight pairs of pins used which are: ai, bj, ck, dl, em, fn, go, hp.

The tests are done with a Philips Achieva 3-Tesla MRI system with 60 cm bore size. The controller is placed approximately 2 meters away from the scanner bore inside the scanner room. Fig. 4.25 shows the system setup.

A Periodic Image Quality Test (PIQT) phantom (Philips, Netherlands) is used. As shown in Fig. 4.26, it has complex geometric features, including uniform cylindrical cross section, and arch/pin section. It has a diameter of about 187 mm. The uniform cylindrical cross section is used for calculation of SNR, and the pin section is used to calculate the distortion.

Totally nine configurations are tested:

1- Baseline: Only the PIQT phantom is inside the scanner. A qualitative image set


Figure 4.25: MRI-compatibility experiment setup.

is acquired to evaluate the image interference and this premise is repeated for every session of the experiment.

2- Baseline again: the same as configuration 1 as a precaution imaging.

3- Robot only: the robot is placed 5mm apart from the phantom but not connected to the controller which is still outside the room.

4- Robot and controller (not powered): the controller is placed inside the MRI room by connecting all wires and cables to the robot but everything is still kept unpowered.

5- Robot and controller (not powered) again: the same as configuration 4 as precaution imaging.

6- Robot and controller (Powered, E-stop ON): the controller is now powered ON but the motors still have no power and no motion since the E-stop is ON.

7- Controller (Powered, E-stop OFF): motor power is enabled by turning off the E-stop but the motors are not in motion.

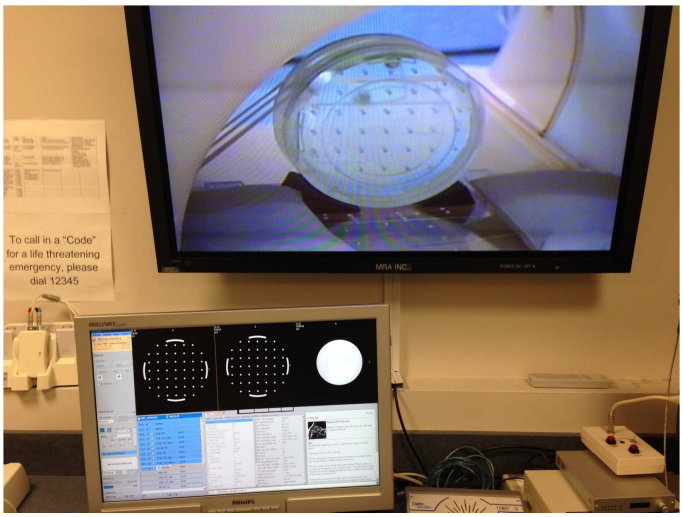


Figure 4.26: Periodic Image Quality Test phantom with univorm cylindrical cross section and pin section.

8- During the Motion: motors are kept running until the MR images are entirely acquired.

9- Baseline again: the same as configuration 1 and 2. The baseline is taken again in the end to make sure the environment doesn't change during the whole experiment.

Each configuration is also imaged with four protocols which are typical for prostate imaging. a) T1-weighted FFE with fat selective per pulse for z-frame image; b) T2-weighted 2D Turbo Spin Echo for initial scan; c) T2-weighted 2D Turbo Spin Echo for needle confirmation image; and d) Balanced FFE sequence for real-time imaging for needle guidance. The detailed parameters for each protocol are shown in Table 4.1 on page 170.

Table 4.1: Detailed scan parameters for each of four protocols for compatibility evaluation

| Protocol | TE (ms) | TR (ms) | FA (deg) | Slice thickness (mm) | FOV (mmxmm) | Pixel size (mmxmm) | Bandwidth (Hz/pixel) |
|---|---|---|---|---|---|---|---|
| T1-weighted FFE | 2.02 | 12 | 75 | 2 | 256x256 | 0.5x0.5 | 399 |
| T2-weighted 2D TSE, initial scan | 100 | 4800 | 90 | 3 | 256x240 | 0.5x0.5 | 203 |
| T2-weighted 2D TSE, needle | 106 | 3030 | 90 | 3 | 256x243 | 0.5x0.5 | 260 |
| Balanced FFE, real-time | 1.98 | 3.96 | 10 | 5 | 256x230 | 0.98x0.98 | 908 |

### 4.8.1 SNR

The uniform cylindrical cross section of the PIQT phantom is used for calculation of SNR. As introduced in equation 4.17 in Section 4.2.2 that signal and background (noise) areas are sampled separately but compared with each other to calculate the SNR. The size of signal sample area (red square) is $50 \times 50$ pixel, and for noise sample area (blue square) is: $35 \times 35$ pixel. The example MR images for each configuration and each protocol are listed in Table 4.2 on page 171.

Table 4.3 - 4.6 from page 172 list the normalized SNR data for five images of each of four protocols and nine configurations.

Correspondingly, Fig. 4.27 - 4.30 show the normalized SNR boxplots of each configuration with the same imaging protocol. Each box includes the data from five images, all normalized to the first configuration - baseline. On each box, the black star is the average, the red central line is the median, the edges of the box are the 25th and 75th percentiles, the whiskers extend to the most extreme data points not considered

Table 4.2: Example MR images for each configuration and each protocol for SNR evaluation.

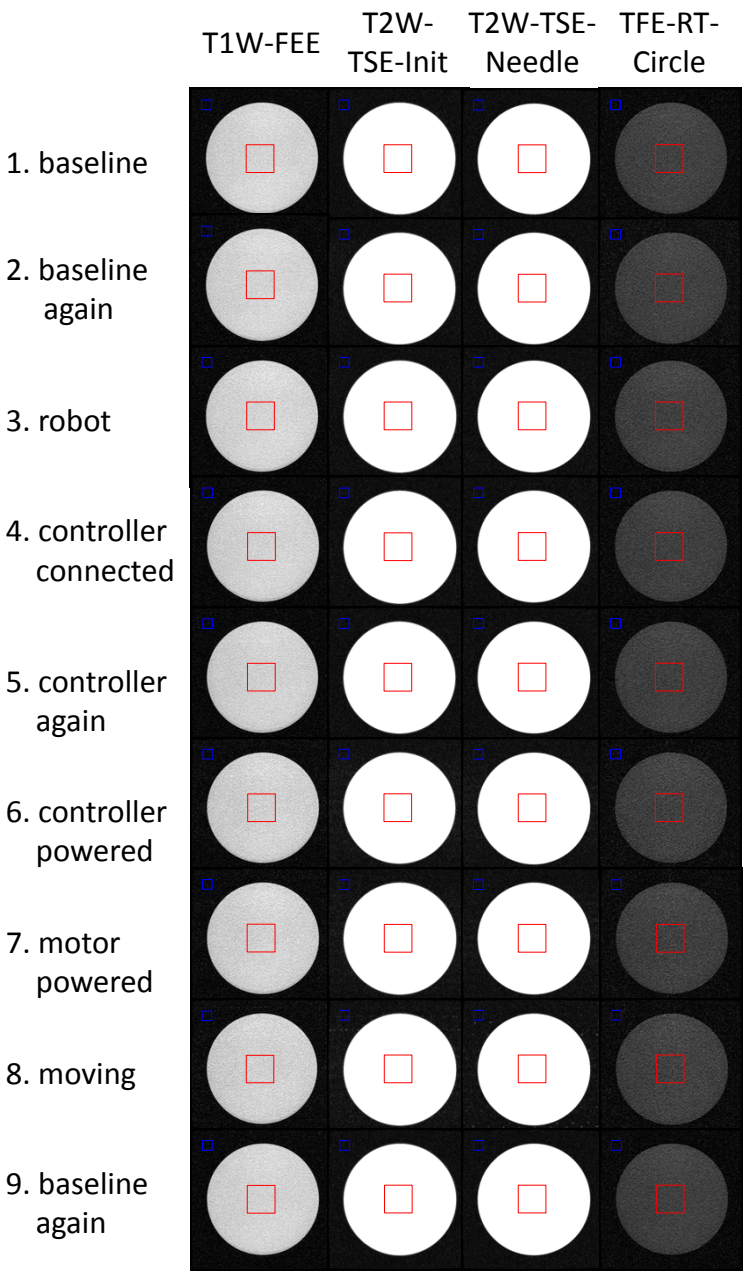

Table 4.3: Normalized SNR of five images for each configuration with protocol T1W_FFE.

| 1. baseline | 2. baseline again | 3. robot | 4. controller connected | 5. controller again | 6. controller powered | 7. motor powered | 8. moving | 9. baseline again |
|---|---|---|---|---|---|---|---|---|
| 0.9852 | 0.8780 | 0.9911 | 0.8997 | 0.8920 | 0.8805 | 0.8707 | 0.8469 | 0.8404 |
| 0.9562 | 1.1005 | 0.9374 | 0.9752 | 0.9913 | 0.8246 | 0.9182 | 0.8307 | 0.9833 |
| 0.9611 | 0.9428 | 0.9275 | 0.9671 | 0.9844 | 0.8593 | 1.0010 | 0.7848 | 0.9699 |
| 1.0980 | 0.9887 | 1.0363 | 0.9642 | 0.9549 | 0.9225 | 0.8902 | 0.9006 | 1.0189 |
| 0.9994 | 1.0391 | 1.0280 | 0.9469 | 1.0220 | 0.8413 | 0.8787 | 0.8779 | 1.0300 |

Table 4.4: Normalized SNR of five images for each configuration with protocol T2W_TSE_Init.

| 1. baseline | 2. baseline again | 3. robot | 4. controller connected | 5. controller again | 6. controller powered | 7. motor powered | 8. moving | 9. baseline again |
|---|---|---|---|---|---|---|---|---|
| 0.9363 | 0.9775 | 0.9579 | 0.9774 | 0.9564 | 0.8005 | 0.8374 | 0.7832 | 0.9775 |
| 0.9585 | 0.9966 | 0.9911 | 1.0507 | 0.9521 | 0.8598 | 0.8992 | 0.8335 | 0.9907 |
| 1.0760 | 0.9869 | 0.9848 | 0.9567 | 1.0151 | 0.8336 | 0.8950 | 0.8236 | 1.0390 |
| 1.0104 | 1.0635 | 1.0015 | 1.0568 | 0.9996 | 0.8772 | 0.8937 | 0.8260 | 1.0578 |
| 1.0187 | 1.0056 | 1.0009 | 0.9857 | 0.9453 | 0.8835 | 0.8872 | 0.8628 | 0.9831 |

Table 4.5: Normalized SNR of five images for each configuration with protocol T2W_TSE_Needle.

| 1. baseline | 2. baseline again | 3. robot | 4. controller connected | 5. controller again | 6. controller powered | 7. motor powered | 8. moving | 9. baseline again |
|---|---|---|---|---|---|---|---|---|
| 0.9170 | 0.9200 | 0.9056 | 0.9646 | 0.9136 | 0.8607 | 0.8859 | 0.8994 | 0.9409 |
| 0.9747 | 0.9775 | 1.0188 | 0.9776 | 0.9721 | 0.8724 | 0.9206 | 0.8650 | 0.9567 |
| 1.0637 | 0.9748 | 0.9798 | 0.9301 | 1.0218 | 0.8316 | 0.9510 | 0.9169 | 1.0318 |
| 1.0255 | 1.0030 | 0.9829 | 0.9691 | 1.0308 | 0.9117 | 0.9336 | 0.8492 | 0.9833 |
| 1.0190 | 0.9645 | 0.9812 | 0.9441 | 0.9922 | 0.8721 | 0.9193 | 0.8612 | 0.9755 |

outliers, and outliers are plotted individually.

For all four protocols, the SNR of 1-baseline, 2-baseline again and 9-baseline again are all at the same level, which is close to one. It means that the whole environment

Table 4.6: Normalized SNR of five images for each configuration with protocol TFE_RT_Circle.

| 1. baseline | 2. baseline again | 3. robot | 4. controller connected | 5. controller again | 6. controller powered | 7. motor powered | 8. moving | 9. baseline again |
|---|---|---|---|---|---|---|---|---|
| 1.0697 | 1.1148 | 1.0548 | 0.9675 | 0.8922 | 0.8268 | 0.7970 | 0.9713 | 0.8833 |
| 0.9687 | 0.9322 | 0.9472 | 0.9757 | 0.5285 | 0.8486 | 0.7991 | 0.9930 | 1.0874 |
| 1.0322 | 0.9721 | 1.0074 | 1.1058 | 0.9659 | 0.8845 | 0.9602 | 0.9648 | 1.2393 |
| 1.0305 | 0.9900 | 1.0894 | 1.0122 | 0.9956 | 0.9380 | 0.8756 | 0.9432 | 1.1046 |
| 0.8989 | 1.0382 | 0.9971 | 0.9637 | 0.9486 | 0.9231 | 0.8668 | 0.9384 | 1.2098 |

stays the same throughout the experiment. This gives the basic ground truth of data from other six configurations.

For the first protocol - T1W FFE, the result of which is shown in Fig. 4.27 and Table 4.3 on page 172. There is a 5% SNR drop when the controller is placed in the scanner room, and about 15% SNR decrease when the motor is powered and moving comparing to the baseline.

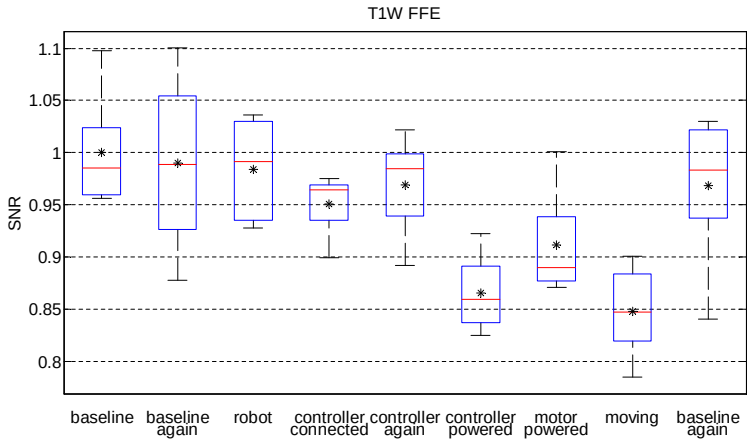


Figure 4.27: Normalized SNR boxplot of each configuration with protocol T1W_FFE.

The second protocol is T2W TSE Initial, the result of which is shown in Fig. 4.28

and Table 4.4 on page 172. The SNR drop when the controller is placed in the scanner room is less than 5%, and the SNR of three configurations of 6-controller powered, 7-motor powered and 8-motor moving are on the similar level of 15% decrease with a worst value of 21.68% comparing to the baseline.

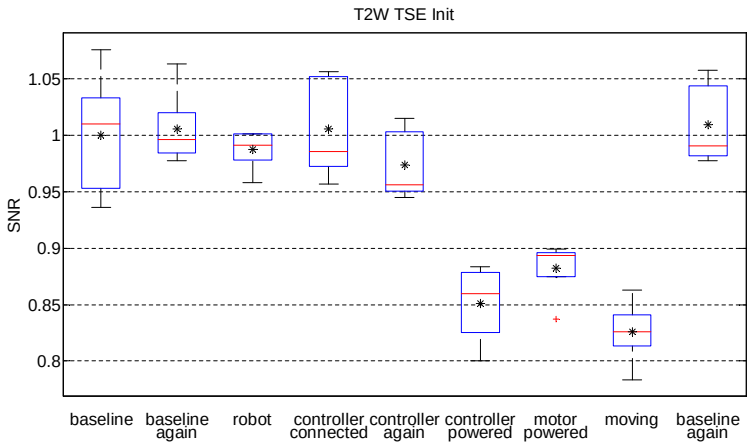


Figure 4.28: Normalized SNR boxplot of each configuration with protocol T2W_TSE_Init.

The result of third protocol - T2W TSE Needle is shown in Fig. 4.29 and Table 4.5 on page 172. It is similar to the second protocol with the average SNR drop of first five configurations of 5%, and which of 6-8 configuration of 14%, with the worst value of 16.84% comparing to the baseline.

The fourth protocol is a real-time imaging protocol the result of which is shown in Fig. 4.30 and Table 4.6 on page 173. It uses much lower flip angle than the former three protocols that result in a much faster imaging speed but also much lower imaging resolution. The SNR data also behaves different from other three protocols. Since the background noise is higher, the noise introduced by controller and motor is not

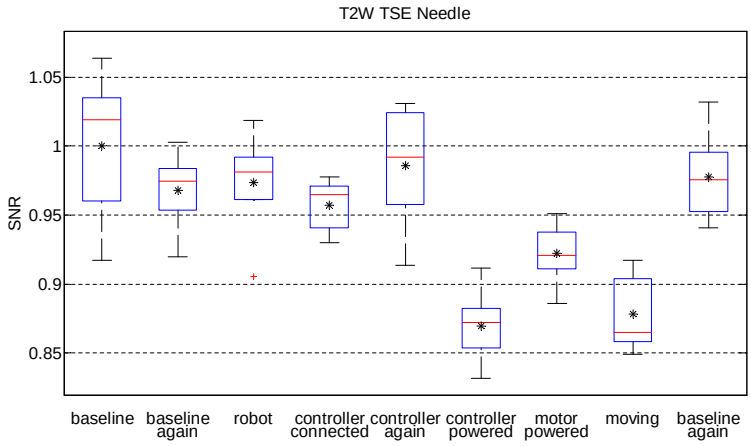


Figure 4.29: Normalized SNR boxplot of each configuration with protocol T2W_TSE_Needle.

as significant as other protocols. Except one outlier, the worst SNR drop in all nine configurations is 13.34%, with an average SNR drop of just 11.58%.

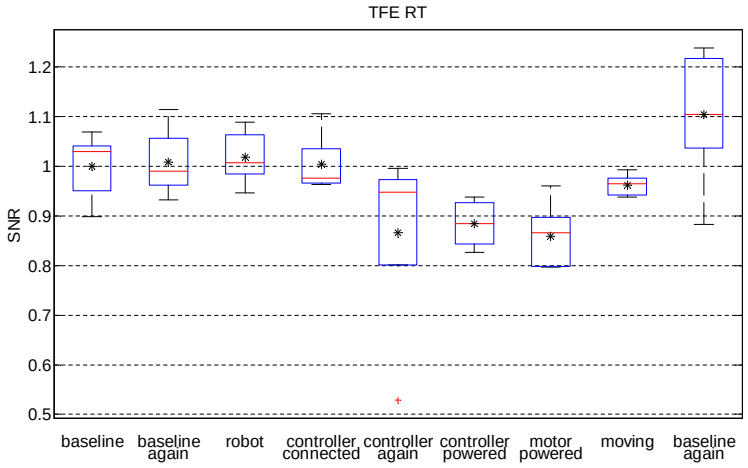


Figure 4.30: Normalized SNR boxplot of each configuration with protocol TFE_RT_Circle.

One observation found in the first three protocols is that the SNR of when the motor is powered is slightly better than the SNR of when the controller is powered but motor is not. The reason could be that when the motor is not powered, the wires

are floating that could generate noise. When it is powered, which means that all the wires are connected to the controller. Although they have no driving signal, they are no longer floating. The noise could be potentially reduced because of that. This doesn't show with the last real-time protocol because the image resolution is not high enough to distinguish this SNR difference.

### 4.8.2 Distortion

As shown in Fig. 4.24, seven pairs of pins are used to calculate the distortion. The actual phantom dimension $L_a$ of each pair is shown in Table. 4.7 on page 176. The example MR images for each configuration and each protocol are listed in Table 4.8 on page 177.

Table 4.7: The actual phantom dimension $L_a$ of each pair of pins used to calculate the distortion.

| Segment | ai | bj | ck | dl | em | fn | go | hp |
|---|---|---|---|---|---|---|---|---|
| Distance/mm | 158.11 | 150.00 | 158.11 | 141.42 | 158.11 | 150.00 | 158.11 | 141.42 |

Based on Equation 4.18 and Table 4.7 on page 176, the distortion percentage of each configuration and each protocol are calculated. As the definition of distortion requires the maximum percentage, all the available images for each configuration and each protocol are calculated separately and the maximum distortion is listed in Table 4.9 on page 178. For T1W_FFE, T2W_TSE_Init, T2W_TSE_Needle and TFE_RT_Circle, 5, 4, 4 and 40 images are used for each configuration respectively.

Table 4.8: Example MR images for each configuration and each protocol for distortion evaluation.

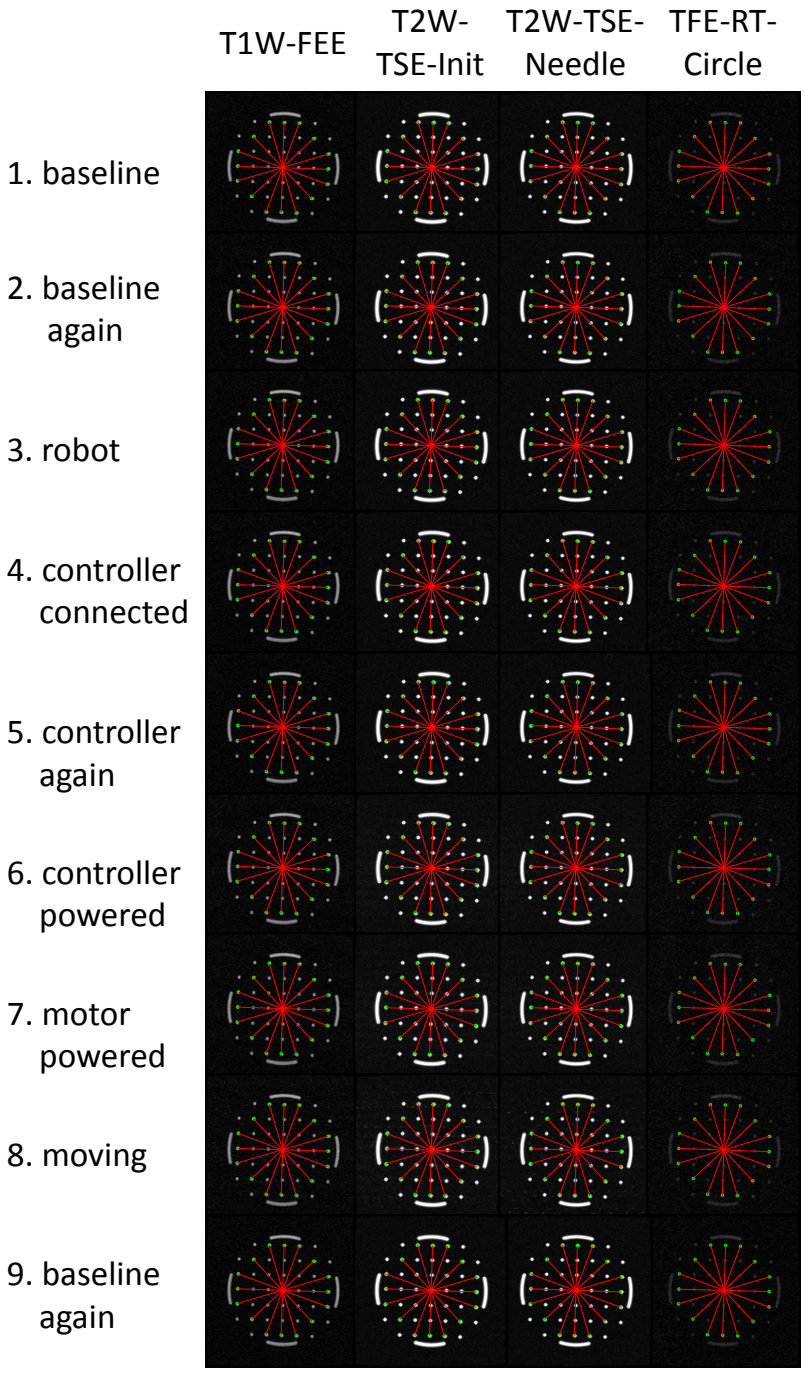

Table 4.9: Maximum distortion for each configuration and each protocol.

| Max Distortion % | T1W_FFE | T2W_TSE _Init | T2W_TSE _Needle | TFE_RT_ Circle |
|---|---|---|---|---|
| 1. baseline | 0.4293 | 0.2079 | 0.2079 | 0.7486 |
| 2. baseline again | 0.3776 | 0.2079 | 0.2236 | 0.7761 |
| 3. robot | 0.2938 | 0.7229 | 0.6737 | 0.7283 |
| 4. controller connected | 0.2565 | 0.7162 | 0.6897 | 0.6914 |
| 5. controller again | 0.2990 | 0.6897 | 0.5628 | 0.8556 |
| 6. controller powered | 0.3060 | 0.7138 | 0.6883 | 0.7713 |
| 7. motor powered | 0.2434 | 0.7138 | 0.6350 | 0.8542 |
| 8. moving | 0.3381 | 0.6907 | 0.5880 | 0.9150 |
| 9. baseline again | 0.4606 | 0.2008 | 0.2085 | 0.7044 |

As it is shown in the Table 4.9 on page 178, firstly, the distortion data for configuration 1, 2 and 9 is on the same level which means that the environment doesn't change during the whole experiment so that the result is reliable. All the max distortions for each configuration and each protocol are less than 1%. This analysis demonstrates negligible geometric distortion of the acquired images due to the robot running during imaging.

## 4.9 Teleoperated Needle Insertion under Live MRI

Fig. 4.31 illustrates the teleoperation system setup with a Philips 3 Tesla MRI inside the scanner room. The slave robot with gelatin phantom will be at the iso-center of the scanner. Master robot is also on the patient bed but out of the imaging area. The robot controller is about 2m away from the scanner. The controller and master-slave robots are connected electronically and pneumatically.

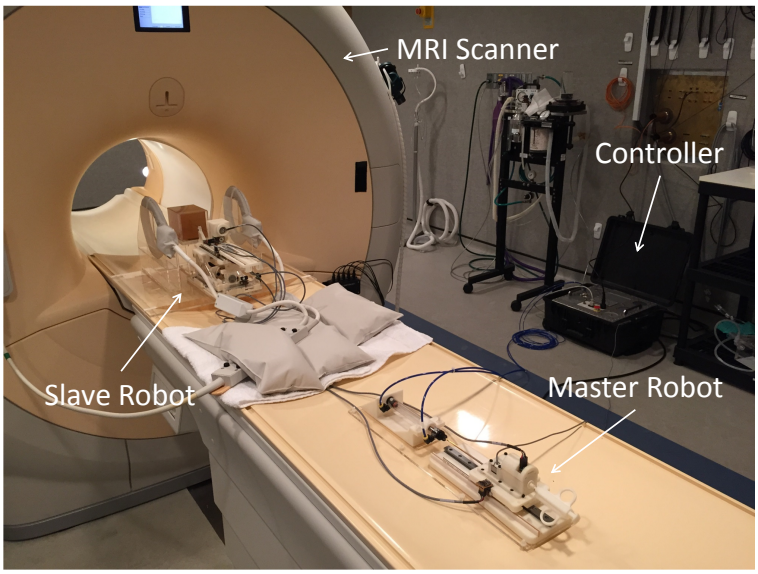


Figure 4.31: MRI-compatible teleoperation system setup with a Philips 3 Tesla MRI scanner.

Outside of the scanner room, three computers are used for controlling the robotic system which is shown in Fig. 4.32 in the console room. One computer runs the robot teleoperation control software which is discussed in section 2.4. Other two laptops run the real-time needle tracking/scanner control software and the needle steering

Matlab algorithm [130].

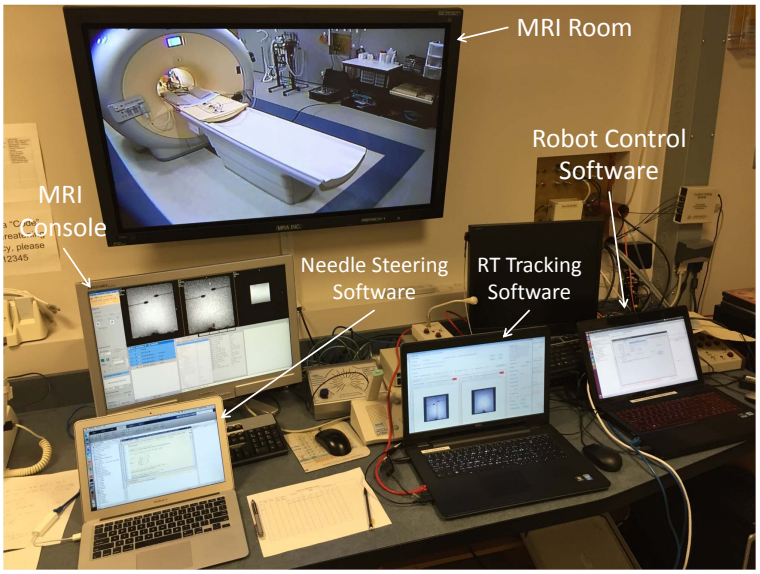


Figure 4.32: System setup in the console room: Three laptops are running robot control application, real-time needle tracking application and needle steering Matlab algorithm separately.

Four experiments have been done to demonstrate the teleoperation inside the MRI room with real-time imaging. They are:

1) Teleoperation with autonomous needle steering with single target;

2) Teleoperation with autonomous needle steering with two targets;

3) 2-DOF teleoperated needle steering;

4) Needle insertion with force feedback.

The real-time MRI acquisition protocol is Spoiled Gradient Echo sequence T1-FFE (Fast Field Echo) to obtain MR images in either sagittal or coronal plane with the approximate speed of 750 ms, TR = 6.93 ms, TE = 3.37 ms, Flip angle = 5°, slice thickness = 10 mm, image size = 288 mm × 288 mm, pixel resolution = 0.382 mm

$\times$ 0.382 mm.

### 4.9.1 Teleoperated Needle Steering

Two different approaches have been done for the teleoperated needle steering experiments: 1. teleoperation with autonomous needle steering and 2. 2-DOF teleoperated needle steering. A bevel-tipped flexible nitinol needle with a diameter of 0.7 mm (22G) and a tip angle of 30° is used in both studies.

#### 4.9.1.1 Teleoperation with Autonomous Needle Steering

The first approach is the teleoperation with autonomous needle steering. It is a collaborated work in our lab. In this approach, the insertion of the needle is done teleoperatedly by the user. The steering of a bevel-tipped needle is done in closed-loop with a real-time autonomous needle tracking system. As the needle is being inserted into the phantom, a software is used to track the needle tip position in real-time and calculate the current needle shape base on the previously stored needle tip positions. Then, by using these information, the MRI scan plane is control to maintain the needle tip always visible during the insertion which is essential for tracking the needle tip. Meanwhile, another software calculate the desired steering angle by comparing the current needle tip position and orientation to the target position, and control the robot with the steering through OpenIGTLink.

To the best of our knowledge, this is the first time that MR-guided teleoperation

with autonomous needle steering is performed. As a separate research topic, needle steering is being researched by my colleagues in the lab. Because the focus of this experiment is to demonstrate teleoperation, please refer to [130] for more details about the needle steering.

Two experiments are performed for teleoperation with autonomous needle steering: single target (C curve) and double targets (S curve).

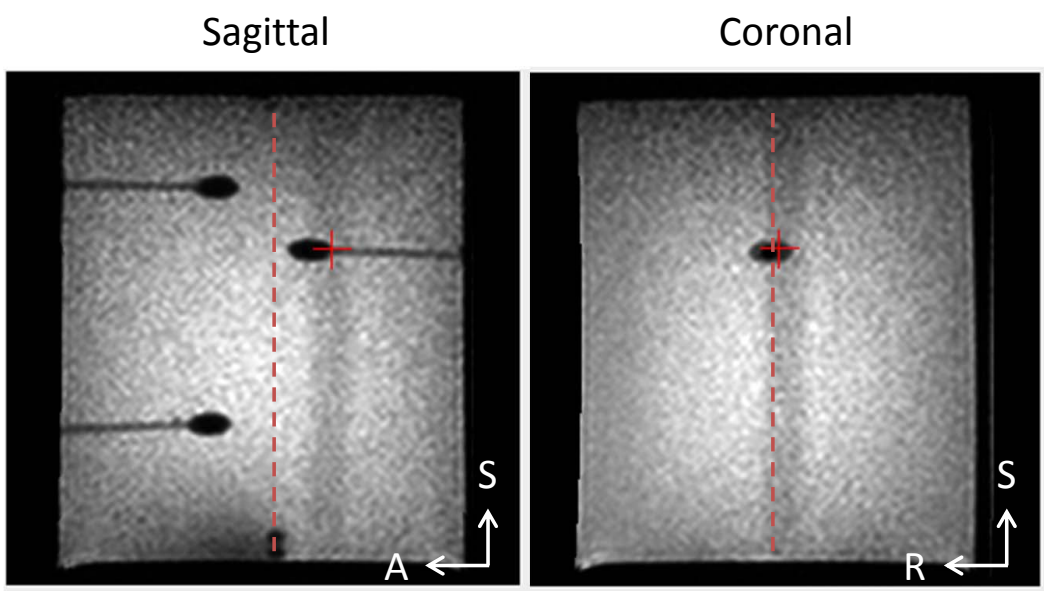


Figure 4.33: Target(red cross) [12.86,58.326, -26.22] (in RAS) is selected before inserting the needle. The initial needle tip position is [13.25,46.87,37.57] (in RAS). Red dashed line indicates the initial needle orientation.

A gelatin phantom is made with three embedded targets (Fig. 4.33 on page 182), two of which are in a line. The other is a single target on the other side.

Fig. 4.33 shows the images of the needle tip and target before insertion. The red dashed line indicates the initial needle orientation and the initial position of the needle tip is [12.86,58.326, -26.22] (in RAS). The red cross is the single target selected in

advance which is [13.25,46.87,37.57] (in RAS). The offset of the needle from the initial position to target is 0.39 mm in R direction and -11.456 mm in A direction.

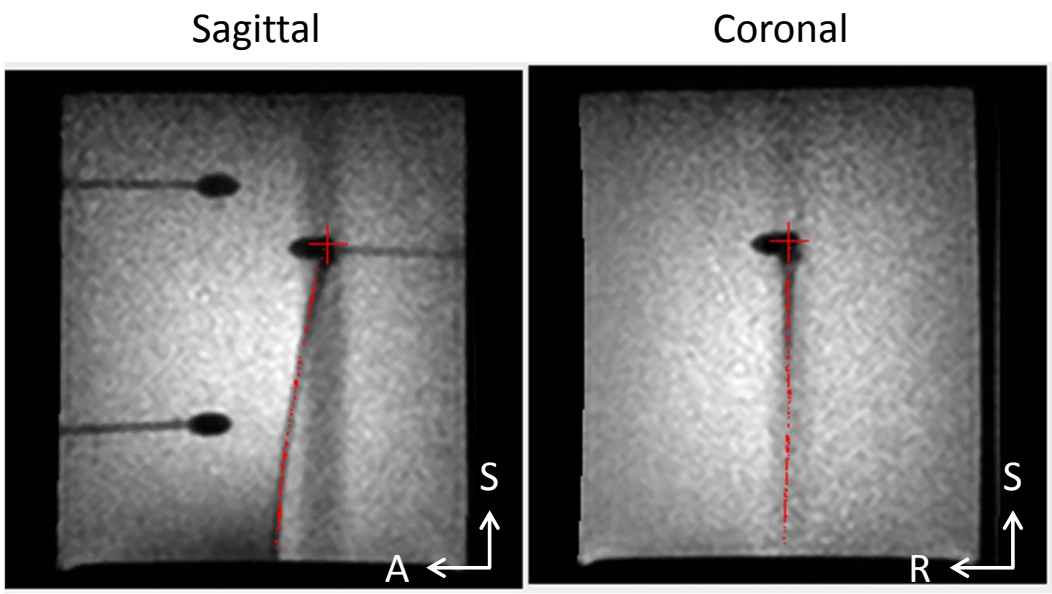


Figure 4.34: Final trajectory of the teleoperated needle steering: Red dots indicate the trajectory of the needle. The final tip position shown as red cross is [11.72,48.39,37.19] (in RAS). The tip error in 3D space is 2.19 mm.

The final images shown in Fig. 4.34 on page 183 and its Matlab plot is shown in Fig. 4.35 on page 184. The needle successfully turned towards the target in sagittal plane and kept straight in coronal plane. The final tip position shown as red cross is [11.72,48.39,37.19] (in RAS). The tip error in 3D space is 2.19mm.

Similar to the previous experiment, Fig. 4.36 on page 185 shows the images of the needle tip and targets before the double target insertion. The red dashed line indicates the initial needle orientation and the initial position of the needle tip is [12.05,59.51, -36.18] (in RAS). The red circle indicates the intermediate target selected next to the obstacle which is in order to be avoided and it is [15.10,59.12, -11.35] (in RAS). The

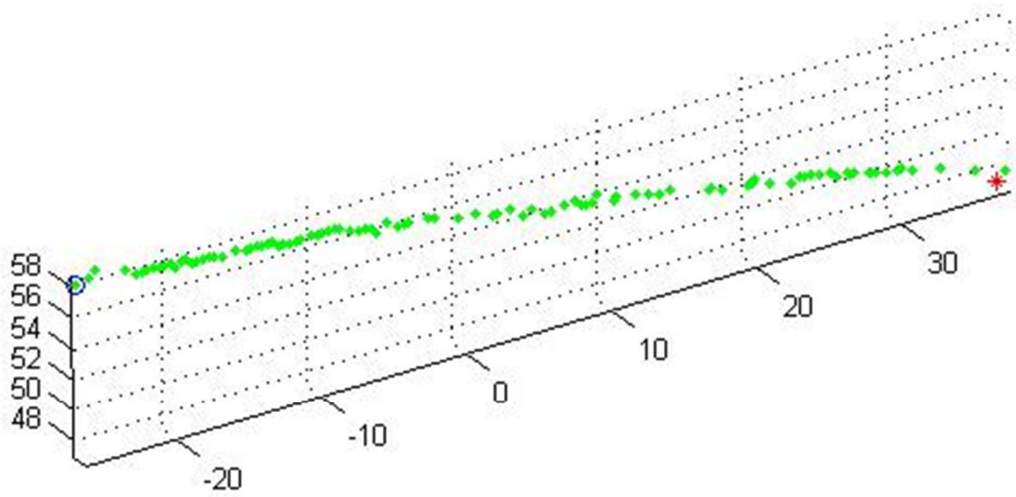


Figure 4.35: Matlab plot of the final needle trajectory (single target): blue circle is the initial starting point of the needle tip, red dots indicate the intermediate needle tip positions, red star indicates the pre-selected target.

red cross is the final target selected in advance which is [12.04,59.12, 39.08] (in RAS). The offset of the needle from the initial position to the first target is 3.05 mm in R direction and -0.39 mm in A direction. The offset of the needle tip from the first target to the second-3.06 target is -3.05 mm in R direction and 0mm in A direction.

The final images are shown in Fig. 4.37 on page 186 and its Matlab plot is shown in Fig. 4.38 on page 187. Although the needle didn't hit the first target, which is not required, it did successfully turn to avoid the obstacle which is desired. The needle later turned back towards the target successfully in sagittal plane. The final tip position shown as red cross is [12.81,57.598, 38.314] (in RAS). The tip error in 3D space is 1.87 mm.

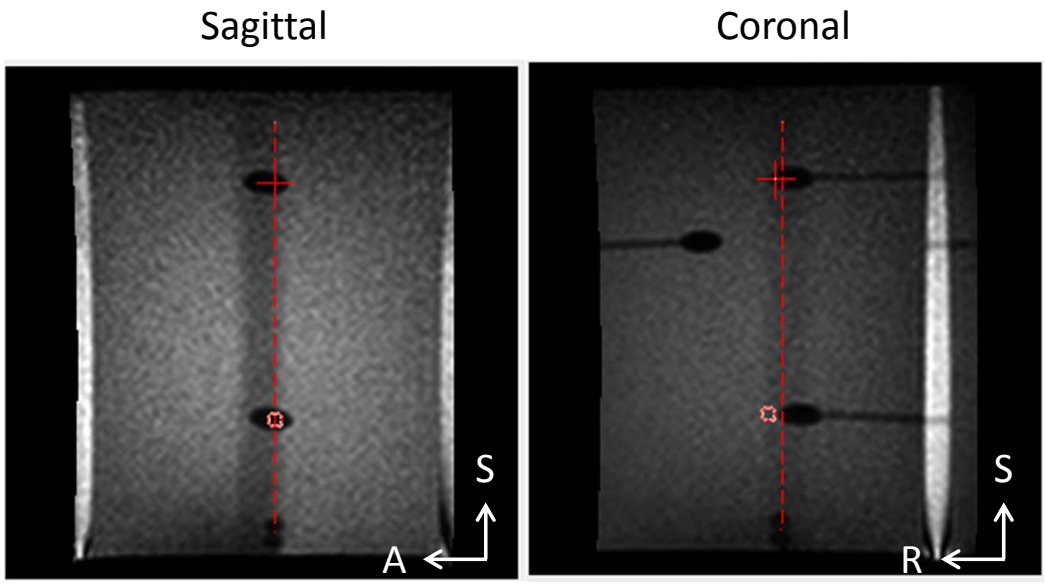


Figure 4.36: The red dashed line indicates the initial needle orientation and the initial position of the needle tip is [12.05,59.51, -36.18] (in RAS). The red circle indicates the intermediate target selected next to the obstacle which is in order to be avoided and it is [15.10,59.12, -11.35] (in RAS). The red cross is the final target selected in advance which is [12.04,59.12, 39.08] (in RAS). Red dashed line indicates the initial needle orientation.

#### 4.9.1.2 2-DOF Teleoperated Needle Steering

As mentioned in the beginning, the second approach of teleoperated needle steering is 2-DOF teleoperation. Instead of autonomous steering, the rotation is also with teleoperated control by the master device. Fig. 4.39 on page 188 shows the images of the needle tip and targets before the double target insertion. The red dashed line indicates the initial needle orientation. The red cross is the same target selected in the previous teleoperation with autonomous steering experiment just for the purpose of illustration. The final target is selected mentally and there is no intermediate target selected because the direction of the needle is controlled by user.

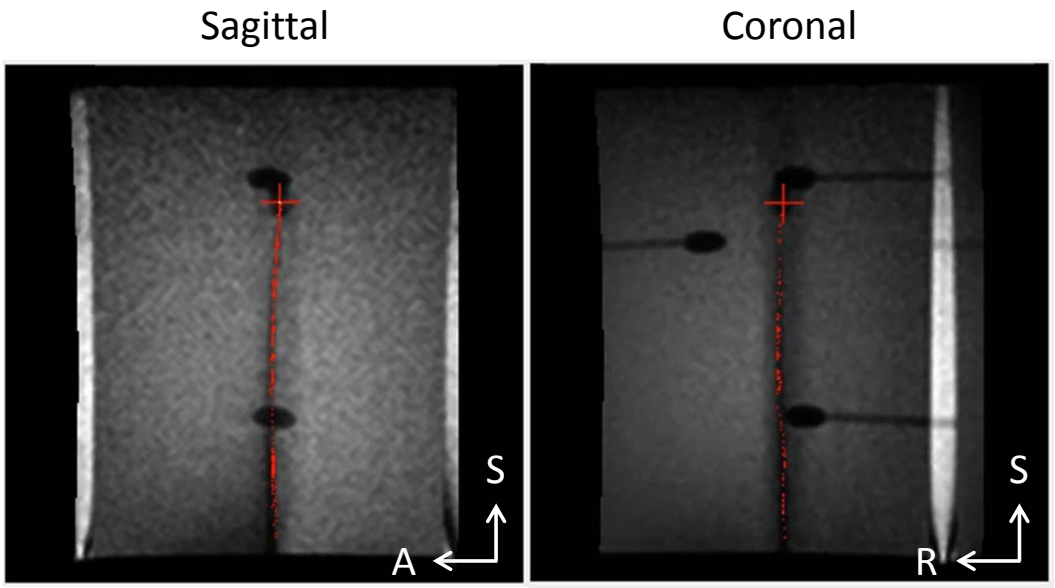


Figure 4.37: Final trajectory of the teleoperated needle steering (double targets): Red dots indicate the trajectory of the needle. The final tip position shown as red cross is [12.81,57.598, 38.314] (in RAS). The tip error in 3D space is 1.87 mm.

The incremental and final real-time images are shown in Fig. 4.40 on page 189 and its Matlab plot is shown in Fig. 4.41 on page 190, the needle got teleoperated around the obstacle to hit the further target behind successfully.

To further examine the trajectory, a set of high resolution MR images are taken in the end. The imaging protocol used is the same one as shown in Table 4.1 on page 170 with the protocol name of "T2-weighted 2D TSE, needle". TE = 106 ms, TR = 303 ms, FA = 90°, slice thickness = 3 mm, FOV = 256 mm × 243 mm. The transverse images at the obstacle and final needle tip position are shown in Fig. 4.42 on page 190.

In addition to the trajectory of the needle, the position of both two joints are also recorded during the insertion and it is shown in Fig. 4.43 on page 191. It

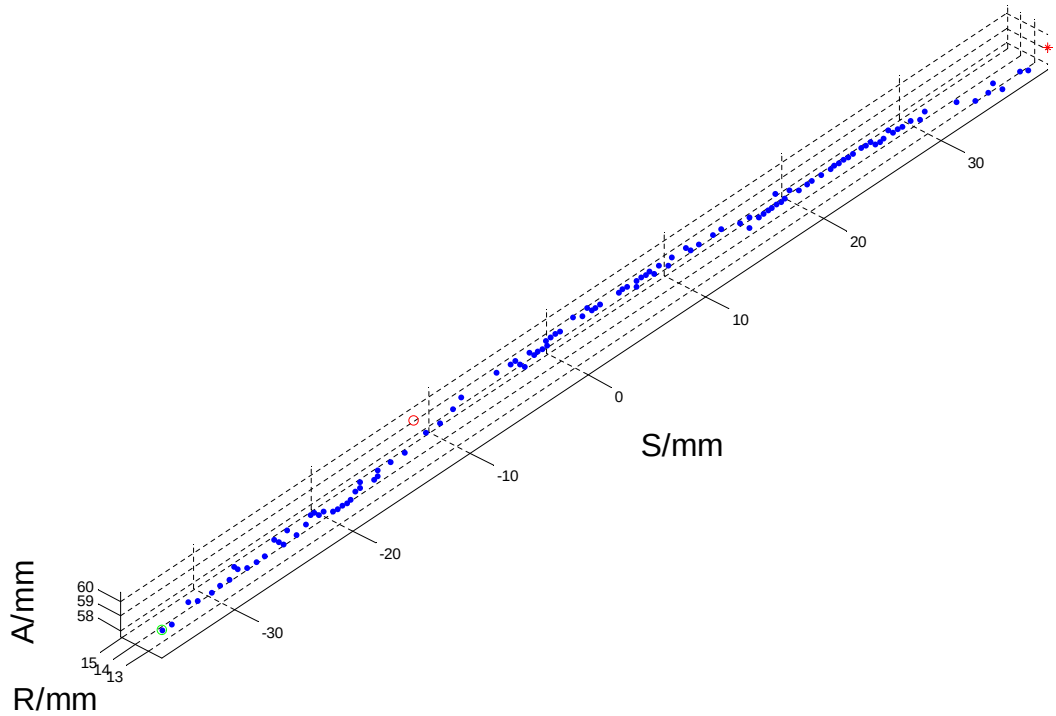


Figure 4.38: Matlab plot of the final needle trajectory (double targets): green circle is the initial starting point of the needle tip, blue dots indicate the intermediate needle tip positions, red circle is the intermediate target used to avoid the obstacle and red star indicates the pre-selected target. Although the needle didn't hit the first target, which is not required, it did successfully turn to avoid the obstacle which is desired. The needle later turned back towards the target successfully.

is obvious that to avoid the obstacle, needle is turned by about 180° before being inserted. During the first part of the insertion, while the needle is being inserted with relatively constant speed, it is still being rotated based on the visual feedback by the user to best avoid the obstacle. Once the needle passes the obstacle, it is rotated by another 180 ° to point to the target and kept inserted until it hits the target.

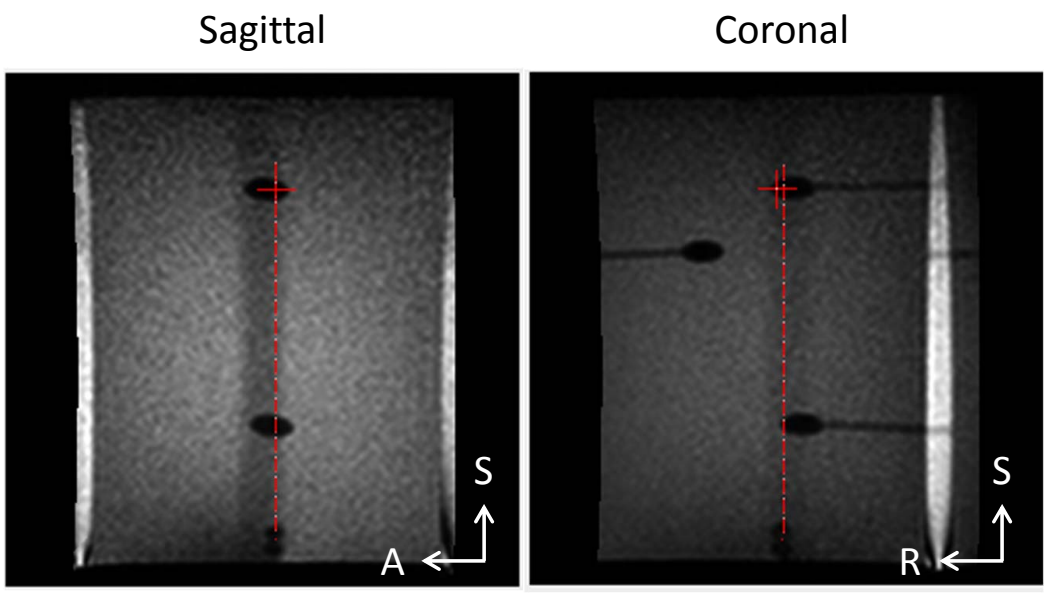


Figure 4.39: Red dashed line indicates the initial needle orientation. The red cross is the same target selected in the previous teleoperation with autonomous steering experiment just for the purpose of illustration. The final target is selected mentally and there is no intermediate target selected because the direction of the needle is controlled by user.

### 4.9.2 Teleoperated Needle Insertion with Force Feedback

As part of the important features of this teleoperation system, force feedback and insertion depth limit are also tested inside the MRI scanner. A flat-tipped nitinol needle is used with a insertion depth limit set at 60 mm. Impedance force feedback is activated with the control method discussed in section 4.6.2. The force applied to the user is based on the position difference of the master and slave robots.

One example insertion and retraction process is shown in Fig. 4.44. The blue and red lines indicate the position of the master and slave robots respectively. The green

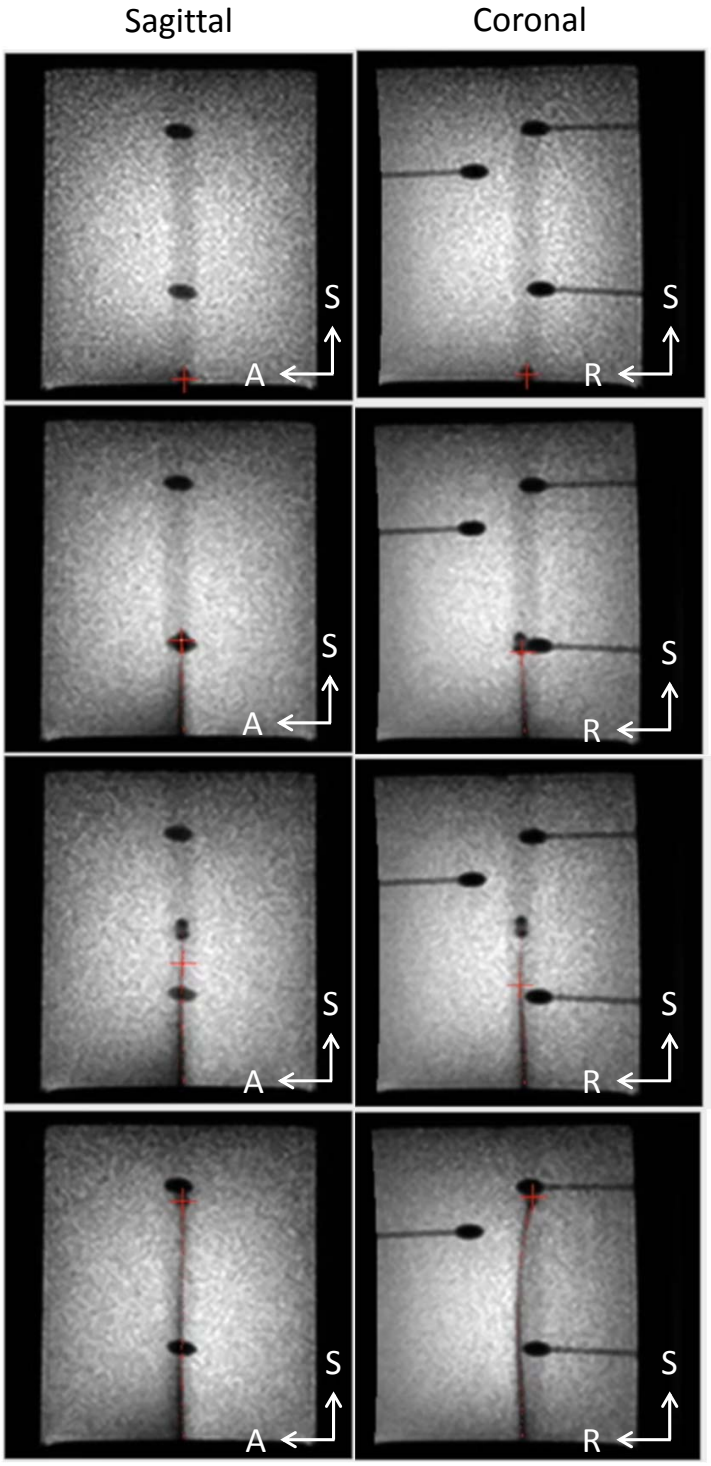


Figure 4.40: Incremental images of the 2-DOF teleoperated needle steering.

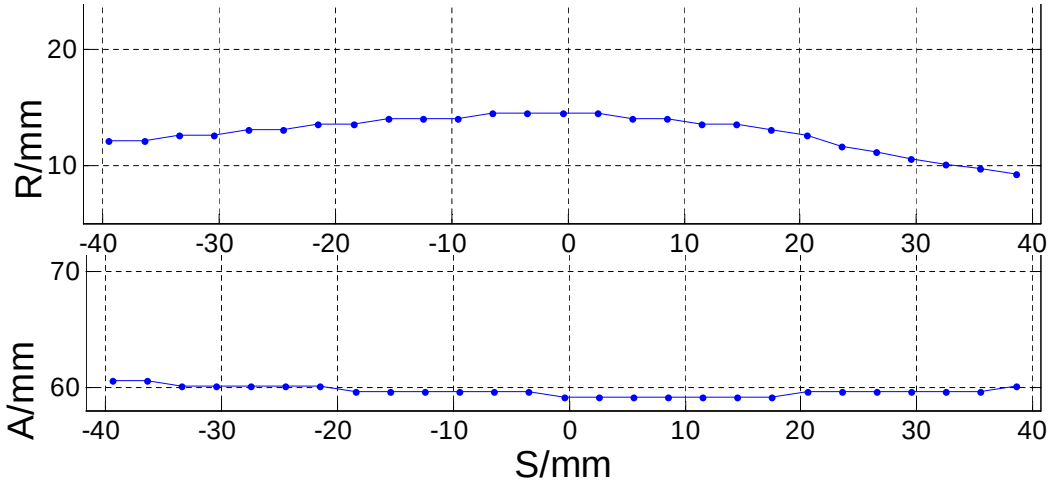


Figure 4.41: Matlab plot of the final needle trajectory: For visualization purpose, the final trajectory is plotted in two 2-D plane because the shift in A direction is very small. It is clear that the needle turned towards R+ direction to avoid the obstacle and then turned back to R- direction to target.

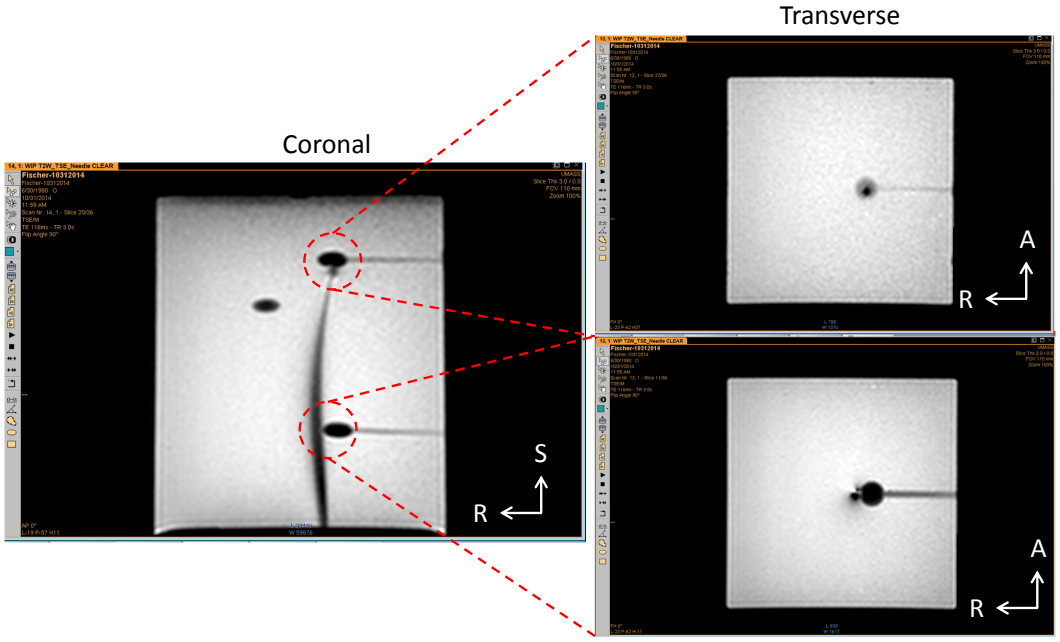


Figure 4.42: Final trajectory of the 2-DOF teleoperated needle steering with transverse images at the obstacle and final needle tip.

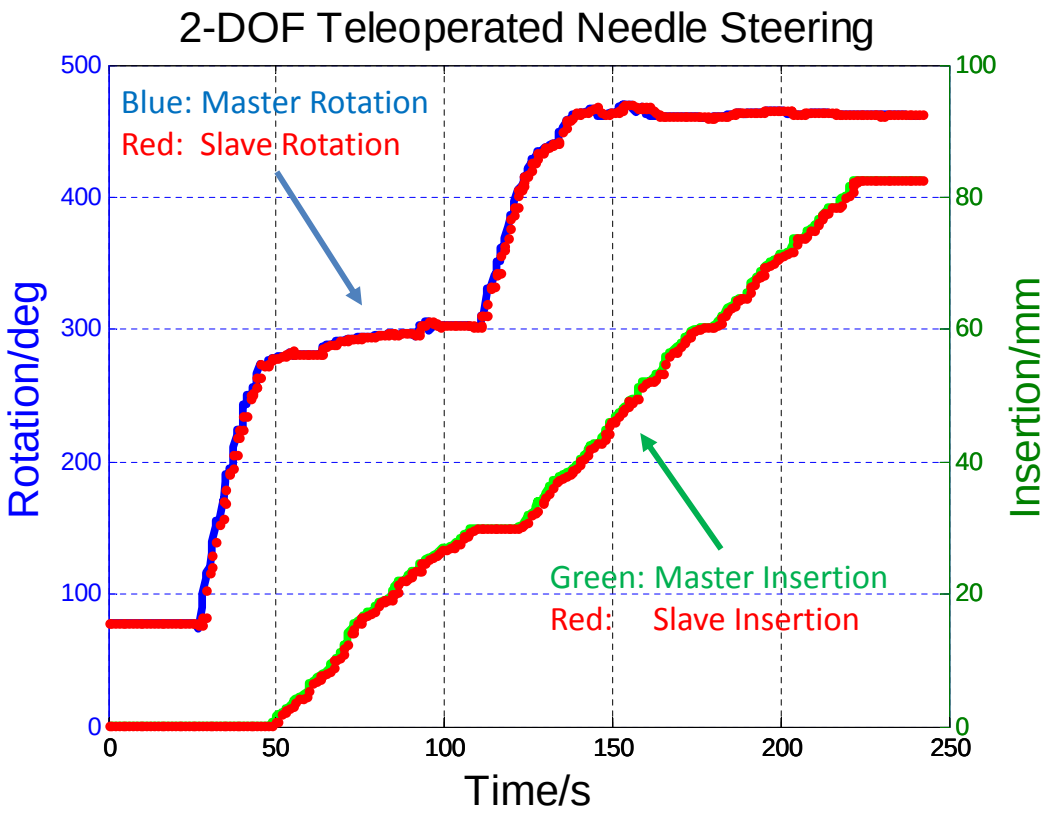


Figure 4.43: Joint positions of 2-DOF Teleoperated needle steering: a pair of blue and red dotted lines are the master and slave position of the rotation joint; another pair of green and red dotted lines are the master and slave position of the insertion joint.

line indicates the force applied to the user. The positive direction of both position and force is the needle insertion direction (S), and the negative direction is the retraction direction (I). As we can see from the plot, at the time about 20 s and 40 s, the master robot is pushed faster than the speed that slave could move. The force applied to the user in the opposite direction in order to prevent user from pushing it too fast. At the time about 60 s, the slave robot reaches the insertion limit of 60mm and stops inserting when the master is still being inserted by the user. As the result of the impedance control, the force in the opposite direction rises once again to stop the

user's insertion. The force feedback has also successfully prevented the fast movement during the needle retraction.

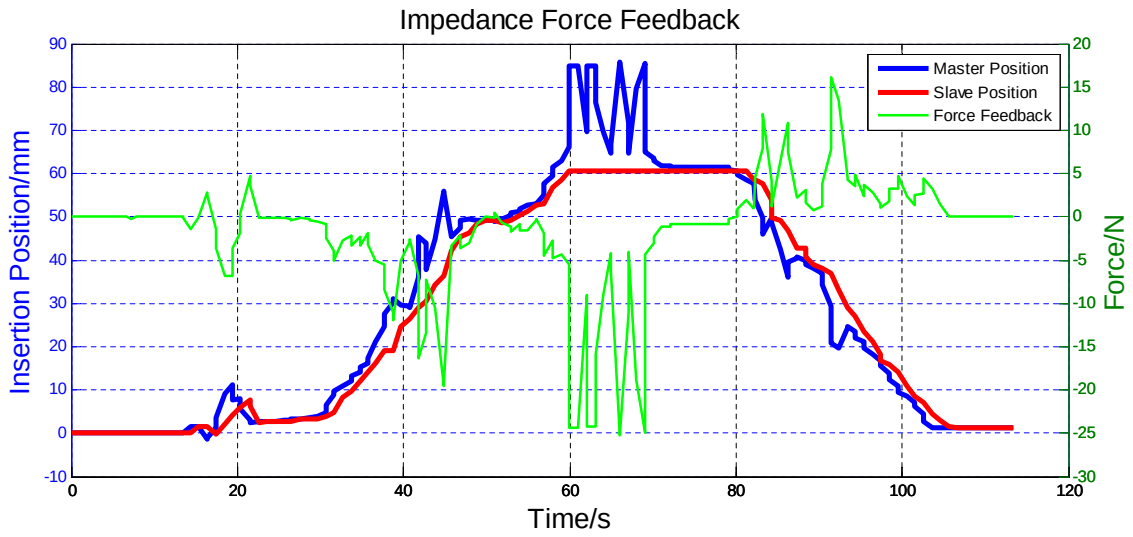


Figure 4.44: The Matlab plot of the teleoperation with impedance force feedback and insertion depth control: the slave robot is teleoperated by the master robot with a insertion depth limit of 60 mm. Impedance force feedback is activated. Blue line: master robot joint position; red line: slave robot joint position; green line: force feedback to the master robot.

## 4.10 Discussion and Conclusions

In this chapter, a surgical master-slave teleoperation system for percutaneous interventional procedures under continuous MRI-guidance is presented. This system consists of a piezoelectrically actuated slave robot for needle placement with integrated fiber optic force sensor utilizing FPI sensing principle. The sensor flexure is optimized by FEA and embedded to the slave robot for measuring needle insertion force. A novel, compact opto-mechanical FPI sensor interface is also integrated

into the MRI-compatible robot control system. A pneumatic-actuated haptic master robot is developed to render the force associated with needle placement interventions to the surgeon. An aluminum load cell is implemented and calibrated to close the impedance control loop of the master robot. A bi-lateral force-position control algorithm is developed to control the hybrid actuated system. The performance of the teleoperation system is evaluated with bentch-top setup. The overall RMS error of position tracking is 0.107 mm with maximum error observed of 0.660 mm and the fastest tracking speed of 7.618 mm/s. The position tracking bandwidth is found to be 0.03 Hz with the total travel of 160.172 mm. Its corresponding speed is 4.805 mm/s. The force tracking bandwidth frequency is found to be 5.508 Hz with the total travel of 30 N. Teleoperated needle steering with force feedback is demonstrated under live MR imaging, where the slave robot resides in the scanner bore and the user manipulates the master beside the patient outside the bore.

However, to reach the goal of clinical use, there are still works need to be done in the future. Although the clinical workflow and sterilization have both been addressed, they are still pending for practical examination in the MRI room with surgeon. The FPI force sensor has been demonstrated with its dynamic properties and actual performance in this chapter but the calibration procedure could still be made autonomous and the temperature compensation is required to prevent it from floating when temperature changes to be actually used in clinical procedure. Although the teleoperation frequency, position and force tracking bandwidth are investigated,

it still requires more thorough stability and transparency evaluation to reach the reliable performance and safety before the real clinical use.

Needle steering is very useful clinically since it could make the insertion more accurate even the entry point is not aligned well. But several issues still need to be addressed before the clinical use. Firstly, unlike the testing phantom, real tissue is usually non-isotropic which makes the model of the needle deflection irregular. Also, the real clinical needles are not always the same as the one used in these experiments. The needle could be larger in diameter and stiffer which makes it harder to make turns. The feasibility of the needle steering for real clinical use should be discussed separately within different clinical applications.

# Chapter 5

# Robot Control of Clinical Grade Needle Placement Robot for Transperineal Prostate Interventions

Part of this chapter has been published as

S. Eslami, **W. Shang**, G. Li, N. Patel, G. S. Fischer, J. Tokuda, N. Hata, C. M. Tempany and I. Iordachita, "In-Bore Prostate Transperineal Interventions with an MRI-guided Parallel Manipulator: System Development and Preliminary Evaluation," International Journal of Medical Robotics and Computer Assisted Surgery (In review) [137]

## 5.1 Overview

This chapter studies the control of a clinical grade MRI-compatible parallel 4-DOF surgical manipulator for minimally invasive in-bore prostate percutaneous interventions through the patient's perineum. The proposed manipulator takes advantage of four sliders actuated by piezoelectric motors and incremental rotary encoders, which are compatible with the MRI environment. Optical limit switches are designed to provide better safety features for real clinical use. An interface circuit board is designed to handle the signal generating and processing of the limit switches. In between of the robot controller and the 4-DOF manipulator, the interface board is also responsible for organizing all the wires for motors and encoders and it is placed in a shielded box at the back of the robot. It is later replaced with a more compact and accurate design. The robot controller is the same as discussed in chapter 2 with minimum modification. The performance of both generations of the limit switch is tested. MRI-guided accuracy and MRI-compatibility of whole robotic system is also evaluated.

The contributions of this chapter are: 1) designed system control architecture of the 4-DOF surgical manipulator; 2) designed two generations of limit switch design and evaluated their performance; 3) evaluated accuracy of the robotic system with MRI-guidance; 4) evaluated MRI-compatibility of the robotic system; and 5) performed two clinical prostate biopsy trials with the robotic system.

## 5.2 Robot Description

Designed collaboratively by our group and primarily Johns Hopkins University, the 4-DOF parallel manipulator (Fig. 5.1) is composed of two similar front and rear trapezoid stage with parallelogram mechanism [118] allowing motion in both lateral and vertical planes. Driven individually by four leadscrews, the linear sliders could also provide 2-DOF angulation motion in addition to 2-DOF Cartesian motion to the needle driver. The angulation gives robot the ability to avoid potential obstacles in the way that may block the path of the needle for the direct insertion (e.g. urethra, pubic arc, bladder, blood vessels and bones).

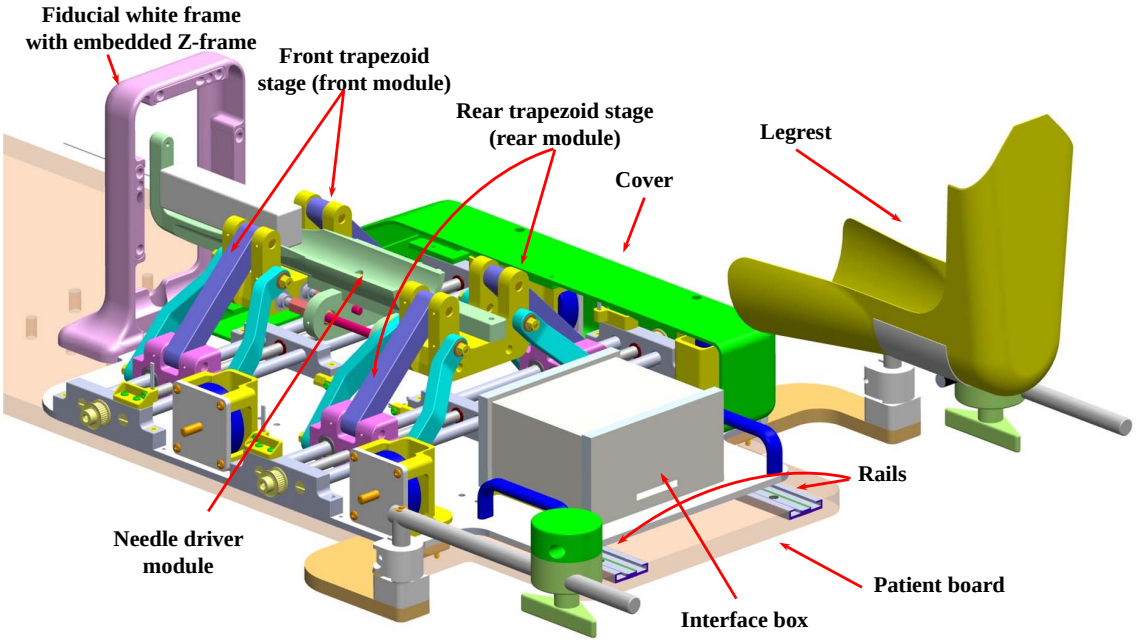


Figure 5.1: Model of 4-DOF manipulator.

As shown in Fig. 5.1, the robot on its base could slides into two rails embedded in

the patient board and could be locked in place. The interface box, which contains the circuit board for processing the limit switch signals and manages all the wiring, is placed at the end of the robot. Four motors with encoders are next to each slider and covered for safely run in the clinical procedure. A fiducial frame in front of the robot is with embedded Z-frame for the purpose of robot registration. It also separate patient's legs to make enough work space for robot.

Figure 5.2 shows the actual implementation of the manipulator prototype. It gives a better view of four pairs of motors and encoders. A pair of limit switches is placed at both end of each slider to prevent it from hitting the supports and being damaged. All the wires go back to the interface box.

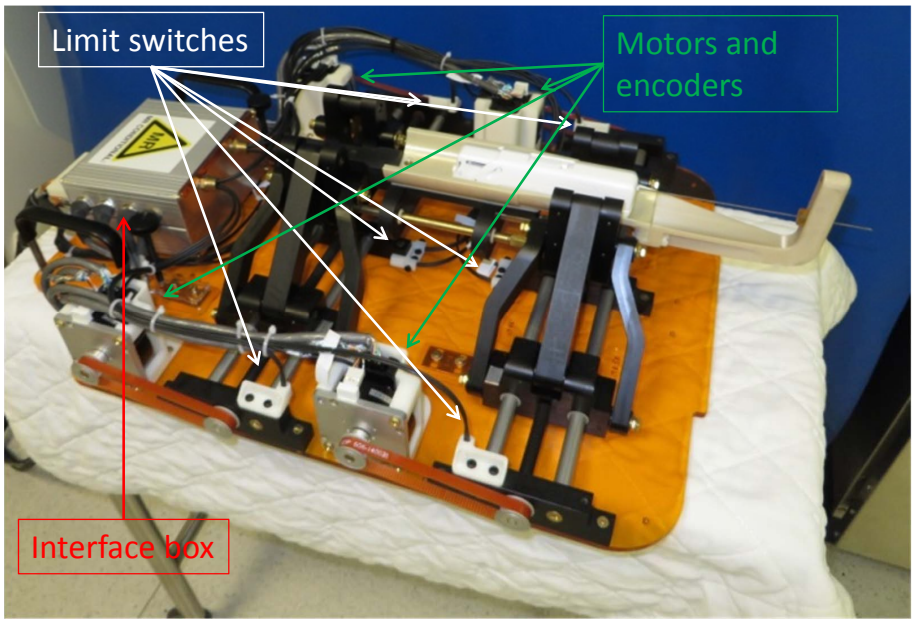


Figure 5.2: Actual prototype of 4-DOF manipulator: showing four pairs of motors and encoders, limit switches and the interface box.

## 5.3 Robot Actuation and Control Method

### 5.3.1 Control Architecture

The manipulator takes advantage of a non-magnetic ultrasonic double shaft motor (USR60-S4N, Shinsei Corp., Tokyo, Japan) which is able to provide maximum 1 (N.m) torque and recommended speed of 100 (rpm), at each slider. There is a rotary incremental quadrature encoder (resolution of 5000 counts/rev, US Digital, Vancouver, Washington) supplied with the piezoelectric motor providing position feedback. Four ultrasonic motors are controlled by the customized MRI-compatible robot controller discussed in chapter 2, providing high precision closed-loop control.

Figure 5.3 represents a diagram of the actuation system where the communication between the robot controller's software and RadVision is through the OpenIGTLink protocol [119]. After the task space (i.e. patient/image coordinates) target position is sent from RadVision through OpenIGTLink, the forward and inverse kinematics calculation is done in the robot control software. The calculated joint space target position is sent to the robot controller communicating through an optical fiber which is inside the MRI scanner room. Encoders, piezoelectric motors, and limit sensors interface with the robot controller and its piezoelectric motor drivers.

The robot is actuated by a customized controller residing in the MRI room during the operation. The wiring for the sensors and actuators is carried out through radio frequency (RF) shielded cables prepared for this purpose. The controller consists of

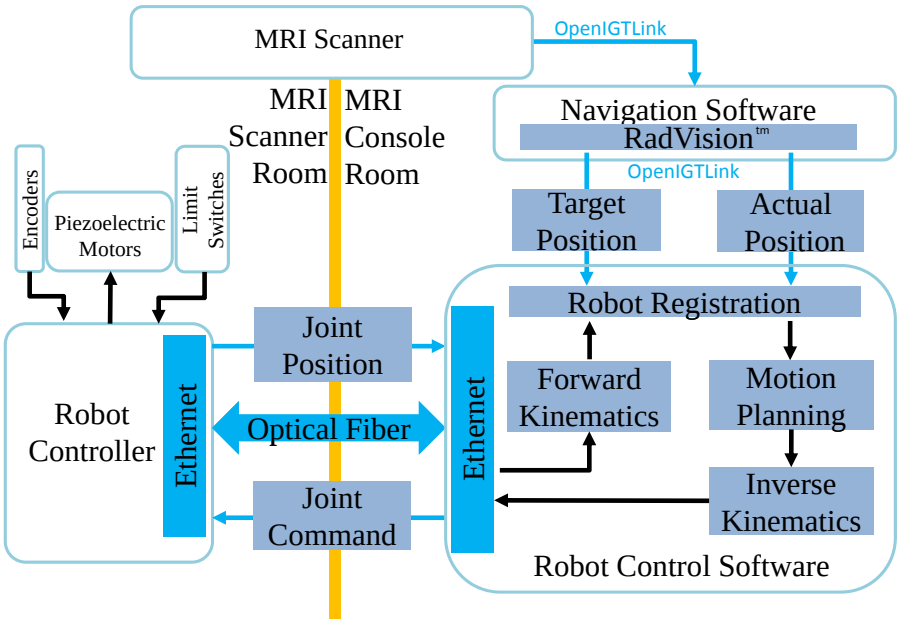


Figure 5.3: System architecture.

four customized piezoelectric motor driver boards to perform low level control task as well as produce the control signal for actuating the motors.

The piezoelectric motor driver board is constructed with a high speed FPGA-based control signal generator [45]. Fig. 5.4 illustrates the actuation principle of the controller's components. In order to get reliable signals, the encoders and limit switches have differential outputs. Their signal is first processed by low-voltage differential signaling (LVDS) driver attached to the sensor and then the LVDS receiver on each driver board inside the controller box. After the encoder data is received by FPGA (Cyclone EP2C8Q208C8, Altera Corp.), a microcontroller (PIC32MX460F512L, Microchip Tech.) is in charge of the joint level control while the calculation of forward and inverse kinematics is done in the robot control application. The motor control sig-

nal is then generated and processed by FPGA, digital-to-analog converter (DAC) and linear amplifier (AMP) to the Shinsei driver (D6060, Shinsei Corp., Tokyo, Japan). Finally the motor driving signal is transmitted out of the controller by the RF shielded cable.

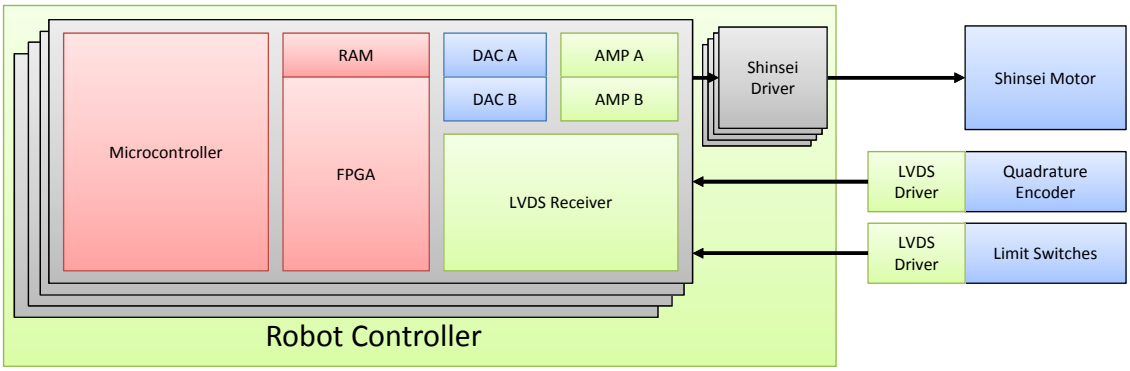


Figure 5.4: Principle of the controller.

### 5.3.2 Development of Limit Switch and Robot Interface Board For MRI-Guided Controller System

#### 5.3.2.1 First Generation

As described before, the interface box, which is placed at the end of the robot, contains the breakout board for processing the limit switch signals and manages all the wiring from the controller to the robot. The breakout board is not only responsible for handling four channels of motor and encoder signal transferring, but also generate

and process four channels of limit switches for the four robot links and each channel contains a pair of two limit switches. Therefore, totally eight optical limit switches are integrated into this breakout board.

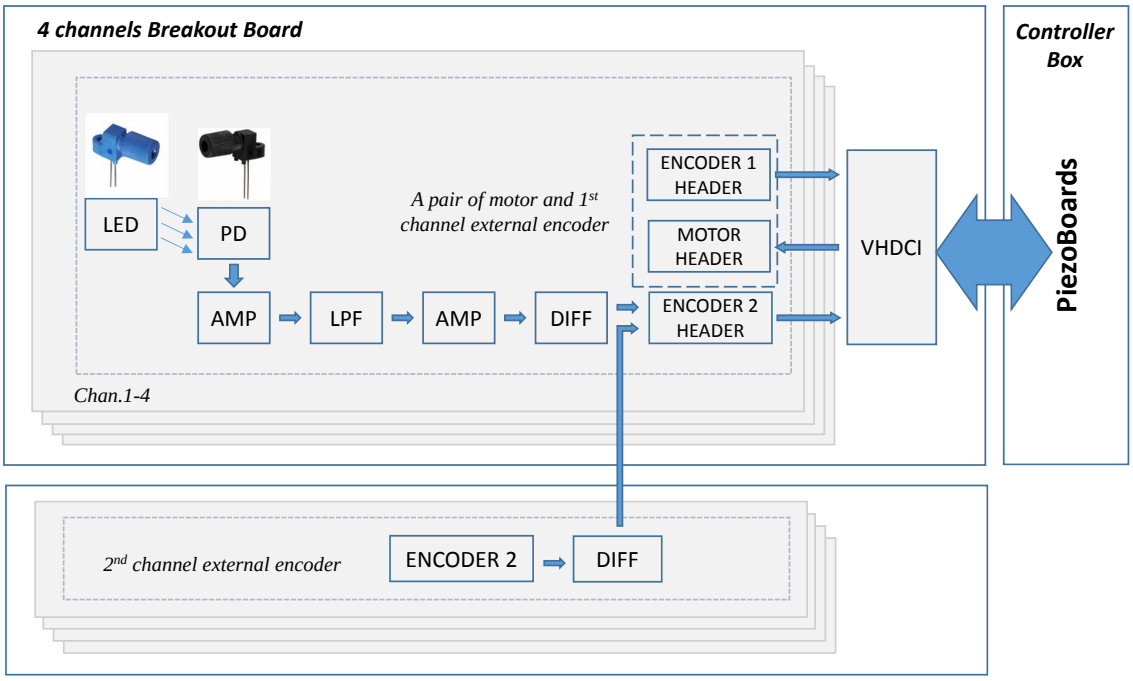


Figure 5.5: Schematic diagram of the breakout board.

Fig. 5.5 shows the schematic of the four channel breakout board design. Each channel equipped with a pair of motor header and encoder header for the closed-loop control of the motor. In addition, a pair of infrared LED (IF-E91A from Industrial Fiber Optics, Tempe, AZ) and photodiode (IF-D91 from Industrial Fiber Optics, Tempe, AZ) is used for one limit switch. The signal is firstly amplified by AD8698 amplifier (Texas Instruments, TEXAS), low pass filtered, amplified again and then goes through differential driver to produce stable signal for control system. A pair of the limit switch signal uses the second encoder header for the channel. For the system

expansion purpose, the second encoder header could also connect to another actual encoder instead of the limit switches. Finally a 68-conductor shielded VHDCI cable is in charge of transmitting all the signals from four channels to the corresponding piezoboards in the controller box.

The detailed circuit design is shown in Fig. 5.6. The left red box shows the LED power circuit. The right three boxes show the first stage amplifier, low-pass filter with the cut-off frequency of 53 HZ and second stage amplifier.

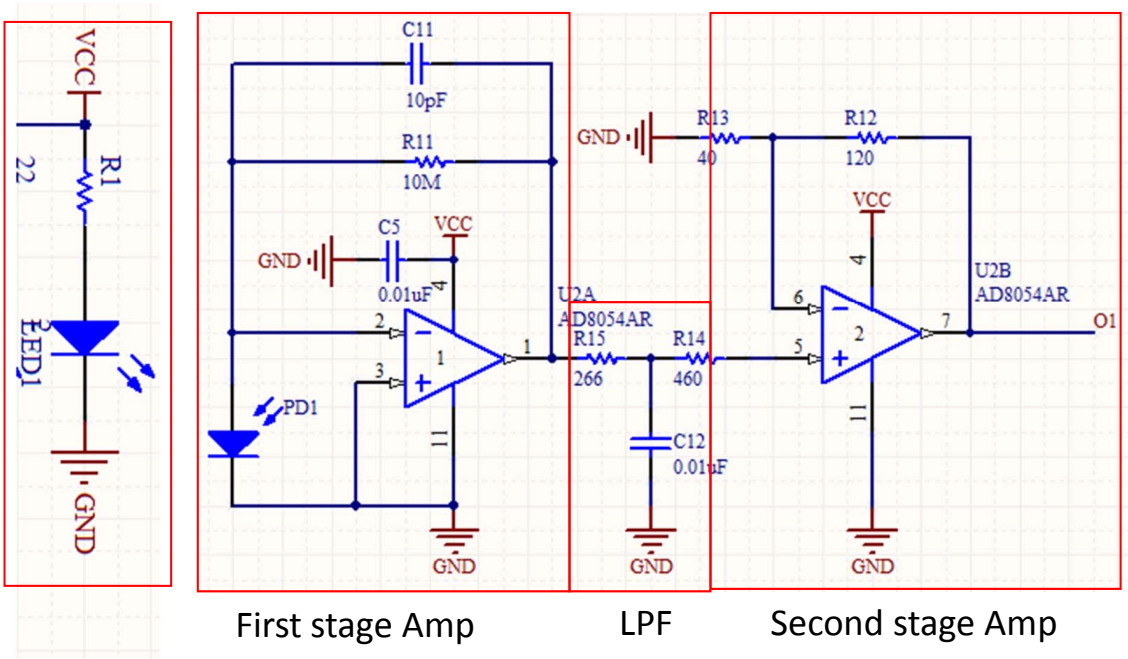


Figure 5.6: Schematic diagram of the circuit board.

Fig. 5.7 shows the actual PCB of the breakout board. LEDs and PDs are on the top part of the board. Motor and encoder connectors are in the middle, and VHDCI connector is on the bottom. An aluminum box is used to keep the breakout board shielded as it is close to the iso-center of the MRI.

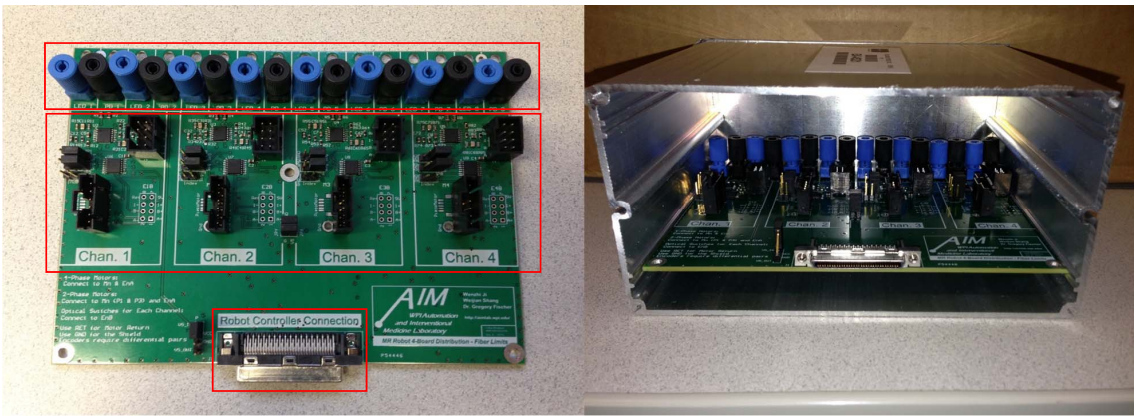


Figure 5.7: Actual PCB of the breakout board(left) inside the shielded aluminum case(right). LEDs and PDs are on the top part of the board. Motor and encoder connectors are in the middle, and VHDCI connector is on the bottom.

Fig. 5.8 shows the sensitivity and repeatability test setup for the 1st generation limit switch by using a Cartesian stage. One pair of LED and photodiode was tested with similar setup as the real scenario. The end of the Cartesian stage was covered with smooth white label which gives good reflection. Firstly, it is found that the axial distance between the end of the fibers and the surface of the while label is between 3.5 mm - 5 mm with the best performance at 4.25 mm. Thus the sensitivity and repeatability tests are done with 4.25 mm in axial distance. The stage is manually moved in perpendicular to the axial direction of the fibers from relative distance of -3.99 mm to 1.99 mm with 0.2 mm increment which is measured by dial gauge. Digital multimeter is used to measure the final output of the first stage of the amplifier. The collected results are shown in Table 5.1 on page 205 and Fig. 5.9 for scatter plot. In addition, a trigger point repeatability test at 0 mm(the stage just covers the fiber) shows it has a good repeatability of 0.041 mm which is shown in Table 5.1 on page 205.

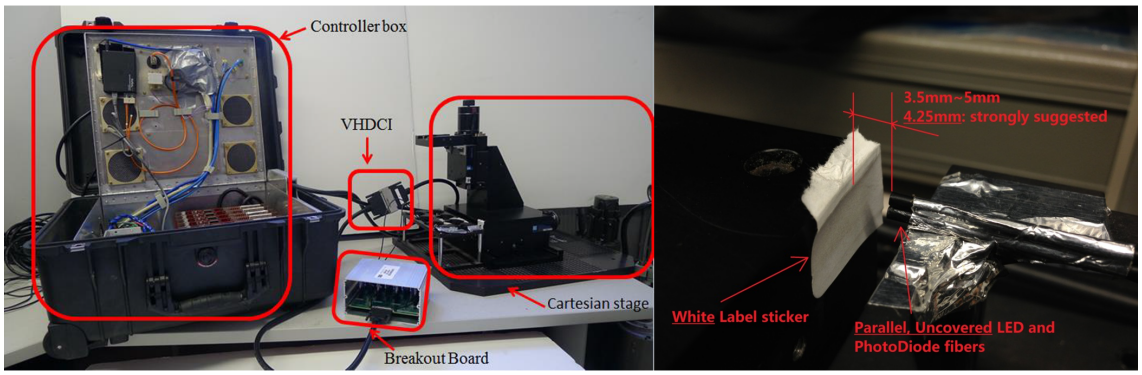


Figure 5.8: Testing setup for sensitivity and repeatability of the first generation sensor. The axial distance between the end of the fibers and the surface of the while label is between 3.5 mm - 5 mm with the best performance at 4.25 mm. The stage is manually moved in perpendicular to the axial direction of the fibers from relative distance of -3.99 mm to 1.99 mm with 0.2 mm increment.

Table 5.1: Sensitivity and repeatability testing result of the first generation limit switch.

| mm | V | mm | V |
|---|---|---|---|
| -3.99 | 0.058 | -0.79 | 0.714 |
| -3.8 | 0.057 | -0.61 | 0.825 |
| -3.61 | 0.055 | -0.41 | 0.921 |
| -3.41 | 0.067 | -0.21 | 0.989 |
| -3.2 | 0.069 | 0 | 1.032 |
| -3 | 0.072 | 0.2 | 1.057 |
| -2.8 | 0.077 | 0.39 | 1.072 |
| -2.59 | 0.082 | 0.6 | 1.078 |
| -2.41 | 0.089 | 0.8 | 1.086 |
| -2.19 | 0.104 | 1 | 1.09 |
| -2.01 | 0.124 | 1.21 | 1.093 |
| -1.81 | 0.161 | 1.39 | 1.093 |
| -1.6 | 0.224 | 1.59 | 1.095 |
| -1.4 | 0.314 | 1.81 | 1.097 |
| -1.2 | 0.437 | 1.99 | 1.098 |
| -0.99 | 0.574 | | |

| Repeatability at 1.01V | |
|---|---|
| No. | mm |
| 1 | 0 |
| 2 | 0.01 |
| 3 | -0.01 |
| 4 | -0.05 |
| 5 | -0.01 |
| 6 | -0.1 |
| 7 | -0.12 |
| 8 | -0.09 |
| 9 | -0.07 |
| 10 | -0.05 |
| 11 | -0.02 |
| 12 | -0.01 |
| 13 | -0.01 |
| Stdev/mm | 0.041 |

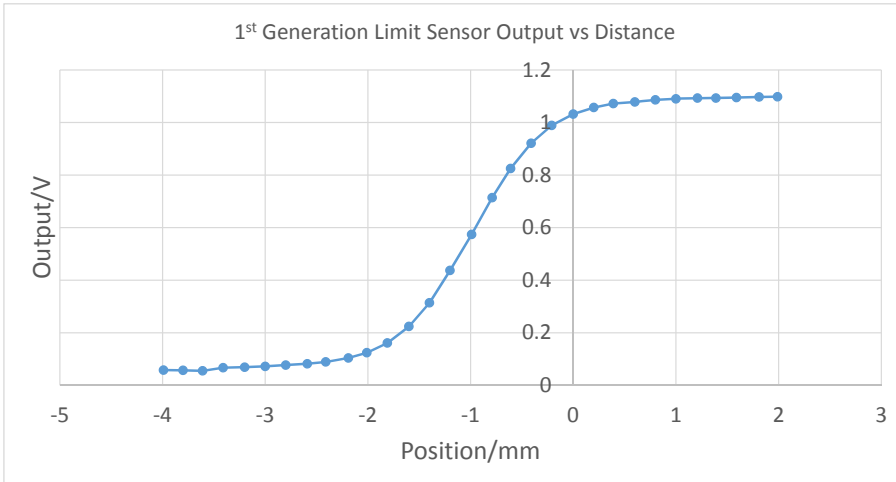


Figure 5.9: Scattered plot of the sensitivity test. The changing range from low level to high level is around 2 mm.

#### 5.3.2.2 Second Generation

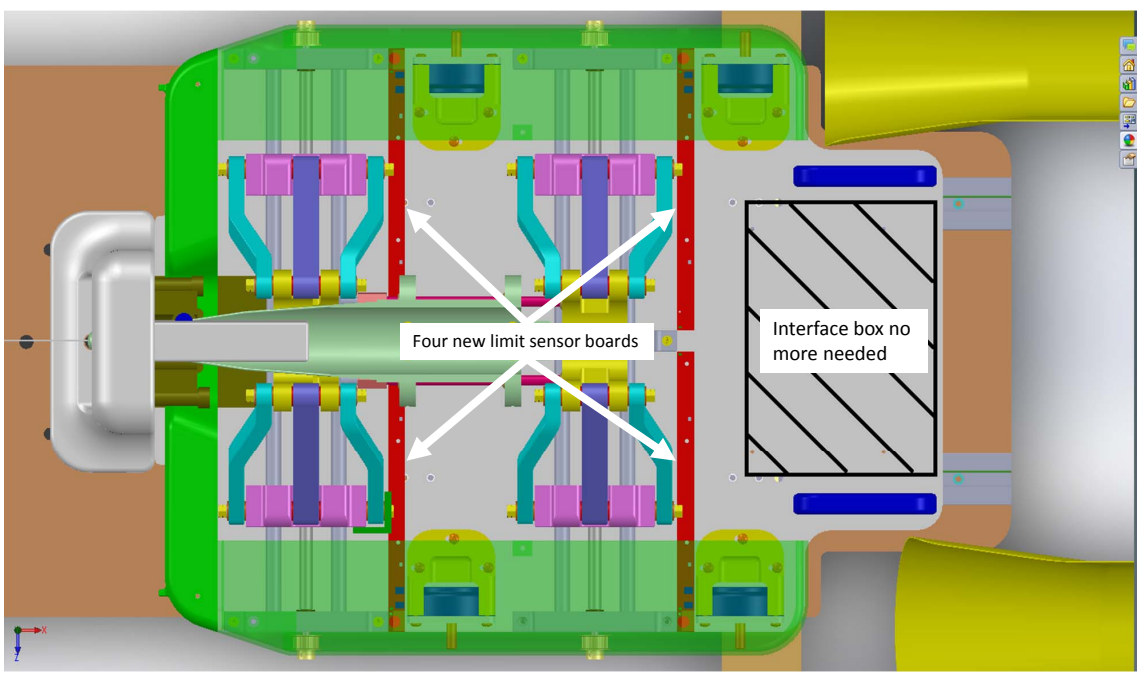


Figure 5.10: Schematic diagram of the robot with second generation limit switch boards: four individual limit switch boards are attached next to each joint and the whole interface box could be removed to make more space to handle the robot.

The interface box with breakout board achieves the design requirement of enabling the limit switches and organizing the wires, but this limit switch design actually brings eight more pairs of optical cables that are not what we want. As shown in 5.2, the box also blocks the handle nearby that could cause problem of lifting or moving the robot. Thus, a second generation limit switch is designed to solve these problems. As shown in Fig. 5.10, four individual limit switch boards are attached next to each joint and the whole interface box could be removed to make more space to handle the robot.

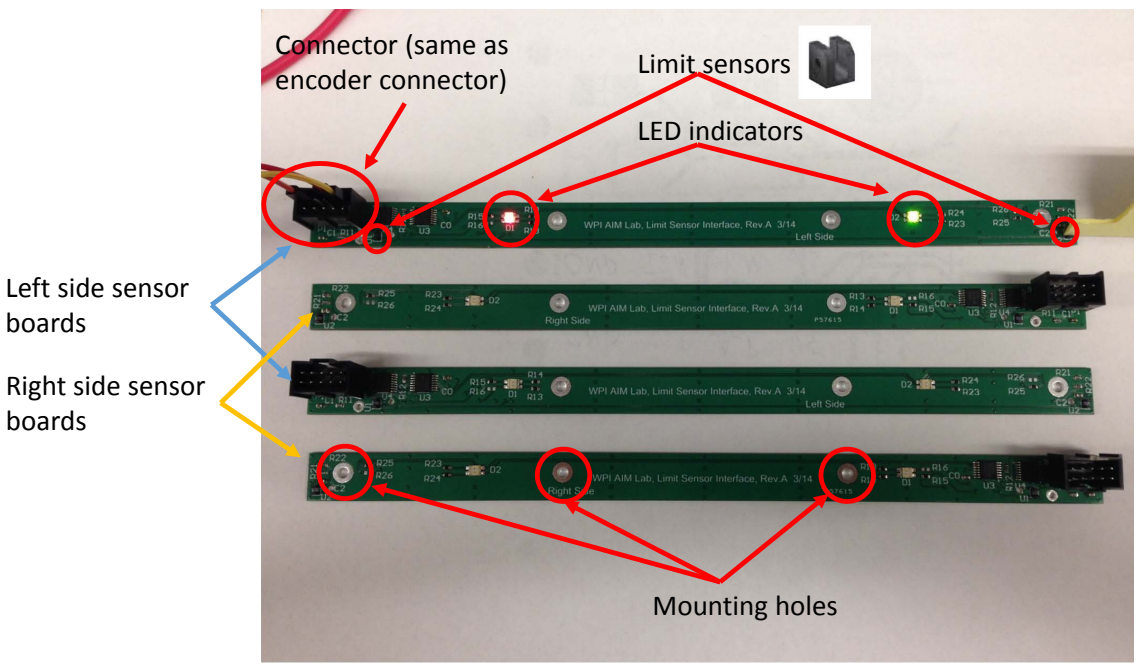


Figure 5.11: Actual PCBs of the second generation of the limit switch boards: with two symmetrical designs for each side of the robot.

Fig. 5.11 shows the actual limit sensor boards for each joint. Similar circuit design was adopted to the new PCB boards but with two stages of inverter instead of just analog amplifier. As a result, it provides more reliable and stable signal output. The

integration of LED indicators also shows the status of each sensor. The choice of sensors is switched to a much more compact photo interrupter (rpi-0128 from ROHM semiconductor, Kyoto, Japan) which is only $1.6mm \times 2.5mm \times 1.8mm$ in size and has the claimed sensitivity of less than 0.5 mm. The connectors use the same type with the encoder connectors that make the whole wiring simple and clean.

The compact size and high sensitivity also comes with difficulty that the gap of the opening of the sensor is only 1.2 mm. The trigger element which is a piece of shim attached to the joint is hard to align well with this small gap. Thus a guide is designed and made by 3D printer with a wider opening to let the shim goes into the gap without problem (Fig. 5.12).

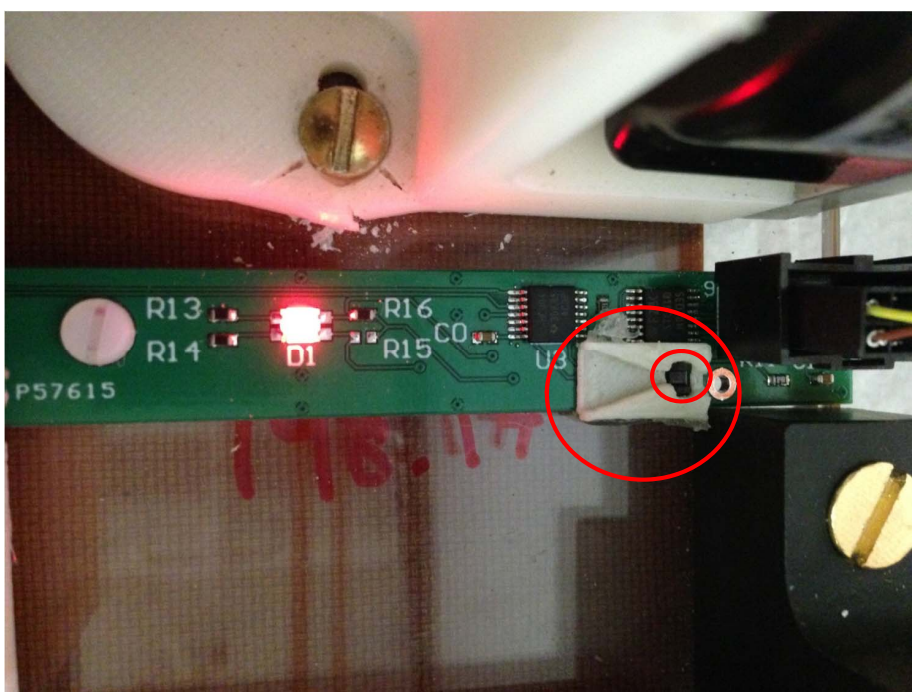


Figure 5.12: A guide (within large red circle) is designed and made by 3D printer with a wider opening to let the shim goes into the gap of the limit sensor (within small red circle) without problem.

Similarly, the sensitivity and repeatability of the second generation limit switch are also tested. In this test, the sensor is attached to the robot and the one of the joint is moved by rotating the lead screw by hand. The position of the joint is also measured by dial gauge and the final output of the sensor is measured by multimeter. Table 5.2 on page 209 shows the recorded data for the sensitivity test with the scatter plot shown in Fig. 5.13.

Table 5.2: Sensitivity and repeatability testing result of the second generation limit switch.

| mm | V | mm | V |
|---|---|---|---|
| 0.258 | 4.104 | 0.368 | 4.100 |
| 0.270 | 4.112 | 0.374 | 4.098 |
| 0.276 | 4.113 | 0.376 | 4.088 |
| 0.290 | 4.112 | 0.378 | 0.001 |
| 0.302 | 4.126 | 0.380 | 0.001 |
| 0.312 | 4.111 | 0.382 | 0.001 |
| 0.320 | 4.117 | 0.384 | 0.001 |
| 0.326 | 4.103 | 0.388 | 0.002 |
| 0.340 | 4.113 | 0.392 | 0.001 |
| 0.344 | 4.109 | 0.396 | 0.002 |
| 0.352 | 4.124 | 0.402 | 0.002 |

| Repeatability | |
|---|---|
| No. | mm |
| 1 | 0.378 |
| 2 | 0.378 |
| 3 | 0.374 |
| 4 | 0.382 |
| 5 | 0.374 |
| 6 | 0.380 |
| 7 | 0.378 |
| 8 | 0.380 |
| 9 | 0.374 |
| 10 | 0.378 |
| Stdev/mm | 0.003 |

As it is shown in both Table 5.2 on page 209 and Fig. 5.13, the output voltage drops from high level (4.088V) to low level (0.001V) within 0.002 mm of movement. It is a huge improvement comparing the 1st generation's 2 mm range. And the repeatability shows a 0.003mm standard deviation error which is also much better than the 0.041 mm for the 1st generation.

Furthermore, the repeatability of all four joints is tested with the moving by actual

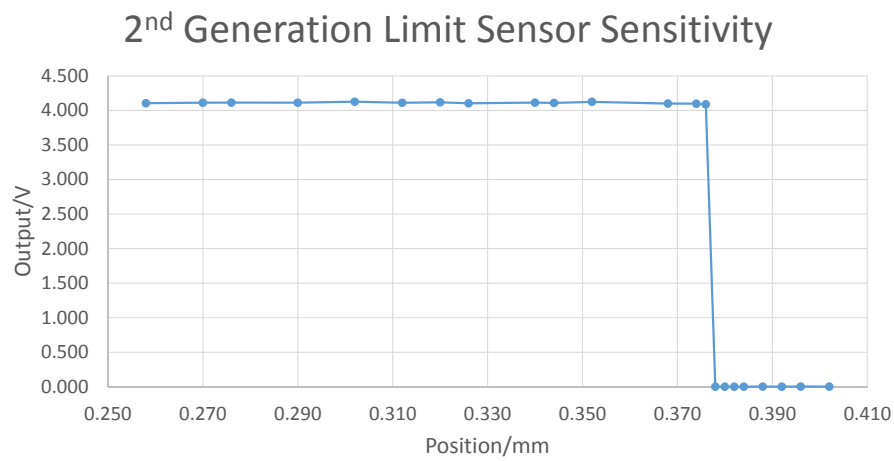


Figure 5.13: Scattered plot of the sensitivity test. The changing range from low level to high level is less than 0.003mm.

motors. Table 5.3 on page 211 shows the consistent result for each joint with standard deviation of 0.007, 0.006, 0.009 and 0.009 mm.

Finally, as the most important task for the limit switches to perform, homing the robot is crucial that all the following registration and kinematics calculation is based on it. The basic homing procedure performs like moving all the joints towards one side of the limit from random position. When touching the limit sensor, each joint is given by a pre measured latch value which is the distance from the desired home position to the limit switch trigger position. After the latch value is applied, the joint is moved back to home which is the zero position. Testing the accuracy of the homing procedure means the test of task space accuracy of the robot affected by all of the limit switches. As shown in Fig. 5.14, a dial gauge is placed at the tip of the needle guide to record the home position for each homing procedure.

Table 5.4 on page 212 shows that from 20 homing trials, the standard deviation of

Table 5.3: Joint space repeatability testing result of the second generation limit switch for each joint: FL=Front Left, RL=Rear Left, FR=Front Right and RR=Rear Right.

| 2nd Generation Limit Switch Joint Space Repeatability | | | | |
|---|---|---|---|---|
| No. | FL | RL | FR | RR |
| 1 | 113490 | 118733 | -213898 | -238502 |
| 2 | 113507 | 118730 | -213910 | -238505 |
| 3 | 113519 | 118712 | -213900 | -238508 |
| 4 | 113477 | 118689 | -213924 | -238524 |
| 5 | 113492 | 118700 | -213935 | -238522 |
| 6 | 113494 | 118710 | -213908 | -238467 |
| 7 | 113473 | 118725 | -213918 | -238485 |
| 8 | 113493 | 118723 | -213953 | -238489 |
| 9 | 113462 | 118703 | -213956 | -238501 |
| 10 | 113499 | 118739 | -213920 | -238550 |
| 11 | 113471 | 118739 | -213972 | -238516 |
| 12 | 113469 | 118726 | -213933 | -238538 |
| Stdev/ticks | 16.298 | 15.451 | 22.361 | 22.051 |
| Stdev/mm | 0.007 | 0.006 | 0.009 | 0.009 |

the homing procedure is 0.015 mm.

## 5.4 MRI-Compatibility Evaluation

MRI-compatibility is tested inside a 3.0T MRI scanner (Achieva, Philips Healthcare, Amsterdam, Netherlands). PIQT phantom was placed at the iso-center of the scanner

Figure 5.14: Test setup for homing procedure task space repeatability.

Table 5.4: Task space homing procedure repeatability testing result with the second generation limit switch: from 20 homing trials, the standard deviation of the homing procedure is 0.015 mm.

| Homing Repeatability | | | |
|---|---|---|---|
| No. | Dial Indicator/mm | No. | Dial Indicator/mm |
| 1 | 0.084 | 11 | 0.056 |
| 2 | 0.058 | 12 | 0.090 |
| 3 | 0.072 | 13 | 0.096 |
| 4 | 0.064 | 14 | 0.086 |
| 5 | 0.086 | 15 | 0.064 |
| 6 | 0.102 | 16 | 0.086 |
| 7 | 0.082 | 17 | 0.104 |
| 8 | 0.058 | 18 | 0.092 |
| 9 | 0.088 | 19 | 0.102 |
| 10 | 0.056 | 20 | 0.052 |
| | | | |
| | Ave/mm | 0.076 | |
| | Stdev/mm | 0.015 | |

and the robot was placed about 5 mm from the phantom. The robot controller was placed approximately two meters away from the scanner bore. Fig. 5.15 shows the setup. Totally seven configurations were considered, which are:

1-Baseline: only the patient board with two embedded aluminum rails is set inside the scanner along with the PIQT phantom.

2-Baseline with leg rests: a pair of leg support is mounted on the patient board.

3-Baseline with robot: the robot is mounted (having four ultrasonic motors accompanied with some aluminum and brass screws, nuts, and shafts) by sliding on the designated rails on the board and locked in place.

4-Controller (not powered): the controller is placed inside the MRI room by connecting all wires and cables to the robot but everything is still kept unpowered.

5-Controller (Powered, E-stop ON): the controller is powered ON but the motors still have no power and no motion since the E-stop is ON.

6-Controller (Powered, E-stop OFF): motor power is enabled by turning off the E-stop but the motors are not in motion.

7-During the Motion: motors are commanded by running at a constant speed of 100 rpm until the MR images are entirely acquired. The robot's belts are decoupled to allow continuous rotation of the motors during the full imaging cycle.

Each configuration was tested with the same four protocols. The protocols are a) T1-weighted FFE, b) T2-weighted 2D TSE for initial scan, c) T2-weighted 2D TSE for needle confirmation and d) Balanced FFE for real-time imaging which are the

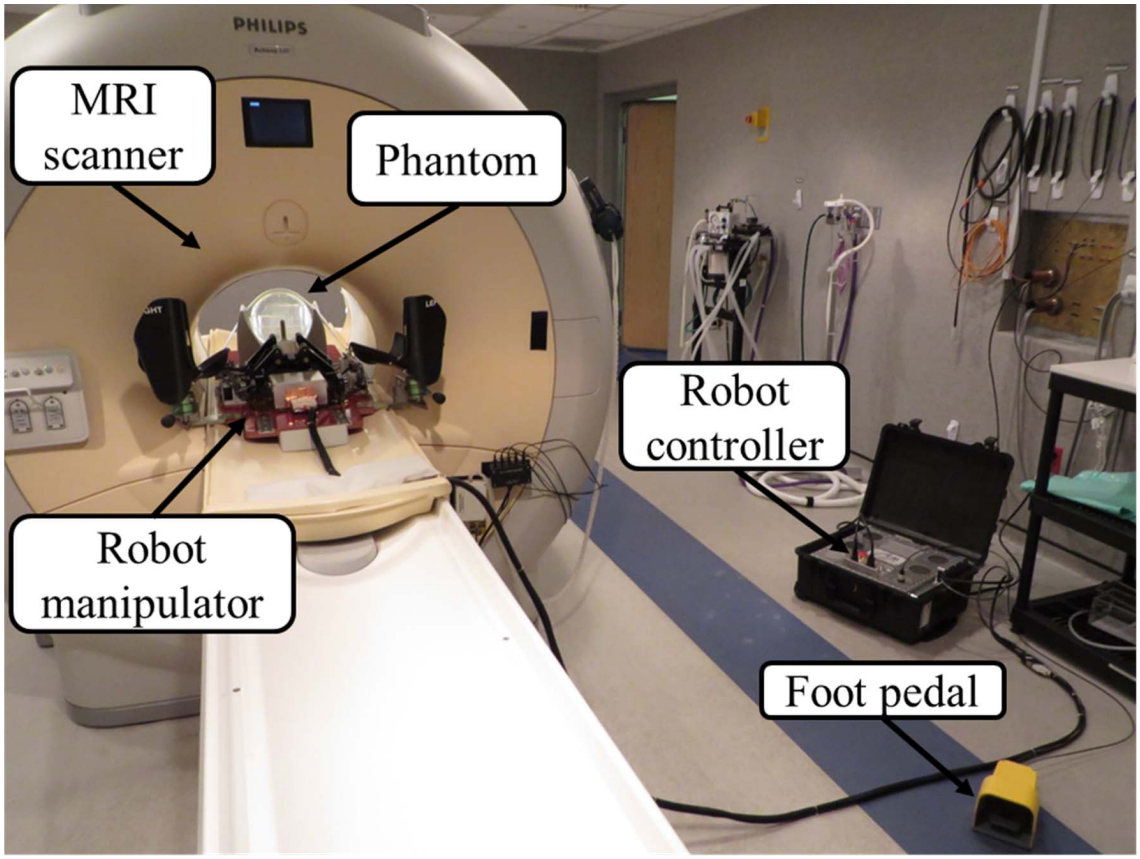


Figure 5.15: MRI-compatibility testing setup.

same as the protocols used in section 4.8. The detailed scan parameters could be found in Table 4.1 on page 170 in section 4.8. The normalized SNR results for all seven configurations could be found in Fig. 5.16. The SNR is with a variation of no more than 18% for the first six configurations. Reduced SNR of live imaging during motion (configuration 7) will never occur in a clinical practice with this system since this robot is only intended to align the needle but not actively manipulate it during imaging.

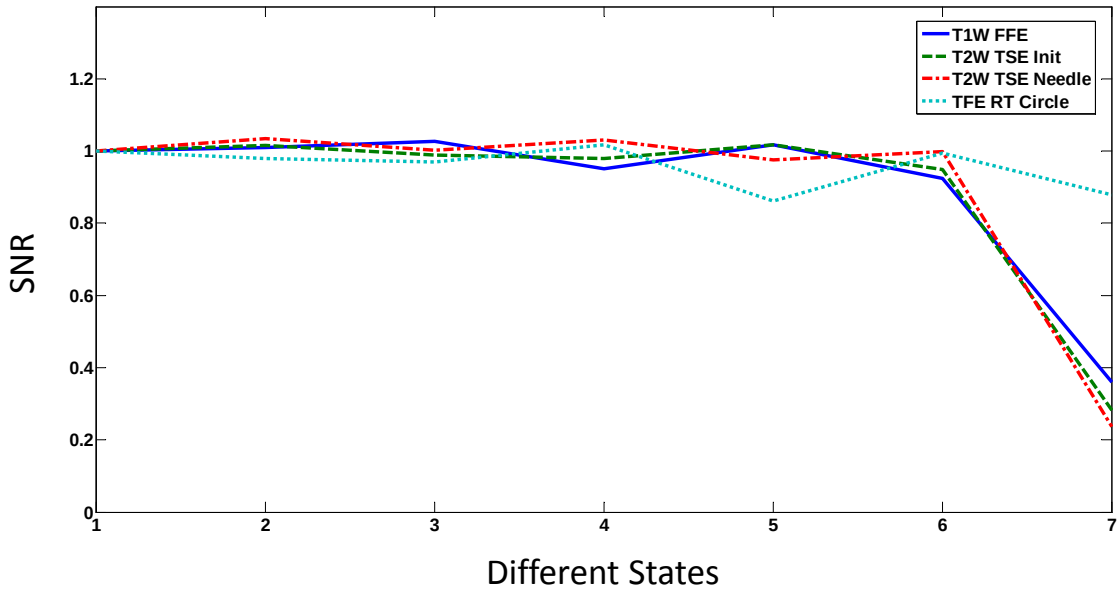


Figure 5.16: SNR results for different configurations: 1) Baseline; 2) With leg supports; 3) With robot; 4) Controller (not powered); 5) Controller (powered, E-stop ON); 6) Controller (powered, E-stop OFF); 7) During motion. [137]

## 5.5 MRI Targeting accuracy

Five groups of totally 25 targets were tested inside the 3T MRI with gelatin phantom. Five targets in each group share the same registration result. Between each group, the robot was intentionally moved and new registration was done at the new position and orientation. The result is shown in Fig. 5.17. The green-red cross indicates the desired target location picked from software and the black artifact indicates the actual needle position. The in-plane translational error in R and A directions as well as the magnitude error are shown in Fig. 5.18. The overall in-plane RMS error is 1.402 mm for all of the 25 targets with different registrations. This result satisfactorily meets the clinical accuracy requirement of 10 mm. By reaching the accuracy of

1.402 mm, it means that we could accurately biopsy the smaller suspicious tumors.

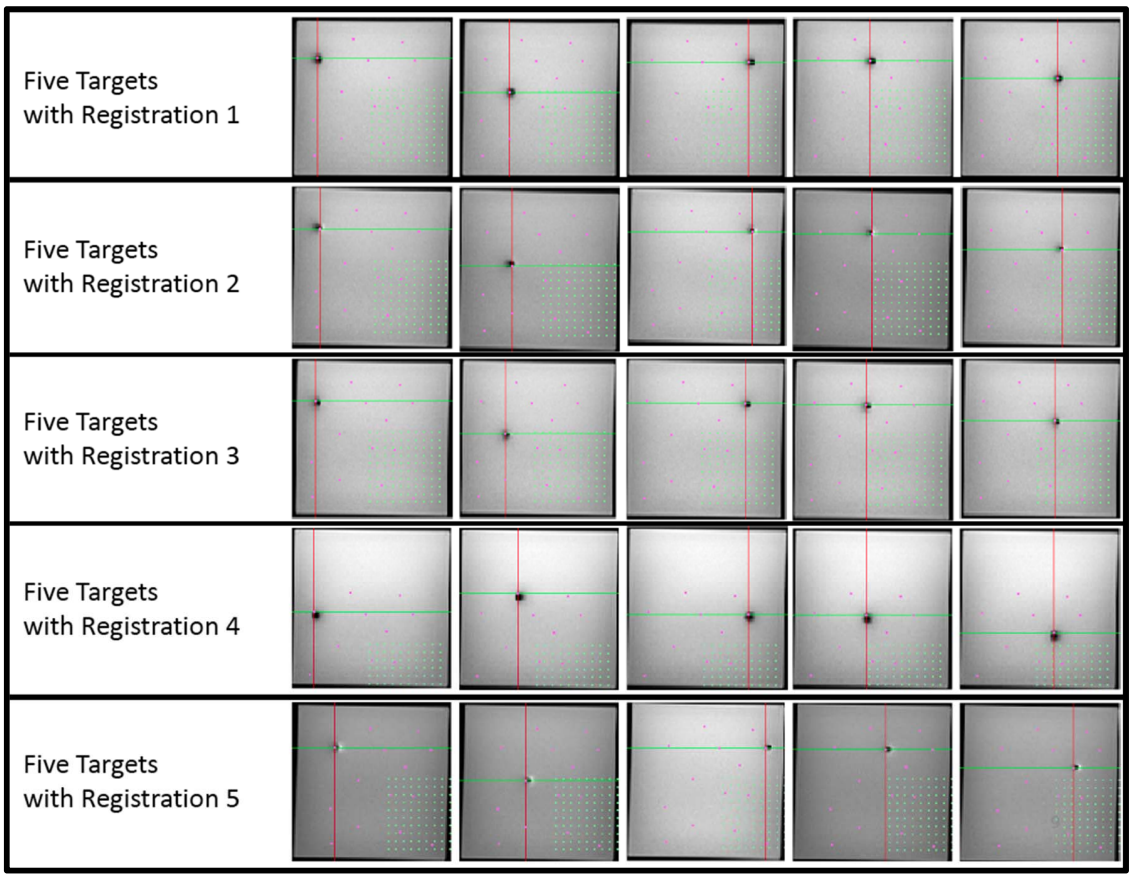


Figure 5.17: Five groups of totally 25 targets were tested inside the 3 T MRI with gelatin phantom. Five targets in each group share the same registration result. Between each group, the robot was intentionally moved and registration was done again at the new position and orientation. The green-red cross indicates the desired target location picked from software and the black artifact indicates the actual needle position.

## 5.6 Clinical Trials

Collaborating with researchers and doctors at Brigham and Women's Hospital and Harvard Medical School, we have successfully performed two clinical prostate biopsy

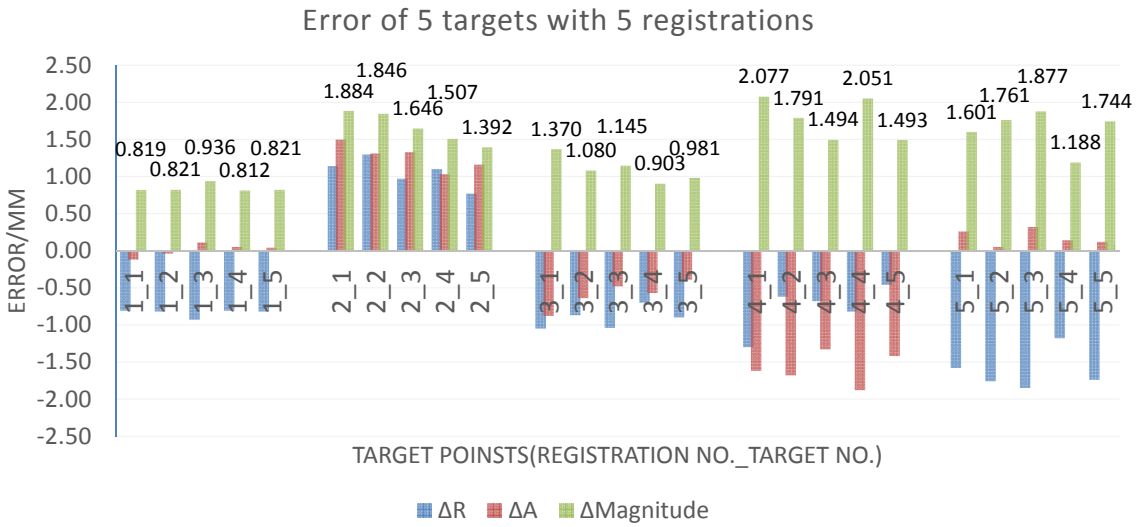


Figure 5.18: The overall in-plane RMS error is found to be 1.402 mm for all of the 25 targets with different registrations.

cases at BWH in Boston, Massachusetts. Similar to the experimental setup shown in Fig. 2.3 and 2.4 on page 55 in Chapter 2, the clinical setup consists of robot control software and navigation software (RadVision) which are in the console room and the 4-DOF robot manipulator, robot controller, foot pedal and MRI-compatible display in the MRI room. The whole setup is shown in Fig. 5.19.

The real clinical workflow is adapted from the workflow proposed in Fig. 2.12 on page 66 in Chapter 2 by changing teleoperated needle insertion to manual insertion (Fig. 5.20). When the patient is being positioned in the scanner bore, the robot would be prepared in parallel. After the robot hardware is tested without error, it is moved to home position by taking advantage of the high precision limit switches. It is then draped and docked in position on the patient board. The registration and target planning are done with RadVision software by taking MR images of Z-frame as well

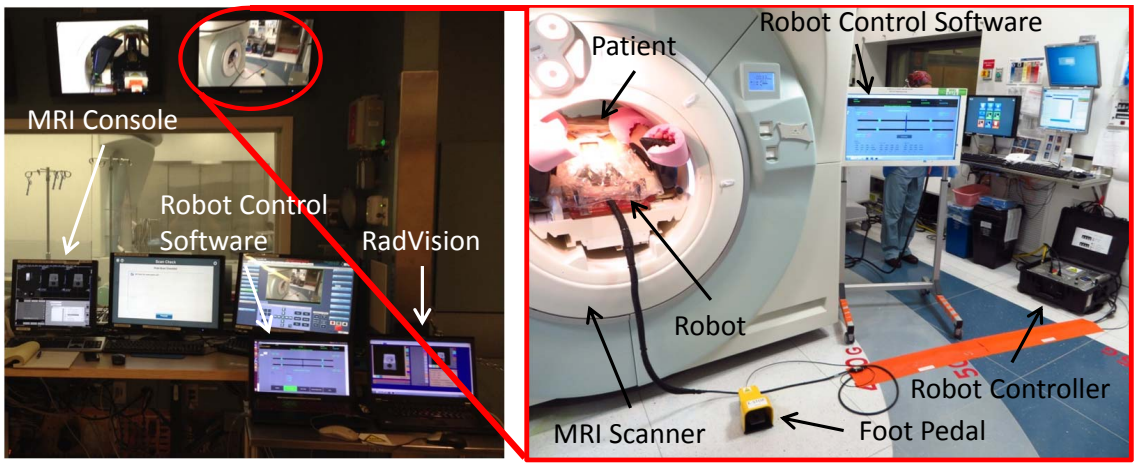


Figure 5.19: Clinical setup of robot assisted prostate biopsy: robot control software and RadVision are running in the console room(left); 4-DOF robot manipulator, robot controller, foot pedal and MRI-compatible display showing the robot control software are in the MRI room(right).

as the target region. The registration transformation matrix and targets information is then transfered to the robot control software through OpenIGTLink so that the robot could be prepared to align accurately to the targets. Once the target is set and robot is ready to move, the surgeon could operate the robot next to the patient by pressing the foot pedal with the MRI-compatible display with robot information on it and is still close enough to the patient to prevent potential safety issues from happening.

The MRI-guided prostate biopsy operating time is found to be reduced by using the robotic device, comparing to manual ways. The average core procedure time of manual cases is said to be 100.63($\pm$26.24) minutes [138]. While it is found to be less than 90 minutes in the robot-assisted cases. With the approval from institutional review board (IRB) at BWH, more clinical cases will be performed in the future.

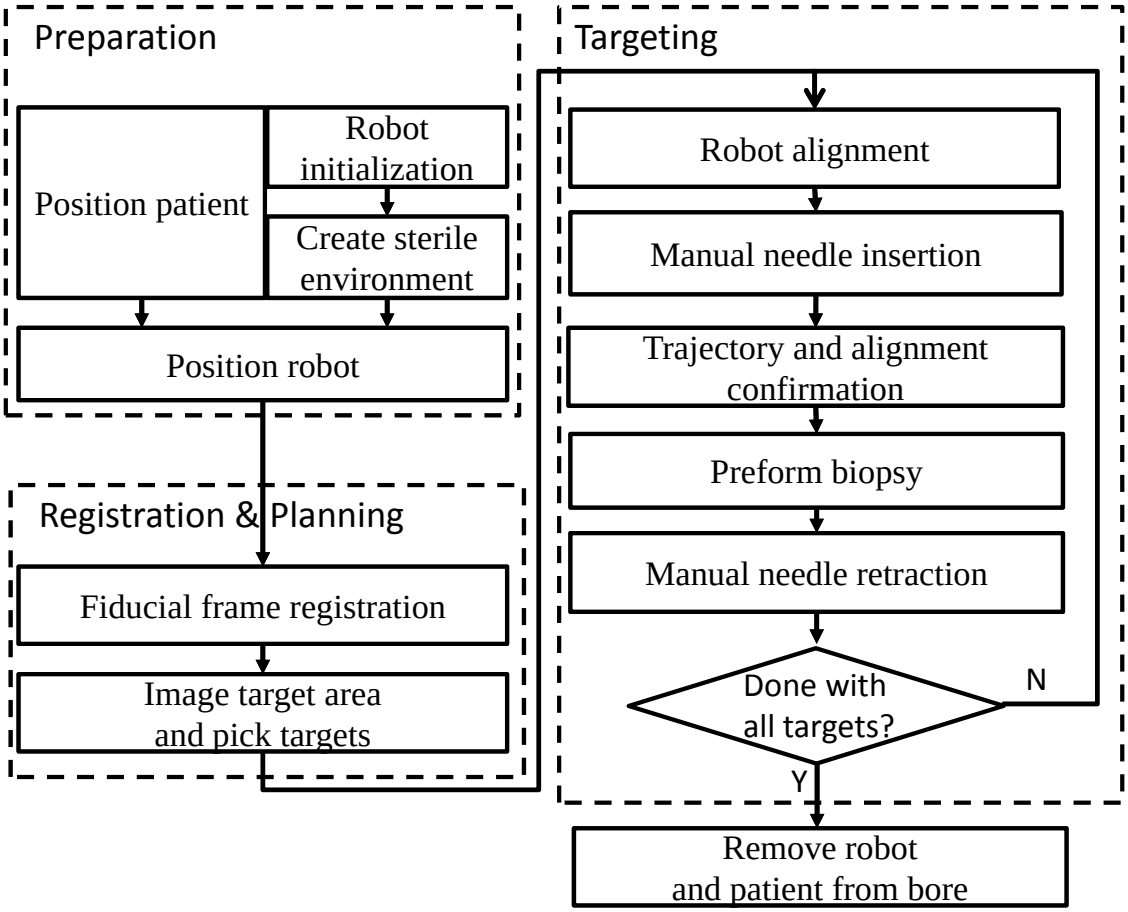


Figure 5.20: Clinical setup of robot assisted prostate biopsy: robot control software and RadVision are running in the console room(left); 4-DOF robot manipulator, robot controller, foot pedal and MRI-compatible display showing the robot control software are in the MRI room(right).

## 5.7 Discussion and Conclusions

A robotic system for clinical transperineal prostate interventions under live MRI guidance is demonstrated in this chapter. The proposed modular system communicates between each module and with MRI system by network through OpenIGTLink. A 4-DOF robot with parallel mechanism is designed for needle placement with ultrasonic motors and is precisely controlled by a custom MRI-compatible robot controller.

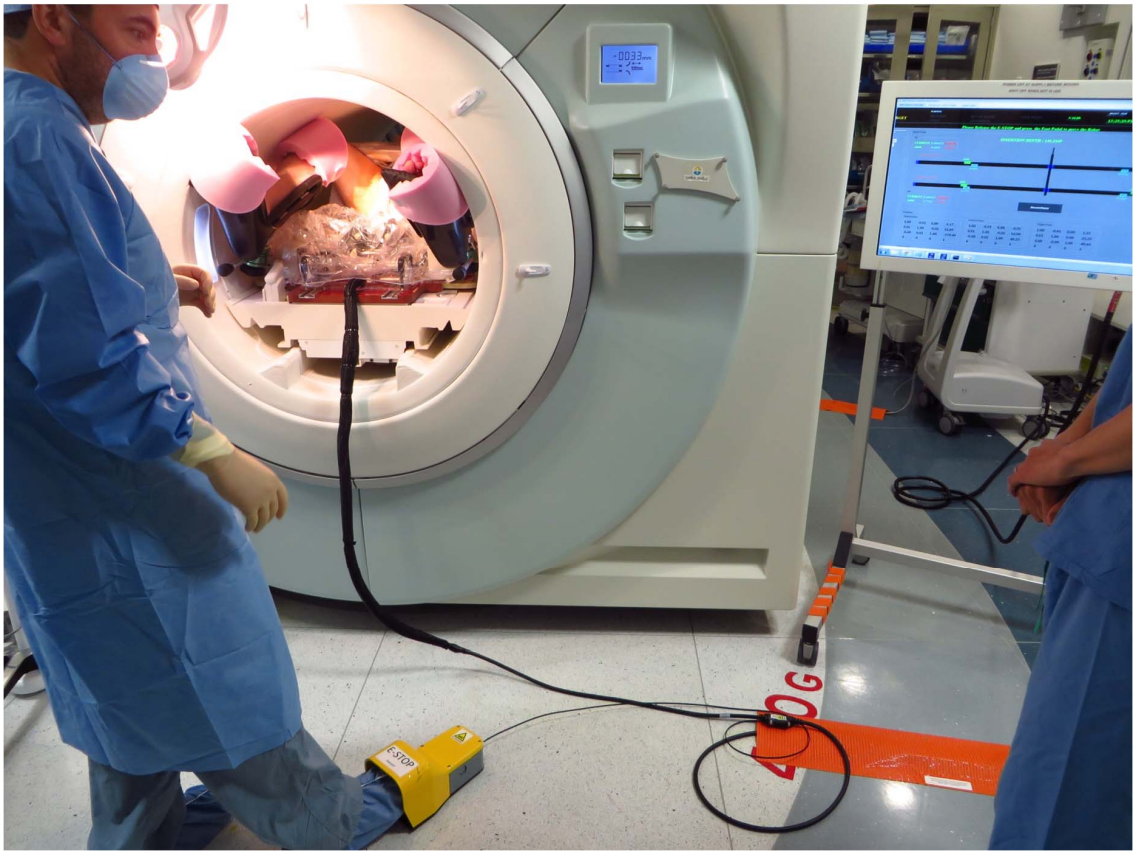


Figure 5.21: Dr. Kemal Tuncali from BWH is operating the robot during a clinical prostate biopsy case.

Two generations of limit switches are design for the important safety and accuracy considerations. To be fully ready for clinical use, comprehensive pre-clinical evaluations of the system are performed. MRI-compatibility of the system is evaluated in a 3 Tesla MRI scanner, showing the SNR loss of less than 18%. The accuracy of this robotic system is tested to be with an in plane translational RMS error of 1.402 mm at the needles tip, which satisfactorily meets the requirement of 10 mm. The first two clinical trials of the robot performing prostate biopsy have been conducted at Brigham and Women's Hospital (BWH) in Boston in May, 2014. The procedure

time of the robot-assisted cases is found to be shorter than the time of manual cases. It is still too early to make conclusion on the speed of the procedure since only two cases are performed. But it is expected to be faster as the surgeon and assistants are getting familiar with this robotic system.

# Chapter 6

# Conclusions and Future Extension

## 6.1 Summary of Work and Contributions

### 6.1.1 Summary of Work

This dissertation discusses the development of teleoperation technologies for MRI. Different key components of an example teleoperation approach for MRI are presented. A clinical grade robot assisted device is also introduced with clinical trials performed. A summary of this work is presented below.

- **System Architecture and Workflow for MRI-Guided Teleoperation System**

  The architecture of the system is developed with the modular hardware and software system that the MRI-compatible teleoperation with real-time MRI-

guidance is reached. The system architecture consists of different modules including MRI-compatible robot controller, master/slave robots, registration and control/visualization software. A workflow is proposed for clinical procedure for the application of performing teleoperated prostate biopsy.

- **Registration and Tracking Methods for MRI-Guided Interventions**

  Two approaches of fiducial type registration and tracking methods are developed. One of the methods utilizes the existing z shaped fiducial frame design but we propose a multi-image registration algorithm which has sub-pixel accuracy with a smaller fiducial frame. It is also proven to be more accurate than other single-image registration methods with the same Z-frame. The second method is a new design with a cylindrical shaped fiducial frame which is especially suitable for registration and tracking for needles. Alongside, a single-image based algorithm is developed to not only reach higher accuracy but also run faster. In addition, a feasibility study done here shows that with self-resonance coils attached, the CHIC fiducial frame gives even better imaging result that could significantly increase the fiducial imaging speed to have better real-time tracking performance.

- **MRI-Guided Teleoperation for Prostate Needle Interventions**

  A surgical master-slave teleoperation system for the application of percutaneous interventional procedures under continuous MRI-guidance is presented.

This system consists of a piezoelectrically actuated slave robot for needle placement with integrated fiber optic force sensor utilizing FPI sensing principle. The sensor flexure is optimized by FEA and embedded to the slave robot for measuring needle insertion force. A novel, compact opto-mechanical FPI sensor interface is also integrated into the MRI-compatible robot control system. A pneumatical-actuated haptic master robot is developed to render the force associated with needle placement interventions to the surgeon. An aluminum load cell is implemented and calibrated to close the impedance control loop of the master robot. Force-position control algorithms are developed to control the hybrid actuated system. Force and position tracking results of the master-slave robot are demonstrated to validate the tracking performance of the integrated system. MRI-compatibility is thoroughly evaluated and teleoperated needle steering with force feedback is demonstrated under live MR imaging, where the slave robot resides in the scanner bore and the user manipulates the master beside the patient outside the bore.

- **Robot Control of Clinical Grade Needle Placement Robot for Transperineal Prostate Interventions**

  The control of robotic system for clinical transperineal prostate interventions under live MRI-guidance is developed. The proposed modular system communicates between each module and with MRI system by network through OpenIGTLink. A 4-DOF robot with parallel mechanism is designed for needle

placement with ultrasonic motors and is precisely controlled by a custom MRI-compatible robot controller. Two generations of limit switches are design for the important safety and accuracy considerations. To be fully ready for clinical use, comprehensive pre-clinical evaluations of the system are performed. MRI-compatibility of the system is evaluated in a 3 Tesla MRI scanner, showing the SNR loss of less than 18%. The accuracy of this robotic system is tested to be with an in plane translational RMS error of 1.402 mm at the needles tip. The first two clinical trials of the robot performing prostate biopsy have been conducted at Brigham and Women's Hospital (BWH) in Boston in May, 2014.

### 6.1.2 Dissertation Contributions

The major contributions of this dissertation are as follows.

- System architecture for general MRI-compatible teleoperated robotic system with real-time MRI-guidance is designed by using modular functional software and hardware parts. A feasible workflow of clinical procedure for performing teleoperated prostate biopsy is proposed with minimal modification from current clinical procedure.

- Two different robot registration and tracking technologies are developed with fiducial based method. A multi-image registration method with a smaller Z shaped fiducial frame is proposed with sub-pixel accuracy. It is proven to be

more accurate than other single-image registration methods.

- A new reconfigurable cylindrical helix imaging coordinate (CHIC) fiducial frame is designed. Its registration algorithm is also developed. In addition, a performance enhanced CHIC fiducial frame with integrated passive self-resonance coils is also studied. Its great potential of improving the performance of current tracking method is shown by the feasibility study.

- An approach of master-slave teleoperation system is developed with hybird piezoelectric and pneumatic actuation technologies. A piezoelectric-actuated slave robot is designed with 3-DOF stage for aligning the robot to hold another 3-DOF needle driver for needle steering. A 2-DOF pneumatic-driven master device with load cell force sensor is designed to interact with human user with haptic feedback.

- A novel FPI fiber optic force sensor is designed and integrated into the slave robot for needle insertion force sensing. And a compact opto-mechanical system is developed.

- A bilateral control scheme and an impedance control scheme are designed. The performance of the teleoperation system is evaluated analytically. The position and force tracking accuracy and bandwidth are examined.

- The performance of the teleoperation system inside MRI is evaluated, which includes thorough analysis of the MRI-compatibility; teleoperated needle steer-

ing inside MRI with teleoperated insertion and autonomous steering; 2-DOF teleoperated needle steering inside MRI and force feedback.

- A system control architecture of a clinical grade 4-DOF surgical manipulator is developed. Two generations of limit switch are designed and evaluated. The extensive per-clinical evaluation of the system is performed with MRI accuracy assessment and MRI-compatibility test.

- Conducted two clinical prostate biopsy trials with the clinical grade 4-DOF surgical robotic system.

## 6.2 Impact and Future Work

Teleoperation is highly desired inside MRI not only for prostate needle interventions, but also for other applications such as brain and liver interventions, because it could release the surgeon from highly constrained workspace without losing the control of the critical steps of the surgery.

By combining the use of force sensors and actuators, force perception, which is removed by introducing teleoperation, is re-enabled and brought back to human. It is a crucial feature for safety that could prevent human user from performing undesired motion such as moving too fast or hitting bones by the needle. To our knowledge, this is the first development for MRI-guided surgical applications with force feedback by utilizing hybrid pneumatic-piezoelectric actuation for master-slave

control, respectively.

However, to reach the goal of clinical use, there is still work to be done in the future. Although the clinical workflow and sterilization have both been addressed, they are still pending for practical examination in the MRI room with surgeon. The FPI force sensor has been demonstrated with its dynamic properties and actual performance in this dissertation but the calibration procedure could still be made automatic and the temperature compensation is required to prevent it from floating when temperature changes to be actually used in clinical procedure. And most importantly, the master haptic device should be intuitive that it should make no confusion to users.

Enabling teleoperation inside MRI room with real-time imaging opens up the doors to many potential research directions. As mentioned before, it could be easily expanded to the applications like liver and neuro surgeries such as teleoperated deep brain stimulation and brain tumor ablation. It is also possible to combine dosimetry and thermal planning with teleoperated radio or thermal therapy. With the demonstrated preliminary result for real-time MRI-guided teleoperated needle steering in this dissertation, more valuable research could be established such as the control of teleoperated needle steering, real-time needle path planning, needle curve and tissue modeling. They are currently being studied in our group. But so far, no one has done the needle shape estimation and path planning with the fused information from both MR images and force sensors.

Combining with the CHIC tracking fiducial discussed in this dissertation, needle

tracking and imaging plan control would become easier and more accurate inside the MRI room by placing the tracking fiducial coaxial with the needle to eliminate the errors introduced by robot kinematics. This fiducial design is not only for MRI guided devices, but also for the applications with other imaging modalities such as CT or US. Another way to improve the performance of the needle steering with MRI is to improve the tracking speed which is highly related to the imaging speed. Segmenting the needle from MR images is harder with faster acquired MR images but the contract of the fiducial could remain high on those images by using self-resonant coils. Preliminary results have already shown the potential of fiducial with self-resonant coils in this dissertation but more research needs to be done to make it more reliable.

Specifically about the fiducial design, it is interesting to find out the relationship between the fiducial size, image used for one-time registration and the accuracy. Initial thought is that smaller cross section would decrease the error produced during the finding of centroids of the fiducial points but it also increases the difficulty of distinguishing and locating the fiducial center. Finally, the combination of fiducial, image based needle segmentation and force sensor based needle shape estimation would definitely bring us much better needle tracking performance.

## 6.3 Lessons Learned

It is always feeling great to see what you've made actually benefits others but the efforts behind it are not costless. It is easy to just follow the instinct when developing something because we all believe that our design would be the best. But if it is designed for a group of people with specific specialties and needs, nothing is more important than learning their requirements. When we designed our robot for the clinical purpose, the control software was made with full of transformation matrices and buttons which allows the user to do whatever they want because we really didnt know what they need and what is the real clinical procedure. After several discussions with surgeons and observing the real prostate biopsy cases, the software user interface was changed with graphical design and only with three buttons left.

It also applies on the hardware side. The robot and controller were all added with LEDs indicating robot's current status including the limit switch status, motor status and targeting status. They look like with no technical contribution at all, but actually work really well for the clinicians. Those are all things which couldn't ignore on the way to our first two clinical trials.

On the other hand, it is always desired to be on the edge of the technology and design something which is novel such as force feedback for teleoperation in MRI. Cutting-edge is often with debates such as the recent discussion on the self-driven vehicles and the drones about their reliability and regulation issues. For us, it is the force feedback for medical robots. Even the most successful medical robot in the market now is still

without force feedback. It is not about the lack of technology but about bringing the most realistic feeling to the user without distraction and confusion. We have the same problem with designing our MRI guided teleoperation system with force feedback. The force feedback is demonstrated but is still easy to get misinterpreted and not very reliable yet. This is definitely what we need to face when designing something which is critical to human life but it shouldn't be the barrier, instead, it should be the driving power for us to push the technology forward.

# Bibliography


[1] V. Horsley and R. Clarke, "The structure and functions of the cerebellum examined by a new method," *Brain: A Journal of Neurology*, p. 45, 1908.

[2] F. A. Jolesz, *Intraoperative imaging and image-guided therapy.* Springer Science & Business Media, 2014.

[3] R. Fu, W. W. Brey, K. Shetty, P. Gorkov, S. Saha, J. R. Long, S. C. Grant, E. Y. Chekmenev, J. Hu, Z. Gan, M. Sharma, F. Zhang, T. M. Logan, R. Brschweller, A. Edison, A. Blue, I. R. Dixon, W. D. Markiewicz, and T. A. Cross, "Ultra-wide bore 900 MHz high-resolution NMR at the national high magnetic field laboratory," *Journal of Magnetic Resonance*, vol. 177, no. 1, pp. 1–8, 2005.

[4] F. A. Jolesz, P. R. Morrison, S. J. Koran, R. J. Kelley, S. G. Hushek, R. W. Newman, M. P. Fried, A. Melzer, R. M. M. Seibel, and H. Jalahej, "Compatible instrumentation for intraoperative MRI: expanding resources," *Journal of Magnetic Resonance Imaging*, vol. 8, no. 1, pp. 8–11, 1998.

[5] ASTM, "Standard practice for marking medical devices and other items for safety in the magnetic resonance environment," *The American Society for Testing and Materials (ASTM)*, vol. F2503-13, 2013.

[6] D. Stoianovici, "Multiimager compatible actuation principles in surgical robotics," *The International Journal of Medical Robotics and Computer Assisted Surgery*, vol. 1, no. 2, pp. 86–100, 2005.

[7] K. Masamune, E. Kobayashi, Y. Masutani, M. Suzuki, T. Dohi, H. Iseki, and K. Takakura, "Development of an MRI-compatible needle insertion manipulator for stereotactic neurosurgery," *Computer Aided Surgery*, vol. 1, no. 4, pp. 242–248, 1995.

[8] G. S. Fischer, S. DiMaio, I. Iordachita, and G. Fichtinger, *Robotic assistant for transperineal prostate interventions in 3T closed MRI*, ser. Lecture Notes in Computer Science. Springer Berlin Heidelberg, 2007, vol. 4791, book section 52, pp. 425–433.

[9] G. S. Fischer, A. Krieger, I. Iordachita, C. Csoma, L. Whitcomb, and G. Fichtinger, "MRI compatibility of robot actuation techniquesa comparative study," *Medical Image Computing and Computer-Assisted InterventionMICCAI 2008*, pp. 509–517, 2008.

[10] Y. Chen, C. D. Mershon, and Z. T. H. Tse, "A 10-mm MR-conditional unidirectional pneumatic stepper motor," *Mechatronics, IEEE/ASME Transactions on*, vol. PP, no. 99, pp. 1–7, 2014.

[11] D. Stoianovici, K. Chunwoo, G. Srimathveeravalli, P. Sebrecht, D. Petrisor, J. Coleman, S. B. Solomon, and H. Hricak, "MRI-safe robot for endorectal prostate biopsy," *Mechatronics, IEEE/ASME Transactions on*, vol. 19, no. 4, pp. 1289–1299, 2014.

[12] B. Yang, U. X. Tan, A. B. McMillan, R. Gullapalli, and J. P. Desai, "Design and control of a 1-DOF MRI-compatible pneumatically actuated robot with long transmission lines," *Mechatronics, IEEE/ASME Transactions on*, vol. 16, no. 6, pp. 1040–1048, 2011.

[13] Y. Wang, H. Su, K. Harrington, and G. S. Fischer, "Sliding mode control of piezoelectric valve regulated pneumatic actuator for MRI-compatible robotic intervention," in *ASME Dynamic Systems and Control Conference-DSCC*, Conference Proceedings.

[14] B. Yang, U. X. Tan, A. McMillan, R. Gullapalli, and J. P. Desai, "Design and implementation of a pneumatically-actuated robot for breast biopsy under continuous MRI," in *Robotics and Automation, 2011. Proceedings. ICRA '11. 2011 IEEE International Conference on*, Conference Proceedings, pp. 674–679.

[15] Y. Koseki, T. Washio, K. Chinzei, and H. Iseki, *Endoscope manipulator for trans-nasal neurosurgery, optimized for and compatible to vertical field open MRI.* Springer, 2002, pp. 114–121.

[16] S. Sang-Eun, J. Tokuda, K. Tuncali, C. M. Tempany, E. Zhang, and N. Hata, "Development and preliminary evaluation of a motorized needle guide template for MRI-guided targeted prostate biopsy," *Biomedical Engineering, IEEE Transactions on*, vol. 60, no. 11, pp. 3019–3027, 2013.

[17] G. Cole, J. Pilitsis, and G. S. Fischer, "Design of a robotic system for MRI-guided deep brain stimulation electrode placement," in *Robotics and Automation, 2009. Proceedings. ICRA '09. 2009 IEEE International Conference on.* IEEE, Conference Proceedings, pp. 4450–4456.

[18] R. Kokes, K. Lister, R. Gullapalli, B. Zhang, A. MacMillan, H. Richard, and J. P. Desai, "Towards a teleoperated needle driver robot with haptic feedback

for RFA of breast tumors under continuous MRI," *Medical Image Analysis*, vol. 13, no. 3, pp. 445–455, 2009.

[19] R. Gassert, R. Moser, E. Burdet, and H. Bleuler, "MRI/fMRI-compatible robotic system with force feedback for interaction with human motion," *Mechatronics, IEEE/ASME Transactions on*, vol. 11, no. 2, pp. 216–224, 2006.

[20] R. Seifabadi, S.-E. Song, A. Krieger, N. Cho, J. Tokuda, G. Fichtinger, and I. Iordachita, "Robotic system for MRI-guided prostate biopsy: feasibility of teleoperated needle insertion and ex vivo phantom study," *International Journal of Computer Assisted Radiology and Surgery*, vol. 7, no. 2, pp. 181–190, 2011.

[21] B. Yang, U. X. Tan, A. McMillan, R. Gullapalli, and J. Desai, *Towards the development of a master-slave surgical system for breast biopsy under continuous MRI*, ser. Springer Tracts in Advanced Robotics. Springer International Publishing, 2013, vol. 88, book section 38, pp. 565–577.

[22] W. Shang, H. Su, G. Li, and G. S. Fischer, "Teleoperation system with hybrid pneumatic-piezoelectric actuation for MRI-guided needle insertion with haptic feedback," in *Intelligent Robots and Systems (IROS), 2013 IEEE/RSJ International Conference on*. IEEE, Conference Proceedings, pp. 4092–4098.

[23] S. Hirose and K. Yoneda, "Development of optical six-axial force sensor and its signal calibration considering nonlinear interference," in *Robotics and Automation, 1990. Proceedings. ICRA '90. 1990 IEEE International Conference on*, Conference Proceedings, pp. 46–53 vol.1.

[24] H. Su and G. S. Fischer, "A 3-axis optical force/torque sensor for prostate needle placement in magnetic resonance imaging environments," in *Technologies for Practical Robot Applications, 2009. TePRA 2009. IEEE International Conference on*. IEEE, Conference Proceedings, pp. 5–9.

[25] I. Iordachita, Z. Sun, M. Balicki, J. Kang, S. Phee, J. Handa, P. Gehlbach, and R. Taylor, "A sub-millimetric, 0.25 mN resolution fully integrated fiber-optic force-sensing tool for retinal microsurgery," *International Journal of Computer Assisted Radiology and Surgery*, vol. 4, no. 4, pp. 383–390, 2009.

[26] W. Shang, H. Su, G. Li, C. Furlong, and G. S. Fischer, "A Fabry-Perot interferometry based MRI-compatible miniature uniaxial force sensor for percutaneous needle placement," in *Sensors, 2013 IEEE*. IEEE, Conference Proceedings, pp. 1–4.

[27] N. C. Institute, "What you need to know about prostate cancer," *U.S. Department of Health and Human Services, National Institutes of Health*, vol. NIH Publication No. 12-1576, 2012.

[28] R. P. Myers, "Structure of the adult prostate from a clinician's standpoint," *Clinical Anatomy*, vol. 13, no. 3, pp. 214–215, 2000.

[29] R. Siegel, J. Ma, Z. Zou, and A. Jemal, "Cancer statistics, 2014," *CA: A Cancer Journal for Clinicians*, vol. 64, no. 1, pp. 9–29, 2014.

[30] J. C. Presti Jr, "Prostate cancer: assessment of risk using digital rectal examination, tumor grade, prostate-specific antigen, and systematic biopsy," *Radiologic Clinics of North America*, vol. 38, no. 1, pp. 49–58, 2000.

[31] K. A. Roehl, J. A. V. Antenor, and W. J. Catalona, "Serial biopsy results in prostate cancer screening study," *The Journal of urology*, vol. 167, no. 6, pp. 2435–2439, 2002.

[32] J. C. Presti Jr, G. J. ODowd, M. C. Miller, R. Mattu, and R. W. Veltri, "Extended peripheral zone biopsy schemes increase cancer detection rates and minimize variance in prostate specific antigen and age related cancer rates: results of a community multi-practice study," *The Journal of Urology*, vol. 169, no. 1, pp. 125–129, 2003.

[33] J. Tokuda, S. E. Song, G. S. Fischer, I. Iordachita, R. Seifabadi, N. B. Cho, K. Tuncali, G. Fichtinger, C. M. Tempany, and N. Hata, "Preclinical evaluation of an MRI-compatible pneumatic robot for angulated needle placement in transperineal prostate interventions," *Int J Comput Assist Radiol Surg*, vol. 7, no. 6, pp. 949–57, 2012.

[34] A. V. D'Amico, R. Cormack, S. Kumar, and C. M. Tempany, "Real-time magnetic resonance imaging-guided brachytherapy in the treatment of selected patients with clinically localized prostate cancer," *Journal of endourology*, vol. 14, no. 4, pp. 367–370, 2000.

[35] G. Fichtinger, T. L. DeWeese, A. Patriciu, A. Tanacs, D. Mazilu, J. H. Anderson, K. Masamune, R. H. Taylor, and D. Stoianovici, "System for robotically assisted prostate biopsy and therapy with intraoperative CT guidance," *Academic Radiology*, vol. 9, no. 1, pp. 60–74, 2002.

[36] H. S. Bassan, R. V. Patel, and M. Moallem, "A novel manipulator for percutaneous needle insertion: Design and experimentation," *Mechatronics, IEEE/ASME Transactions on*, vol. 14, no. 6, pp. 746–761, 2009.

[37] J. Vogan, A. Wingert, J. S. Plante, S. Dubowsky, M. Hafez, D. Kacher, and F. Jolesz, "Manipulation in MRI devices using electrostrictive polymer actuators: with an application to reconfigurable imaging coils," in *Robotics and Automation, 2004. Proceedings. ICRA '04. 2004 IEEE International Conference on*, vol. 3, Conference Proceedings, pp. 2498–2504 Vol.3.

[38] A. Khanicheh, A. Muto, C. Triantafyllou, B. Weinberg, L. Astrakas, A. Tzika, and C. Mavroidis, "MR compatible erf driven hand rehabilitation device," in *Rehabilitation Robotics, 2005. ICORR 2005. 9th International Conference on*, Conference Proceedings, pp. 7–12.

[39] H. Mingyen, A. B. McMillan, J. M. Simard, R. Gullapalli, and J. P. Desai, "Toward a meso-scale SMA-actuated MRI-compatible neurosurgical robot," *Robotics, IEEE Transactions on*, vol. 28, no. 1, pp. 213–222, 2012.

[40] P. Vartholomeos, L. Qin, and P. E. Dupont, "MRI-powered actuators for robotic interventions," in *Intelligent Robots and Systems (IROS), 2011 IEEE/RSJ International Conference on*, Conference Proceedings, pp. 4508–4515.

[41] N. Yu, C. Hollnagel, A. Blickenstorfer, S. S. Kollias, and R. Riener, "Comparison of MRI-compatible mechatronic systems with hydrodynamic and pneumatic actuation," *Mechatronics, IEEE/ASME Transactions on*, vol. 13, no. 3, pp. 268–277, 2008.

[42] I. Sato, R. Nakamura, and K. Masamune, "MRI compatible manipulator with MRI-guided needle insertion support system," in *Micro-NanoMechatronics and Human Science (MHS), 2010 International Symposium on*, Conference Proceedings, pp. 77–82.

[43] G. S. Fischer, I. Iordachita, C. Csoma, J. Tokuda, P. W. Mewes, C. M. Tempany, N. Hata, and G. Fichtinger, "Pneumatically operated MRI-compatible needle placement robot for prostate interventions," in *Robotics and Automation, 2008. Proceedings. ICRA '08. 2008 IEEE International Conference on.* IEEE, Conference Proceedings, pp. 2489–2495.

[44] Y. Wang, "MRI-compatible pneumatic actuation control algorithm evaluation and test system development," *M.S. Thesis, Worcester Polytechnic Institute, Worcester, MA*, 2010.

[45] G. Cole, K. Harrington, H. Su, A. Camilo, J. Pilitsis, and G. S. Fischer, "Closed-loop actuated surgical system utilizing real-time in-situ MRI guidance," in *12th International Symposium on Experimental Robotics-ISER*, Conference Proceedings, pp. 2489–2495.

[46] Y. Wang, G. A. Cole, H. Su, J. G. Pilitsis, and G. S. Fischer, "MRI compatibility evaluation of a piezoelectric actuator system for a neural interventional robot," in *Engineering in Medicine and Biology Society, 2009. EMBC 2009. Annual International Conference of the IEEE.* IEEE, Conference Proceedings, pp. 6072–6075.

[47] N. Nathoo, M. C. avusoglu, M. A. Vogelbaum, and G. H. Barnett, "In touch with robotics: neurosurgery for the future," *Neurosurgery*, vol. 56, no. 3, 2005.

[48] M. Li, A. Kapoor, D. Mazilu, and K. A. Horvath, "Pneumatic actuated robotic assistant system for aortic valve replacement under MRI guidance," *Biomedical Engineering, IEEE Transactions on*, vol. 58, no. 2, pp. 443–451, 2011.

[49] A. Krieger, S. E. Song, N. B. Cho, I. Iordachita, P. Guion, G. Fichtinger, and L. L. Whitcomb, "Development and evaluation of an actuated MRI-compatible robotic system for MRI-guided prostate intervention," *IEEE ASME Trans Mechatron*, vol. 18, no. 1, pp. 273–284, 2012.

[50] G. S. Fischer, I. Iordachita, C. Csoma, J. Tokuda, S. P. DiMaio, C. M. Tempany, N. Hata, and G. Fichtinger, "MRI-compatible pneumatic robot for transperineal prostate needle placement," *Mechatronics, IEEE/ASME Transactions on*, vol. 13, no. 3, pp. 295–305, 2008.

[51] N. V. Tsekos, A. Khanicheh, E. Christoforou, and C. Mavroidis, "Magnetic resonance-compatible robotic and mechatronics systems for image-guided interventions and rehabilitation: a review study," *Annu. Rev. Biomed. Eng.*, vol. 9, pp. 351–387, 2007.

[52] H. Elhawary, A. Zivanovic, B. Davies, and M. Lamperth, "A review of magnetic resonance imaging compatible manipulators in surgery," *Proceedings of the Institution of Mechanical Engineers, Part H: Journal of Engineering in Medicine*, vol. 220, no. 3, pp. 413–424, 2006.

[53] M. Turkseven and J. Ueda, "Design of an MRI compatible haptic interface," in *Intelligent Robots and Systems (IROS), 2011 IEEE/RSJ International Conference on*, Conference Proceedings, pp. 2139–2144.

[54] M. Hara, G. Matthey, A. Yamamoto, D. Chapuis, R. Gassert, H. Bleuler, and T. Higuchi, "Development of a 2-DOF electrostatic haptic joystick for MRI/fMRI applications," in *Robotics and Automation, 2009. Proceedings. ICRA '09. 2009 IEEE International Conference on*, Conference Proceedings, pp. 1479–1484.

[55] R. Seifabadi, I. Iordachita, and G. Fichtinger, "Design of a teleoperated needle steering system for MRI-guided prostate interventions," in *Biomedical Robotics and Biomechatronics (BioRob), 2012 4th IEEE RAS EMBS International Conference on*, Conference Proceedings, pp. 793–798.

[56] Z. T. H. Tse, H. Elhawary, M. Rea, B. Davies, I. Young, and M. Lamperth, "Haptic needle unit for MR-guided biopsy and its control," *Mechatronics, IEEE/ASME Transactions on*, vol. 17, no. 1, pp. 183–187, 2012.

[57] S. Zuo, K. Masamune, K. Kuwana, M. Tomikawa, S. Ieiri, T. Ohdaira, M. Hashizume, and T. Dohi, *Nonmetallic RigidFlexible Outer Sheath with Pneumatic Shapelocking Mechanism and Double Curvature Structure*, ser. Lecture Notes in Computer Science. Springer Berlin Heidelberg, 2011, vol. 6891, book section 22, pp. 169–177.

[58] A. Melzer, B. Gutmann, T. Remmele, R. Wolf, A. Lukoscheck, M. Bock, H. Bardenheuer, and H. Fischer, "Innomotion for percutaneous image-guided interventions," *Engineering in Medicine and Biology Magazine, IEEE*, vol. 27, no. 3, pp. 66–73, 2008.

[59] N. Zemiti, I. Bricault, C. Fouard, B. Sanchez, and P. Cinquin, "Lpr: A ct and MR-compatible puncture robot to enhance accuracy and safety of image-guided interventions," *Mechatronics, IEEE/ASME Transactions on*, vol. 13, no. 3, pp. 306–315, 2008.

[60] I. Bricault, N. Zemiti, E. Jouniaux, C. Fouard, E. Taillant, F. Dorandeu, and P. Cinquin, "Light puncture robot for CT and MRI interventions," *Engineering in Medicine and Biology Magazine, IEEE*, vol. 27, no. 3, pp. 42–50, 2008.

[61] N. V. Tsekos, E. Yacoub, P. V. Tsekos, I. G. Koutlas, B. T. Larson, and A. G. Erdman, "Design of an MRI-compatible robotic stereotactic device for minimally invasive interventions in the breast," *Journal of Biomechanical Engineering*, vol. 126, no. 4, pp. 458–465, 2004, 10.1115/1.1785803.

[62] E. G. Christoforou, I. Seimenis, E. Andreou, and N. V. Tsekos, "Development and initial testing of a general-purpose, MR-compatible, manually-actuated manipulator for image-guided interventions," in *Biomedical Robotics and Biomechatronics (BioRob), 2012 4th IEEE RAS and EMBS International Conference on*, Conference Proceedings, pp. 737–742.

[63] R. Gassert, E. Burdet, and K. Chinzei, "Opportunities and challenges in MR-compatible robotics," *Engineering in Medicine and Biology Magazine, IEEE*, vol. 27, no. 3, pp. 15–22, 2008.

[64] R. Gassert, A. Yamamoto, D. Chapuis, L. Dovat, H. Bleuler, and E. Burdet, "Actuation methods for applications in MR environments," *Concepts in Magnetic Resonance Part B: Magnetic Resonance Engineering*, vol. 29B, no. 4, pp. 191–209, 2006.

[65] K. Chinzei and K. Miller, "Towards MRI guided surgical manipulator," *Medical science monitor*, vol. 7, no. 1, pp. 153–163, 2001.

[66] Y. Sekiguchi, Y. Kobayashi, H. Watanabe, Y. Tomono, T. Noguchi, Y. Takahashi, K. Toyoda, M. Uemura, S. Ieiri, and T. Ohdaira, "In vivo experiments

of a surgical robot with vision field control for single port endoscopic surgery," in *Engineering in Medicine and Biology Society, EMBC, 2011 Annual International Conference of the IEEE*. IEEE, Conference Proceedings, pp. 7045–7048.

[67] M. Beck, T. Mittlmeier, P. Gierer, C. Harms, and G. Gradl, "Benefit and accuracy of intraoperative 3D-imaging after pedicle screw placement: a prospective study in stabilizing thoracolumbar fractures," *European Spine Journal*, vol. 18, no. 10, pp. 1469–1477, 2009.

[68] C. R. Grindle, J. M. Curry, M. D. Kang, J. J. Evans, and M. R. Rosen, "Preoperative magnetic resonance imaging protocol for endoscopic cranial base image-guided surgery," *American journal of otolaryngology*, vol. 32, no. 6, pp. 451–454, 2011.

[69] A. Krieger, I. I. Iordachita, P. Guion, A. K. Singh, A. Kaushal, C. Menard, P. A. Pinto, K. Camphausen, G. Fichtinger, and L. L. Whitcomb, "An MRI-compatible robotic system with hybrid tracking for MRI-guided prostate intervention," *Biomedical Engineering, IEEE Transactions on*, vol. 58, no. 11, pp. 3049–3060, 2011.

[70] J. A. Derbyshire, G. A. Wright, R. M. Henkelman, and R. S. Hinks, "Dynamic scanplane tracking using MR position monitoring," *Journal of Magnetic Resonance Imaging*, vol. 8, no. 4, pp. 924–932, 2005.

[71] C. M. Hillenbrand, D. R. Elgort, E. Y. Wong, A. Reykowski, F. K. Wacker, J. S. Lewin, and J. L. Duerk, "Active device tracking and highresolution intravascular MRI using a novel catheterbased, opposedsolenoid phased array coil," *Magnetic resonance in medicine*, vol. 51, no. 4, pp. 668–675, 2004.

[72] F. K. Wacker, C. M. Hillenbrand, J. L. Duerk, and J. S. Lewin, "MR-guided endovascular interventions: device visualization, tracking, navigation, clinical applications, and safety aspects," *Magnetic resonance imaging clinics of North America*, vol. 13, no. 3, p. 431, 2005.

[73] A. Krieger, G. Metzger, G. Fichtinger, E. Atalar, and L. Whitcomb, "A hybrid method for 6-DOF tracking of MRI-compatible robotic interventional devices," in *Robotics and Automation, 2006. ICRA '06. Proceedings 2006 IEEE International Conference on*. IEEE, Conference Proceedings, pp. 3844–3849.

[74] M. Burl, G. A. Coutts, and I. R. Young, "Tuned fiducial markers to identify body locations with minimal perturbation of tissue magnetization," *Magnetic resonance in medicine*, vol. 36, no. 3, pp. 491–493, 1996.

[75] G. A. Coutts, D. J. Gilderdale, M. Chui, L. Kasuboski, and N. M. Desouza, "Integrated and interactive position tracking and imaging of interventional tools

and internal devices using small fiducial receiver coils," *Magnetic resonance in medicine*, vol. 40, no. 6, pp. 908–913, 1998.

[76] M. Rea, D. McRobbie, H. Elhawary, Z. T. Tse, M. Lamperth, and I. Young, "Sub-pixel localisation of passive micro-coil fiducial markers in interventional MRI," *Magnetic Resonance Materials in Physics, Biology and Medicine*, vol. 22, no. 2, pp. 71–76, 2009.

[77] S. DiMaio, E. Samset, G. S. Fischer, I. Iordachita, G. Fichtinger, F. Jolesz, and C. Tempany, "Dynamic MRI scan plane control for passive tracking of instruments and devices," *Medical Image Computing and Computer-Assisted InterventionMICCAI 2007*, pp. 50–58, 2007.

[78] R. Susil, J. Anderson, and R. Taylor, "A single image registration method for CT guided interventions," in *Medical Image Computing and Computer-Assisted InterventionMICCAI99*. Springer, Conference Proceedings, pp. 798–808.

[79] S. Lee, G. Fichtinger, and G. S. Chirikjian, "Numerical algorithms for spatial registration of line fiducials from cross-sectional images," *Medical Physics*, vol. 29, p. 1881, 2002.

[80] W. Shang and G. S. Fischer, "A high accuracy multi-image registration method for tracking MRI-guided robots," in *Proc. of SPIE Vol*, vol. 8316, Conference Proceedings, pp. 83 161V–1.

[81] A. Patriciu, D. Petrisor, M. Muntener, D. Mazilu, M. Schr, and D. Stoianovici, "Automatic brachytherapy seed placement under MRI guidance," *IEEE transactions on bio-medical engineering*, vol. 54, no. 8, p. 1499, 2007.

[82] H. Su, W. Shang, G. A. Cole, K. Harrington, and G. S. Fischer, "Haptic system design for MRI-guided needle based prostate brachytherapy," in *Haptics Symposium, 2010 IEEE*. IEEE, Conference Proceedings, pp. 483–488.

[83] R. Riener, T. Villgrattner, R. Kleiser, T. Nef, and S. Kollias, "fMRI-compatible electromagnetic haptic interface," in *Engineering in Medicine and Biology Society, 2005. IEEE-EMBS 2005. 27th Annual International Conference of the*, Conference Proceedings, pp. 7024–7027.

[84] D. Chapuis, X. Michel, R. Gassert, C. Chee-Meng, E. Burdet, and H. Bleuler, "A haptic knob with a hybrid ultrasonic motor and powder clutch actuator," in *EuroHaptics Conference, 2007 and Symposium on Haptic Interfaces for Virtual Environment and Teleoperator Systems. World Haptics 2007. Second Joint*, Conference Proceedings, pp. 200–205.

[85] T. L. Brooks, "Telerobotic response requirements," in *Systems, Man and Cybernetics, 1990. Conference Proceedings., IEEE International Conference on.* IEEE, Conference Proceedings, pp. 113–120.

[86] S. E. Salcudean, *Control for teleoperation and haptic interfaces.* Springer, 1998, pp. 51–66.

[87] R. Gassert, D. Chapuis, H. Bleuler, and E. Burdet, "Sensors for applications in magnetic resonance environments," *Mechatronics, IEEE/ASME Transactions on*, vol. 13, no. 3, pp. 335–344, 2008.

[88] D. Chapuis, R. Gassert, L. Sache, E. Burdet, and H. Bleuler, "Design of a simple MRI/fMRI compatible force/torque sensor," in *Intelligent Robots and Systems, 2004. (IROS 2004). Proceedings. 2004 IEEE/RSJ International Conference on*, vol. 3, Conference Proceedings, pp. 2593–2599 vol.3.

[89] N. Takahashi, M. Tada, J. Ueda, Y. Matsumoto, and T. Ogasawara, "An optical 6-axis force sensor for brain function analysis using fMRI," in *Sensors, 2003. Proceedings of IEEE*, vol. 1, Conference Proceedings, pp. 253–258 Vol.1.

[90] M. Tada and T. Kanade, "Development of an MR-compatible optical force sensor," in *Engineering in Medicine and Biology Society, 2004. IEMBS '04. 26th Annual International Conference of the IEEE*, vol. 1, Conference Proceedings, pp. 2022–2025.

[91] K. Chinzei, N. Hata, F. Jolesz, and R. Kikinis, *MR compatible surgical assist robot: system integration and preliminary feasibility study*, ser. Lecture Notes in Computer Science. Springer Berlin Heidelberg, 2000, vol. 1935, book section 95, pp. 921–930.

[92] M. Tada and T. Kanade, "Design of an MR-compatible three-axis force sensor," in *Intelligent Robots and Systems, 2005. (IROS 2005). 2005 IEEE/RSJ International Conference on*, Conference Proceedings, pp. 3505–3510.

[93] T. Tokuno, M. Tada, and K. Umeda, "High-precision MRI-compatible force sensor with parallel plate structure," in *Biomedical Robotics and Biomechatronics, 2008. BioRob 2008. 2nd IEEE RAS and EMBS International Conference on*, Conference Proceedings, pp. 33–38.

[94] P. Puangmali, K. Althoefer, and L. D. Seneviratne, "Mathematical modeling of intensity-modulated bent-tip optical fiber displacement sensors," *Instrumentation and Measurement, IEEE Transactions on*, vol. 59, no. 2, pp. 283–291, 2010.

[95] P. Polygerinos, A. Ataollahi, T. Schaeffter, R. Razavi, L. D. Seneviratne, and K. Althoefer, "MRI-compatible intensity-modulated force sensor for cardiac catheterization procedures," *Biomedical Engineering, IEEE Transactions on*, vol. 58, no. 3, pp. 721–726, 2011.

[96] P. Polygerinos, D. Zbyszewski, T. Schaeffter, R. Razavi, L. D. Seneviratne, and K. Althoefer, "MRI-compatible fiber-optic force sensors for catheterization procedures," *Sensors Journal, IEEE*, vol. 10, no. 10, pp. 1598–1608, 2010.

[97] S. B. Kesner and R. D. Howe, "Design principles for rapid prototyping forces sensors using 3-D printing," *Mechatronics, IEEE/ASME Transactions on*, vol. 16, no. 5, pp. 866–870, 2011.

[98] U. X. Tan, Y. Bo, R. Gullapalli, and J. P. Desai, "Triaxial MRI-compatible fiber-optic force sensor," *Robotics, IEEE Transactions on*, vol. 27, no. 1, pp. 65–74, 2011.

[99] P. Polygerinos, L. D. Seneviratne, R. Razavi, T. Schaeffter, and K. Althoefer, "Triaxial catheter-tip force sensor for MRI-guided cardiac procedures," *Mechatronics, IEEE/ASME Transactions on*, vol. 18, no. 1, pp. 386–396, 2013.

[100] J. Peirs, J. Clijnen, D. Reynaerts, H. V. Brussel, P. Herijgers, B. Corteville, and S. Boone, "A micro optical force sensor for force feedback during minimally invasive robotic surgery," *Sensors and Actuators A: Physical*, vol. 115, no. 23, pp. 447–455, 2004.

[101] P. Puangmali, H. Liu, L. D. Seneviratne, P. Dasgupta, and K. Althoefer, "Miniature 3-axis distal force sensor for minimally invasive surgical palpation," *Mechatronics, IEEE/ASME Transactions on*, vol. 17, no. 4, pp. 646–656, 2012.

[102] K. Yokoyama, H. Nakagawa, D. C. Shah, H. Lambert, G. Leo, N. Aeby, A. Ikeda, J. V. Pitha, T. Sharma, R. Lazzara, and W. M. Jackman, "Novel contact force sensor incorporated in irrigated radiofrequency ablation catheter predicts lesion size and incidence of steam pop and thrombus," *Circulation: Arrhythmia and Electrophysiology*, vol. 1, no. 5, pp. 354–362, 2008.

[103] P. Yong-Lae, R. Seok Chang, R. J. Black, K. K. Chau, B. Moslehi, and M. R. Cutkosky, "Exoskeletal force-sensing end-effectors with embedded optical fiber-Bragg-grating sensors," *Robotics, IEEE Transactions on*, vol. 25, no. 6, pp. 1319–1331, 2009.

[104] X. He, M. A. Balicki, J. U. Kang, P. L. Gehlbach, J. T. Handa, R. H. Taylor, and I. I. Iordachita, "Force sensing micro-forceps with integrated fiber Gragg grating for vitreoretinal surgery," vol. 8218, Conference Proceedings, pp. 82 180W–82 180W–7, 10.1117/12.909602, 2012.

[105] K. M. Moerman, A. M. J. Sprengers, A. J. Nederveen, and C. K. Simms, "A novel MRI compatible soft tissue indentor and fibre bragg grating force sensor," *Medical Engineering and Physics*, vol. 35, no. 4, pp. 486–499, 2013.

[106] P. Yong-Lae, S. Elayaperumal, B. Daniel, R. Seok Chang, S. Mihye, J. Savall, R. J. Black, B. Moslehi, and M. R. Cutkosky, "Real-time estimation of 3-D needle shape and deflection for MRI-guided interventions," *Mechatronics, IEEE/ASME Transactions on*, vol. 15, no. 6, pp. 906–915, 2010.

[107] S. Yin and P. Ruffin, *Fiber optic sensors*. John Wiley and Sons, Inc., 2006. [Online]. Available: http://dx.doi.org/10.1002/9780471740360.ebs0480

[108] H. Su, M. Zervas, C. Furlong, and G. S. Fischer, "A miniature MRI-compatible fiber-optic force sensor utilizing Fabry-Perot interferometer," *MEMS and Nanotechnology, Volume 4*, pp. 131–136, 2011.

[109] H. Su, M. Zervas, G. A. Cole, C. Furlong, and G. S. Fischer, "Real-time MRI-guided needle placement robot with integrated fiber optic force sensing," in *Robotics and Automation, 2011. Proceedings. ICRA '11. 2011 IEEE International Conference on*. IEEE, Conference Proceedings, pp. 1583–1588.

[110] H. Su, W. Shang, G. Cole, G. Li, K. Harrington, A. Camilo, J. Tokuda, C. M. Tempany, N. Hata, and G. S. Fischer, "Piezoelectrically actuated robotic system for MRI-guided prostate percutaneous therapy," *Mechatronics, IEEE/ASME Transactions on*, vol. (In press), 2014.

[111] G. Li, H. Su, G. A. Cole, W. Shang, K. Harrington, A. Camilo, J. G. Pilitsis, and G. S. Fischer, "Robotic system for MRI-guided stereotactic neurosurgery," *Biomedical Engineering, IEEE Transactions on*, vol. (In press), 2014.

[112] G. Li, H. Su, W. Shang, J. Tokuda, N. Hata, C. M. Tempany, and G. S. Fischer, "A fully actuated robotic assistant for MRI-guided prostate biopsy and brachytherapy," in *SPIE Medical Imaging*. International Society for Optics and Photonics, Conference Proceedings, pp. 867 117–867 117–8.

[113] H. Su, D. C. Cardona, W. Shang, A. Camilo, G. A. Cole, D. C. Rucker, R. J. Webster, and G. S. Fischer, "A MRI-guided concentric tube continuum robot with piezoelectric actuation: A feasibility study," in *Robotics and Automation, 2012. Proceedings. ICRA '12. 2012 IEEE International Conference on*, Conference Proceedings, pp. 1939–1945.

[114] H. Su, W. Shang, K. Harrington, A. Camilo, G. Cole, J. Tokuda, N. Hata, C. Tempany, and G. S. Fischer, "A networked modular hardware and software system for MRI-guided robotic prostate interventions," in *Proceedings of SPIE*, vol. 8316, Conference Proceedings, p. 83161Z.

[115] D. Yakar, M. G. Schouten, D. G. H. Bosboom, J. O. Barentsz, T. W. J. Scheenen, and J. J. Ftterer, "Feasibility of a pneumatically actuated MR-compatible robot for transrectal prostate biopsy guidance," *Radiology*, vol. 260, no. 1, pp. 241–247, 2011.

[116] C. Meeuwis, J. Veltman, H. Hall, R. M. Mus, C. Boetes, J. Barentsz, and R. Mann, "MR-guided breast biopsy at 3T: diagnostic yield of large core needle biopsy compared with vacuum-assisted biopsy," *European Radiology*, vol. 22, no. 2, pp. 341–349, 2012.

[117] J. Tokuda, K. Tuncali, I. Iordachita, S.-E. Song, A. Fedorov, S. Oguro, A. Lasso, F. M. Fennessy, C. M. Tempany, and N. Hata, "In-bore setup and software for 3T MRI-guided transperineal prostate biopsy," *Physics in medicine and biology*, vol. 57, no. 18, p. 5823, 2012.

[118] S. Eslami, G. S. Fischer, S. Sang-Eun, J. Tokuda, N. Hata, C. M. Tempany, and I. Iordachita, "Towards clinically optimized MRI-guided surgical manipulator for minimally invasive prostate percutaneous interventions: constructive design," in *Robotics and Automation, 2013. Proceedings. ICRA '13. 2013 IEEE International Conference on*, Conference Proceedings, pp. 1228–1233.

[119] J. Tokuda, G. S. Fischer, X. Papademetris, Z. Yaniv, L. Ibanez, P. Cheng, H. Liu, J. Blevins, J. Arata, A. J. Golby, T. Kapur, S. Pieper, E. C. Burdette, G. Fichtinger, C. M. Tempany, and N. Hata, "Openigtlink: an open network protocol for image-guided therapy environment," *The International Journal of Medical Robotics and Computer Assisted Surgery*, vol. 5, no. 4, pp. 423–434, 2009.

[120] F. Szufnarowski and A. Schneider, "Force control of a piezoelectric actuator based on a statistical system model and dynamic compensation," *Mechanism and Machine Theory*, vol. 46, no. 10, pp. 1507–1521, 2011.

[121] W. Shang, Y. Ma, I. Dobrev, H. Su, and G. S. Fischer, "Cylindrical helix imaging coordinate(CHIC) fiducial registration and tracking for minimally invasive surgical robots," *Biomedical Engineering, IEEE Transactions on.*, vol. (In review), 2014.

[122] Y. Ma, I. Dobrev, W. Shang, H. Su, S. R. Janga, and G. S. Fischer, "CHIC: Cylindrical helix imaging coordinate registration fiducial for MRI-guided interventions," in *Engineering in Medicine and Biology Society (EMBC), 2012 Annual International Conference of the IEEE*, Conference Proceedings, pp. 2808–2812.

[123] W. Ji, J. D. Matte, G. Li, Y. Ma, H. Su, W. Shang, and G. S. Fischer, "Reconfigurable fiducial-integrated modular needle driver for MRI-guided

percutaneous interventions," *Journal of Medical Devices*, vol. 7, no. 3, pp. 030 915–030 915, 2013, 10.1115/1.4024486.

[124] R. A. Brown, "A stereotactic head frame for use with ct body scanners," *Investigative radiology*, vol. 14, no. 4, pp. 300–304, 1979.

[125] R. A. Brown, T. S. Roberts, and A. G. Osborn, "Stereotaxic frame and computer software for CT-directed neurosurgical localization," *Investigative Radiology*, vol. 15, no. 4, pp. 308–312, 1980.

[126] N. Otsu, "A threshold selection method from gray-level histograms," *Automatica*, vol. 11, no. 285-296, pp. 23–27, 1975.

[127] J. Egger, J. Tokuda, L. Chauvin, B. Freisleben, C. Nimsky, T. Kapur, and W. Wells, "Integration of the openigtlink network protocol for imageguided therapy with the medical platform mevislab," *The International Journal of Medical Robotics and Computer Assisted Surgery*, 2012.

[128] C. Flask, D. Elgort, E. Wong, A. Shankaranarayanan, J. Lewin, M. Wendt, and J. L. Duerk, "A method for fast 3D tracking using tuned fiducial markers and a limited projection reconstruction fisp (lprfisp) sequence," *Journal of Magnetic Resonance Imaging*, vol. 14, no. 5, pp. 617–627, 2001.

[129] M. Rea, D. McRobbie, H. Elhawary, Z. T. H. Tse, M. Lamprth, and I. Young, "System for 3-D real-time tracking of MRI-compatible devices by image processing," *Mechatronics, IEEE/ASME Transactions on*, vol. 13, no. 3, pp. 379–382, 2008.

[130] N. A. Patel, T. v. Katwijk, G. Li, P. Moreira, W. Shang, S. Misra, and G. S. Fischer, "Closed-loop flexible needle steering with real-time MRI guidance," in *Robotics and Automation, 2015. Proceedings. ICRA '15. 2015 IEEE International Conference on*, vol. (In review), Conference Proceedings.

[131] G. Li, N. A. Patel, W. Shang, and G. S. Fischer, "Modeling of continuous uncoupled rotation velocity-independent (curv) asymmetric tip needle steering," in *Robotics and Automation, 2015. Proceedings. ICRA '15. 2015 IEEE International Conference on*, vol. (In review), Conference Proceedings.

[132] NEMA, "Determination of two-dimensional geometric distortion in diagnostic magnetic resonance images," *National Electrical Manufacturers Association Standards Publication MS*, vol. 2-2008, 2008.

[133] "Roctest limited, sensoptic fiber optic sensors Fabry-Perot strain gage models fos and fos-b instruction manual man-00051r1," 1999.

[134] T. K. Gangopadhyay, "Prospects for fibre Bragg gratings and Fabry-Perot interferometers in fibre-optic vibration sensing," *Sensors and Actuators A: Physical*, vol. 113, no. 1, pp. 20–38, 2004.

[135] C. Parthiban, C. Esser, and M. R. Zinn, "Evaluation of a parallel actuation approach for MR-compatible haptics," in *Haptics Symposium (HAPTICS), 2012 IEEE*, Conference Proceedings, pp. 563–570.

[136] NEMA, "Determination of signal-to-noise ratio (SNR) in diagnostic magnetic resonance imaging," *National Electrical Manufacturers Association Standards Publication MS*, pp. 1–2008, 2008.

[137] S. Eslami, W. Shang, G. Li, N. Patel, G. S. Fischer, J. Tokuda, N. Hata, C. M. Tempany, and I. Iordachita, "In-bore prostate transperineal interventions with an MRI-guided parallel manipulator: System development and preliminary evaluation," *International Journal of Medical Robotics and Computer Assisted Surgery*, vol. (In review), 2014.

[138] G. Tilak, K. Tuncali, S.-E. Song, J. Tokuda, O. Olubiyi, F. Fennessy, A. Fedorov, T. Penzkofer, C. Tempany, and N. Hata, "3T MR-guided in-bore transperineal prostate biopsy: A comparison of robotic and manual needle-guidance templates," *Journal of Magnetic Resonance Imaging*, 2014.